

Theoretical development and characterisation of a Josephson Traveling Wave Parametric Amplifier for very low power microwave signals

Original

Theoretical development and characterisation of a Josephson Traveling Wave Parametric Amplifier for very low power microwave signals / Greco, Angelo. - (2022 Oct 12), pp. 1-173.

Availability:

This version is available at: 11583/2972562 since: 2022-10-24T11:28:20Z

Publisher:

Politecnico di Torino

Published

DOI:

Terms of use:

openAccess

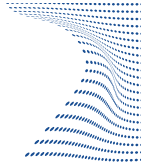
This article is made available under terms and conditions as specified in the corresponding bibliographic description in the repository

Publisher copyright

(Article begins on next page)



ScuDo
Scuola di Dottorato - Doctoral School
WHAT YOU ARE, TAKES YOU FAR



Doctoral Dissertation
Doctoral Program in Metrology (34.th cycle)

Theoretical development and characterisation of a Josephson Traveling Wave Parametric Amplifier for very low power microwave signals

Angelo Greco

* * * * *

Supervisors

PhD. E., Enrico

Doctoral Examination Committee:

PhD. Miano A., Referee, Yale University

PhD. Pashkin Y., Referee, Lancaster University

Politecnico di Torino

June 29, 2022

This thesis is licensed under a Creative Commons License, Attribution - Noncommercial-NoDerivative Works 4.0 International: see www.creativecommons.org. The text may be reproduced for non-commercial purposes, provided that credit is given to the original author.

I hereby declare that, the contents and organisation of this dissertation constitute my own original work and does not compromise in any way the rights of third parties, including those relating to the security of personal data.

.....

Angelo Greco
Turin, June 29, 2022

Summary

The technological progress in terms of micro and nano-fabrication, together with the growing ability to enhance the performance of superconducting materials allowed in the last two decades to practically incorporate the rules of quantum mechanics into 2-dimensional electrical circuits. This combination produced from one side ordered and controllable quantum systems, that can be engineered and built by default to observe in laboratory exotic quantum phenomena, and from the other side pushed a whole new branch of theoretical physics that joins quantum mechanics and electrical engineering.

In this thesis we address the problem of noiseless microwave amplification for very low power signals, eventually reaching the single photon level. We tackle this problem adopting an approach that relies on superconducting transmission lines, since these objects put together two fundamental ingredients, low temperatures and a lossless nature. The key physical aspect that we exploit to achieve lossless amplification is parametric amplification, which allows a natural energy transfer from different modes, eventually transferring power from a strong pump tone to a weak signal tone, that we actually mean to amplify. To engineer such a transmission line we adopt circuit-Quantum ElectroDynamics techniques, hence we treat quantum mechanically microscopic systems modeling them as electrical circuits. The fundamental feature of these devices is the presence of Josephson junctions, a lossless nonlinear element which confers the needed nonlinearity to the system to trigger the parametric amplification process.

In this work we develop a quantum mechanical theory to describe a nonlinear transmission line amplifier, named Josephson Traveling Wave Parametric Amplifier, that works both in 3-wave mixing and 4-wave mixing regime. We perform analytical simulations based on the output of the quantum model and find a set of circuit parameters to realise a physical layout. Using electromagnetic simulations we design and test sections of the transmission line in order to ensure the best impedance matching possible, and after that we fabricate and characterise the device in a cryogenic environment. The cryogenic characterisation reveals a working mixing effect between the internal modes but low gain and narrow bandwidth, meaning that some important features of the device are not fully caught by the analytic quantum theory. For this reason a modified numerical approach is used

to identify a working set of circuit parameters, together with a different structure of transmission line. The new circuit includes a periodic load of resonators that modifying the dispersion relation of the line avoids the creation of stray modes, which are a serious cause of gain reduction. This technique, which takes the name of Resonant Phase Matching, shows high gain in the numerical simulations, and we finally realise a physical layout of transmission line through an electromagnetic simulation approach.

Acknowledgements

I would like to acknowledge all the people from INRiM that helped me during my PhD period, in particular Roberto Rocci for being a loyal friend and a unique labmate.

Thanks to my colleagues from NPL, George, Jonathan, Tom and Kitty, for welcoming me so kindly and being patient with me.

Then thanks to all the project partners I had the chance to work with during these years. I have learnt a lot from them so I hope I could be somehow helpful too.

A mio padre

*che mi accompagnò per il tragitto ma
non varcò con me la soglia*

Contents

List of Tables	X
List of Figures	XI
1 Introduction	1
1.0.1 Motivations	1
2 Circuit Quantum Electrodynamics and Linear Amplifiers	11
2.1 Classical transmission line theory	11
2.2 Canonical quantization of the electromagnetic field	15
2.3 Quantization of a non-dissipative superconducting circuit	19
2.4 Linear amplifiers, quantum limits on added noise and parametric amplification	25
3 Josephson Traveling Wave Parametric Amplifier embedding rf-SQUIDs	31
3.1 Quantum model for a Josephson Traveling Wave Parametric Amplifier embedding rf-SQUIDs	31
3.1.1 Quantization of a Josephson Traveling Wave Parametric Amplifier	32
3.1.2 Three-Wave Mixing	46
3.1.3 Four-Wave Mixing	49
3.1.4 Time evolution of the ladder operators: coupled mode equations	52
3.1.5 Gain	59
3.1.6 Squeezing	64
3.2 JTWPA with high chromatic dispersion	67
3.2.1 Resonant Phase Matching	67
3.2.2 Coupled Mode Equations	72
4 Fabrication and cryogenic characterisation of JTWPAs	75
4.1 Fabrication and characterisation of JJs	75
4.2 Electromagnetic simulations for the layout definition of the JTWPA	81
4.2.1 L_g	85

4.2.2	L_{dist}	86
4.2.3	C_{dist}	88
4.2.4	C_{inter}	88
4.2.5	L_J and C_J	89
4.2.6	Characteristic impedance	90
4.3	Cryogenic measurements of JTWPA	95
4.4	Modeling JTWPA with RPM through CME	105
4.5	Layout definition of JTWPA with RPM through electromagnetic simulations	108
4.5.1	Resonator	109
4.5.2	L_g	110
4.5.3	L_J and C_J	110
4.5.4	Characteristic impedance	111
4.5.5	Cutoff	111
5	Conclusions and perspectives	115
A	Tables of circuital parameter sets	117
B	Curly brackets operators algebra and time derivatives	119
C	\hat{H}_N vs. $\delta\Phi$ in the second quantization regime	121
D	Curly brackets development and energy-conservative permutations selection	133
D.1	Development of the energy-conservative terms in 4WM	134
D.2	Self-phase, cross-phase and 4WM coupling constant	140
E	Solution of the coupled mode equations for $\hat{a}_s^{CR}(t)$ and $\hat{a}_i^{CR}(t)$	145
F	Identities for the squeezing spectrum calculation	149
G	Calculation of resonator plus C_g equivalent impedance	151
	Bibliography	153

List of Tables

A.1	Circuit parameters and magnetic field flux bias (working points) used for numerical evaluations in the Quantum Mechanical approach. . .	118
A.2	Circuit parameters used for numerical evaluations in the CME approach.	118

List of Figures

1.1	Example of an amplification chain for cryogenic single photons microwave experiments. The cryogenic environment is kept at ≈ 10 mK, which corresponds to an average thermal energy of $1 \mu\text{eV}$. A single photon at 10 GHz (green signal), that corresponds to an energy of $\approx 40 \mu\text{eV}$, undergoes several amplification stages at different base temperatures, which add noise (blue and red signals).	3
1.2	Comparison between different microwave amplification technologies: High Electron Mobility Transistor (HEMT), Josephson Parametric Amplifier (JPA) and Traveling Wave Parametric Amplifier (TWPA).	4
1.3	(a) Sketch of a swing process. An oscillating system at a frequency ω_s is excited by parametric amplification via periodical changes of the center of mass position at a frequency $\omega_p = 2\omega_s$. (b) LC circuit with variable (nonlinear) C and L components.	5
2.1	Circuit diagram of a section of transmission line.	12
2.2	Schematic of an electrical circuit consisting of elements forming branches that meet at nodes. A loop is formed when there is more than one path between two nodes.	20
2.3	Example of spanning tree for a generic circuit. The ground is indicated by the letter g . Closure branches are dashed, and $\tilde{\Phi}$ indicates a constant magnetic flux threading the loop formed by the three inductors.	22
2.4	Simple LC resonator.	25
2.5	(Left) Sketch of a weak link, (Right) RCSJ circuit model of a Josephson junction.	29
2.6	Plot of the Josephson inductance as a function of the generalised flux across the junction.	30

3.1	Electrical schematic that represents a repetition of three elementary cells of size a in the JTWPA. Each cell consists of a superconducting loop containing a geometrical inductance L_g , a Josephson junction, with an associated capacitance C_J and inductance L_J , and a shunt capacitor C_g . The loops can be biased through both an external constant in space and time magnetic field B or a DC current I_{DC} flowing in the signal line. $\Delta\hat{\Phi}$ is the phase difference across the nodes of a cell, while \hat{V}_{C_g} is the voltage drop across the coupling capacitor.	32
3.2	Coupling constants of the Hamiltonian operator in Eq. (3.58) as functions of $\Delta\Phi_{DC}$. (a) Non-interacting-mode Hamiltonian coupling constants, (b) 4WM contribution to the non-interacting-mode coupling constants, (c) SPM and XPM coupling constants.	53
3.3	Coupling constants of the mixing terms of the Hamiltonian operator in Eq. (3.58) as functions of $\Delta\Phi_{DC}$	54
3.4	Gain profiles in the 3WM (a) and 4WM (b) regimes as function of the signal frequency. The darker coloured curves are calculated considering the contribution of the phase mismatch while the light coloured curved in the approximation of negligible phase mismatch. (a) The pump currents are (blue) $I_p/I_c = 0.06$ and (red) $I_p/I_c = 0.04$. (b) The pump currents are (light blue) $I_p/I_c = 0.13$ and (orange) $I_p/I_c = 0.10$	61
3.5	Added noise number as a function of the normalised pump current, calculated for a coherent input state (dashed) and a Fock input state with no (light red) and one (dark red) idler input photons. The plots are done considering a pump frequency of 12 GHz and a signal frequency of 5 GHz.	64
3.6	Squeezing spectra in the 3WM (a) and 4WM (b) regimes as function of the signal frequency. The dashed curves are calculated considering the contribution of the phase mismatch while the solid curved in the approximation of negligible phase mismatch. (a) The pump currents are (blue) $I_p/I_c = 0.06$ and (red) $I_p/I_c = 0.04$. (b) The pump currents are (light blue) $I_p/I_c = 0.13$ and (orange) $I_p/I_c = 0.10$	66
3.7	Ideal vs real frequency mixing scheme in PDC regime. The JTWPA receives in input a pump mode ω_p and a signal mode ω_s , giving in output a ideal set of modes, namely ω_p , ω_s and $\omega_i = \omega_p - \omega_s$ and a real set of modes, hence ω_p , ω_s , $\omega_i = \omega_p - \omega_s$, $\omega_{p+p} = \omega_p + \omega_p$ (Second Pump Harmonic Generation), $\omega_{p+s} = \omega_p + \omega_s$ (Signal Up-Conversion), $\omega_{p+i} = \omega_p + \omega_i$ (Idler Up-Conversion) and many more.	68

3.8	Unit cell of a JTWPA equipped with RPM. The LC resonator that shunts the signal line to ground is capacitively couples through a coupling capacitance C_c and is formed by an inductance L_r and a capacitance C_c	69
3.9	Comparison between the engineered dispersion relation (3.119) (blue) and a linear dispersion relation with low chromatic dispersion. Inset: zoom of the stop band opened by the presence of the RPM.	70
3.10	(a) Phase mismatch calculated sweeping on the pump frequency for $\omega_s = 6$ GHz. Both the blue solid line and the black dashed line are calculated for the set of parameters in Table A.2 but for the latter the stop band introduced by the resonator has been removed. (b) Phase mismatch calculated sweeping on the signal frequency for a fixed pump frequency of $\omega_p = 14.4$ GHz. Both the blue solid line and the black dashed line are calculated for the set of parameters in Table A.2 but for the latter the stop band introduced by the resonator has been removed.	71
4.1	Scheme of the measurement setup used to measure the critical currents of JJs. A voltage generator in series of a resistor R supply the excitation current to the DUT, which is then measured by a voltmeter in series of a transimpedance amplifier with gain Z. The voltage drop across the DUT is measured by a second voltmeter in series of a voltage amplifier with gain G. The current and voltage lines are filtered with low pass filters in order to reduce the presence of high frequency noise. An in-plane field \vec{B} is provided to the DUT.	75
4.2	Micrograph of a JJ embedded in the rf-SQUIDs.	76
4.3	IV characteristic of a JJ. The blue solid line represents the positive branch while the red dashed line the retrapping branch.	77
4.4	Critical current of a JJ measured as a function of the in-plane magnetic field (black dots). The orange and red curves represent two fits calculated using respectively a Fraunhofer pattern (4.1) and a double Fraunhofer pattern (4.2).	78
4.5	The figure shows a fitting curve of the J_c vs $\sqrt{P} \cdot t$ relation interpolating some experimental measurements (red dots) of JJ critical current densities.	81
4.6	(a) Plot of the oxide barrier thickness as a function of the oxidation parameters. (b) Intrinsic capacitance of a JJ with area $0.4 \mu\text{m}^2$ and dielectric thickness d	82
4.7	The picture shows a schematic of the JTWPA elementary cell complete of its stray inductances and capacitances.	83
4.8	Picture of the CPW meander used to house the nonlinear elements, indicating the structure of the stackup used for the simulations.	83
4.9	Physical layout of L_{meander} and simulated inductance.	85

4.10	Physical layout of $L_{g1} + L_{g2}$ and simulated inductance.	85
4.11	Physical layout of the coplanar waveguide used to extrapolate L_{dist} and simulated inductance.	87
4.12	Simulated metalization used to extrapolate the distributed capacitance of the coplanar waveguide.	87
4.13	Physical layout of C_{inter} and simulated capacitance.	89
4.14	Physical layout of the elementary cell showing the dimensional parameter "Grd" indicating the length of the fingers of the interdigitated ground capacitors.	91
4.15	Parametric simulations of the S21 amplitude parameter as a function of the length of "Grd". The simulations are performed for different numbers of unit cells (blue = 1 cell, orange = 2 cells, green = 4 cells, red = 8 cells).	92
4.16	S21 magnitude as a function of the number of unit cells. The red dots indicate the simulated points while a blue curve the parabolic fit.	93
4.17	Parametric simulations of the Loss Factor as a function of the length of "Grd". The simulations are performed for different numbers of unit cells (blue = 1 cell, orange = 2 cells, green = 4 cells, red = 8 cells).	94
4.18	Loss Factor as a function of the number of unit cells. The red dots indicate the simulated points while a blue curve the linear fit. . . .	94
4.19	Micrograph of a JTWPA.	96
4.20	Left: picture of the refrigerator DRY ICE 300 mK used to characterise sample A. Right: schematic of the microwave circuit used for the VNA characterisation of sample A.	96
4.21	(a) Transmission spectra of the JTWPA measured for different pump powers. (b) Subtraction between the transmission spectra shown in (a) and the Thru trace.	98
4.22	Schematic of the microwave circuit used for the idlers power measurement of sample B.	99
4.23	Plot of the 3WM and 4WM idlers power as a function of the DC bias current provided to the JTWPA.	99
4.24	Schematic of the microwave circuit used for the measurement of second and third harmonics generation of sample A.	101
4.25	Measured signal power as a function of the pump power. The pump frequency is 11.7 GHz, while the signal tone is supplied at 6.4 GHz at about -110 dBm considered at the device input (the pump power in the x axis is considered at the device input while the signal power in the y axis at the device output).	102

4.26	Simulations of the JTWPA with $\omega_0 = 156$ GHz and $\omega_J = 112$ GHz using CME-5 (pump frequency 11.7 GHz, signal frequency 6.4 GHz). (a) Gain simulations as a function of the length of the TL for different pump powers. (b) Gain simulation as a function of the pump power.	102
4.27	Power of the second and third harmonics generated by the JTWPA considered at the device output, as a function of the pump power (considered at the device input) in 3WM and 4WM bias points. The second harmonic is at 8.24 GHz while the third harmonic is at 12.36 GHz.	104
4.28	Gain of the JTWPA as a function of the pump frequency for a pump power of $P_p(0) = -85$ dBm, $P_p(0) = -82$ dBm and $P_p(0) = -80$ dBm.	106
4.29	Gain profile as a function of the amplifier's length calculated for a pump frequency of 13 GHz and 4.4 GHz. The inset shows a zoom of the curve calculated for a pump frequency of 13 GHz. The input pump power is $P_p(0) = -81$ dBm while the input signal power is $P_p(0) = -107$ dBm.	107
4.30	Numerical simulation of the gain of a JTWPA with RPM for different pump powers as a function of the signal frequency. The pump frequency is 14.4 GHz for all the curves and the black dashed curve is calculated for a JTWPA without RPM.	108
4.31	Left: layout of the resonator capacitively coupled to a CPW used for the simulations. Right: S21 scattering parameter simulated between Port 1 and Port 2 of the layout on the left. The dashed vertical lines indicate the frequencies at the -3 dB point, indicated by the horizontal solid line.	109
4.32	Left: layout of L_{meander} . Right: inductance simulated between Port 1 and Port 2.	110
4.33	Left: layout of $L_{g1} + L_{g2}$. Right: inductance simulated between Port 1 and Port 2.	111
4.34	Left: layout of a cluster formed by 4 elementary cells plus 1 resonator. Right: parametric simulation of the S21 scattering parameter as a function of the length of the interdigitated capacitance fingers "Grd".	112
4.35	Simulation of the S11 and S21 scattering parameters for the JTWPA equipped with RPM with a 50Ω characteristic impedance between 2 GHz and 42 GHz.	112

Chapter 1

Introduction

1.0.1 Motivations

The *First Quantum Revolution* took place at the beginning of the last century led by that crazy wave-particle duality concept, so the idea that a particle could be described somehow as a wave and at the same time waves could be treated as particles. This idea was the substrate of nearly all the breakthroughs that compose the *First Quantum Revolution*. The wave-like behaviour of electrons is what allowed us to explain the structure of the periodic table, the chemical bonds and all the metals, semiconductors and insulators physics in general, on the other hand, the concept of the light particle called photon gave us the understanding of the photoelectric effect and lasers [19].

The XXI century is the theatre of the *Second Quantum Revolution*, which differs from its predecessor mainly for the paradigms on which it is founded. If the *First Quantum Revolution* was focused on understanding the natural world at microscopic scales, the *Second Quantum Revolution* takes as its aim bringing the quantum world into our modern technology, in our devices and in our way of thinking. In this view, we are no longer passive observers of the quantum world but rather active actors who bend it to our needs.

The difference between science and technology is the ability to engineer your surroundings to your ends, and not just explain them. A strong example of this fact, that is one of the motivations of this thesis, is that in addition to explaining the periodic table we can produce new artificial atoms [61, 53], which have properties that cannot be found in nature and can be used to engineer new materials with unprecedented optical and electronic properties. The great boost towards the fabrication of artificial atoms comes from the will to access nature-given forbidden regions of the electromagnetic spectrum, where the generation and manipulation of single quanta of light is of great interest for many fields of modern technology. In the last twenty years circuit-Quantum ElectroDynamics (cQED), that deals with

studying on-chip fundamental interaction between light and matter, [6, 33] had an incredible development just to carry out the task of creating superconducting atoms in which the energy of the quantum jumps sits in the microwave range of the electromagnetic spectrum. In this way artificial atoms, which take the physical form of superconducting circuits, become absorbers and emitters of single microwave photons, that through these devices can be manipulated for technological purposes.

The detection and manipulation of single microwave photons is a key aspect in several fields.

An example is represented by cosmology and the run for the discovery of dark matter. A suitable candidate for the composition of dark matter is indeed the axion, a hypothetical particle that would have no electric charge, very small mass and very low interaction with strong and weak forces. Despite their elusive nature, axions are thought to interact with electromagnetic fields and through the Primarkoff effect turning themselves into microwave photons and vice versa when passing through very strong magnetic fields. A good part of the strategies adopted to detect axions include their transformation in microwave photons through the Primarkoff effect, hence necessarily involving the detection of the latter with very high accuracy and efficiency [41, 45].

Superconducting quantum computing is another field that daily deals with microwave photons. Qubits are the elementary units that compose quantum processors and are realised in the form of artificial atoms [7, 1]. The protocols used to program and command these single units are physically implemented by short microwave pulses which need to be reliably detected and generated for the efficient functioning of these emerging technologies.

Quantum illumination is as well a field where not only the detection but also the generation and manipulation of quantum microwave fields at the single-photon level is required. Indeed, this concept of quantum detection can outperform its classical counterpart when dealing with low reflectivity targets and a very bright thermal background [16, 35, 3]. Nonetheless, this detection protocol makes use in some of its realisations of entangled microwave photon pairs, needing performing detectors to receive the signals after the interaction with the target took place.

In all the above-mentioned fields the main challenge remains the detection of single microwave photons, a problem that we want to tackle in this thesis.

The fact that the energy of microwave photons is so low imposes several technological challenges for their detection and use. Fig. 1.1 shows a sketch of an amplification chain for a single photon signal at 10 GHz. Being the scale energy of single microwave photons in the order of tenth of μeV , which is several orders of magnitude lower than room temperature thermal energy that is on average 25 meV, requires the apparatus for their creation and detection to be cooled down at cryogenic temperatures so as to reduce thermal noise well below the single microwave

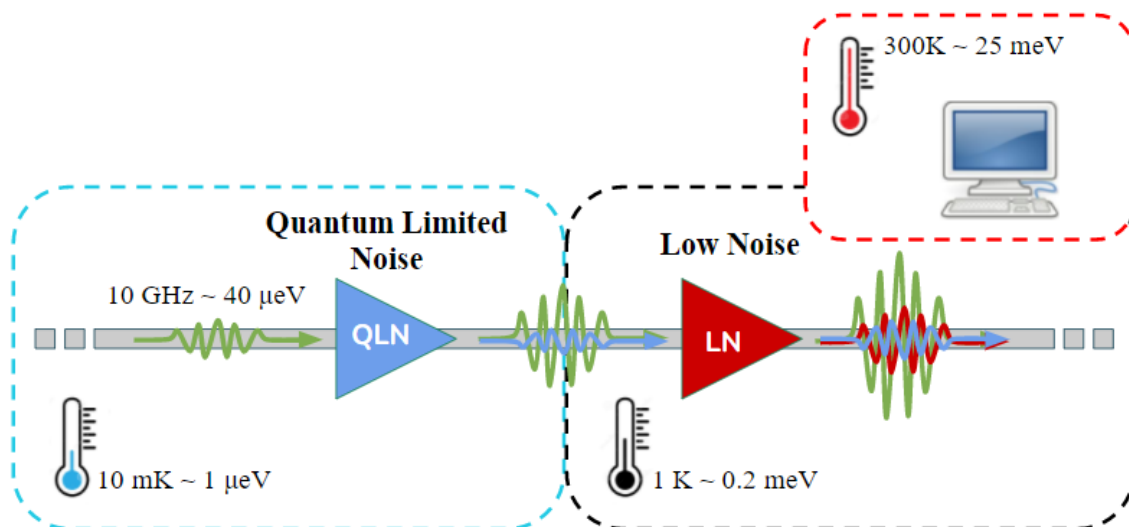


Figure 1.1: Example of an amplification chain for cryogenic single photons microwave experiments.

The cryogenic environment is kept at ≈ 10 mK, which corresponds to an average thermal energy of $1 \mu\text{eV}$. A single photon at 10 GHz (green signal), that corresponds to an energy of $\approx 40 \mu\text{eV}$, undergoes several amplification stages at different base temperatures, which add noise (blue and red signals).

photon level. The temperatures required range around 10 mK, that is the temperature where the average occupation number of energy levels of tenth of μeV is well below the unity.

Each one of these experiments requires in general several amplification stages to make these tiny signals detectable and each of these stages needs to add the lowest noise possible to avoid the degradation of the signal. So in general, the added noise should be as little as possible, ideally, the minimum allowed by the laws of quantum mechanics, otherwise said “quantum-limited noise”. In this thesis, we will deal with phase-preserving linear amplifiers, hence devices where the output and input fields are linearly correlated, without any phase dependence. As we will find out, the quantum-limited noise on this type of amplifier is half a photon at the reference frequency.

This brings us to the conclusion that for an efficient use of microwave photons we need low noise amplifiers in a cryogenic environment. Fig. 1.2 illustrates a comparison between three different classes of commonly adopted low noise amplifiers. The most commonly used and commercially available cryogenic amplifiers are the High Electron Mobility Transistors, or HEMT, which provide very high gain and wide bandwidth, but do not have quantum-limited noise since their average noise temperature at cryogenic temperature is around 4 K [27]. This fact makes them


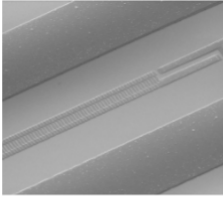
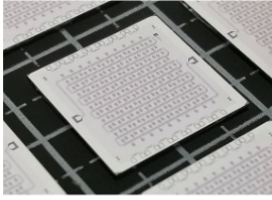
			
	High Electron Mobility Transistor <u>HEMT</u>	Josephson Parametric Amplifier <u>JPA</u>	Traveling Wave Parametric Amplifier <u>TWPA</u>
• Device	Transistor	Resonator	Transmission line
• Technology	Semiconductor	Superconductor	Superconductor
• Noise	—	+	+
• Gain	+	+	~
• Bandwidth	+	—	+
• Saturation power	+	—	~

Figure 1.2: Comparison between different microwave amplification technologies: High Electron Mobility Transistor (HEMT), Josephson Parametric Amplifier (JPA) and Traveling Wave Parametric Amplifier (TWPA).

suitable for a second or third stage of amplification but not as the primary one, that in general needs to be quantum limited.

A very widely studied variety of amplifiers are the Josephson Parametric Amplifiers, or JPA, which are non-linear resonator shaped amplifiers constituted by a series of identical sections embedding Josephson junctions, which provide the nonlinearity needed for parametric amplification [60, 8, 48]. These devices, being superconducting, offer very low losses and added noise, making them nearly quantum limited. They also show very high gains at the cost of a narrow bandwidth and saturation power, caused by their resonant nature.

Another widely studied kind of amplifier is represented by the Traveling Wave Parametric Amplifiers, or TWPAs, which are most of times realised in superconducting material, hence offering low added noise and losses, but on the other hand, they present a much wider bandwidth, since their structure is designed as a transmission line and not as a resonator.

By the way, the latter have not demonstrated gain and noise figure comparable with the first two kinds of devices yet, but many efforts are being made in this direction [57, 36].

Among the three categories, the traveling wave parametric amplifier is the only one

that promises to be the device that can actually achieve all the performance needed in modern experiments in terms of bandwidth, saturation power, quantum limited noise and gain.

TWPAs obtain their nonlinearity through some kind of nonlinear reactance. The nonlinearity that characterises these devices emerges through the phenomenon of parametric amplification. Indeed, a non-linear component of an LC circuit can change periodically the resonance frequency of the whole system, leading to broadband amplification. We see two examples of parametric amplification in Fig. 1.3.

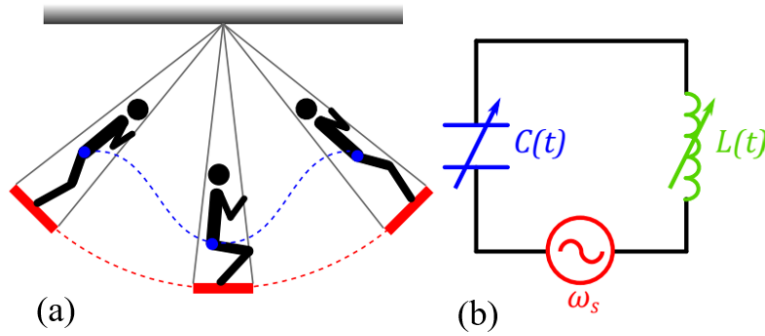


Figure 1.3: (a) Sketch of a swing process. An oscillating system at a frequency ω_s is excited by parametric amplification via periodical changes of the center of mass position at a frequency $\omega_p = 2\omega_s$. (b) LC circuit with variable (nonlinear) C and L components.

In (a) we see a sketch of a playground swing oscillating at frequency ω_s , and a child pumping the swing by periodically bending his knees at frequency $\omega_p = 2\omega_s$. The action of bending the knees physically corresponds to periodically changing the momentum of inertia of the whole system, which finally leads to an amplification of the swing oscillation, practically realising a mechanical parametric amplifier. In (b) a simple example of LC circuit can be seen, where the reactive components are variable with time. This scheme realises the electrical concept of a parametric oscillator, where the resonant frequency of the circuit is dynamically tuned with respect to a signal generator at frequency ω_s . A modulation of the circuit parameters at $\omega_p = 2\omega_s$ leads to parametric amplification of the electrical oscillations in the circuit [20].

The nonlinearity of parametric devices is often given by an inductor. A nonlinear inductor is generally an element of which the inductance depends on the current passing through it. This electrical component is physically realised mainly in two different ways. The first way is to exploit the kinetic inductance of a superconducting transmission line, in this case the device takes the name of Kinetic Inductance

Traveling wave parametric amplifier, or KIT. The second way consists in exploiting the nonlinear inductance provided by a series of Josephson junctions, in this case the device takes the name of Josephson Traveling Wave Parametric Amplifier, or JTWPA.

KIT amplifiers use the properties of the kinetic inductance of superconductors to develop the needed nonlinearity for parametric amplification. The superconductor has indeed a total inductance $L_{\text{tot}} = L_{\text{g}} + L_{\text{k}}$, with L_{g} is the geometric inductance given by the geometrical properties of the device, while L_{k} is the current dependant kinetic inductance. The relation between L_{k} and the current passing through the superconductor can hence be expressed as

$$L_{\text{k}}(I) = L_0 \cdot \left(1 + \frac{I^2}{I_*^2} \right) \quad (1.1)$$

where I_* is a scaling parameter of the order of the critical current and $L_0 = (\hbar R_{\text{s}})/(\pi\Delta)$, with R_{s} the sheet resistance of the film, Δ is the superconducting gap of the film and \hbar is the reduced Planck constant. Highly resistive superconductors are particularly feasible for this aim since their R_{s} is high, and practically can reach a a very high fraction of the total inductance. For an amplifier with only RF signals, the current passing through the nonlinear inductance is $I = I_{\text{RF}}$, which includes all possible RF components in the line. Namely, a first RF component used as a pump tone at frequency f_{P} and a second RF component at frequency f_{S} that is the signal to be amplified. Under the correct signal and pump power combination we observe parametric amplification of the signal accompanied by the generation of an idler tone at frequency $f_{\text{I}} = 2f_{\text{P}} - f_{\text{S}}$.

The introduction of a DC bias, can strongly modify the response of the device by tuning the nonlinearity given by the superconducting material. It is indeed true that now the current in the amplifier can be expressed as $I = I_{\text{DC}} + I_{\text{RF}}$, giving a formula for the kinetic inductance in the form

$$L_{\text{k}}(I) = L_0 \cdot \left(1 + \frac{I_{\text{DC}}^2}{I_*^2} + 2 \left(\frac{I_{\text{DC}} I_{\text{RF}}}{I_*^2} \right) + \frac{I_{\text{RF}}^2}{I_*^2} \right) \quad (1.2)$$

This allows parametric amplification of the signal with the generation of an idler tone at frequency $f_{\text{I}} = f_{\text{P}} - f_{\text{S}}$. Based on these fundamental properties KITs have been greatly developed in the past years. [54] proved that nonlinear transmission lines, in the form of coplanar waveguides made of high kinetic inductance superconductors like NbTiN, show a deep modulation of the nonlinearities in the device by means of a simple DC current passign through it. In this case the performance reached was of more than 15 dB on a bandwidth from 4 to 8 GHz. Different implementations of a KIT were realised in [12], where is given the proof of an engineering dispersion relation by means of periodic characteristic impedance or lumped element resonator loading. In this way a modified dispersion relation is created in

the transmission line, hence providing bandgaps useful for promoting mixing of wanted tones and avoid the generation of stray tones. KITs have also been used to realise measurements schemes for superconducting qubit readout [47], showing an enhancement in the readout fidelity of the amplification chain. The reading out use of quantum devices is possible due to the optimal noise figure of these devices, as accurately shown in [37], where the gain and bandwidth of a periodically impedance loaded KIT is characterised together with its noise figure when put in an amplification chain. Here sophisticated measurements of the added noise show a remarkable noise temperature of 0.66 K, that confirms this technology as one of the leading candidates in extremely low noise cryogenic amplification.

In general KITs have hence high gain, that is stable over a several GHz bandwidth, moreover their added noise is extremely low and approaching in some cases the standard quantum limit. By the way, since the nonlinearity given by the superconductor kinetic inductance is quite diluted in the transmission line these devices need to be very long, in the order of some tenth cm. This non negligible fact makes their realisation not trivial and in general cause of a low fabrication yield. Moreover, the general need of high DC currents to drive the system in the wanted nonlinear condition (\approx mA) poses as well severe restrictions for what concerns the cryogenic setup, introducing possible overheating problems of the cryogenic setup.

On the other hand, JTWPAs exploit the nonlinearity of typical of the Josephson element to achieve parametric amplification. It is indeed well known that a Josephson junction can be seen as nonlinear inductors, that in the case of tunnel junctions, show an inverse cosinusoidal relation between the phase drop φ across it and the associated inductance $L_J(\varphi)$

$$L_J(\varphi) = \frac{L_0}{\cos(\varphi)} \quad (1.3)$$

The first realisation of a JTWPA was simply a transmission line composed of a series of Josephson junctions [62]. This attempt obtained about 15 dB over a narrow bandwidth of 125 MHz, showing practically the proof of principle of this technology. This design allowed a mixing of the pump, signal and idler tones such that $2f_P = f_S + f_I$. In the last two decades many efforts have been put in the development of Josephson based traveling wave amplifiers. The chain of single junctions, of which the nonlinearities can be only partially tuned in this simple configuration, has been substituted by other Josephson elements that allow an in-situ tuning by means of DC currents or magnetic fields. [66] realised a JTWPA that exploits a series of rf-SQUIDs, hence a parallel of an inductor and a Josephson junction, which represents tunable Josephson elements. Indeed a DC current passing through the device or a magnetic field perpendicular to the plane of the SQUID loop induce a stable phase difference φ_{DC} across the single cells, setting the amplifier in a new working point that allows a tone mixing such that $f_P = f_S + f_I$. An even further

degree of tunability has been reached by modifying the latter Josephson element in a so called Symmetric TWPA [38], where the inductor of the rf-SQUID is substituted by a second rf-SQUID. The possibility to separately tune the magnetic fluxes piercing the two loops of a single Josephson cell by means of individual flux lines allows to very precisely modify the nonlinearities of the transmission line, leading to a in-situ maximisation of the gain and adjusting at the same time the characteristic impedance of the device, ensuring a good electromagnetic match with the surrounding environment. Moreover, JTWPAs can just as KITs be accompanied with an engineered dispersion relations. It has indeed experimentally been proved [36] that the use of periodic resonator loading creates bandgaps in the dispersion relation of Josephson based devices, leading to a significant enhancement of the gain, bandwidth and added noise. Further steps can be made by engineering the sequence of elementary cells of JTWPAs. A brilliant example of this aspect is given in [46], where the authors build a JTWPA using as Josephson element a Superconducting Nonlinear Asymmetric Inductive eLement (SNAIL). A SNAIL is a superconducting loop where on one side we find a series of three large Josephson junctions while on the opposite side we find a single smaller junction. In this work, a chain of SNAILS, properly engineered in terms of junction's critical currents and relative rotation of the SNAILS, is used to spatially tune the nonlinearities along the transmission line. This last approach was particularly succesful to obtain stable amplification bandwidth wider than 4 GHz between 10 and 20 dB, depending on the pump frequency applied, avoiding detrimental bandgaps in the transmission characteristic.

JTWPAs have in general highly tunable nonlinearities given by the flexibility offered by Josephson structures. The structural degrees of freedom allows to engineer a wide variety of elementary cells able to provide highly nonlinear-density structures, meaning shorter and more compact devices. On the other hand, the need of fabricating thousands of tunnel barriers to build the Josephson elements imposes a high degree of precision and repeatability. This request can be challenging since the spread of the circuit parameters is one of the main reasons behind the loss of performance of these devices.

In this thesis we focus on the theoretical development of a quantum mechanical method to describe JTWPAs in the presence of signals at the single photon level. This is due to the fact that parametric amplification is explained at microscopic scales in terms of elementary excitations of the material. The medium undergoes quantum jumps between its energy levels, converting high frequency photons in low frequency ones and vice versa. The presence of elementary excitations of light requires as a consequence a quantum description. The quantum model developed in Chapter 3 finds analytical forms for the quantum mechanical coupling constants of wave mixing events, that are the physical base of parametric amplification at the microscopic scale. We moreover determine some important features of the device

like the gain and quantum added noise, which will show that the device actually work as a quantum limited amplifier. In Chapter 4 we describe the cryogenic characterisation of a first generation of JTWPAs that shows the phenomenon of nonlinear wave mixing and harmonic generation.

The work goes on facing the problem of the numerical simulation of JTWPAs with engineered dispersion relations, which theoretically show gain in the order of 20 dB and a several GHz bandwidth. A physical layout for these devices is then found through electromagnetic simulations, which allow to solve the problem of the characteristic impedance matching between the device and its electromagnetic environment.

Chapter 2

Circuit Quantum Electrodynamics and Linear Amplifiers

2.1 Classical transmission line theory

A transmission line (TL) is a structure created to convey electromagnetic signals between two points separated by a certain distance. Normally this distance is comparable to or larger than the wavelength of the electromagnetic signal considered hence the wavelike nature of the signal must be taken into account. The simplest TL is modeled by two coupled conductors which are assumed to be uniform for all their length, meaning that the physical properties that characterise the propagation of the electromagnetic signals, like the dielectric medium, conductor geometry and shape, remains the same for all physical system. From the theory of electrical circuits it is known that a TL is characterised by a combination of inductors, which store the magnetic component of the electromagnetic wave, capacitors, which store the electric energy and resistors (or alternatively conductances) which represent the ohmic losses in the conductors and the dielectric losses in the medium. Figure 2.1 shows the circuit that is generally used to describe a TL [42]. Due to the fact that the whole machinery of electrotechnics can be used just in the quasi-static approximation, hence at frequencies where the wavelength of the electromagnetic signal is much larger than the typical dimension, the TL is divided into small sections where the quasi-stationary approximation holds, defining many infinitesimal sections of length dz , which show a series inductance $L \cdot dz$, series resistance $R \cdot dz$, shunt capacitance $C \cdot dz$ and shunt conductance $G \cdot dz$. If we apply the Kirchhoff's voltage and current laws to the circuit in Figure 2.1 we get respectively

$$V(z + dz, t) - V(z, t) + L \cdot dz \frac{\partial I(z, t)}{\partial t} + R \cdot dz I(z, t) = 0 \quad (2.1)$$

$$I(z + dz, t) - I(z, t) + C \cdot dz \frac{\partial V(z, t)}{\partial t} + G \cdot dz V(z, t) = 0 \quad (2.2)$$

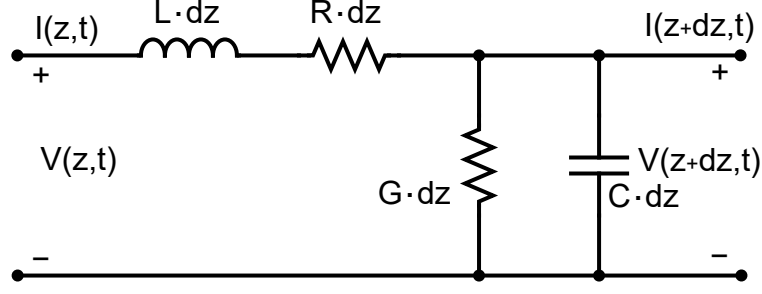


Figure 2.1: Circuit diagram of a section of transmission line.

where the current direction is intended from left to right of Figure 2.1. Dividing then by dz and taking the limit $dz \rightarrow 0$ we arrive at

$$\frac{\partial V(z,t)}{\partial z} + L \frac{\partial I(z,t)}{\partial t} + RI(z,t) = 0 \quad (2.3)$$

$$\frac{\partial I(z,t)}{\partial z} + C \frac{\partial V(z,t)}{\partial t} + GV(z,t) = 0 \quad (2.4)$$

The limit of $dz \rightarrow 0$ can be considered physically valid until when the wavelength of the electromagnetic signal $\lambda \gg dz$. Taking now the derivatives with respect to space and time of Eq. (2.3) and (2.4) we get

$$\frac{\partial^2 V(z,t)}{\partial z^2} + L \frac{\partial^2 I(z,t)}{\partial t \partial dz} + R \frac{\partial I(z,t)}{\partial z} = 0 \quad (2.5)$$

$$\frac{\partial^2 I(z,t)}{\partial z \partial t} + C \frac{\partial^2 V(z,t)}{\partial t^2} + G \frac{\partial V(z,t)}{\partial t} = 0 \quad (2.6)$$

Substituting Equations (2.4) and (2.6) into (2.5), and Equations (2.3) and (2.5) into (2.6) one obtains

$$\frac{\partial^2 V(z,t)}{\partial z^2} + LC \frac{\partial^2 V(z,t)}{\partial t^2} - (RC + LG) \frac{\partial V(z,t)}{\partial t} - RGV(z,t) = 0 \quad (2.7)$$

$$\frac{\partial^2 I(z,t)}{\partial z^2} + LC \frac{\partial^2 I(z,t)}{\partial t^2} - (RC + LG) \frac{\partial I(z,t)}{\partial t} - RGI(z,t) = 0 \quad (2.8)$$

In many physical situation we can consider a transmission line that has no ohmic or dielectric losses, superconducting TL are indeed a good example of that. In this case the coefficient that characterise the series resistance and shunt conductance

can be neglected $R, G \approx 0$, leading to

$$\frac{\partial V(z, t)}{\partial z} + L \frac{\partial I(z, t)}{\partial t} = 0 \quad (2.9)$$

$$\frac{\partial I(z, t)}{\partial z} + C \frac{\partial V(z, t)}{\partial t} = 0 \quad (2.10)$$

$$\frac{\partial^2 V(z, t)}{\partial z^2} + LC \frac{\partial^2 V(z, t)}{\partial t^2} = 0 \quad (2.11)$$

$$\frac{\partial^2 I(z, t)}{\partial z^2} + LC \frac{\partial^2 I(z, t)}{\partial t^2} = 0 \quad (2.12)$$

Equations (2.3), (2.4), (2.9) and (2.10) are known as the Telegrapher's equations while Equations (2.5), (2.6), (2.11) and (2.12) are called the transmission-line equations. The solutions of Equations (2.11) and (2.12) are a linear composition of a forward and backward moving wavelike functions. As an example for the solution of Equation(2.11) one can write

$$V(z, t) = V^+ \left(t - \frac{z}{v} \right) - V^- \left(t + \frac{z}{v} \right) \quad (2.13)$$

where $v = 1/\sqrt{LC}$ is identified as the phase velocity of the electromagnetic wave, and V^+ and V^- are arbitrary functions that satisfy the equations of motion. We can show the relation between the instantaneous voltage $V(z, t)$ and current $I(z, t)$ in the TL by calculating the space derivative of Equation (2.13) and substituting it into Equation (2.9)

$$\frac{\partial I(z, t)}{\partial t} = \frac{1}{Lv} \left[\frac{\partial V^+ \left(t - \frac{z}{v} \right)}{\partial t} - \frac{\partial V^- \left(t + \frac{z}{v} \right)}{\partial t} \right] \quad (2.14)$$

Then integrating with respect to time we get

$$I(z, t) = \frac{1}{Lv} \left[V^+ \left(t - \frac{z}{v} \right) - V^- \left(t + \frac{z}{v} \right) \right] + I_0(z) \quad (2.15)$$

We now take the time derivative of (2.13) and spatial derivative of (2.15) and substitute them into (2.10) obtaining

$$\frac{1}{Lv} \left[\frac{\partial V^+ \left(t - \frac{z}{v} \right)}{\partial z} - \frac{\partial V^- \left(t + \frac{z}{v} \right)}{\partial z} \right] + \frac{\partial I_0(z)}{\partial z} = -C \frac{1}{Lv} \left[\frac{\partial V^+ \left(t - \frac{z}{v} \right)}{\partial t} - \frac{\partial V^- \left(t + \frac{z}{v} \right)}{\partial t} \right] \quad (2.16)$$

which is true only if I_z is a constant. If we neglect this constant term the instantaneous current becomes

$$I(z, t) = \frac{1}{Z_0} \left[V^+ \left(t - \frac{z}{v} \right) - V^- \left(t + \frac{z}{v} \right) \right] \quad (2.17)$$

where it has been defined $Z_0 = \sqrt{L/C}$ hence the characteristic impedance of the line. It can be noted that for every t and z holds that

$$\frac{V(z, t)}{I(z, t)} = Z_0 \quad (2.18)$$

Most of times it is convenient while working with transmission lines to define the left-moving and right-moving wave amplitudes instead of working with voltages and currents

$$A^\rightarrow(z, t) = \frac{1}{2} \left[\frac{1}{\sqrt{V(z, t)}} + \sqrt{Z_0} I(z, t) \right] \quad (2.19)$$

$$A^\leftarrow(z, t) = \frac{1}{2} \left[\frac{1}{\sqrt{V(z, t)}} - \sqrt{Z_0} I(z, t) \right] \quad (2.20)$$

The unit of these quantities is $[\text{watt}]^{1/2}$ and are defined such that the power $P(z, t)$ flowing in the forward direction is expressed as

$$P(z, t) = [A^\rightarrow(z, t)]^2 - [A^\leftarrow(z, t)]^2 \quad (2.21)$$

Eq. (2.19) and (2.20) can be used to solve the Telegrapher's equations giving the solution in terms of fluxes of energy moving through the line. In particular, Eq. (2.9) and (2.10) become

$$\frac{\partial}{\partial z} A^\rightleftharpoons(z, t) = \pm \frac{1}{v} \frac{\partial}{\partial t} A^\rightleftharpoons(z, t) \quad (2.22)$$

In this view, hence working with fluxes of energy, the energy density $U(z, t)$ is related to the power $P(z, t)$ by the usual conservation law

$$\frac{\partial U}{\partial t} = - \frac{\partial P}{\partial z}$$

that using the definition of P given in (2.21) becomes

$$\frac{\partial U(z, t)}{\partial t} = \frac{2}{v} \left[A^\rightarrow(z, t) \frac{\partial}{\partial t} A^\rightarrow(z, t) + A^\leftarrow(z, t) \frac{\partial}{\partial t} A^\leftarrow(z, t) \right] \quad (2.23)$$

$$= \frac{1}{v} \frac{\partial}{\partial t} \left[[A^\rightarrow(z, t)]^2 + [A^\leftarrow(z, t)]^2 \right] \quad (2.24)$$

thus the total energy in the transmission line at a certain time t is

$$H = \frac{1}{v} \int_{-\infty}^{+\infty} \left([A^\rightarrow(z, t)]^2 + [A^\leftarrow(z, t)]^2 \right) dz \quad (2.25)$$

Eq. (2.25) gives an operational definition for the total amount of energy in a generic TL, that can be extended also in the case of nonlinear TL.

2.2 Canonical quantization of the electromagnetic field

In order to give a proper description of the electromagnetic field in presence of very low power signals, eventually to the level of the single elementary excitation, the classical description needs to be substituted with the quantum mechanical theory. This theory cannot be derived from the classical formulation but the transition from a classical to quantum description can be easily made if the classical equations are put in a particular form, performing the so called "quantization" of classical fields. The whole procedure is based on replacing the classical harmonic oscillator with the quantum-mechanical harmonic oscillator, for this reason the classical fields need to explicitly show their harmonic dependence. We will now show this procedure in the emblematic case of the free field, hence the electromagnetic field in vacuum, and then we will proceed by doing the same thing when the fields are confined in electrical circuit.

We start from the Maxwell's equations [34] formulated using the vector and scalar potential formalism in the Coulomb gauge¹, considering a portion of space where there are no charges and currents. In this picture we can write a wave equation for the vector potential \mathbf{A}

$$-\nabla^2 \mathbf{A} + \frac{1}{c^2} \frac{\partial^2 \mathbf{A}}{\partial t^2} = 0 \quad (2.26)$$

with c the speed of light in vacuum. Eq. (2.26) defines the space and time behaviour of the free field.

Now, since the quantization of the electromagnetic field is done by replacing the vector potential \mathbf{A} with its quantum-mechanical counterpart operator $\hat{\mathbf{A}}$, we need to recast the classical theory in a way that this substitution is immediate. To do so, we consider a cubic region of space of side L that we call "quantization cavity" and we take running waves, subjecting them to periodic boundary conditions at the limits of the quantization box. Moreover, the vector potential is expressed as the sum of all the contributions coming from the normal modes of the cavity

$$\begin{aligned} \mathbf{A}(\mathbf{r}, t) &= \sum_{\mathbf{k}} \sum_{\lambda=1,2} \mathbf{e}_{\mathbf{k}\lambda} A_{\mathbf{k}\lambda}(\mathbf{r}, t) \\ &= \sum_{\mathbf{k}} \sum_{\lambda=1,2} \mathbf{e}_{\mathbf{k}\lambda} \left(A_{\mathbf{k}\lambda}(t) e^{+i\mathbf{k}\cdot\mathbf{r}} + A_{\mathbf{k}\lambda}^*(t) e^{-i\mathbf{k}\cdot\mathbf{r}} \right) \end{aligned} \quad (2.27)$$

¹The Coulomb gauge condition states that the vector potential satisfies the condition $\nabla \cdot \mathbf{A} = 0$, hence identifying \mathbf{A} as a wholly transverse vector.

here λ is the index that labels the polarisation of the mode k , and the components of the wavevector \mathbf{k} take the values

$$k_x = 2\pi n_x/L \quad k_y = 2\pi n_y/L \quad k_z = 2\pi n_z/L \quad (2.28)$$

with $n_{x,y,z} \in \mathbb{Z}$. The decomposition in normal modes allows to explicit the sinusoidal components of the electromagnetic field and to make use of the mathematics structure for the analysis of purely harmonic signals. The $\mathbf{e}_{\mathbf{k}\lambda}$ are unit polarisation vectors and the Coulomb gauge condition is satisfied if the wave vector and the polarisation vector are transverse

$$\mathbf{e}_{\mathbf{k}\lambda} \cdot \mathbf{k} = 0$$

The modes of the vector potential independently satisfy the harmonic equation of motion (derived from Eq. (2.26))

$$\frac{\partial^2 A_{\mathbf{k}\lambda}(t)}{\partial t^2} + \omega_k^2 A_{\mathbf{k}\lambda}(t) = 0 \quad (2.29)$$

where we defined the mode angular frequency

$$\omega_k = ck \quad (2.30)$$

The electromagnetic field is quantized by conversion of the classical harmonic oscillator to its quantum-mechanical counterpart. This conversion is suggested by the form of the total field energy, which can be calculated taking a solution to Eq. (2.29) in the form

$$A_{\mathbf{k}\lambda}(t) = A_{\mathbf{k}\lambda} e^{-i\omega_k t} \quad (2.31)$$

so substituting Eq. (2.31) into (2.27) we find

$$A_{k\lambda}(\mathbf{r}, t) = A_{\mathbf{k}\lambda} e^{-i\omega_k t + i\mathbf{k}\cdot\mathbf{r}} + A_{\mathbf{k}\lambda}^*(t) e^{+i\omega_k t - i\mathbf{k}\cdot\mathbf{r}} \quad (2.32)$$

To compute the total energy in the quantization cavity we need to calculate the electric and magnetic fields using the definition of \mathbf{A} just found. From the definitions of vector potential it follows that the transverse electric field is

$$\begin{aligned} \mathbf{E}(\mathbf{r}, t) &= -\frac{\partial \mathbf{A}}{\partial t} \\ &= \sum_{\mathbf{k}} \sum_{\lambda=1,2} \mathbf{e}_{\mathbf{k}\lambda} E_{\mathbf{k}\lambda}(\mathbf{r}, t) \\ &= \sum_{\mathbf{k}} \sum_{\lambda=1,2} \mathbf{e}_{\mathbf{k}\lambda} i\omega_k \left(A_{\mathbf{k}\lambda} e^{-i\omega_k t + i\mathbf{k}\cdot\mathbf{r}} + A_{\mathbf{k}\lambda}^*(t) e^{+i\omega_k t - i\mathbf{k}\cdot\mathbf{r}} \right) \end{aligned} \quad (2.33)$$

and the magnetic field is

$$\begin{aligned}
 \mathbf{B}(\mathbf{r}, t) &= \nabla \times \mathbf{A} \\
 &= \sum_{\mathbf{k}} \sum_{\lambda=1,2} \frac{\mathbf{k} \times \mathbf{e}_{\mathbf{k}\lambda}}{k} B_{\mathbf{k}\lambda}(\mathbf{r}, t) \\
 &= \sum_{\mathbf{k}} \sum_{\lambda=1,2} \frac{\mathbf{k} \times \mathbf{e}_{\mathbf{k}\lambda}}{k} ik \left(A_{\mathbf{k}\lambda} e^{-i\omega_{\mathbf{k}}t + i\mathbf{k}\cdot\mathbf{r}} + A_{\mathbf{k}\lambda}^*(t) e^{+i\omega_{\mathbf{k}}t - i\mathbf{k}\cdot\mathbf{r}} \right) \quad (2.34)
 \end{aligned}$$

The total energy of the electromagnetic field in the quantization cavity is then

$$\mathcal{E}_R = \frac{1}{2} \int_{cavity} dV \left[\epsilon_0 \mathbf{E}(\mathbf{r}, t) \cdot \mathbf{E}(\mathbf{r}, t) + \mu_0^{-1} \mathbf{B}(\mathbf{r}, t) \cdot \mathbf{B}(\mathbf{r}, t) \right] \quad (2.35)$$

Substituting Eq. (2.33) and (2.34) into (2.35) the total energy \mathcal{E}_R can be found in terms of the vector potential. The spatial integrals are in the form

$$\int_{cavity} dV e^{\pm i(\mathbf{k}-\mathbf{k}')\cdot\mathbf{r}} = V \delta_{\mathbf{k},\mathbf{k}'} \quad (2.36)$$

and

$$\int_{cavity} dV e^{\pm i(\mathbf{k}+\mathbf{k}')\cdot\mathbf{r}} = V \delta_{\mathbf{k},-\mathbf{k}'} \quad (2.37)$$

with $V = L^3$ the volume of the quantization cavity. The total energy in the cavity then becomes

$$\begin{aligned}
 \mathcal{E}_R &= \frac{1}{2} \sum_{\mathbf{k}} \sum_{\lambda,\lambda'} V \left[(A_{\mathbf{k}\lambda} A_{\mathbf{k}\lambda'}^* + A_{\mathbf{k}\lambda}^* A_{\mathbf{k}\lambda'}) \times \right. \\
 &\quad \times \left(\epsilon_0 \omega_k^2 \mathbf{e}_{\mathbf{k}\lambda} \mathbf{e}_{\mathbf{k}\lambda'} + \mu_0^{-1} \mathbf{k} \times \mathbf{e}_{\mathbf{k}\lambda} \cdot \mathbf{k} \times \mathbf{e}_{\mathbf{k}\lambda'} \right) - \\
 &\quad - \left(A_{\mathbf{k}\lambda} A_{-\mathbf{k}\lambda'} e^{-2i\omega_{\mathbf{k}}t} + A_{\mathbf{k}\lambda}^* A_{-\mathbf{k}\lambda'}^* e^{2i\omega_{\mathbf{k}}t} \right) \times \\
 &\quad \left. \times \left(\epsilon_0 \omega_k^2 \mathbf{e}_{\mathbf{k}\lambda} \mathbf{e}_{-\mathbf{k}\lambda'} - \mu_0^{-1} \mathbf{k} \times \mathbf{e}_{\mathbf{k}\lambda} \cdot \mathbf{k} \times \mathbf{e}_{-\mathbf{k}\lambda'} \right) \right] \quad (2.38)
 \end{aligned}$$

The components of this complicated relation that depend on the polarisation vectors simplify thanks to the property of the vector product

$$\mathbf{k} \times \mathbf{e}_{\mathbf{k}\lambda} \cdot \mathbf{k} \times \mathbf{e}_{\pm\mathbf{k}\lambda'} = k^2 \mathbf{e}_{\mathbf{k}\lambda} \cdot \mathbf{e}_{\pm\mathbf{k}\lambda'} \quad (2.39)$$

Moreover, explicitly calculating the time-dependent terms it is found that they cancel out due to a cancellation between the relevant parts of the electric and magnetic fields energies. The total radiative energy reduces to a sum of time-independent contributions from the individual modes

$$\begin{aligned}
 \mathcal{E}_R &= \sum_{\mathbf{k}} \sum_{\lambda} \mathcal{E}_{\mathbf{k}\lambda} \\
 &= \sum_{\mathbf{k}} \sum_{\lambda} \epsilon_0 V \omega_k^2 (A_{\mathbf{k}\lambda} A_{\mathbf{k}\lambda'}^* + A_{\mathbf{k}\lambda}^* A_{\mathbf{k}\lambda'}) \quad (2.40)
 \end{aligned}$$

We note that the total energy in the quantization cavity is the mere sum of the energy of all the independent modes that populate the cavity. This fact is exactly the contact point between the electromagnetic radiative energy and the quantum-mechanical harmonic oscillator, that we recall here having a Hamiltonian operator equal to

$$\begin{aligned}\hat{\mathcal{H}}_R &= \sum_{\mathbf{k}} \sum_{\lambda} \hat{\mathcal{H}}_{\mathbf{k}\lambda} \\ &= \frac{1}{2} \sum_{\mathbf{k}} \sum_{\lambda} \hbar\omega_k \left(\hat{a}_{\mathbf{k}\lambda} \hat{a}_{\mathbf{k}\lambda}^\dagger + \hat{a}_{\mathbf{k}\lambda}^\dagger \hat{a}_{\mathbf{k}\lambda} \right)\end{aligned}\quad (2.41)$$

where $\hat{a}_{\mathbf{k}\lambda}$ is the ladder operator referred to the \mathbf{k} -th mode and λ polarisation, with eigenvalues

$$E_k = \left(k + \frac{1}{2} \right) \hbar\omega \quad (2.42)$$

The total energy of a multimode harmonic oscillator is again the sum of the energies of all its independent modes, so, by similarity, if we compare the expression (2.40) with the quantum mechanical formula of the total energy of a harmonic oscillator (2.41), we understand that the conversion from the classical vector potential amplitudes to the quantum mechanical mode operators is

$$A_{\mathbf{k}\lambda} \rightarrow \sqrt{\hbar/2\epsilon V \omega_k} \hat{a}_{\mathbf{k}\lambda} \quad A_{\mathbf{k}\lambda}^* \rightarrow \sqrt{\hbar/2\epsilon V \omega_k} \hat{a}_{\mathbf{k}\lambda}^\dagger \quad (2.43)$$

Using this substitutions Eq. (2.27) becomes

$$\begin{aligned}\hat{\mathbf{A}}(\mathbf{r}, t) &= \sum_{\mathbf{k}} \sum_{\lambda=1,2} \mathbf{e}_{\mathbf{k}\lambda} \hat{A}_{\mathbf{k}\lambda}(\mathbf{r}, t) \\ &= \sum_{\mathbf{k}} \sum_{\lambda=1,2} \mathbf{e}_{\mathbf{k}\lambda} \sqrt{\hbar/2\epsilon_0 V \omega_k} \left(\hat{a}_{\mathbf{k}\lambda} e^{-i\omega_k t + i\mathbf{k}\cdot\mathbf{r}} + \hat{a}_{\mathbf{k}\lambda}^\dagger e^{+i\omega_k t - i\mathbf{k}\cdot\mathbf{r}} \right)\end{aligned}\quad (2.44)$$

One can now recover the quantum mechanical operators that express the electric and magnetic fields by performing the substitutions (2.43) in (2.33) and (2.34)

$$\hat{\mathbf{E}}(\mathbf{r}, t) = \sum_{\mathbf{k}} \sum_{\lambda} \mathbf{e}_{\mathbf{k}\lambda} \sqrt{\hbar\omega_k/2\epsilon_0 V} \left(\hat{a}_{\mathbf{k}\lambda} e^{-\omega_k t + i\mathbf{k}\cdot\mathbf{r}} + \hat{a}_{\mathbf{k}\lambda}^\dagger e^{+\omega_k t - i\mathbf{k}\cdot\mathbf{r}} \right) \quad (2.45)$$

$$\hat{\mathbf{B}}(\mathbf{r}, t) = \sum_{\mathbf{k}} \sum_{\lambda} \mathbf{k} \times \mathbf{e}_{\mathbf{k}\lambda} \sqrt{\hbar/2\epsilon_0 \omega_k V} \left(\hat{a}_{\mathbf{k}\lambda} e^{-\omega_k t + i\mathbf{k}\cdot\mathbf{r}} + \hat{a}_{\mathbf{k}\lambda}^\dagger e^{+\omega_k t - i\mathbf{k}\cdot\mathbf{r}} \right) \quad (2.46)$$

and write the Hamiltonian operator for the radiative fields in the cavity

$$\hat{\mathcal{H}}_R = \frac{1}{2} \int_{cavity} dV \left[\epsilon_0 \hat{\mathbf{E}}(\mathbf{r}, t) \cdot \hat{\mathbf{E}}(\mathbf{r}, t) + \mu_0^{-1} \hat{\mathbf{B}}(\mathbf{r}, t) \cdot \hat{\mathbf{B}}(\mathbf{r}, t) \right] \quad (2.47)$$

The integral that defines the Hamiltonian operator is evaluated just the same way we did for (2.35), and gives the same result of (2.40) but with ladder operators instead of classical amplitudes. $\hat{\mathcal{H}}_R$ can thus be rewritten as

$$\hat{\mathcal{H}}_R = \sum_{\mathbf{k}} \sum_{\lambda} \hbar\omega_k \left(\hat{a}_{\mathbf{k}\lambda}^\dagger \hat{a}_{\mathbf{k}\lambda} + \frac{1}{2} \right) \quad (2.48)$$

of which the energy eigenvalues are known from the formulation of the quantum harmonic oscillator. The energy level allowed in the cavity result in this way

$$E_{\mathbf{k}\lambda} = \hbar\omega_k \left(k + \frac{1}{2} \right) \quad (2.49)$$

with $n_{\mathbf{k}\lambda}$ the numbers of elementary excitations in the cavity. The ground state of the electromagnetic field where no photons are excited in any mode is called *vacuum state*, and is the energy state of the cavity where $n_{\mathbf{k}\lambda} = 0$ with energy

$$E_0 = \frac{1}{2} \sum_{\mathbf{k}} \sum_{\lambda} \hbar\omega_k = \sum_{\mathbf{k}} \hbar\omega_k \quad (2.50)$$

known as the *zero point energy*.

2.3 Quantization of a non-dissipative superconducting circuit

To this moment we have quantum mechanically described electromagnetic field in the free space only, where a proper description can be given in terms of electric and magnetic fields. But if we want to describe the electromagnetic interaction when it is confined in a generic circuit we need to change approach in order to find the more natural way to describe its behaviour.

Referring to Fig. (2.2), we see that a generic electrical circuit is represented and described as a network of elements that connect nodes. The piece of wire together with the element in between two nodes is said branch (b), and the behaviour of a generic element at a time t is described by the voltage $v_b(t)$ across the element and the current $i_b(t)$ flowing through it. The voltage and current are defined starting from the electric and magnetic fields in a very general way

$$v_b(t) = \int_{\text{beginning of } b}^{\text{end of } b} \mathbf{E}(\mathbf{r}, t) \cdot d\mathbf{l} \quad (2.51)$$

$$i_b(t) = \frac{1}{\mu_0} \oint_{\text{around } b} \mathbf{B}(\mathbf{r}, t) \cdot d\mathbf{s} \quad (2.52)$$

The path of the loop integral in Eq. (2.52) is taken around the branch b . It follows that the energy absorbed until the time t by a generic element is the time integral

current is only a function of the flux $\Phi(t)$ is said to be an *inductive* element

$$v(t) = f(Q(t)) \quad \text{Capacitive element} \quad (2.56)$$

$$i(t) = g(\Phi(t)) \quad \text{Inductive element} \quad (2.57)$$

Eq. (2.56) and (2.57) are called *constitutive equations* of the capacitive and inductive elements respectively.

Just as in classical problems of Hamiltonian mechanics, the degrees of freedom of the system have to be described in terms of generalised coordinates. By the way, in electrical circuits there are less degrees of freedom than there are branches, because in addition to the constitutive relations one has the Kirchoff's laws

$$\sum_{\text{all } b \text{ around } l} \Phi_b = \tilde{\Phi}_l \quad (2.58)$$

$$\sum_{\text{all } b \text{ arriving at } n} Q_b = \tilde{Q}_n \quad (2.59)$$

so, not to have redundant variables, one has to find a way to define a minimal set of coordinates. For this purpose, there are two mainly used methods, the *method of nodes* and the *method of loops*. They are equivalent because they describe the same physical situation in two different ways, but one or the other make easier performing the calculation of the Hamiltonian depending on the layout of the circuit. In this case we will explain the method of nodes, but we underline that using the method of loops would lead to the very same results.

In the method of nodes we make a first distinction between *active* nodes, in which inductances and capacitances meet, and *passive* nodes, where only capacitances or inductances are connected. In this method we use the property of the capacitive subnetwork to contain only linear elements. This assumption allows to express the energy of a capacitance in terms of voltage, hence the derivative of flux. For this reason we can express the energy of a capacitive element as $E_c = (C/2)\dot{\Phi}^2$, exploiting the constitutive relation for a linear capacitance $Q = CV$, with C the capacitance of the element and Q the charge accumulated on it. In this way we broke the symmetry between charge and flux, since the flux is identified as the position coordinate, its time derivative is the generalised velocity, the inductive energy is the potential energy and the capacitive energy is the kinetic energy.

To use the method of nodes one has first to make sure that at every node to which an inductance is connected a capacitance is connected as well, there are thus no passive nodes in the sub-network of inductances (one can also consider the parasitic capacitances typical of an electrical element, hence there is no need to fictitiously modify the circuit in the case this requirement is not met). In practice we have to make sure that every node is connected to any other node by a path involving only capacitances.

The active nodes are labeled from 1 to N , while the passive nodes from $N + 1$ to P .

We define the $P \times P$ inverse inductance matrix $[L^{-1}]_{jk}$, whose non-diagonal elements are $-1/L_{jk}$, where L_{jk} is the value of the inductance connecting the nodes j and k (in this case no inductance between two nodes means that the matrix element will be zero). The diagonal matrix element will be the opposite of the sum of the values in the corresponding row or column. We also introduce the $P \times P$ capacitance matrix $[C]_{rs}$ whose non-diagonal elements are $-C_{rs}$, where C_{rs} is the capacitance between node r and s . Finally, the diagonal elements of the capacitance matrix are calculated taking the opposite of the sum of values in the corresponding row or column.

We find use for these matrices defining the *spanning tree* of the capacitance sub-network, which consists of the choice of a special node called "ground", and a set of branches that connect the ground to every other nodes through capacitances, without forming any loops. This means that there is only one path between the ground and any other node (see Fig. 2.3 as an example of spanning tree of a generic 2 nodes circuit). In this way, we can assign a flux to each node by adding the branch fluxes in the path between the ground and the node. We now define

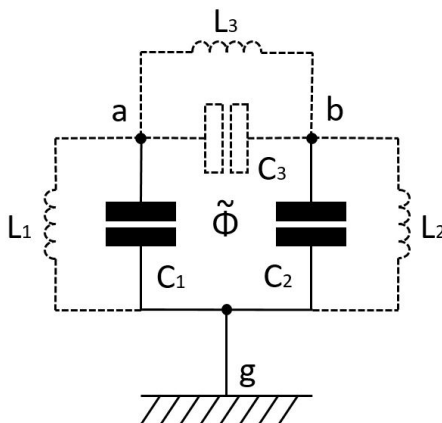


Figure 2.3: Example of spanning tree for a generic circuit. The ground is indicated by the letter g. Closure branches are dashed, and $\tilde{\Phi}$ indicates a constant magnetic flux threading the loop formed by the three inductors.

the node flux column vector with $P - 1$ components $\vec{\phi}$. The components of $\vec{\phi}$, the node fluxes, are connected to the branch fluxes by the simple relations

$$\Phi_{b \in T} = \phi_n - \phi_{n'} \quad (2.60)$$

$$\Phi_{b \in \bar{T}} = \phi_n - \phi_{n'} + \tilde{\Phi}_b \quad (2.61)$$

with T the particular spanning tree branches and \bar{T} its complement of this set (n and n' label the nodes connected by the branch). Moreover, the generic static flux threading a loop is indicated by $\tilde{\Phi}_b$.

Now that we are able to express the branches flux in terms of flux nodes we can write the potential and kinetic energies exploiting these new coordinates

$$\mathcal{E}_{pot} = \frac{1}{2} \vec{\phi}^t [\mathbf{L}^{-1}] \vec{\phi} + \sum_b \frac{1}{L_b} (\phi_n - \phi_{n'}) \tilde{\Phi}_b \quad (2.62)$$

$$\mathcal{E}_{kin} = \frac{1}{2} \vec{\phi}^t [\mathbf{C}] \vec{\phi} \quad (2.63)$$

Here, the matrix $[\mathbf{L}^{-1}]$ is different from $[L^{-1}]$ because this time the rows and columns that correspond to the ground node have been canceled, similarly, the matrix $[\mathbf{C}]$ respect with $[C]$. The sum in the potential energy runs over all the inductive branches, where n and n' are the nodes connected by the branch b .

Now that we have an explicit form of the kinetic and potential energies, it is straightforward to define the Lagrangian \mathcal{L} of the circuit as

$$\mathcal{L} = \mathcal{E}_{kin} - \mathcal{E}_{pot} \quad (2.64)$$

$$= \frac{1}{2} \vec{\phi}^t [\mathbf{C}] \vec{\phi} - \frac{1}{2} \vec{\phi}^t [\mathbf{L}^{-1}] \vec{\phi} - \sum_b \frac{1}{L_b} (\phi_n - \phi_{n'}) \tilde{\Phi}_b \quad (2.65)$$

Just to give an example of how this formalism works we write the Lagrangian of the circuit in Fig. 2.3

$$\mathcal{L}(\phi_a, \dot{\phi}_a, \phi_b, \dot{\phi}_b) = \frac{C_1 \dot{\phi}_a^2}{2} + \frac{C_2 \dot{\phi}_b^2}{2} + \frac{C_3 (\dot{\phi}_a - \dot{\phi}_b)^2}{2} - \left[\frac{\phi_a^2}{2L_1} + \frac{\phi_b^2}{2L_2} + \frac{(\phi_a - \phi_b + \tilde{\Phi})^2}{2L_3} \right] \quad (2.66)$$

where the degrees of freedom are the fluxes ϕ_a and ϕ_b at the nodes a and b . The Lagrangian of Eq. (2.66) can be used in the Euler-Lagrange equations

$$\frac{d}{dt} \frac{\partial \mathcal{L}}{\partial \dot{\phi}_n} - \frac{\partial \mathcal{L}}{\partial \phi_n} = 0 \quad (2.67)$$

to recover the equations of motion of the generalised coordinates

$$(C_1 + C_3) \ddot{\phi}_a + \left(\frac{1}{L_1} + \frac{1}{L_3} \right) \phi_a - \frac{\phi_b - \tilde{\Phi}}{L_3} = 0 \quad (2.68)$$

$$(C_2 + C_3) \ddot{\phi}_b + \left(\frac{1}{L_2} + \frac{1}{L_3} \right) \phi_b - \frac{\phi_a + \tilde{\Phi}}{L_3} = 0 \quad (2.69)$$

that is a system of coupled equations which can be solved to find out the dynamical behaviour of the circuit.

Through the definition of the conjugate momenta to the node fluxes

$$q_n = \frac{\partial \mathcal{L}}{\partial \dot{\phi}_n} \quad (2.70)$$

we can write the Hamiltonian of the circuit. The conjugate momenta have the physical interpretation of the algebraic sum of the charges on the capacitances connected to the node n , for this reason they are called *node charges*. Expressing the kinetic energy of the circuit in terms of the q_n variables, one finds the Hamiltonian

$$\mathcal{H} = \frac{1}{2} \vec{q}^t [\mathbf{C}] \vec{q} + \frac{1}{2} \vec{\phi}^t [\mathbf{L}^{-1}] \vec{\phi} + \sum_b \frac{1}{L_b} (\phi_n - \phi_{n'}) \tilde{\Phi}_b \quad (2.71)$$

Again, referring to the circuit in Fig. 2.3 one can straightforwardly calculate the Hamiltonian using Eq. (2.70) and (2.71), finding

$$\begin{aligned} \mathcal{H}(\phi_a, q_a, \phi_b, q_b) = & \frac{1}{C_1 C_2 + C_1 C_3 + C_2 C_3} \left[\frac{(C_2 + C_3) q_a^2}{2} + \frac{(C_1 + C_3) q_b^2}{2} + C_3 q_a q_b \right] + \\ & + \left[\frac{\phi_a^2}{2L_1} + \frac{\phi_b^2}{2L_2} + \frac{(\phi_a - \phi_b + \tilde{\Phi})^2}{2L_3} \right] \end{aligned} \quad (2.72)$$

The first term of (2.72) expresses the electrostatic energy as a function of the node charges while the second term is the magnetic energy as a function of the node fluxes. In this last expression, the role of $\tilde{\Phi}$ as an offset in the magnetic energy is very clear. If the circuit is composed by linear inductors only the main effect of $\tilde{\Phi}$ is the induce an offset in the DC current, on the contrary in the case of nonlinear inductors like Josephson junctions it deeply changes the dynamics of the system. At this point, just like we did in the previous section, the passage to the quantum mechanical description is straightforward, since the classical variables can be replaced by the corresponding operators

$$\begin{aligned} \phi & \rightarrow \hat{\phi} \\ q & \rightarrow \hat{q} \\ \mathcal{H} & \rightarrow \hat{\mathcal{H}} \end{aligned}$$

In this framework the commutator of the node fluxes and their conjugate node charges is

$$[\hat{\phi}_n, \hat{q}_n] = i\hbar \quad (2.73)$$

It is useful now taking as an operational example the most simple circuit than can be though including a capacitor and an inductor, hence the simple LC resonator shown in Fig. 2.4. Taking as the variables the flux in the inductor L and the charge on the capacitor q we write the Hamiltonian

$$\mathcal{H} = \frac{q^2}{2C} + \frac{\phi^2}{2L} \quad (2.74)$$

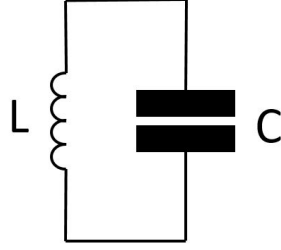


Figure 2.4: Simple LC resonator.

Now, making use of the ladder operators, which satisfy the commutator

$$[\hat{a}, \hat{a}^\dagger] = 1 \quad (2.75)$$

we rewrite in the second quantization framework the charge and flux operators

$$\hat{\phi} = \sqrt{\frac{\hbar Z_0}{2}}(\hat{a} + \hat{a}^\dagger) \quad (2.76)$$

$$\hat{q} = \sqrt{\frac{\hbar}{2Z_0}}(\hat{a} + \hat{a}^\dagger) \quad (2.77)$$

with $Z_0 = \sqrt{L/C}$. The Hamiltonian operator then becomes

$$\mathcal{H} = \frac{\hbar}{2\sqrt{LC}}(\hat{a}^\dagger \hat{a} + \hat{a} \hat{a}^\dagger) = \hbar\omega_0(\hat{a}^\dagger \hat{a} + \frac{1}{2}) \quad (2.78)$$

with $\omega_0 = \sqrt{1/LC}$ the resonant frequency of the circuit. The form of the Hamiltonian (2.78) tells us that the LC resonator has an energy spectrum equal to a harmonic oscillator with its characteristic frequency given by its inductance and capacitance components. For this reason, its energy spectrum remarks the one already seen in Eq. (2.49) for the free field in a quantization box, but this time the electric and magnetic energies are confined in circuit elements.

2.4 Linear amplifiers, quantum limits on added noise and parametric amplification

The quantum mechanical framework developed in the previous section can be used to describe the behaviour of electrical circuits at the single photon level, regardless of the wavelength in use. By the way, this same approach has been exploited in the past years to study micro and nano-sized circuits, most of times adopted in the microwave range, hence for frequencies roughly between 1 GHz and

20 GHz, used to realise very low noise amplifiers [31, 4, 5].

These devices have generally the theoretical description of linear amplifiers, hence objects that take an input mode and multiply it by a real constant, giving in output simply an input field amplified g times. This condition can be expressed as

$$\hat{a}_{out} = g\hat{a}_{in} + \hat{L}^\dagger \quad (2.79)$$

where \hat{a}_{out} and \hat{a}_{in} are the destruction operators of respectively the output and input fields, and \hat{L} is the *added-noise operator*. The added noise operator is a quantum-mechanical requirement for the commutation relations to hold so as not to violate unitarity when imposing the transformation (2.79). Indeed it has been shown that every linear amplifier has to add some noise only due to the fact that an amplification is taking place [25, 9]. When dealing with phase-preserving linear amplifiers, hence where the output field is not a function of the input signal phase, the least amount of noise that can be added is half a quantum at the operating frequency [10]. This can be shown calculating a bound on the *second-moment added noise*. We start stating that for the canonical commutation relations to hold it must be

$$[L, L^\dagger] = g^2 - 1 \quad (2.80)$$

which implies an uncertainty principle on the added noise operator

$$\langle |\Delta L|^2 \rangle = \frac{1}{2} \langle \Delta \hat{L} \Delta \hat{L}^\dagger + \Delta \hat{L}^\dagger \Delta \hat{L} \rangle = \langle |\hat{L}|^2 \rangle - |\langle \hat{L} \rangle|^2 \geq \frac{1}{2} (g^2 - 1) \quad (2.81)$$

where we used the definition of symmetric variance and used the notation $|\hat{a}| = 1/2(\hat{a}\hat{a}^\dagger + \hat{a}^\dagger\hat{a})$. The total output noise is then the sum of the amplified noise plus the noise added by the amplifier itself

$$\langle |\Delta \hat{a}_{out}|^2 \rangle = g^2 \langle |\Delta \hat{a}_{in}|^2 \rangle + \langle |\Delta \hat{L}|^2 \rangle \quad (2.82)$$

An inferior bound on the output added noise can be calculated evaluating the added noise of the input annihilation operator, which has a decomposition in terms of quadratures \hat{x}_1 and \hat{x}_2 equal to

$$\hat{a}_{in} = \frac{1}{\sqrt{2}} (\hat{x}_1 + i\hat{x}_2) \quad (2.83)$$

The symmetric variance of \hat{a}_{in} has hence an uncertainty principle

$$\langle |\Delta \hat{a}_{in}|^2 \rangle = \frac{1}{2} (\langle \Delta \hat{x}_1^2 \rangle + \langle \Delta \hat{x}_2^2 \rangle) \geq \langle \Delta \hat{x}_1^2 \rangle^{1/2} \cdot \langle \Delta \hat{x}_2^2 \rangle^{1/2} \geq \frac{1}{2} \quad (2.84)$$

hence the lower bound is the half quantum of zero-point noise. With this in hand, we can write a lower bound for Eq. (2.82), substituting in it Eq. (2.81) and (2.84)

$$\langle |\Delta \hat{a}_{out}|^2 \rangle \geq g^2 - \frac{1}{2} \quad (2.85)$$

It is usually more useful and easily readable to define a new entity that quantifies the added noise of an amplifier, namely the *added-noise number* \mathcal{A} , which takes its definition from

$$\frac{\langle |\Delta \hat{a}_{out}|^2 \rangle}{g^2} = \langle |\Delta \hat{a}_{in}|^2 \rangle + \frac{\langle |\Delta \hat{L}|^2 \rangle}{g^2} = \langle |\Delta \hat{a}_{in}|^2 \rangle + \mathcal{A} \quad (2.86)$$

\mathcal{A} is the second-moment added noise referred to the input field, and provides a dimensionless measure of the amplifier's performance. It is constrained as well, indeed

$$\mathcal{A} = \frac{\langle |\Delta \hat{L}|^2 \rangle}{g^2} \geq \frac{1}{2} \left(1 - \frac{1}{g^2} \right) \quad (2.87)$$

which tends to $1/2$ for $g \rightarrow \infty$, hence in the high gain limit. The added-noise number is defined as the noise the amplifier adds to the signal, the noise being referred to the input and given in units of number quanta. For high gains is lower bounded to one half, just as expected by an ideal linear phase-preserving amplifier. The simplest and most studied model of an ideal linear amplifier is represented by a *parametric amplifier* [40, 13]. In a parametric amplifier the primary mode (the one that we mean to amplify), described by the annihilation operator \hat{a} , interacts with a secondary or ancillary mode, described by the annihilation operator $\hat{b} = (\hat{y}_1 + i\hat{y}_2)/\sqrt{2}$. The Hamiltonian of the system is

$$\hat{\mathcal{H}} = \hbar\omega \left(\hat{a}^\dagger \hat{a} + \hat{b}^\dagger \hat{b} \right) + i\hbar k \left(\hat{a} \hat{b} e^{2i\omega t} - \hat{a}^\dagger \hat{b}^\dagger e^{-2i\omega t} \right) \quad (2.88)$$

which contains a free-field term and an interaction term, which describes the pairwise creation or annihilation of quanta in the two modes. The energy for the creation of the two modes is supplied by a third pump tone at frequency 2ω , of which the dynamics is not usually considered because excited in a high amplitude state, that can in certain limits being considered classical. We see the effect of the pump tone in the *coupling strength parameter* k , which grows together with the pump amplitudes, and in the phase term $e^{\pm 2i\omega t}$, which oscillates at the pump frequency. Moving in the interaction picture one can forget about the free field term of $\hat{\mathcal{H}}$ and write the simpler form

$$\hat{\mathcal{H}}_I = i\hbar k \left(\hat{a} \hat{b} - \hat{a}^\dagger \hat{b}^\dagger \right) \quad (2.89)$$

which can be used to write the evolution operator

$$\hat{U}_I(t) = e^{-i\hat{\mathcal{H}}_I t/\hbar} = e^{kt(\hat{a}\hat{b} - \hat{a}^\dagger\hat{b}^\dagger)} \equiv S(kt) \quad (2.90)$$

having defined the *two-mode squeezing operator* $S(kt)$. Now, working in the Heisenberg picture, it can be easily shown by performing the commutators that define the time evolution of the annihilation operators (supposing no explicit time dependence of the operators)

$$\frac{d\hat{a}_{out}}{dt} = [\hat{\mathcal{H}}, \hat{a}_{out}] \quad \frac{d\hat{b}_{out}}{dt} = [\hat{\mathcal{H}}, \hat{b}_{out}] \quad (2.91)$$

that the input-output relation (2.79) becomes

$$\begin{aligned} \hat{a}_{out} &= \hat{S}^\dagger \hat{a}_{in} \hat{S} \\ &= \hat{a}_{in} \cosh(kt) - \hat{b}_{in}^\dagger \sinh(kt) \\ &= g\hat{a}_{in} - \hat{b}_{in}^\dagger \sqrt{g^2 - 1} \end{aligned} \quad (2.92)$$

where we identified the gain $g = \cosh(kt)$ and $\hat{L} = -\hat{b} \sinh(kt) = \hat{b} \sqrt{g^2 - 1}$. If the input ancillary mode is initially in the vacuum state the added-noise number saturates (2.87) and the parametric amplifier realises an ideal linear amplifier.

Usually, it is possible to practically realise parametric amplifiers through the use of a nonlinear medium. This is particularly true for wavelength in the visible spectrum [11], since nonlinear crystals are daily used in Spontaneous Parametric Down Conversion (SPDC) experiments to generate entangled couples of photons or in the seeded Parametric Down Conversion (PDC) to again, generate entangled couples, but at a particular frequency, namely, the one of the seed. By the way, the fact that all the formalism developed to this point is independent on the frequency used stays, indeed the very same parametric processes are realised in the microwave range using those nano and micro-sized circuits we were talking about at the beginning of this section. The question is, where can we take the nonlinearity needed for a parametric process in the microwave range? Dealing with reactive circuit elements the answer quite unique, hence with Josephson junctions. A Josephson junction [2] is a weak link between two superconducting leads, and can be realised in a multitude of ways. The most common one, when speaking about superconducting integrated electronics, is a sandwich of two superconducting layers separated by a very thin layer of dielectric material. One of the electrical model for a Josephson junction is a parallel of a nonlinear inductor, a capacitor and a resistor, in the so called RCSJ model, which stands for "Resistively Capacitance Shunted Junction" model. The capacitance attributed to the junction comes from the parallel plate capacitor-like structure that forms the junction itself, where two conductive plates

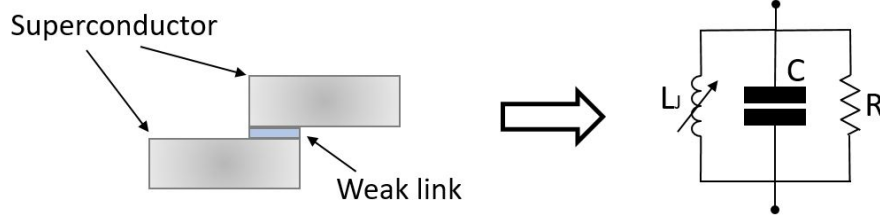


Figure 2.5: (Left) Sketch of a weak link, (Right) RCSJ circuit model of a Josephson junction.

are separated by an insulating layer. Instead, the resistor accounts for the tunneling of quasi-particles from one superconducting lead to the other, and for very low temperatures and good quality junctions can often be neglected when describing most electromagnetic effects. The nonlinear inductance, that is the most relevant peculiarity of the Josephson junction, takes its origin from a very fundamental fact, that is the discreteness of the Cooper pair charge that tunnels across the thin insulating barrier.

The Josephson element can be described in terms of the generalised flux variable defined in (2.54)

$$\Phi_J(t) = \int_{-\infty}^t v_J(t') dt' \quad (2.93)$$

where v_J is the voltage across the junction. If we call $i(t)$ the current flowing through the Josephson element, we can write the *current-phase relation* of a Josephson junction that links the current and the flux (equivalently the phase) to the current

$$i(t) = I_c \sin\left(\frac{2e}{\hbar} \Phi_J(t)\right) \quad (2.94)$$

where I_c is the maximum current that the junction can support without dissipation. The scale of the nonlinearity is set by the flux quantum $\Phi_0 = \hbar/2e$, that depends on the Cooper pair charge $2e$, microscopic source of the nonlinearity. As mentioned before, the Josephson junction acts like a nonlinear inductor [2] of inductance

$$L_J(i) = \pm \frac{\hbar}{2eI_0} \frac{1}{\sqrt{1 - (i/I_0)^2}} \quad (2.95)$$

of which the value depends on the current i flowing through it (Fig. 2.6). At zero bias the Josephson junction behaves as a nonlinear inductor of zero current value equal to $L_0 = \hbar/2eI_c$. Using Equation (2.94) one can obtain the relation for the Josephson inductance as a function of Φ_J

$$L_J(\Phi_J) = \frac{\hbar}{2eI_0} \frac{1}{\cos(\Phi_J/\Phi_0)} \quad (2.96)$$

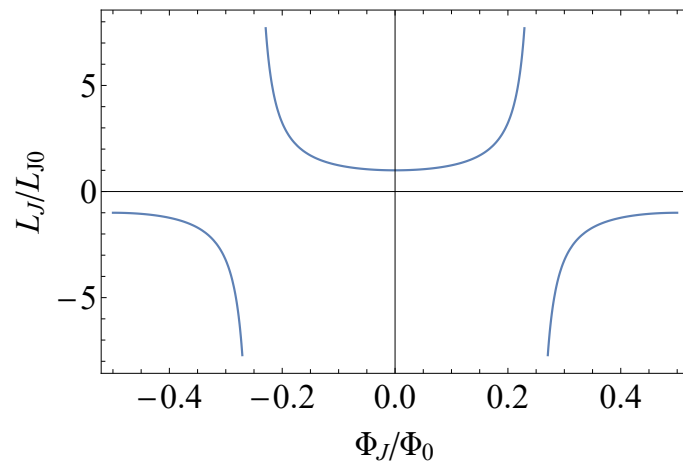


Figure 2.6: Plot of the Josephson inductance as a function of the generalised flux across the junction.

Chapter 3

Josephson Traveling Wave Parametric Amplifier embedding rf-SQUIDs

3.1 Quantum model for a Josephson Traveling Wave Parametric Amplifier embedding rf-SQUIDs

Superconducting electronics has gained in the last two decades a strong interest coming from the quantum computation and information community. Transmission lines realised as quasi-1D metamaterials with embedded Josephson junctions enable strong photon-photon on-chip interactions [30], that realise quantum optics phenomena in the microwave range. As a result, these technologies allow the control and tunability of wave mixing processes, that can be used to engineer non-classical light and provide quantum limited amplification of single-photon level signals. The word "metamaterial" is used in this frame to point out the fact that these devices realise artificially some fundamental features that are typical of natural compounds in other wavelength ranges. As an example, it has been shown that a weak signal travelling in a metamaterial can interact with a strong pump tone, activating parametric amplification [14]. JTWPAs are a the class of devices where these phenomena are fostered and they represents the solid state analogous of optical nonlinear crystals [51]. In this framework, different experiments showed that JTWPAs can act as parametric amplifiers, almost reaching the quantum limit of added noise [36] on several GHz wide bandwidth.

JTWPAs promise to be appropriate devices for single quantum amplification in the microwave regime, moreover showing valuable multiplexing capabilities due to their wide bandwidth. Indeed, it has been shown how the Four-Wave Mixing (4WM) induced in all the Kerr-like media allows amplifying very tiny signals over several GHz bandwidths with a nearly quantum-limited noise. Nevertheless, recent works

[64, 65] showed that enabling a Three-Wave Mixing (3WM) interaction, through the introduction of a quadratic nonlinearity in the medium, could provide experimental benefits for what concerns feasibility and integration capabilities. In particular, a three-wave mixer generally requires a lower input pump power, easier output filtering and shows a higher dynamic range.

In this chapter we develop a quantum model for a JTWPA covering both the 3WM and 4WM regimes. Our theory exploits c-QED techniques to model a JTWPA made up of a chain of Radio Frequency Superconducting QUantum Interference Devices (rf-SQUIDs) capacitively shunted to ground. The proposed layout can be biased by a DC current or an externally applied magnetic field to activate 3WM or 4WM of the microwave traveling modes.

3.1.1 Quantization of a Josephson Traveling Wave Parametric Amplifier

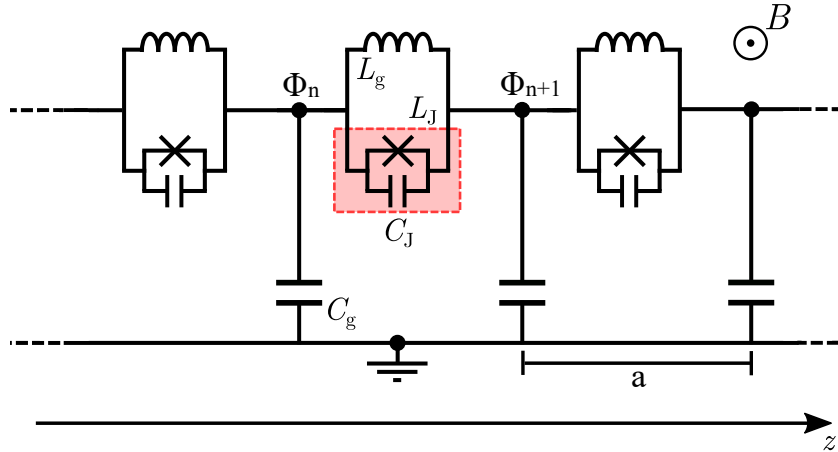


Figure 3.1: Electrical schematic that represents a repetition of three elementary cells of size a in the JTWPA. Each cell consists of a superconducting loop containing a geometrical inductance L_g , a Josephson junction, with an associated capacitance C_J and inductance L_J , and a shunt capacitor C_g . The loops can be biased through both an external constant in space and time magnetic field B or a DC current I_{DC} flowing in the signal line. $\Delta\hat{\Phi}$ is the phase difference across the nodes of a cell, while \hat{V}_{C_g} is the voltage drop across the coupling capacitor.

Our JTWPA can be modeled as a TL of which the signal line is composed of an array of N rf-SQUIDs [64]. As represented in Fig. 3.1, each elementary cell is composed by a superconducting loop containing a Josephson junction (with an associated capacitance C_J and an associated inductance L_J) and a geometrical inductance L_g . Furthermore, each loop is coupled to the ground line through a

capacitor C_g .

Being superconducting, the system can be considered non-dissipative and, for the sake of simplicity, all the elementary cells are considered identical. We define a as the physical length of the elementary cell along the z -direction (i.e., the propagating direction of the signals), considering a single elementary cell as the cluster composed by an rf-SQUID plus a ground capacitor.

In presence of an electromagnetic field, each cell stores a certain amount of energy that can be expressed as a function of the conjugate coordinates $\hat{\Phi}$ and \hat{Q} , the generalized magnetic flux and charge at a certain node respectively, which obey the commutation relation $[\hat{\Phi}, \hat{Q}] = i\hbar$. The generalised magnetic flux at a certain node can be found using the method of nodes treated in Section 2.3, that this time can be restricted to just a single cell of the TL instead of considering the whole circuit. The nodes taken into account for the spanning tree are the ones indicated in Fig. 3.1 by the presence of the generalised flux $\hat{\Phi}_n$ and $\hat{\Phi}_{n+1}$, that will be our generalised coordinates. Under the assumption that the differences between the $\hat{\Phi}$ (and \hat{Q}) of a couple of consecutive nodes are small enough, these quantities can be considered as functions of both time and space (i.e., $\hat{\Phi}(z, t)$ and $\hat{Q}(z, t)$). We then define the flux difference operator between two subsequent nodes as [23]

$$\Delta\hat{\Phi}(z, t) = \hat{\Phi}(z + a, t) - \hat{\Phi}(z, t) \quad (3.1)$$

The Hamiltonian of the system can be calculated as the total amount of energy in the TL, which is found as the sum of the energy stored in each of its elements [52]. Thus, being the system under analysis a repetition of identical elementary units, the total energy stored in the whole medium can be simply expressed as a sum of the energy stored in all the cells.

The circuit elements that compose the circuit in Fig. 3.1 are discrete components (the lumped element approach is considered to be valid), so every cell has its own ground capacitor, Josephson capacitor, geometrical inductance and Josephson junction.

The sum that defines the Hamiltonian hence runs over the index n which labels all the cells.

$$\hat{H} = \sum_{n=0}^N \hat{H}_n \quad (3.2a)$$

$$= \sum_{n=0}^N \left(\hat{H}_{L_g} + \hat{H}_{L_j} + \hat{H}_{C_j} + \hat{H}_{C_g} \right) \quad (3.2b)$$

where in the right-hand side of equation (3.2b) one can recognize respectively the energy associated to the geometrical inductance L_g , the Josephson inductance L_j , the Josephson capacitance C_j and the ground capacitance C_g and N is the number of unit cells composing the transmission line. Each term in (3.2b) can be expressed as a function of $\hat{\Phi}(z, t)$ and $\hat{Q}(z, t)$ just as previously shown in Sec. 2.3. Thus,

defining $I(t)$ the current flowing through a certain element and $V(t)$ the voltage drop across it, the energy stored in the electrical component at a certain time t can be expressed as the time-integrated power $P(t) = V(t) \cdot I(t)$:

$$U(t) = \int_{t_0}^t P(t') dt' = \int_{t_0}^t I(t') \cdot V(t') dt' \quad (3.3)$$

The current flowing through a generic inductance L induces a magnetic flux $\Phi(t) = LI(t)$, and can be related to the voltage drop across the element by the relation

$$V(t) = L \frac{dI(t)}{dt} \quad (3.4)$$

Hence we can express the energy stored in L_g as

$$\begin{aligned} H_{L_g}(t) &= \int_{t_0}^t I_{L_g}(t') \cdot V_{L_g}(t') dt' = \int_{t_0}^t I_{L_g}(t') \cdot L_g \frac{dI_{L_g}}{dt'} dt' = \\ &= L_g \int_{I_{L_g}(t_0)}^{I_{L_g}(t)} dI_{L_g} = \frac{L_g}{2} I_{L_g}^2 \Big|_{I_{L_g}(t_0)}^{I_{L_g}(t)} = \frac{L_g}{2} I_{L_g}^2(t) = \frac{L_g}{2} \left(\frac{\Delta\Phi(t)}{L_g} \right)^2 = \\ &= \frac{(\Delta\Phi(t))^2}{2L_g} \end{aligned} \quad (3.5)$$

having assumed $I_{L_g}(t_0) = 0$.

Using now the relation between the magnetic-flux and voltage drop

$$V(t) = \frac{d\Phi(t)}{dt} \quad (3.6)$$

one can compute the the energy stored in the Josephson inductance L_J , with critical current I_c , as

$$\begin{aligned} H_{L_J}(t) &= \int_{t_0}^t I_{L_J}(t') \cdot V_{L_J}(t') dt' = \int_{t_0}^t I_c \sin \left(\frac{\Delta\Phi(t')}{\varphi_0} \right) \cdot \frac{d\Delta\Phi(t')}{dt'} dt' = \\ &= I_c \int_{\Delta\Phi(t_0)}^{\Delta\Phi(t)} \sin \left(\frac{\Delta\Phi}{\varphi_0} \right) d\Delta\Phi = -\varphi_0 I_c \cos \left(\frac{\Delta\Phi}{\varphi_0} \right) \Big|_{\Delta\Phi(t_0)}^{\Delta\Phi(t)} = \\ &= \varphi_0 I_c \left(1 - \cos \left(\frac{\Delta\Phi(t)}{\varphi_0} \right) \right) \end{aligned} \quad (3.7)$$

having assumed $\Delta\Phi(t_0) = 0$ and $\varphi_0 = \Phi_0/2\pi$ the reduced flux quantum.

Using now the relation between the current flowing through a capacitance C and the voltage drop V across its terminals

$$I(t) = C \frac{dV(t)}{dt} \quad (3.8)$$

the energy stored in the ground capacitance C_g can be expressed as

$$\begin{aligned} H_{C_g}(t) &= \int_{t_0}^t I_{C_g}(t') \cdot V_{C_g}(t') dt' = \int_{t_0}^t C_g \frac{dV_{C_g}(t')}{dt'} \cdot V_{C_g}(t') dt' = \\ &= C_g \int_{V_{C_g}(t_0)}^{V_{C_g}(t)} V_{C_g} dV_{C_g} = \frac{C_g}{2} V_{C_g}^2 \Big|_{V_{C_g}(t_0)}^{V_{C_g}(t)} = \frac{C_g}{2} V_{C_g}^2(t) \end{aligned} \quad (3.9)$$

having assumed $V_{C_g}(t_0) = 0$.

Eq. (3.9) can be recast using the constitutive equation of a linear capacitor $C = Q/V$ to switch between voltage and charge variable, hence

$$H_{C_g}(t) = \frac{C_g}{2} V_{C_g}^2(t) = \frac{1}{2C_g} Q_{C_g}^2 \quad (3.10)$$

Lastly, exploiting relations (3.6) and (3.8), the energy stored in C_J can be expressed as

$$\begin{aligned} H_{C_J}(t) &= \int_{t_0}^t I_{C_J}(t') \cdot V_{C_J}(t') dt' = \int_{t_0}^t C_J \frac{dV_{C_J}(t')}{dt'} \cdot V_{C_J}(t') dt' = \\ &= C_J \int_{t_0}^t \frac{d}{dt'} \left[\frac{d\Delta\Phi(t')}{dt'} \right] \cdot \frac{d\Delta\Phi(t')}{dt'} dt' = \frac{C_J}{2} \int_{t_0}^t \frac{d}{dt'} \left[\left(\frac{d\Delta\Phi(t')}{dt'} \right)^2 \right] dt' = \\ &= \frac{C_J}{2} \left(\frac{d\Delta\Phi(t)}{dt} \right)^2 \end{aligned} \quad (3.11)$$

being $\Delta\Phi(t_0) = 0$.

Putting equations (3.5), (3.7), (3.9) and (3.11) into (3.2b) one obtains for the Hamiltonian operator

$$\hat{H} = \sum_{n=0}^N \left(\frac{1}{2L_g} \Delta\hat{\Phi}(an, t)^2 + \varphi_0 I_c \left(1 - \cos \left(\frac{\Delta\hat{\Phi}(an, t)}{\varphi_0} \right) \right) + \frac{C_J}{2} \left(\frac{\partial \Delta\hat{\Phi}(an, t)}{\partial t} \right)^2 + \frac{1}{2C_g} \hat{Q}(an, t)^2 \right) \quad (3.12)$$

As can be seen, the flux difference function $\Delta\hat{\Phi}(z, t)$, defined for every z , is calculated at discrete points in correspondence to the multiple integers an of the unit cell length a . This is done because we still consider the flux difference function calculated at the nodes between the unit cells, hence in discrete point.

In order to express \hat{H} in a more handy form, we go from a discrete sum to an approximated continuous sum substituting the summation sign with an integral [34] and adding the scale factor a , that is considered to be small with respect to the electromagnetic wavelengths in use. The integration upper limit is the length of

the amplifier $l = aN$, where N is the number of unit cells.

$$\hat{H} = \int_0^l \left(\frac{1}{2L_g} \Delta \hat{\Phi}(z, t)^2 + \varphi_0 I_c \left(1 - \cos \left(\frac{\Delta \hat{\Phi}(z, t)}{\varphi_0} \right) \right) + \frac{C_J}{2} \left(\frac{\partial \Delta \hat{\Phi}(z, t)}{\partial t} \right)^2 + \frac{1}{2C_g} \hat{Q}(z, t)^2 \right) \frac{dz}{a} \quad (3.13)$$

The integral can be considered as an approximation of the discrete sum in Eq. (3.12), where the flux difference across two subsequent cells is to be considered due to the presence of a finite number of Josephson junctions, for which the energy is defined in relation with the flux difference across them.

The presence of an external magnetic field or a DC current through the signal line induces a constant offset in the flux difference across a cell, just like the $\tilde{\Phi}$ component introduced in Sec. 2.3. This means that $\Delta \hat{\Phi}(z, t)$ can be considered as the sum of two components, a constant one $\Delta \Phi_{\text{DC}}$ and a time-dependent one $\delta \hat{\Phi}(z, t)$

$$\Delta \hat{\Phi}(z, t) = \Delta \Phi_{\text{DC}} + \delta \hat{\Phi}(z, t) \quad (3.14)$$

We choose now to switch from the first to the second quantization framework, thus expressing \hat{H} in terms of ladder operators. We start doing so by writing the voltage drop on C_g using a normal mode decomposition, assuming that sinusoidal waves are passing through the line [55, 26]. So, by proceeding the same way we did for Eq. (2.45) we write

$$\hat{V}_{C_g}(z, t) = \sum_n \sqrt{\frac{\hbar \omega_n}{2C_g N}} \left(\hat{a}_n e^{i(k_n z - \omega_n t)} + \text{H.c.} \right) \quad (3.15)$$

where ω_n and k_n are the angular frequency and wavenumber of the n -th mode while \hat{a}_n is its annihilation operator of the n -th mode. In this view, positive indexes denote progressive waves ($k_n > 0$ and $\omega_n > 0$), while negative indexes denote regressive waves ($k_{-n} = -k_n < 0$ and $\omega_{-n} = \omega_n$).

The link between the voltage drop and the current passing through a cell is straightforwardly found recalling the Telegrapher's equations derived in (2.9), which exploit the inductance of the cell for the n -th mode L_n

$$\frac{\partial V_n}{\partial z} = -\frac{L_n}{a} \frac{\partial I_n}{\partial t} \quad (3.16)$$

The AC current passing through the unit cell is then

$$\hat{I}(z, t) = \sum_n \hat{I}_n(z, t) = \sum_n \text{sgn}(n) \sqrt{\frac{\hbar \omega_n}{2L_n N}} \left(\hat{a}_n e^{i(k_n z - \omega_n t)} + \hat{a}_n^\dagger e^{-i(k_n z - \omega_n t)} \right) \quad (3.17)$$

L_n can be explicitly calculated as the parallel between the effective inductance $L_{\text{eff},n}$, which is composed by the geometrical inductance L_g modified by the

capacitive effect of C_J and the nonlinear Josephson inductance L_J .

We can calculate $L_{\text{eff},n}$ by keeping in mind that the impedance of an inductor L for the mode n is $Z_L = j\omega_n L$, while the impedance of a capacitor C for the same mode is $Z_C = 1/j\omega_n C$. We hence define a new inductance $L_{\text{eff},n}$ with an impedance equal to the impedance of the parallel formed by L_g and C_J

$$\begin{aligned}\frac{1}{Z_{L_{\text{eff},n}}} &= \frac{1}{Z_{L_g}} + \frac{1}{Z_{C_J}} \\ \frac{1}{j\omega_n L_{\text{eff},n}} &= \frac{1}{j\omega_n L_g} + j\omega_n C_J \\ \frac{1}{L_{\text{eff},n}} &= \frac{1}{L_g} - \omega_n^2 C_J = \frac{1 - \omega_n^2 L_g C_J}{L_g} \\ L_{\text{eff},n} &= \frac{L_g}{1 - \omega_n^2 L_g C_J} \equiv \Lambda_n L_g\end{aligned}\quad (3.18)$$

where the dispersion coefficient of the n -th node $\Lambda_n = 1/(1 - \omega_n^2 L_g C_J)$ has been defined.

The equivalent inductance of a Josephson junction has been already discussed at the end of Sec. 2.4 and is

$$L_J(I) = L_{J,0} \frac{1}{\sqrt{1 - (I/I_c)^2}} \quad (3.19)$$

Now promoting the scalar quantities to operators and switching from the current to the flux variable using the Josephson current-flux relation, we find

$$L_J(\Delta\Phi) = \frac{\varphi_0}{I_c} \frac{1}{\cos(\Delta\Phi/\varphi_0)} \equiv L_{J_0} \frac{1}{\cos(\Delta\Phi/\varphi_0)} \quad (3.20)$$

with $L_{J_0} = \varphi_0/I_c$. Using equations (3.18) and (3.20) the inductance of a unit cell for the n -th mode \hat{L}_n is

$$\frac{1}{L_n} = \frac{1}{L_J} + \frac{1}{L_{\text{eff},n}} \quad (3.21)$$

Hence

$$L_n = \frac{\Lambda_n L_g}{1 + \Lambda_n \frac{L_g}{L_{J_0}} \cos(\Delta\Phi/\varphi_0)} \quad (3.22)$$

We can finally calculate the time-dependent component of equation (3.14), that can be found by exploiting the constitutive equation for a linear inductor together with a mode decomposition for the AC current through the cell I_n and the inductance L_n for the corresponding mode as

$$\delta\Phi = \sum_n L_n I_n \quad (3.23)$$

It follows that, by replacing the classical variables by the corresponding operators and using equations (3.14), (3.17) and (3.22) into (3.23), the time-dependent flux operator is

$$\begin{aligned}
 \delta\hat{\Phi} &= \sum_n \text{sgn}(n) \sqrt{\frac{\hbar\omega_n}{2\hat{L}_n N}} \hat{L}_n \left(\hat{a}_n e^{i(k_n z - \omega_n t)} + \hat{a}_n^\dagger e^{-i(k_n z - \omega_n t)} \right) = \\
 &= \sum_n \text{sgn}(n) \sqrt{\frac{\hbar\omega_n}{2N}} \sqrt{\hat{L}_n} \left(\hat{a}_n e^{i(k_n z - \omega_n t)} + \hat{a}_n^\dagger e^{-i(k_n z - \omega_n t)} \right) = \\
 &= \sum_n \text{sgn}(n) \sqrt{\frac{\hbar\omega_n}{2N}} \sqrt{\Lambda_n L_g} \left(1 + \Lambda_n \frac{L_g}{L_{J_0}} \cos \frac{\Delta\Phi_{DC} + \delta\hat{\Phi}}{\varphi_0} \right)^{-1/2} \cdot \\
 &\quad \cdot \left(\hat{a}_n e^{i(k_n z - \omega_n t)} + \hat{a}_n^\dagger e^{-i(k_n z - \omega_n t)} \right) = \\
 &= \sum_n \left(1 + \Lambda_n \frac{L_g}{L_{J_0}} \cos \frac{\Delta\Phi_{DC} + \delta\hat{\Phi}}{\varphi_0} \right)^{-1/2} \delta\hat{\Phi}_n^{(0)}
 \end{aligned}$$

where we have identified the zero order AC flux component on the n -th mode $\delta\hat{\Phi}_n^{(0)}$

$$\begin{aligned}
 \delta\hat{\Phi}_n^{(0)} &\equiv \text{sgn}(n) \sqrt{\frac{\hbar\omega_n}{2N}} \sqrt{\Lambda_n L_g} \left(\hat{a}_n e^{i(k_n z - \omega_n t)} + \hat{a}_n^\dagger e^{-i(k_n z - \omega_n t)} \right) = \\
 &= c_n \left(\hat{a}_n e^{i(k_n z - \omega_n t)} + \hat{a}_n^\dagger e^{-i(k_n z - \omega_n t)} \right)
 \end{aligned} \tag{3.24}$$

with

$$c_n = \text{sgn}(n) \sqrt{\frac{\hbar\omega_n}{2N}} \sqrt{L_g \Lambda_n}$$

Equation (3.24) is an implicit relation for the flux operator $\delta\hat{\Phi}$, which can be solved at zero order by the substitution $\delta\hat{\Phi} \mapsto \delta\hat{\Phi}^{(0)}$ in the right-hand side, so that we get

$$\delta\hat{\Phi} = \sum_n \left[\left(1 + \Lambda_n \frac{L_g}{L_{J_0}} \cos \frac{\Delta\Phi_{DC} + \delta\hat{\Phi}^{(0)}}{\varphi_0} \right)^{-1/2} \delta\hat{\Phi}_n^{(0)} \right] \tag{3.25}$$

To reach an handy form of $\delta\hat{\Phi}$ it is necessary to Taylor expand the square root of Eq. (3.25) for small $\delta\hat{\Phi}^{(0)}$ around the working DC bias point $\Delta\Phi_{DC}$, obtaining

$$\delta\hat{\Phi} = \sum_n \left[q_{0,n} + q_{1,n} \left(\delta\hat{\Phi}^{(0)} \right) + q_{2,n} \left(\delta\hat{\Phi}^{(0)} \right)^2 + q_{3,n} \left(\delta\hat{\Phi}^{(0)} \right)^3 + O \left(\delta\hat{\Phi}^{(0)} \right)^4 \right] \delta\hat{\Phi}_n^{(0)} \tag{3.26}$$

We stress that the terms $q_{0,n}$, $q_{1,n}$, $q_{2,n}$ and $q_{3,n}$ are coefficients of a Taylor expansion and result to be functions of the bias condition $\Delta\Phi_{DC}$ and of the circuit parameters. It's worth noting here how the lowest perturbative order approach adopted in

Eq. (3.25) takes into account interactions of modes at the first order, that means a single multimodes interaction, while the power expansion truncation up to the third order in Eq. (3.26) limits our model to the interaction of a single mode ($\delta\hat{\Phi}_n^{(0)}$) with up to three modes. The maximum order of expansion was chosen to take into account scattering events involving at most 4 photons. This procedure provides a valid approximation for the nonlinear time-dependent flux operator $\delta\hat{\Phi}$ that can be substituted into equation (3.13) to obtain the Hamiltonian of the system in terms of ladder operators.

In order to plug Eq. (3.26) into (3.13) it is convenient to express the latter as a function of $\delta\hat{\Phi}$. We then start recasting the cosine into the Josephson energy term use the trigonometric addition formula

$$\begin{aligned} \cos\left(\frac{\Delta\hat{\Phi}}{\varphi_0}\right) &= \cos\left(\frac{\Delta\Phi_{DC}}{\varphi_0} + \frac{\delta\hat{\Phi}}{\varphi_0}\right) = \\ &= \cos\left(\frac{\Delta\Phi_{DC}}{\varphi_0}\right) \cos\left(\frac{\delta\hat{\Phi}}{\varphi_0}\right) - \sin\left(\frac{\Delta\Phi_{DC}}{\varphi_0}\right) \sin\left(\frac{\delta\hat{\Phi}}{\varphi_0}\right) = \\ &= p_1 \cos\left(\frac{\delta\hat{\Phi}}{\varphi_0}\right) - p_2 \sin\left(\frac{\delta\hat{\Phi}}{\varphi_0}\right) \end{aligned} \quad (3.27)$$

where we have defined

$$\begin{aligned} p_1 &= \cos\left(\frac{\Delta\Phi_{DC}}{\varphi_0}\right) \\ p_2 &= \sin\left(\frac{\Delta\Phi_{DC}}{\varphi_0}\right) \end{aligned}$$

We can now perform a Maclaurin expansion truncated at the fourth order of equation (3.27)

$$\begin{aligned} \cos\left(\frac{\Delta\hat{\Phi}}{\varphi_0}\right) &\approx p_1 \left(1 - \frac{1}{2} \left(\frac{\delta\hat{\Phi}}{\varphi_0}\right)^2 + \frac{1}{24} \left(\frac{\delta\hat{\Phi}}{\varphi_0}\right)^4\right) - p_2 \left(\left(\frac{\delta\hat{\Phi}}{\varphi_0}\right) - \frac{1}{6} \left(\frac{\delta\hat{\Phi}}{\varphi_0}\right)^3\right) = \\ &= p_1 - p_2 \left(\frac{\delta\hat{\Phi}}{\varphi_0}\right) - \frac{p_1}{2} \left(\frac{\delta\hat{\Phi}}{\varphi_0}\right)^2 + \frac{p_2}{6} \left(\frac{\delta\hat{\Phi}}{\varphi_0}\right)^3 + \frac{p_1}{24} \left(\frac{\delta\hat{\Phi}}{\varphi_0}\right)^4 \end{aligned} \quad (3.28)$$

and substitute into Eq. (3.13) obtaining

$$\begin{aligned}
 \hat{H} &= \frac{1}{2a} \int_{l_q} dz \left[2I_c \varphi_0 \left(1 - p_1 + p_2 \left(\frac{\delta \hat{\Phi}}{\varphi_0} \right) + \frac{p_1}{2} \left(\frac{\delta \hat{\Phi}}{\varphi_0} \right)^2 - \frac{p_2}{6} \left(\frac{\delta \hat{\Phi}}{\varphi_0} \right)^3 + \frac{p_1}{24} \left(\frac{\delta \hat{\Phi}}{\varphi_0} \right)^4 \right) + \right. \\
 &\quad \left. + \frac{1}{L_g} (\Delta \Phi_{DC} + \delta \hat{\Phi})^2 + C_J \left(\frac{\partial}{\partial t} [\Delta \Phi_{DC} + \delta \hat{\Phi}] \right)^2 + C_g \hat{V}_{C_g}^2 \right] = \\
 &= \frac{1}{2a} \int_{l_q} dz \left[2I_c \varphi_0 (1 - p_1) + \frac{\Delta \Phi_{DC}^2}{L_g} + \left(2I_c p_2 + \frac{2\Delta \Phi_{DC}}{L_g} \right) (\delta \hat{\Phi}) + \right. \\
 &\quad \left. + \left(\frac{I_c p_1}{\varphi_0} + \frac{1}{L_g} \right) (\delta \hat{\Phi})^2 - \frac{I_c p_2}{3\varphi_0^2} (\delta \hat{\Phi})^3 + C_J \left(\frac{\partial}{\partial t} [\delta \hat{\Phi}] \right)^2 + C_g \hat{V}_{C_g}^2 \right]
 \end{aligned} \tag{3.29}$$

We proceed by solving the spatial integral of (3.29), substituting first (3.15) and (3.26). To simplify this process, it is convenient to exploit a different notation.

We redefine $\delta \hat{\Phi}^{(0)}$ in terms of the curly brackets operator (see appendix B) as

$$\delta \hat{\Phi}^{(0)} = \sum_n \delta \hat{\Phi}_n^{(0)} = \sum_n c_n \{ \hat{a} + \hat{a}^\dagger \}_n e^{i(\Delta k_n z - \Delta \omega_n t)} \tag{3.30}$$

This choice will make all the equations much more compact and easily readable. It is also useful to rewrite (3.29) as a sum of several pieces

$$\hat{H} = h_0 + \hat{H}_I + \hat{H}_{II} + \hat{H}_{III} + \hat{H}_{IV} + \hat{H}_V \tag{3.31}$$

where the operators have been divided respect to their power

$$\begin{aligned}
 h_0 &= \frac{1}{2a} \int_{l_q} dz \left[2I_c \varphi_0 (1 - p_1) + \frac{\Delta \Phi_{DC}^2}{L_g} \right] \\
 \hat{H}_I &= \frac{1}{2a} \int_{l_q} dz \left[(2I_c p_2) (\delta \hat{\Phi}) \right] \\
 \hat{H}_{II} &= \frac{1}{2a} \int_{l_q} dz \left[\left(\frac{I_c p_1}{\varphi_0} + \frac{1}{L_g} \right) (\delta \hat{\Phi})^2 + C_g \hat{V}_{C_g}^2 \right] \\
 \hat{H}_{III} &= -\frac{1}{2a} \int_{l_q} dz \left[\frac{I_c p_2}{3\varphi_0^2} (\delta \hat{\Phi})^3 \right] \\
 \hat{H}_{IV} &= \frac{1}{2a} \int_{l_q} dz \left[\frac{I_c p_1}{12\varphi_0^3} (\delta \hat{\Phi})^4 \right] \\
 \hat{H}_V &= \frac{1}{2a} \int_{l_q} dz \left[C_J \left(\frac{\partial}{\partial t} [\delta \hat{\Phi}] \right)^2 \right]
 \end{aligned}$$

In Appendix C every \hat{H}_X is separately calculated in terms of ladder operators and the integration bounds are chosen to be asymmetric, hence $\int_{l_q} = \int_0^{a^N}$. The creation and annihilation operators are considered to be slowly varying with respect to space, hence have been treated as constants during the integration. This situation is physically achieved when there is not a stiff variation in the circuit parameters between close cells. The only space dependent quantity is the exponential factor into (3.30). At the end of the calculation of \hat{H}_I in Appendix C the term proportional to $\frac{2\Delta\Phi_{DC}}{L_g}$ is subtracted by the Hamiltonian since it is an offset in the magnetic energy caused by the presence of L_g , that unphysically linearly raises the overall energy of the system breaking the periodicity.

Summing up all the expressions found for h_0 , \hat{H}_I , \hat{H}_{II} , \hat{H}_{III} , \hat{H}_{IV} and \hat{H}_V , gathering the terms accordingly to the number of indexes, we derive the complete Hamiltonian for the JTWPA (refere to Appendix B for further details on the mathematical

notation used): ¹

$$\begin{aligned}
 \hat{H} = N & \left[I_c \varphi_0 (1 - p_1) + \frac{\Delta \Phi_{DC}^2}{2L_g} \right] + \\
 & - \sum_n \left[\left(\frac{I_c p_2}{a} \right) q_{0,n} \right] c_n \{ \hat{a} + \hat{a}^\dagger \}_n \frac{i}{\Delta k_n} \left(e^{i \Delta k_n a N} - 1 \right) e^{-i \Delta \omega_n t} + \\
 & - \sum_{n,l} \left[\left(\frac{I_c p_2}{a} \right) q_{1,n} + \left[\frac{1}{2a} \left(\frac{I_c p_1}{\varphi_0} + \frac{1}{L_g} \right) + \frac{C_J}{2a} \Delta \omega_n \Delta \omega_l \right] q_{0,n} q_{0,l} + \frac{\hbar}{4a N} \frac{\sqrt{\omega_n \omega_l}}{c_n c_l} \right] \cdot \\
 & \quad \cdot c_n c_l \{ \hat{a} + \hat{a}^\dagger \}_{n,l} \frac{i}{\Delta k_{n,l}} \left(e^{i \Delta k_{n,l} a N} - 1 \right) e^{-i \Delta \omega_{n,l} t} + \\
 & - \sum_{n,l,m} \left[\left(\frac{I_c p_2}{a} \right) q_{2,n} + \frac{1}{a} \left(\frac{I_c p_1}{\varphi_0} + \frac{1}{L_g} \right) q_{0,n} q_{1,l} - \frac{I_c p_2}{6a \varphi_0^2} q_{0,n} q_{0,l} q_{0,m} + \right. \\
 & \quad \left. + \frac{C_J}{2a} [q_{0,n} q_{1,l} \Delta \omega_n \Delta \omega_{m,l} + q_{1,n} q_{0,l} \Delta \omega_l \Delta \omega_{n,m}] \right] \cdot \\
 & \quad \cdot c_n c_l c_m \{ \hat{a} + \hat{a}^\dagger \}_{n,l,m} \frac{i}{\Delta k_{n,l,m}} \left(e^{i \Delta k_{n,l,m} a N} - 1 \right) e^{-i \Delta \omega_{n,l,m} t} + \\
 & - \sum_{n,l,m,s} \left[\left(\frac{I_c p_2}{a} \right) q_{3,n} + \frac{1}{2a} \left(\frac{I_c p_1}{\varphi_0} + \frac{1}{L_g} \right) (2q_{0,n} q_{2,l} + q_{1,n} q_{1,l}) + \right. \\
 & \quad - \frac{I_c p_2}{2a \varphi_0^2} q_{1,n} q_{0,l} q_{0,m} - \frac{I_c p_1}{24a \varphi_0^3} q_{0,n} q_{0,l} q_{0,m} q_{0,s} + \\
 & \quad \left. + \frac{C_J}{2a} [q_{1,n} q_{1,l} (\Delta \omega_m \Delta \omega_{s,l} + \Delta \omega_n \Delta \omega_{m,l}) + q_{2,n} q_{0,l} \Delta \omega_l \Delta \omega_{2m,n} + q_{0,n} q_{2,l} \Delta \omega_n \Delta \omega_{2m,l}] \right] \cdot \\
 & \quad \cdot c_n c_l c_m c_s \{ \hat{a} + \hat{a}^\dagger \}_{n,l,m,s} \frac{i}{\Delta k_{n,l,m,s}} \left(e^{i \Delta k_{n,l,m,s} a N} - 1 \right) e^{-i \Delta \omega_{n,l,m,s} t}
 \end{aligned} \tag{3.32}$$

An important remark should be made about equation (3.32), namely that it doesn't fulfill *a priori* the energy conservation required by the three and four photons process that it describes. In other terms, this Hamiltonian operator also describes non-energy conservative interaction between modes.

To clarify this concept, we can analyze some of the terms contained in this operator. All the terms deriving from the sum over a single-index will be proportional either to a single annihilation operator or a creation operator. Thus, these terms describe events in which a single photon is destroyed or created, not conserving energy in the scattering.

¹In this expression we exploit the equivalence $2\Delta\omega_m = 2(\pm\omega_m) = \pm(2\omega_m) = \Delta\omega_{2m}$.

Some of the terms deriving from the sum over the double-index will be proportional to a combination of ladder operators with the form $\hat{a}_n \hat{a}_l$ or $\hat{a}_n^\dagger \hat{a}_l^\dagger$. Once again all of these terms don't fulfill the energy conservation law because they represent the creation or annihilation of two photons.

Regarding the terms proportional to combination of ladder operators of the form $\hat{a}_n^\dagger \hat{a}_l$ or $\hat{a}_n \hat{a}_l^\dagger$ they will be physically acceptable just in the case of $n = l$ (i.e., in the case in which a photon of energy $\hbar\omega_n$ is created (destroyed) and a photon with energy $\hbar\omega_l = \hbar\omega_n$ is destroyed (created)).

More in general, if we want a Hamiltonian operator that describes physical scatterings we have to discard in Eq. (3.32) all the combinations of ladder operators that don't respect the energy conservation law, and for those particular combinations that fulfill this requirement, it will always be $\Delta\omega_{n,l} = 0$, $\Delta\omega_{n,l,m} = 0$ or $\Delta\omega_{n,l,m,s} = 0$. Furthermore, if we limit from this point our analysis just to the combinations of progressive modes (i.e., the ones associated to positive indexes) the imposition of the energy conservation law will automatically select a set of terms for which, supposing a small chromatic dispersion, will be true that $\Delta k a N \ll 1$. Under this assumption

$$-\frac{i \left(e^{i\Delta k a N} - 1 \right)}{\Delta k} \approx -\frac{i \left(1 + i\Delta k a N - 1 \right)}{\Delta k} = aN \quad \text{where} \quad \Delta k = \Delta k_{n,l}, \Delta k_{n,l,m} \text{ or } \Delta k_{n,l,m,s} \quad (3.33)$$

With these considerations, the Hamiltonian can be rewritten as

$$\begin{aligned}
 \hat{H} = & N \left[I_c \varphi_0 \left(1 - \cos \left(\frac{\Delta \Phi_{DC}}{\varphi_0} \right) \right) + \frac{\Delta \Phi_{DC}^2}{2L_g} \right] + \\
 & + \sum_n \frac{\hbar \omega_n}{2} \left(\hat{a}_n^\dagger \hat{a}_n + \frac{1}{2} \right) + \\
 & + \sum_n N \left[(I_c p_2) q_{1,n} + \left(\frac{I_c p_1}{\varphi_0} + \frac{1}{L_g} + C_J \Delta \omega_n^2 \right) \frac{q_{0,n}^2}{2} \right] 2c_n^2 \left(\hat{a}_n^\dagger \hat{a}_n + \frac{1}{2} \right) + \\
 & + \sum_{n,l,m} N \left[(I_c p_2) q_{2,n} + \left(\frac{I_c p_1}{\varphi_0} + \frac{1}{L_g} \right) q_{0,n} q_{1,l} - \frac{I_c p_2}{6\varphi_0^2} q_{0,n} q_{0,l} q_{0,m} + \right. \\
 & \quad \left. + \frac{C_J}{2} [q_{0,n} q_{1,l} \Delta \omega_n \Delta \omega_{m,l} + q_{1,n} q_{0,l} \Delta \omega_l \Delta \omega_{n,m}] \right] c_n c_l c_m \left\{ \hat{a} + \hat{a}^\dagger \right\}_{n,l,m} \delta_{\Delta \omega_{n,l,m}, 0} + \\
 & + \sum_{n,l,m,s} N \left[(I_c p_2) q_{3,n} + \frac{1}{2} \left(\frac{I_c p_1}{\varphi_0} + \frac{1}{L_g} \right) (2q_{0,n} q_{2,l} + q_{1,n} q_{1,l}) + \right. \\
 & \quad - \frac{I_c p_2}{2\varphi_0^2} q_{1,n} q_{0,l} q_{0,m} - \frac{I_c p_1}{24\varphi_0^3} q_{0,n} q_{0,l} q_{0,m} q_{0,s} + \\
 & \quad \left. + \frac{C_J}{2} [q_{1,n} q_{1,l} (\Delta \omega_m \Delta \omega_{s,l} + \Delta \omega_n \Delta \omega_{m,l}) + q_{2,n} q_{0,l} \Delta \omega_l \Delta \omega_{2m,n} + q_{0,n} q_{2,l} \Delta \omega_n \Delta \omega_{2m,l}] \right] \cdot \\
 & \cdot c_n c_l c_m c_s \left\{ \hat{a} + \hat{a}^\dagger \right\}_{n,l,m,s} \delta_{\Delta \omega_{n,l,m,s}, 0} \tag{3.34}
 \end{aligned}$$

where $\delta_{\Delta \omega_{n,l,m}, 0}$ and $\delta_{\Delta \omega_{n,l,m,s}, 0}$ are Kronecker deltas, that are 0 for all the non energy-conservative combinations of ladder operators.

Therefore, Eq. (3.34) is the complete Hamiltonian for a JTWPA modelling all the energy-conservative interactions up to four photons arising from the nonlinearity given by the rf-SQUIDs embedded in it.

We can rewrite Equation (3.34) in a more compact and handy form using the curly bracket operators

$$\begin{aligned}
 \hat{H} = & h_0 + \hat{H}_1 + \hat{H}_{3WM} + \hat{H}_{4WM} = \\
 = & h_0 + \sum_n \hbar \chi_1^{(n)} \left(\hat{a}_n^\dagger \hat{a}_n + \frac{1}{2} \right) + \\
 & + \sum_{n,l,m} \hbar \chi_3^{(n,l,m)} \left\{ \hat{a} + \hat{a}^\dagger \right\}_{n,l,m} \delta_{\Delta \omega_{n,l,m}, 0} + \\
 & + \sum_{n,l,m,s} \hbar \chi_4^{(n,l,m,s)} \left\{ \hat{a} + \hat{a}^\dagger \right\}_{n,l,m,s} \delta_{\Delta \omega_{n,l,m,s}, 0} \tag{3.35}
 \end{aligned}$$

where we defined some important quantities that characterize the Hamiltonian.

h_0 is the energy stored into the medium due to the external bias conditions

$$h_0 = N \left[I_c \varphi_0 \left(1 - \cos \left(\frac{\Delta \Phi_{DC}}{\varphi_0} \right) \right) + \frac{\Delta \Phi_{DC}^2}{2L_g} \right] \quad (3.36)$$

one can indeed notice that this piece of the Hamiltonian goes to zero if one switches off the external bias, hence brings to zero $\Delta \Phi_{DC}$.

Then we introduce the term representing the energy deriving from the propagation of a photon of energy $\hbar \omega_n$ in the nonlinear medium, or the non-interacting-modes Hamiltonian constant of the n -th mode

$$\begin{aligned} \chi_1^{(n)} &= \frac{\omega_n}{2} + 2NL_g \Lambda_n \frac{\omega_n}{2N} \left[(I_c p_2) q_{1,n} + \left(\frac{I_c p_1}{\varphi_0} + \frac{1}{L_g} + C_J \Delta \omega_n^2 \right) \frac{q_{0,n}^2}{2} \right] = \\ &= \frac{\omega_n}{2} \left(1 + 2L_g \Lambda_n \left[(I_c p_2) q_{1,n} + \left(\frac{I_c p_1}{\varphi_0} + \frac{1}{L_g} + C_J \Delta \omega_n^2 \right) \frac{q_{0,n}^2}{2} \right] \right) \end{aligned} \quad (3.37)$$

The term containing the sum over three indexes leads to the identification of the 3WM coupling constant of ordered modes (n, l, m) , describing all the physical scattering processes involving three photons (e.g. Parametric Down Conversion, Second Harmonic Generation, etc.)

$$\begin{aligned} \chi_3^{(n,l,m)} &= \frac{N}{\hbar} \left[(I_c p_2) q_{2,n} + \left(\frac{I_c p_1}{\varphi_0} + \frac{1}{L_g} \right) q_{0,n} q_{1,l} - \frac{I_c p_2}{6\varphi_0^2} q_{0,n} q_{0,l} q_{0,m} + \right. \\ &\quad \left. + \frac{C_J}{2} [q_{0,n} q_{1,l} \Delta \omega_n \Delta \omega_{m,l} + q_{1,n} q_{0,l} \Delta \omega_l \Delta \omega_{n,m}] \right] c_n c_l c_m \\ &= \sqrt{\frac{\hbar L_g^3}{8N}} \sqrt{\omega_n \Lambda_n \omega_l \Lambda_l \omega_m \Lambda_m} \left[(I_c p_2) q_{2,n} + \left(\frac{I_c p_1}{\varphi_0} + \frac{1}{L_g} \right) q_{0,n} q_{1,l} + \right. \\ &\quad \left. - \frac{I_c p_2}{6\varphi_0^2} q_{0,n} q_{0,l} q_{0,m} + \frac{C_J}{2} [q_{0,n} q_{1,l} \Delta \omega_n \Delta \omega_{m,l} + q_{1,n} q_{0,l} \Delta \omega_l \Delta \omega_{n,m}] \right] \end{aligned} \quad (3.38)$$

While the term containing the sum over four indexes leads to the definition of the 4WM coupling constant of ordered modes (n, l, m, s) , describing all the physical

scattering processes involving four photons

$$\begin{aligned}
 \chi_4^{(n,l,m,s)} &= \frac{N}{\hbar} \left[(I_c p_2) q_{3,n} + \frac{1}{2} \left(\frac{I_c p_1}{\varphi_0} + \frac{1}{L_g} \right) (2q_{0,n} q_{2,l} + q_{1,n} q_{1,l}) + \right. \\
 &\quad - \frac{I_c p_2}{2\varphi_0^2} q_{1,n} q_{0,l} q_{0,m} - \frac{I_c p_1}{24\varphi_0^3} q_{0,n} q_{0,l} q_{0,m} q_{0,s} + \\
 &\quad \left. + \frac{C_J}{2} [q_{1,n} q_{1,l} (\Delta\omega_m \Delta\omega_{s,l} + \Delta\omega_n \Delta\omega_{m,l}) + q_{2,n} q_{0,l} \Delta\omega_l \Delta\omega_{2m,n} + q_{0,n} q_{2,l} \Delta\omega_n \Delta\omega_{2m,l}] \right] c_n c_l c_m c_s \\
 &= \frac{\hbar L_g^2}{4N} \sqrt{\omega_n \Lambda_n \omega_l \Lambda_l \omega_m \Lambda_m \omega_s \Lambda_s} \left[(I_c p_2) q_{3,n} + \frac{1}{2} \left(\frac{I_c p_1}{\varphi_0} + \frac{1}{L_g} \right) (2q_{0,n} q_{2,l} + q_{1,n} q_{1,l}) + \right. \\
 &\quad - \frac{I_c p_2}{2\varphi_0^2} q_{1,n} q_{0,l} q_{0,m} - \frac{I_c p_1}{24\varphi_0^3} q_{0,n} q_{0,l} q_{0,m} q_{0,s} + \\
 &\quad \left. + \frac{C_J}{2} [q_{1,n} q_{1,l} (\Delta\omega_m \Delta\omega_{s,l} + \Delta\omega_n \Delta\omega_{m,l}) + q_{2,n} q_{0,l} \Delta\omega_l \Delta\omega_{2m,n} + q_{0,n} q_{2,l} \Delta\omega_n \Delta\omega_{2m,l}] \right] \\
 &\hspace{15em} (3.39)
 \end{aligned}$$

3.1.2 Three-Wave Mixing

The Parametric Down Conversion (PDC) process is the scattering in which a pump photon gets converted into a pair of lower frequency photons. This process is stimulated by the presence in the medium of a non-zero initial photonic population in a certain mode n , and for this reason the process is said "parametric". The energy transfer from one mode to another can be explained by adding a nonlinear component to the dielectric polarization density vector that describes the interaction of the electromagnetic field into the nonlinear medium.

Once you admit the existence of at least two modes into a nonlinear material, the natural consequence is the arise of more spectral components of the electromagnetic field that oscillate at frequencies that are sums and differences of the initial ones. Anyway, the classical view of this phenomenon is somehow limited. Indeed, if we consider just one input tone, we will predict an output field that oscillates at the same frequency and with the same phase of the input one, without any other harmonics. This prevision is totally inaccurate, indeed experimental observations tell us that the same process of frequency conversion arises also spontaneously, just by feeding the nonlinear medium with a single tone. This effect takes the name of Spontaneous Parametric Down Conversion (SPDC) and needs a quantum mechanical description, in terms of creation and annihilation operators to be accurately modelled. The effects of PDC induced by an input mode at frequency different from the pump one are so pronounced that an arbitrary weak input tone (even a one single photon) can be amplified through this transfer of energy. Straightforwardly, this "seeded" PDC can be used to amplify and manipulate very weak signals and

non-classical states.

In this section we will thoroughly analyse the PDC through a 3WM process. This event occurs when a pump photon, with the highest frequency (ω_p) interacts through the nonlinear medium with a couple of signal and idler modes (with, respectively, frequencies ω_s and ω_i). The relation between the frequencies of these photons must withstand the energy conservation law, and so it must be

$$\omega_p = \omega_s + \omega_i \quad (3.40)$$

We here analyze the specific case of the 3WM interaction between three modes that fulfill the energy conservation law reported in Eq. (3.40). This implies that, among all the infinite values that the indexes within the definition of \hat{H}_{3WM} (see Eq. (3.35)) can assume, we will just take into account the case in which n, l , and m assume a value among the set $\{p, s, i\}$.

First, we explicitly write the 3-index curly brackets operator:

$$\begin{aligned} \{\hat{a} + \hat{a}^\dagger\}_{n,l,m} &= (\hat{a}_n + \hat{a}_n^\dagger) (\hat{a}_l + \hat{a}_l^\dagger) (\hat{a}_m + \hat{a}_m^\dagger) \\ &= (\hat{a}_n + \hat{a}_n) (\hat{a}_l \hat{a}_m + \hat{a}_l^\dagger \hat{a}_m + \hat{a}_l \hat{a}_m^\dagger + \hat{a}_l^\dagger \hat{a}_m^\dagger) \\ &= \hat{a}_n \hat{a}_l \hat{a}_m + \hat{a}_n \hat{a}_l^\dagger \hat{a}_m + \hat{a}_n \hat{a}_l \hat{a}_m^\dagger + \hat{a}_n \hat{a}_l^\dagger \hat{a}_m^\dagger + \\ &\quad + \hat{a}_n^\dagger \hat{a}_l \hat{a}_m + \hat{a}_n^\dagger \hat{a}_l^\dagger \hat{a}_m + \hat{a}_n^\dagger \hat{a}_l \hat{a}_m^\dagger + \hat{a}_n^\dagger \hat{a}_l^\dagger \hat{a}_m^\dagger \end{aligned} \quad (3.41)$$

For a given quantum state $|\psi\rangle$ the only combinations of creation and annihilation operators that respect the energy conservation are:

- Combinations in which a pump photon is annihilated and a couple of signal and idler photons are created (i.e., combination of operators in the form $\hat{a}_s^\dagger \hat{a}_i^\dagger \hat{a}_p$);
- Combinations in which a couple of signal and idler photons are annihilated and a pump photon is created (i.e., combination of operators in the form $\hat{a}_p^\dagger \hat{a}_s \hat{a}_i$)

Therefore, we can rewrite Eq. (3.41) deleting the non energy-conservative combinations of operator and then, for each combination of operators, bring the creation operators on the left-side and the annihilation operators on the right-side. To do that, we exploit the canonical commutation relation $[\hat{a}_n, \hat{a}_l^\dagger] = \delta_{n,l}$:

$$\begin{aligned} \{\hat{a} + \hat{a}^\dagger\}_{n,l,m} &= \cancel{\hat{a}_n \hat{a}_l \hat{a}_m} + (\hat{a}_l^\dagger \hat{a}_n + \delta_{n,l}) \hat{a}_m + \hat{a}_n (\hat{a}_m^\dagger \hat{a}_l + \delta_{m,l}) + (\hat{a}_l^\dagger \hat{a}_n + \delta_{n,l}) \hat{a}_m^\dagger + \\ &\quad + \hat{a}_n^\dagger \hat{a}_l \hat{a}_m + \hat{a}_n^\dagger \hat{a}_l^\dagger \hat{a}_m + \hat{a}_n^\dagger (\hat{a}_m^\dagger \hat{a}_l + \delta_{m,l}) + \cancel{\hat{a}_n^\dagger \hat{a}_l^\dagger \hat{a}_m^\dagger} = \\ &= \hat{a}_l^\dagger \hat{a}_n \hat{a}_m + \cancel{\delta_{n,l} \hat{a}_m} + \hat{a}_n \hat{a}_m^\dagger \hat{a}_l + \cancel{\hat{a}_n \delta_{m,l}} + \hat{a}_l^\dagger \hat{a}_n \hat{a}_m^\dagger + \cancel{\delta_{n,l} \hat{a}_m^\dagger} + \\ &\quad + \hat{a}_n^\dagger \hat{a}_l \hat{a}_m + \hat{a}_n^\dagger \hat{a}_l^\dagger \hat{a}_m + \hat{a}_n^\dagger \hat{a}_m^\dagger \hat{a}_l + \cancel{\hat{a}_n^\dagger \delta_{m,l}} = \\ &= \hat{a}_l^\dagger \hat{a}_n \hat{a}_m + (\cancel{\hat{a}_m^\dagger \hat{a}_n} + \cancel{\delta_{n,m}}) \hat{a}_l + \hat{a}_l^\dagger (\hat{a}_m^\dagger \hat{a}_n + \cancel{\delta_{n,m}}) + \hat{a}_n^\dagger \hat{a}_l \hat{a}_m + \hat{a}_n^\dagger \hat{a}_l^\dagger \hat{a}_m + \hat{a}_n^\dagger \hat{a}_m^\dagger \hat{a}_l = \\ &= \hat{a}_l^\dagger \hat{a}_n \hat{a}_m + \hat{a}_m^\dagger \hat{a}_n \hat{a}_l + \hat{a}_l^\dagger \hat{a}_m^\dagger \hat{a}_n + \hat{a}_n^\dagger \hat{a}_l \hat{a}_m + \hat{a}_n^\dagger \hat{a}_l^\dagger \hat{a}_m + \hat{a}_n^\dagger \hat{a}_m^\dagger \hat{a}_l \end{aligned} \quad (3.42)$$

Hence, we can write the 3WM Hamiltonian as

$$\begin{aligned}
 \hat{H}_{3\text{WM}} &= \sum_{n,l,m} \hbar \chi_3^{(n,l,m)} \{\hat{a} + \hat{a}^\dagger\}_{n,l,m} \delta_{\Delta\omega_{n,l,m},0} = \\
 &= \sum_{n,l,m=\{p,s,i\}} \hbar \chi_3^{(n,l,m)} \left[\hat{a}_l^\dagger \hat{a}_n \hat{a}_m + \hat{a}_m^\dagger \hat{a}_n \hat{a}_l + \hat{a}_n^\dagger \hat{a}_l \hat{a}_m + \hat{a}_l^\dagger \hat{a}_m^\dagger \hat{a}_n + \hat{a}_n^\dagger \hat{a}_l^\dagger \hat{a}_m + \hat{a}_n^\dagger \hat{a}_m^\dagger \hat{a}_l \right]
 \end{aligned} \tag{3.43}$$

We can now explicit the sum over the three indexes n, l, m . For instance, regarding the first term $\hat{a}_l^\dagger \hat{a}_n \hat{a}_m$, among all the possible combinations just two of them can represent an interaction between three photons that conserve the total energy (Eq. (3.40)), the first is the one in which $n = s, l = p$, and $m = i$ while the other is the one in which $n = i, l = p$, and $m = s$. This greatly limits the number of possible indices combinations.

Being $\chi_3^{(n,l,m)}$ a function of $\Delta\omega_n, \Delta\omega_l$, and $\Delta\omega_m$ its expression will depend on the particular combination of ladder operators to whom this coefficient is associated with (see Appendix B for more details). To make this dependence more explicit we will include in the expression of $\chi_3^{(n,l,m)}$ also a reference to the associated operators. For instance, the 3WM coupling constant associated to $\hat{a}_p^\dagger \hat{a}_s \hat{a}_i$ will be $\chi_3^{(p^\dagger, s, i)}$ and in its definition is $\Delta\omega_n = \Delta\omega_s = \omega_s, \Delta\omega_l = \Delta\omega_p = -\omega_p$, and $\Delta\omega_m = \Delta\omega_i = \omega_i$. Under all these assumptions, the calculation of the sum in Eq. (3.43) gives

$$\begin{aligned}
 \hat{H}_{3\text{WM}} &= \hbar \left[\chi_3^{(s, p^\dagger, i)} \hat{a}_p^\dagger \hat{a}_s \hat{a}_i + \chi_3^{(i, p^\dagger, s)} \hat{a}_p^\dagger \hat{a}_i \hat{a}_s + \chi_3^{(s, i, p^\dagger)} \hat{a}_p^\dagger \hat{a}_s \hat{a}_i + \chi_3^{(i, s, p^\dagger)} \hat{a}_p^\dagger \hat{a}_i \hat{a}_s + \right. \\
 &\quad + \chi_3^{(p^\dagger, s, i)} \hat{a}_p^\dagger \hat{a}_s \hat{a}_i + \chi_3^{(p^\dagger, i, s)} \hat{a}_p^\dagger \hat{a}_i \hat{a}_s + \chi_3^{(p, s^\dagger, i^\dagger)} \hat{a}_s^\dagger \hat{a}_i^\dagger \hat{a}_p + \chi_3^{(p, i^\dagger, s^\dagger)} \hat{a}_i^\dagger \hat{a}_s^\dagger \hat{a}_p + \\
 &\quad \left. + \chi_3^{(s^\dagger, i^\dagger, p)} \hat{a}_s^\dagger \hat{a}_i^\dagger \hat{a}_p + \chi_3^{(i^\dagger, s^\dagger, p)} \hat{a}_i^\dagger \hat{a}_s^\dagger \hat{a}_p + \chi_3^{(s^\dagger, p, i^\dagger)} \hat{a}_s^\dagger \hat{a}_i^\dagger \hat{a}_p + \chi_3^{(i^\dagger, p, s^\dagger)} \hat{a}_i^\dagger \hat{a}_s^\dagger \hat{a}_p \right]
 \end{aligned} \tag{3.44}$$

This expression can be further simplified considering that the coupling constants with the same ordered indices are identical (e.g., $\chi_3^{(s, p^\dagger, i)} = \chi_3^{(s^\dagger, p, i^\dagger)} \equiv \chi_3^{(s, p, i)}$, $\chi_3^{(i, p^\dagger, s)} = \chi_3^{(i^\dagger, p, s^\dagger)} \equiv \chi_3^{(i, p, s)}$, etc.) and that the commutation relations for different modes give $[\hat{a}_s, \hat{a}_i] = 0$ and $[\hat{a}_s^\dagger, \hat{a}_i^\dagger] = 0$, which allow to group some terms and write

$$\begin{aligned}
 \hat{H}_{3\text{WM}} &= \hbar \left[\chi_3^{(p, s, i)} + \chi_3^{(p, i, s)} + \chi_3^{(s, p, i)} + \chi_3^{(i, p, s)} + \chi_3^{(s, i, p)} + \chi_3^{(i, s, p)} \right] \left(\hat{a}_p^\dagger \hat{a}_s \hat{a}_i + \hat{a}_s^\dagger \hat{a}_i^\dagger \hat{a}_p \right) = \\
 &= \hbar \chi_3^{\{p, s, i\}} \left(\hat{a}_p^\dagger \hat{a}_s \hat{a}_i + \hat{a}_s^\dagger \hat{a}_i^\dagger \hat{a}_p \right)
 \end{aligned} \tag{3.45}$$

where

$$\chi_3^{\{p, s, i\}} \equiv \frac{1}{2} \left(\chi_3^{(p, s, i)} + \chi_3^{(p, i, s)} + \chi_3^{(s, p, i)} + \chi_3^{(i, p, s)} + \chi_3^{(s, i, p)} + \chi_3^{(i, s, p)} \right) \tag{3.46}$$

is one half of the sum of all the possible indexes permutations of Eq. (3.38) neglecting permutations sign degeneracy.

Eq. (3.45) is then the interaction Hamiltonian that describes 3WM in a JTWPA. It has a standard form very well known in quantum optics, but we stress the fact that the coupling constant $\chi_3^{\{p,s,i\}}$ is known just considering the structure of the circuit and the bias condition, and it is not a mere free parameter of the theory.

3.1.3 Four-Wave Mixing

Just like in the case of the 3WM interaction, amplification can occur also due to the nonlinearity that causes the 4WM interaction. In this section we will analyze the specific case of the 4WM between three modes that fulfill the energy-conservation law, hence the pump-degenerate 4WM scattering

$$2\omega_p = \omega_s + \omega_j \quad (3.47)$$

This implies that, among all the infinite values that the indexes within the definition of \hat{H}_{4WM} (see Eq. (3.35)) can assume, we will just take into account the case in which n, l, m, s assume a value among the set $\{p, s, j\}$.

First, we write the 4-index curly bracket operator explicitly:

$$\begin{aligned} \{\hat{a} + \hat{a}^\dagger\}_{n,l,m,s} &= (\hat{a}_n + \hat{a}_n^\dagger)(\hat{a}_l + \hat{a}_l^\dagger)(\hat{a}_m + \hat{a}_m^\dagger)(\hat{a}_s + \hat{a}_s^\dagger) = \\ &= (\hat{a}_n\hat{a}_l + \hat{a}_n\hat{a}_l^\dagger + \hat{a}_n^\dagger\hat{a}_l + \hat{a}_n^\dagger\hat{a}_l^\dagger)(\hat{a}_m\hat{a}_s + \hat{a}_m\hat{a}_s^\dagger + \hat{a}_m^\dagger\hat{a}_s + \hat{a}_m^\dagger\hat{a}_s^\dagger) = \\ &= \hat{a}_n\hat{a}_l\hat{a}_m\hat{a}_s + \hat{a}_n\hat{a}_l\hat{a}_m\hat{a}_s^\dagger + \hat{a}_n\hat{a}_l\hat{a}_m^\dagger\hat{a}_s + \hat{a}_n\hat{a}_l\hat{a}_m^\dagger\hat{a}_s^\dagger + \\ &\quad + \hat{a}_n\hat{a}_l^\dagger\hat{a}_m\hat{a}_s + \hat{a}_n\hat{a}_l^\dagger\hat{a}_m\hat{a}_s^\dagger + \hat{a}_n\hat{a}_l^\dagger\hat{a}_m^\dagger\hat{a}_s + \hat{a}_n\hat{a}_l^\dagger\hat{a}_m^\dagger\hat{a}_s^\dagger + \\ &\quad + \hat{a}_n^\dagger\hat{a}_l\hat{a}_m\hat{a}_s + \hat{a}_n^\dagger\hat{a}_l\hat{a}_m\hat{a}_s^\dagger + \hat{a}_n^\dagger\hat{a}_l\hat{a}_m^\dagger\hat{a}_s + \hat{a}_n^\dagger\hat{a}_l\hat{a}_m^\dagger\hat{a}_s^\dagger + \\ &\quad + \hat{a}_n^\dagger\hat{a}_l^\dagger\hat{a}_m\hat{a}_s + \hat{a}_n^\dagger\hat{a}_l^\dagger\hat{a}_m\hat{a}_s^\dagger + \hat{a}_n^\dagger\hat{a}_l^\dagger\hat{a}_m^\dagger\hat{a}_s + \hat{a}_n^\dagger\hat{a}_l^\dagger\hat{a}_m^\dagger\hat{a}_s^\dagger \end{aligned} \quad (3.48)$$

The only terms that can fulfill the energy conservation requirement given in Eq. (3.47) are those made of a couple of creation operators and a couple of annihilation operators. These terms can describe one of the following events:

- Annihilation of two pump photons and creation of a couple of signal-idler photons (i.e. terms in the form $\hat{a}_p^\dagger\hat{a}_p^\dagger\hat{a}_s\hat{a}_j$ or $\hat{a}_p^\dagger\hat{a}_p^\dagger\hat{a}_j\hat{a}_s$);
- Annihilation of a couple of signal-idler photons and creation of two pump photons (i.e. terms in the form $\hat{a}_p\hat{a}_p\hat{a}_s^\dagger\hat{a}_j^\dagger$ or $\hat{a}_p\hat{a}_p\hat{a}_j^\dagger\hat{a}_s^\dagger$);
- Annihilation and creation of a couple of tones. These are non-mixing terms with the form $\hat{a}_p^\dagger\hat{a}_p^\dagger\hat{a}_p\hat{a}_p$, $\hat{a}_s^\dagger\hat{a}_s^\dagger\hat{a}_s\hat{a}_s$, $\hat{a}_j^\dagger\hat{a}_j^\dagger\hat{a}_j\hat{a}_j$, $\hat{a}_p^\dagger\hat{a}_p^\dagger\hat{a}_s\hat{a}_s$, $\hat{a}_p^\dagger\hat{a}_p^\dagger\hat{a}_j\hat{a}_j$, or $\hat{a}_s^\dagger\hat{a}_s^\dagger\hat{a}_j\hat{a}_j$

Hence, under the hypothesis of energy-conservation in a four-wave mixing interaction, $\hat{H}_{4\text{WM}}$ can be written as

$$\begin{aligned}
 \hat{H}_{4\text{WM}} &= \sum_{n,l,m,s} \hbar \chi_4^{(n,l,m,s)} \{\hat{a} + \hat{a}^\dagger\}_{n,l,m,s} \delta_{\Delta\omega_{n,l,m,s},0} = \\
 &= \sum_{n,l,m,s=\{p,s,j\}} \hbar \left[\chi_4^{(n,l,m^\dagger,s^\dagger)} \hat{a}_n \hat{a}_l \hat{a}_m^\dagger \hat{a}_s^\dagger + \chi_4^{(n,l^\dagger,m,s^\dagger)} \hat{a}_n \hat{a}_l^\dagger \hat{a}_m \hat{a}_s^\dagger + \chi_4^{(n,l^\dagger,m^\dagger,s)} \hat{a}_n \hat{a}_l^\dagger \hat{a}_m^\dagger \hat{a}_s + \right. \\
 &\quad \left. + \chi_4^{(n^\dagger,l,m,s^\dagger)} \hat{a}_n^\dagger \hat{a}_l \hat{a}_m \hat{a}_s^\dagger + \chi_4^{(n^\dagger,l,m^\dagger,s)} \hat{a}_n^\dagger \hat{a}_l \hat{a}_m^\dagger \hat{a}_s + \chi_4^{(n^\dagger,l^\dagger,m,s)} \hat{a}_n^\dagger \hat{a}_l^\dagger \hat{a}_m \hat{a}_s \right]
 \end{aligned} \tag{3.49}$$

Writing explicitly the six terms contained in Eq. (3.49) (see Appendix D) we can recast $\hat{H}_{4\text{WM}}$ as

$$\begin{aligned}
 \hat{H}_{4\text{WM}} &= \hbar \xi_0 + \hbar \xi_p \hat{a}_p^\dagger \hat{a}_p + \hbar \xi_s \hat{a}_s^\dagger \hat{a}_s + \hbar \xi_j \hat{a}_j^\dagger \hat{a}_j + \\
 &\quad + \hbar \xi_{pp} \hat{a}_p^\dagger \hat{a}_p^\dagger \hat{a}_p \hat{a}_p + \hbar \xi_{ss} \hat{a}_s^\dagger \hat{a}_s^\dagger \hat{a}_s \hat{a}_s + \hbar \xi_{jj} \hat{a}_j^\dagger \hat{a}_j^\dagger \hat{a}_j \hat{a}_j + \\
 &\quad + \hbar \xi_{ps} \hat{a}_p^\dagger \hat{a}_p^\dagger \hat{a}_s \hat{a}_s + \hbar \xi_{pj} \hat{a}_p^\dagger \hat{a}_p^\dagger \hat{a}_j \hat{a}_j + \hbar \xi_{sj} \hat{a}_s^\dagger \hat{a}_s^\dagger \hat{a}_j \hat{a}_j + \\
 &\quad + \hbar \chi_4^{\{p,p,s,j\}} (\hat{a}_p^\dagger \hat{a}_p^\dagger \hat{a}_s \hat{a}_j + \hat{a}_p \hat{a}_p \hat{a}_s^\dagger \hat{a}_j^\dagger)
 \end{aligned} \tag{3.50}$$

It is now worth making a small digression to analyse all the terms in Eq. (3.50), so as to understand their physical meanings.

The terms proportional to a single index (ξ_p, ξ_s, ξ_j) express the energy of the non-interactive modes, that is modified by the 4WM nonlinearity of the medium, and add energy proportionally to the amount of photons in the device.

The terms proportional to two indices express the interaction between two traveling modes, quantifying the *self-phase modulation* (SPM) and *cross-phase modulation* (XPM) caused by the the 4-photons interaction.

ξ_{pp} is the SPM parameter of the pump tone, associated to the energy conservative permutation of four ladder operators with $n, l, m, s = \{p\}$.

$$\xi_{pp} \equiv \sum_{n,l,m,s=\{p\}} \chi_4^{(n,l,m,s)} = \chi_4^{(p,p,p^\dagger,p^\dagger)} + \chi_4^{(p,p^\dagger,p,p^\dagger)} + \chi_4^{(p,p^\dagger,p^\dagger,p)} + \chi_4^{(p^\dagger,p,p,p^\dagger)} + \chi_4^{(p^\dagger,p,p^\dagger,p)} + \chi_4^{(p^\dagger,p^\dagger,p,p)} \tag{3.51}$$

ξ_{ss} is the SPM parameter of the signal tone, associated to the energy conservative permutation of four ladder operators with $n, l, m, s = \{s\}$.

$$\xi_{ss} \equiv \sum_{n,l,m,s=\{s\}} \chi_4^{(n,l,m,s)} = \chi_4^{(s,s,s^\dagger,s^\dagger)} + \chi_4^{(s,s^\dagger,s,s^\dagger)} + \chi_4^{(s,s^\dagger,s^\dagger,s)} + \chi_4^{(s^\dagger,s,s,s^\dagger)} + \chi_4^{(s^\dagger,s,s^\dagger,s)} + \chi_4^{(s^\dagger,s^\dagger,s,s)} \tag{3.52}$$

ξ_{jj} is the SPM parameter of the idler tone, associated to the energy conservative permutation of four ladder operators with $n, l, m, s = \{j\}$.

$$\xi_{jj} \equiv \sum_{n,l,m,s=\{j\}} \chi_4^{(n,l,m,s)} = \chi_4^{(j,j,j^\dagger,j^\dagger)} + \chi_4^{(j,j^\dagger,j,j^\dagger)} + \chi_4^{(j,j^\dagger,j^\dagger,j)} + \chi_4^{(j^\dagger,j,j,j^\dagger)} + \chi_4^{(j^\dagger,j,j^\dagger,j)} + \chi_4^{(j^\dagger,j^\dagger,j,j)} \quad (3.53)$$

ξ_{ps} is the XPM parameter between the pump and the signal tones, calculated as the sum of all the coefficients $\chi_4^{(n,l,m,s)}$ associated to the energy-conservative permutation of four ladder operators with $n, l, m, s = \{p, s\}$

$$\begin{aligned} \xi_{ps} \equiv \sum_{n,l,m,s=\{p,s\}} \chi_4^{(n,l,m,s)} = & \chi_4^{(p,s,p^\dagger,s^\dagger)} + \chi_4^{(p,s,s^\dagger,p^\dagger)} + \chi_4^{(s,p,p^\dagger,s^\dagger)} + \chi_4^{(s,p,s^\dagger,p^\dagger)} + \\ & + \chi_4^{(p,p^\dagger,s,s^\dagger)} + \chi_4^{(s,s^\dagger,p,p^\dagger)} + \chi_4^{(p,s^\dagger,s,p^\dagger)} + \chi_4^{(s,p^\dagger,p,s^\dagger)} + \\ & + \chi_4^{(p,p^\dagger,s^\dagger,s)} + \chi_4^{(s,s^\dagger,p^\dagger,p)} + \chi_4^{(p,s^\dagger,p^\dagger,s)} + \chi_4^{(s,p^\dagger,s^\dagger,p)} + \\ & + \chi_4^{(p^\dagger,p,s,s^\dagger)} + \chi_4^{(s^\dagger,s,p,p^\dagger)} + \chi_4^{(p^\dagger,s,p,s^\dagger)} + \chi_4^{(s^\dagger,p,s,p^\dagger)} + \\ & + \chi_4^{(p^\dagger,p,s^\dagger,s)} + \chi_4^{(s^\dagger,s,p^\dagger,p)} + \chi_4^{(p^\dagger,s,s^\dagger,p)} + \chi_4^{(s^\dagger,p,p^\dagger,s)} + \\ & + \chi_4^{(p^\dagger,s^\dagger,p,s)} + \chi_4^{(p^\dagger,s^\dagger,s,p)} + \chi_4^{(s^\dagger,p^\dagger,p,s)} + \chi_4^{(s^\dagger,p^\dagger,s,p)} \quad (3.54) \end{aligned}$$

ξ_{pj} is the XPM parameter between the pump and the idler tones, calculated as the sum of all the coefficients $\chi_4^{(n,l,m,s)}$ associated to the energy-conservative permutation of four ladder operators with $n, l, m, s = \{p, j\}$

$$\begin{aligned} \xi_{pj} \equiv \sum_{n,l,m,s=\{p,j\}} \chi_4^{(n,l,m,s)} = & \chi_4^{(p,j,p^\dagger,j^\dagger)} + \chi_4^{(p,j,j^\dagger,p^\dagger)} + \chi_4^{(j,p,p^\dagger,j^\dagger)} + \chi_4^{(j,p,j^\dagger,p^\dagger)} + \\ & + \chi_4^{(p,p^\dagger,j,j^\dagger)} + \chi_4^{(j,j^\dagger,p,p^\dagger)} + \chi_4^{(p,j^\dagger,j,p^\dagger)} + \chi_4^{(j,p^\dagger,p,j^\dagger)} + \\ & + \chi_4^{(p,p^\dagger,j^\dagger,j)} + \chi_4^{(j,j^\dagger,p^\dagger,p)} + \chi_4^{(p,j^\dagger,p^\dagger,j)} + \chi_4^{(j,p^\dagger,j^\dagger,p)} + \\ & + \chi_4^{(p^\dagger,p,j,j^\dagger)} + \chi_4^{(j^\dagger,j,p,p^\dagger)} + \chi_4^{(p^\dagger,j,p,j^\dagger)} + \chi_4^{(j^\dagger,p,j,p^\dagger)} + \\ & + \chi_4^{(p^\dagger,p,j^\dagger,j)} + \chi_4^{(j^\dagger,j,p^\dagger,p)} + \chi_4^{(p^\dagger,j,j^\dagger,p)} + \chi_4^{(j^\dagger,p,p^\dagger,j)} + \\ & + \chi_4^{(p^\dagger,j^\dagger,p,j)} + \chi_4^{(p^\dagger,j^\dagger,j,p)} + \chi_4^{(j^\dagger,p^\dagger,p,j)} + \chi_4^{(j^\dagger,p^\dagger,j,p)} \quad (3.55) \end{aligned}$$

ξ_{sj} is the XPM parameter between the signal and the idler tones, calculated as the sum of all the coefficients $\chi_4^{(n,l,m,s)}$ associated to the energy-conservative permutation of four ladder operators with $n, l, m, s = \{s, j\}$

$$\begin{aligned}
 \xi_{sj} \equiv \sum_{n,l,m,s=\{p,j\}} \chi_4^{(n,l,m,s)} &= \chi_4^{(s,j,s^\dagger,j^\dagger)} + \chi_4^{(s,j,j^\dagger,s^\dagger)} + \chi_4^{(j,s,s^\dagger,j^\dagger)} + \chi_4^{(j,s,j^\dagger,s^\dagger)} + \\
 &+ \chi_4^{(s,s^\dagger,j,j^\dagger)} + \chi_4^{(j,j^\dagger,s,s^\dagger)} + \chi_4^{(s,j^\dagger,j,s^\dagger)} + \chi_4^{(j,s^\dagger,s,j^\dagger)} + \\
 &+ \chi_4^{(s,s^\dagger,j^\dagger,j)} + \chi_4^{(j,j^\dagger,s^\dagger,s)} + \chi_4^{(s,j^\dagger,s^\dagger,j)} + \chi_4^{(j,s^\dagger,j^\dagger,s)} + \\
 &+ \chi_4^{(s^\dagger,s,j,j^\dagger)} + \chi_4^{(j^\dagger,j,s,s^\dagger)} + \chi_4^{(s^\dagger,j,s,j^\dagger)} + \chi_4^{(j^\dagger,s,j,s^\dagger)} + \\
 &+ \chi_4^{(s^\dagger,s,j^\dagger,j)} + \chi_4^{(j^\dagger,j,s^\dagger,s)} + \chi_4^{(s^\dagger,j,j^\dagger,s)} + \chi_4^{(j^\dagger,s,s^\dagger,j)} + \\
 &+ \chi_4^{(s^\dagger,j^\dagger,s,j)} + \chi_4^{(s^\dagger,j^\dagger,j,s)} + \chi_4^{(j^\dagger,s^\dagger,s,j)} + \chi_4^{(j^\dagger,s^\dagger,j,s)} \quad (3.56)
 \end{aligned}$$

Finally, exploiting the fact that the coefficient $\chi_4^{(n,l,m,s)}$ associated to a particular ladder operator combination and its hermitian conjugate are identical (i.e., $\chi_4^{(p,p,s^\dagger,i^\dagger)} = \chi_4^{(p^\dagger,p^\dagger,s,i)}$, $\chi_4^{(s^\dagger,p,i^\dagger,p)} = \chi_4^{(s,p^\dagger,i,s^\dagger)}$, etc ...), we define the 4WM coupling constant $\chi_4^{\{p,p,s,i\}}$ as one half of the sum of all the coefficients $\chi_4^{(n,l,m,s)}$ associated to the energy-conservative permutation of four ladder operators with two indexes equal to p , one index equal to s and the last one equal to j

$$\begin{aligned}
 \chi_4^{\{p,p,s,i\}} \equiv \frac{1}{2} \left(\chi_4^{(p^\dagger,p^\dagger,s,i)} + \chi_4^{(p^\dagger,p^\dagger,i,s)} + \chi_4^{(p^\dagger,s,p^\dagger,i)} + \chi_4^{(p^\dagger,i,p^\dagger,s)} + \chi_4^{(p^\dagger,s,i,p^\dagger)} + \chi_4^{(p^\dagger,i,s,p^\dagger)} \right. \\
 \left. + \chi_4^{(s,p^\dagger,p^\dagger,i)} + \chi_4^{(i,p^\dagger,p^\dagger,s)} + \chi_4^{(s,p^\dagger,i,p^\dagger)} + \chi_4^{(i,p^\dagger,s,p^\dagger)} + \chi_4^{(s,i,p^\dagger,p^\dagger)} + \chi_4^{(i,s,p^\dagger,p^\dagger)} \right) \quad (3.57)
 \end{aligned}$$

3.1.4 Time evolution of the ladder operators: coupled mode equations

We can now write a Hamiltonian operator that takes into account the 3WM and 4WM scatterings taking place in the system

$$\begin{aligned}
 \hat{H}^{\{p,s,i,j\}} &= \hbar\chi_0 + \hbar\xi_0 + \\
 &+ \sum_{n=\{p,s,i,j\}} \hbar\chi_1^{(n)} \left(\hat{a}_n^\dagger \hat{a}_n + \frac{1}{2} \right) + \sum_{n=\{p,s,i,j\}} \hbar\xi_n \hat{a}_n^\dagger \hat{a}_n + \\
 &+ \sum_{n,l=\{p,s,i,j\}} \hbar\xi_{n,l} \hat{a}_n^\dagger \hat{a}_n \hat{a}_l^\dagger \hat{a}_l + \\
 &+ \hbar\chi_3^{\{p,s,i\}} \left(\hat{a}_p^\dagger \hat{a}_s \hat{a}_i + \hat{a}_s^\dagger \hat{a}_i^\dagger \hat{a}_p \right) \\
 &+ \hbar\chi_4^{\{p,p,s,j\}} \left(\hat{a}_p^\dagger \hat{a}_p^\dagger \hat{a}_s \hat{a}_j + \hat{a}_p \hat{a}_p \hat{a}_s^\dagger \hat{a}_j^\dagger \right) \quad (3.58)
 \end{aligned}$$

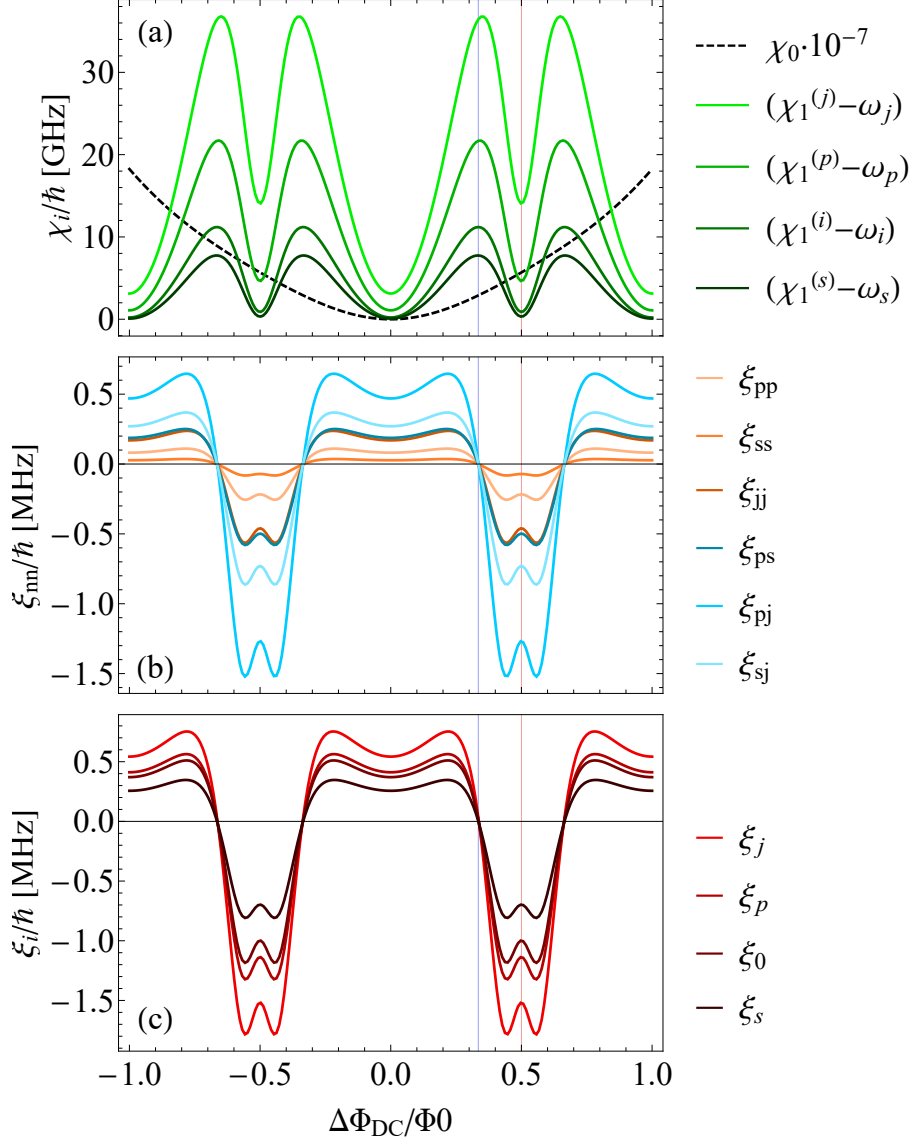


Figure 3.2: Coupling constants of the Hamiltonian operator in Eq. (3.58) as functions of $\Delta\Phi_{DC}$. (a) Non-interacting-mode Hamiltonian coupling constants, (b) 4WM contribution to the non-interacting-mode coupling constants, (c) SPM and XPM coupling constants.

The coefficients that characterise the non-mixing part of Eq. (3.58) (first to third rows) are plotted in Fig. 3.2 as function of the flux bias $\Delta\Phi_{DC}$ ².

²The circuit parameters used for the computation of all the plots concerning the quantum mechanical dynamics are shown in Tab. A.1

In Fig. 3.2 (a) the term χ_0 , that describes the energy contribution given by the external bias conditions, has a parabolic shape with its minimum for $\Delta\Phi_{DC} = 0$, hence for no external magnetic flux. In the same figure, the non-interacting-mode Hamiltonian constants are shown. These coefficients express the energy attributed to the presence of a single excitation at frequencies ω_p , ω_s , ω_i and ω_j , and have a periodicity of Φ_0 with $\Delta\Phi_{DC}$.

Fig. 3.2 (b) shows the 4WM correction to the non-interacting-modes. These coefficients give a small contribution to the total amount of energy added for each excitation compared to $\chi_1^{(n)}$, being on average four orders of magnitude less intense. On the other hand in Fig. 3.2 (c) one can observe the the 4WM coupling constants that characterise the SPM and XPM. These coefficients depend on couple of modes since they express the tendency of a particular traveling wave to interact with other modes or to self interact with themselves. The plots have a red vertical line for $\Delta\Phi_{DC}/\Phi_0 = 0.50$ that corresponds to the 4WM working point, hence where the Kerr nonlinearity is stronger and the 3WM coupling constant is zero. Moreover, the plots present one blue vertical line at $\Delta\Phi_{DC}/\Phi_0 = 0.335$ where the 4WM based nonlinearities have a zero. This value is the Kerr-free working points where usually 4WM can be neglected, and all the Kerr-related effects like SPM and XPM are strongly suppressed.

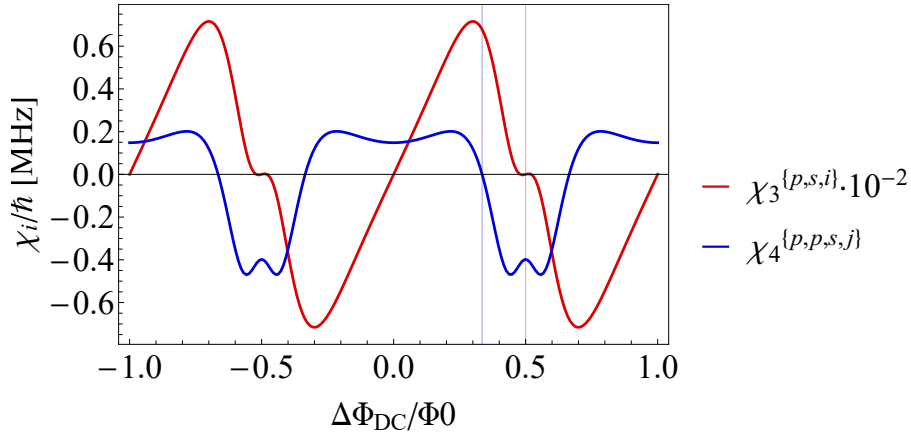


Figure 3.3: Coupling constants of the mixing terms of the Hamiltonian operator in Eq. (3.58) as functions of $\Delta\Phi_{DC}$.

Fig. 3.3 shows $\chi_3^{\{p,s,i\}}$ and $\chi_4^{\{p,p,s,j\}}$, hence the 3WM and 4WM coupling constants, respectively in the fourth and fifth rows of Eq. (3.58), as functions of $\Delta\Phi_{DC}$. One can observe that the maxima (minima) of one curve almost correspond to the minima (maxima) of the other curve. This fact tells us that for an appropriate bias choice one or the other coupling constant can be almost maximised while the other is made zero, giving the possibility to foster the wanted nonlinear behaviour.

Given the tunability of the coupling constants $\chi_3^{\{p,s,i\}}$ and $\chi_4^{\{p,p,s,j\}}$ with $\Delta\Phi_{DC}$, we can write two different Hamiltonians starting from Eq. 3.2, where the 3WM or 4WM coupling constants are neglected. Both these operators are valid expressions of the Hamiltonian in the so called *pure regimes*, hence where the 3WM or the 4WM are suppressed through the modulation of the bias condition (respectively $\chi_3^{\{p,s,i\}} \approx 0$ or $\chi_4^{\{p,p,s,j\}} \approx 0$). This choice, that from one side can be seen as a limit in the description of *mixed states* (e.g. states where both 3WM and 4WM are present), from the other side greatly eases the mathematical formulation of the problem. This is true because mixed states impose solving the dynamics of at least 4 different modes (pump, signal, 3WM idler, 4WM idler), that can be much more complicated than solving it for only 3 modes, as required when the system is in a pure state (pump, signal, 3WM idler or 4WM idler).

With this in hand, the 3WM Hamiltonian takes the form

$$\begin{aligned} \hat{H}_{3WM}^{\{p,s,i\}} &= \hbar\chi_0 + \hbar\xi_0 + \\ &+ \sum_{n=\{p,s,i\}} \hbar\chi_1^{(n)} \left(\hat{a}_n^\dagger \hat{a}_n + \frac{1}{2} \right) + \sum_{n=\{p,s,i\}} \hbar\xi_n \hat{a}_n^\dagger \hat{a}_n + \\ &+ \sum_{n,l=\{p,s,i\}} \hbar\xi_{n,l} \hat{a}_n^\dagger \hat{a}_n \hat{a}_l^\dagger \hat{a}_l + \\ &+ \hbar\chi_3^{\{p,s,i\}} \left(\hat{a}_p^\dagger \hat{a}_s \hat{a}_i + \hat{a}_s^\dagger \hat{a}_i^\dagger \hat{a}_p \right) \end{aligned} \quad (3.59)$$

while the 4WM Hamiltonian

$$\begin{aligned} \hat{H}_{4WM}^{\{p,s,j\}} &= h_0 + \hbar\xi_0 + \\ &\sum_{n=\{p,s,j\}} \hbar\chi_1^{(n)} \left(\hat{a}_n^\dagger \hat{a}_n + \frac{1}{2} \right) + \sum_{n=\{p,s,j\}} \hbar\xi_n \hat{a}_n^\dagger \hat{a}_n + \\ &+ \sum_{n,l=\{p,s,j\}} \hbar\xi_{n,l} \hat{a}_n^\dagger \hat{a}_n \hat{a}_l^\dagger \hat{a}_l + \\ &+ \hbar\chi_4^{\{p,p,s,j\}} \left(\hat{a}_p^\dagger \hat{a}_p^\dagger \hat{a}_s \hat{a}_j + \hat{a}_p \hat{a}_p \hat{a}_s^\dagger \hat{a}_j^\dagger \right) \end{aligned} \quad (3.60)$$

It should be noted that in Eq. (3.59) the SPM and XPM terms among the pump, signal and idler tones have not been neglected nonetheless they derive from a 4WM interaction. This is due to the fact that, despite the $\chi_4^{\{p,p,s,j\}}$ nonlinearity is suppressed by the bias condition, these terms are not exactly zero because all of them have different zero points depending on the modes frequencies, and we will see that they can give a contribution to the dynamic of the system.

Working in the Heisenberg picture of quantum mechanics, we can now compute the time evolution of the creation and annihilation operators keeping in mind that the dynamics of the operators is regulated by the Heisenberg equation $\frac{d\hat{a}_H(t)}{dt} =$

$\frac{i}{\hbar}[\hat{H}, \hat{a}_H(t)] + \left(\frac{\partial \hat{a}}{\partial t}\right)_H$. From here we will drop the H subscript and we admit that there is no explicit time dependence on the ladder operators.

In most of the practical realisations of JTWPAs involving very tiny signals, like single photons, the pump tone results to be much more intense than the signal and idler ones in every piece of the TL, hence computing the Heisenberg equations the SPM and XPM which do not involve the pump mode can be neglected.

We start calculating the Heisenberg equations in the 3WM case

$$\frac{d\hat{a}_p}{dt} = \frac{i}{\hbar} \left[\hat{H}_{3\text{WM}}^{\{p,s,i\}}, \hat{a}_p \right] = -i \left[\left(\chi_1^{(p)} + \xi_p + \xi_{pp} + 2\xi_{pp}\hat{a}_p\hat{a}_p^\dagger + \xi_{ps}\hat{a}_s^\dagger\hat{a}_s + \xi_{pi}\hat{a}_i^\dagger\hat{a}_i \right) \hat{a}_p + \chi_3^{\{p,s,i\}} \hat{a}_s\hat{a}_i \right] \quad (3.61)$$

$$\frac{d\hat{a}_s}{dt} = \frac{i}{\hbar} \left[\hat{H}_{3\text{WM}}^{\{p,s,i\}}, \hat{a}_s \right] = -i \left[\left(\chi_1^{(s)} + \xi_s + \xi_{ss} + \xi_{ps}\hat{a}_p^\dagger\hat{a}_p \right) \hat{a}_s + \chi_3^{\{p,s,i\}} \hat{a}_p\hat{a}_i^\dagger \right] \quad (3.62)$$

$$\frac{d\hat{a}_i}{dt} = \frac{i}{\hbar} \left[\hat{H}_{3\text{WM}}^{\{p,s,i\}}, \hat{a}_i \right] = -i \left[\left(\chi_1^{(i)} + \xi_i + \xi_{ii} + \xi_{pi}\hat{a}_p^\dagger\hat{a}_p \right) \hat{a}_i + \chi_3^{\{p,s,i\}} \hat{a}_p\hat{a}_s^\dagger \right] \quad (3.63)$$

The system composed by equations (3.61), (3.62) and (3.63), which form a *Quantum Coupled Mode Equations* (QCME) system, can be analytically solved by applying the *undepleted pump approximation* [52], hence turning the ladder pump operators into classical variables, on the basis of its intensity compared to the signal and idler tones

$$\sqrt{\frac{2\hbar\omega_p}{C_g N}} \hat{a}_p \mapsto A_p \quad (3.64)$$

The dynamics of the pump tone can now be solved from Eq. (3.61) by substituting Eq. (3.64) and neglecting the terms proportional to combinations of signal and idler ladder operators only

$$\begin{aligned} \sqrt{\frac{C_g N}{2\hbar\omega_p}} \frac{dA_p}{dt} &\approx -i \left(\left(\chi_1^{(p)} + \xi_p + \xi_{pp} \right) \sqrt{\frac{C_g N}{2\hbar\omega_p}} A_p + 2\xi_{pp} \left(\frac{C_g N}{2\hbar\omega_p} \right)^{\frac{3}{2}} |A_{p,0}|^2 A_p \right) \\ \frac{dA_p}{dt} &\approx -i \left(\chi_1^{(p)} + \xi_p + \xi_{pp} + 2\xi_{pp} \frac{C_g N}{2\hbar\omega_p} |A_{p,0}|^2 \right) A_p \end{aligned} \quad (3.65)$$

which have the solution

$$\begin{aligned} A_p(t) &= |A_{p,0}| e^{-i \left(\chi_1^{(p)} + \xi_p + \xi_{pp} + 2\xi_{pp} \frac{C_g N}{2\hbar\omega_p} |A_{p,0}|^2 \right) t} \\ &= |A_{p,0}| e^{\Psi_p t} \end{aligned} \quad (3.66)$$

with

$$\Psi_p = -i \left(\chi_1^{(p)} + \xi_p + \xi_{pp} + 2\xi_{pp} \frac{C_g N}{2\hbar\omega_p} |A_{p,0}|^2 \right) \quad (3.67)$$

$|A_{p,0}|$ is the voltage amplitude at $t = 0$, the time in which the tone enters in the non-linear medium. For sake of simplicity we have assumed the initial phase of A_p equal to zero.

Similarly, invoking the undepleted pump approximation and substituting Eq. (3.67), the time evolution for the signal annihilation operators can be written as

$$\begin{aligned}
 \frac{d\hat{a}_s}{dt} &= -i \left[\left(\chi_1^{(s)} + \xi_s + \xi_{ss} + \xi_{ps} \left(\frac{C_g N}{2\hbar\omega_p} \right) |A_{p,0}|^2 + \right) \hat{a}_s + \chi_3^{\{p,s,j\}} \sqrt{\frac{C_g N}{2\hbar\omega_p}} |A_{p,0}| \hat{a}_j^\dagger \right] \\
 &= -i \left[\Psi_s \hat{a}_s + \chi_3^{\{p,s,i\}} \sqrt{\frac{C_g N}{2\hbar\omega_p}} |A_{p,0}| \hat{a}_i^\dagger \right] \\
 &= -i \left[\Psi_s \hat{a}_s + \chi_3 |A_{p,0}| \hat{a}_i^\dagger \right]
 \end{aligned} \tag{3.68}$$

with

$$\begin{aligned}
 \chi_3 &= \sqrt{\frac{C_g N}{2\hbar\omega_p}} \chi_3^{\{p,s,i\}} \\
 \Psi_s &= -i \left(\chi_1^{(s)} + \xi_s + \xi_{ss} + \xi_{ps} \frac{C_g N}{2\hbar\omega_s} |A_{p,0}|^2 \right)
 \end{aligned} \tag{3.69}$$

while for the idler tone we have

$$\frac{d\hat{a}_i}{dt} = -i \left[\Psi_s \hat{a}_s + \chi_3 |A_{p,0}| \hat{a}_s^\dagger \right] \tag{3.70}$$

$$\Psi_i = -i \left(\chi_1^{(i)} + \xi_i + \xi_{ii} + \xi_{pi} \frac{C_g N}{2\hbar\omega_i} |A_{p,0}|^2 \right) \tag{3.71}$$

Moving to a co-rotating frame, hence imposing that $\hat{a}_s = \hat{a}_s^{CR} e^{-i\Psi_s t}$ and $\hat{a}_i = \hat{a}_i^{CR} e^{-i\Psi_i t}$

$$\begin{aligned}
 \frac{d\hat{a}_s^{CR}}{dt} &= -i\chi_3 |A_{p,0}| \left(\hat{a}_i^{CR} \right)^\dagger e^{-i(\Psi_p - \Psi_s - \Psi_i)t} \\
 &= -i\chi_3 |A_{p,0}| \left(\hat{a}_i^{CR} \right)^\dagger e^{-i\Psi t} \\
 &= -i\Upsilon_3 \left(\hat{a}_i^{CR} \right)^\dagger e^{-i\Psi t}
 \end{aligned} \tag{3.72}$$

and

$$\begin{aligned}
 \frac{d\hat{a}_i^{CR}}{dt} &= -i\chi_3 |A_{p,0}| \left(\hat{a}_s^{CR} \right)^\dagger e^{-i(\Psi_p - \Psi_s - \Psi_i)t} \\
 &= -i\chi_3 |A_{p,0}| \left(\hat{a}_s^{CR} \right)^\dagger e^{-i\Psi t} \\
 &= -i\Upsilon_3 \left(\hat{a}_s^{CR} \right)^\dagger e^{-i\Psi t}
 \end{aligned} \tag{3.73}$$

where we defined the *phase mismatch density* for the 3WM process as

$$\begin{aligned}\Psi &= \Psi_p - \Psi_s - \Psi_i = \\ &= \chi_1^{(p)} - \chi_1^{(s)} - \chi_1^{(i)} + \xi_p - \xi_s - \xi_i + \\ &+ \xi_{pp} - \xi_{ss} - \xi_{ii} + \left(2\xi_{pp} \frac{C_g N}{2\hbar\omega_p} - \xi_{ps} \frac{C_g N}{2\hbar\omega_p} - \xi_{pi} \frac{C_g N}{2\hbar\omega_p} \right) |A_{p,0}|^2\end{aligned}\quad (3.74)$$

and the 3WM *interaction parameter*

$$\Upsilon_3 = \chi_3 |A_{p,0}| \quad (3.75)$$

The solution of the system formed by Eq. (3.72) and (3.73) is a well known mathematical problem, and can be demonstrated being (Appendix E, we drop the CR apex, nonetheless we are still in the co-rotating frame approximation, for clarity of the notation)

$$\hat{a}_{s(i)}(t) = \left[\hat{a}_{s(i),0}^{CR} \left(\cosh(gt) + \frac{i\Psi}{2g} \sinh(gt) \right) - \frac{i\Upsilon_3}{g} \left(\hat{a}_{i(s),0} \right)^\dagger \sinh(gt) \right] e^{-i(\Psi/2)t} \quad (3.76)$$

where we introduced the complex *gain factor*

$$g = \sqrt{\Upsilon_3^2 - \left(\frac{\Psi}{2} \right)^2} \quad (3.77)$$

In the 4WM case we start from a system of coupled equations very similar to the one composed by Eq. (3.61), (3.62) and (3.63), indeed we have

$$\begin{aligned}\frac{d\hat{a}_p}{dt} &= \frac{i}{\hbar} \left[\hat{H}_{4WM}^{\{p,s,j\}}, \hat{a}_p \right] = \\ &= -i \left[\left(\theta_p + \xi_{pp} + 2\xi_{pp} \hat{a}_p^\dagger \hat{a}_p + \xi_{ps} \hat{a}_s^\dagger \hat{a}_s + \xi_{pj} \hat{a}_j^\dagger \hat{a}_j \right) \hat{a}_p + 2\chi_4^{\{p,p,s,i\}} \hat{a}_p^\dagger \hat{a}_s \hat{a}_j \right]\end{aligned}\quad (3.78)$$

$$\begin{aligned}\frac{d\hat{a}_s}{dt} &= \frac{i}{\hbar} \left[\hat{H}_{4WM}^{\{p,s,i\}}, \hat{a}_s \right] = \\ &= -i \left[\left(\theta_s + \xi_{ss} + 2\xi_{ss} \hat{a}_s^\dagger \hat{a}_s + \xi_{ps} \hat{a}_p^\dagger \hat{a}_p + \xi_{sj} \hat{a}_j^\dagger \hat{a}_j \right) \hat{a}_s + \chi_4^{\{p,p,s,i\}} \hat{a}_p \hat{a}_p \hat{a}_j^\dagger \right]\end{aligned}\quad (3.79)$$

$$\begin{aligned}\frac{d\hat{a}_i}{dt} &= \frac{i}{\hbar} \left[\hat{H}_{4WM}^{\{p,s,i\}}, \hat{a}_i \right] = \\ &= -i \left[\left(\theta_j + \xi_{jj} + 2\xi_{jj} \hat{a}_j^\dagger \hat{a}_j + \xi_{pj} \hat{a}_p^\dagger \hat{a}_p + \xi_{sj} \hat{a}_s^\dagger \hat{a}_s \right) \hat{a}_j + \chi_4^{\{p,p,s,j\}} \hat{a}_p \hat{a}_p \hat{a}_s^\dagger \right]\end{aligned}\quad (3.80)$$

This system can be solved exactly the same way we solved the 3WM one, since it is formed by the same set of equations. The relations that give the dynamics of the ladder operators in the 4WM case are then

$$\frac{d\hat{a}_s}{dt} = -i\Upsilon_4 \hat{a}_j^\dagger e^{-i\Psi t} \quad (3.81)$$

$$\frac{d\hat{a}_i}{dt} = -i\Upsilon_4 \hat{a}_s^\dagger e^{-i\Psi t} \quad (3.82)$$

with

$$\chi_4 = \frac{C_g N}{2\hbar\omega_p} \chi_4^{\{p,p,s,j\}} \quad (3.83)$$

$$\Upsilon_4 = \chi_4 |A_{p,0}|^2 \quad (3.84)$$

and

$$\begin{aligned} \Psi &= 2\Psi_p - \Psi_s - \Psi_j = \\ &= 2\chi_1^{(p)} - \chi_1^{(s)} - \chi_1^{(j)} + 2\xi_p - \xi_s - \xi_j + \\ &+ 2\xi_{pp} - \xi_{ss} - \xi_{jj} + \left(4\xi_{pp} \frac{C_g N}{2\hbar\omega_p} - \xi_{ps} \frac{C_g N}{2\hbar\omega_p} - \xi_{pj} \frac{C_g N}{2\hbar\omega_p} \right) |A_{p,0}|^2 \end{aligned} \quad (3.85)$$

The solution in the 4WM case is therefore

$$\hat{a}_{s(j)}(t) = \left[\hat{a}_{s(j),0} \left(\cosh(gt) + \frac{i\Psi}{2g} \sinh(gt) \right) - \frac{i\Upsilon_4}{g} \hat{a}_{j(s),0}^\dagger \sinh(gt) \right] e^{-i(\Psi/2)t} \quad (3.86)$$

where the complex gain factor is

$$g = \sqrt{\Upsilon_4^2 - \left(\frac{\Psi}{2}\right)^2} \quad (3.87)$$

3.1.5 Gain

The mathematical structure developed at this point can be straightforwardly generalised from a discrete modes view to a continuous modes approach, labeling the interacting modes with ω and calling the 3WM idler as $\omega' = \omega_p - \omega$ while the 4WM idler as $\omega' = 2\omega_p - \omega$. Moreover, from now on, to reduce the complexity of notation, we will use a single set of equations to describe both the 3WM and 4WM cases, that get distinguished just by the use of the correct interaction factor Υ (Eq. (3.75) and (3.84)) and phase mismatch density Ψ (Eq. (3.74) and (3.85)). In this view equation (3.76) and (3.86) are generically indicated as

$$\begin{aligned} \hat{a}_\omega &= \left[\hat{a}_{\omega,0} \left(\cosh(gt) + \frac{i\Psi}{2g} \sinh(gt) \right) - \frac{i\Upsilon}{g} \hat{a}_{\omega',0}^\dagger \sinh(gt) \right] e^{-i(\Psi/2)t} = \\ &= \left[u(\omega, t) \hat{a}_{\omega,0} + iv(\omega, t) \hat{a}_{\omega',0}^\dagger \right] e^{-i(\Psi/2)t} \end{aligned} \quad (3.88)$$

having introduced the functions

$$u(\omega, t) = \cosh(g(\omega)t) + \frac{i\Psi(\omega)}{2g(\omega)} \sinh(g(\omega)t) \quad (3.89)$$

$$v(\omega, t) = -\frac{\Upsilon(\omega)}{g(\omega)} \sinh(g(\omega)t) \quad (3.90)$$

These definitions satisfy the relation $|u(\omega, t)|^2 - |v(\omega, t)|^2 = 1$, that reflects the form of Eq. (2.92) concerning the amplitude gain of a linear amplifier and its added noise. By making use of equation (3.88), hence the time evolution of the ladder operators, it is now possible to define the number of output signal photons as the average number of photons of frequency ω after a certain time t spent into the JTWPA. We here remember that talking about time spent in the amplifier rather than length of it, is a prerogative of the Heisenberg description in the domain of time, nonetheless, the length of the JTWPA and the time spent by a signal into it are always linked together by the phase velocity of the considered mode.

Now, to evaluate the average number of output photons we first calculate the number operator for the mode ω

$$\hat{n}_\omega = \hat{a}_\omega^\dagger \hat{a}_\omega \quad (3.91)$$

$$= \left(u^* \hat{a}_{\omega,0}^\dagger - iv^* \hat{a}_{\omega',0} \right) \left(u \hat{a}_{\omega,0} + iv \hat{a}_{\omega',0}^\dagger \right) \quad (3.92)$$

$$= |u|^2 \hat{a}_{\omega,0}^\dagger \hat{a}_{\omega,0} + |v|^2 \hat{a}_{\omega',0} \hat{a}_{\omega',0}^\dagger + iu^* v \hat{a}_{\omega,0}^\dagger \hat{a}_{\omega',0}^\dagger - uv^* \hat{a}_{\omega',0} \hat{a}_{\omega,0} \quad (3.93)$$

$$= |u|^2 \hat{a}_{\omega,0}^\dagger \hat{a}_{\omega,0} + |v|^2 \left(\hat{a}_{\omega',0}^\dagger \hat{a}_{\omega',0} + 1 \right) + iu^* v \hat{a}_{\omega,0}^\dagger \hat{a}_{\omega',0}^\dagger - uv^* \hat{a}_{\omega',0} \hat{a}_{\omega,0} \quad (3.94)$$

and then calculating the average value over a generic state $|\Psi\rangle$ we land to

$$\langle \hat{n}_\omega \rangle = \langle \hat{a}_\omega^\dagger \hat{a}_\omega \rangle = |u|^2 \langle \hat{a}_{\omega,0}^\dagger \hat{a}_{\omega,0} \rangle + |v|^2 \left[\langle \hat{a}_{\omega',0}^\dagger \hat{a}_{\omega',0} \rangle + 1 \right] + iu^* v \langle \hat{a}_{\omega,0}^\dagger \hat{a}_{\omega',0}^\dagger \rangle - iuv^* \langle \hat{a}_{\omega',0} \hat{a}_{\omega,0} \rangle \quad (3.95)$$

Equation (3.95) is a general relation to estimating the number of outgoing signal photons regardless of the nature of the incoming state (Fock, coherent, thermal, etc.).

Having obtained the average number of outgoing photons we can now evaluate the parametric gain that the JTWPA can offer. We adopt the description of a parametric amplifier assimilated to a linear amplifier as already anticipated in Sec. 2.4, of which the typical output field is expressed by Eq. 2.79, hence $\hat{a}_\omega = \sqrt{G} \hat{a}_{\omega,0} + \hat{L}^\dagger$. It is then straightforward to calculate the output photon number of a linear amplifier taking the complex conjugate of \hat{a}_ω and then computing the average value of their product

$$\begin{aligned} \langle \hat{n}_\omega \rangle &= G \langle (\hat{a}_{\omega,0})^\dagger \hat{a}_{\omega,0} \rangle + \\ &+ \langle \hat{L}^\dagger \hat{L} \rangle + \sqrt{G} \left(\langle (\hat{a}_{\omega,0})^\dagger \hat{L}^\dagger \rangle + \langle \hat{L} \hat{a}_{\omega,0} \rangle \right) = \\ &= G \langle \hat{n}_{\omega,0} \rangle + \langle \mathcal{N} \rangle \end{aligned} \quad (3.96)$$

where $\langle \hat{n}_{\omega,0} \rangle$ is the average number of photons in input.

In Equation (3.96) we can identify two key features of a linear amplifier: the *photon number gain* G , that is the contribution to the total number of output

photons given by the sole input field, and the added noise photon number $\langle \mathcal{N} \rangle$, which embeds the contribution given by the amplifier itself. By comparing Equation (3.95) and (3.96) we can write the gain and the added noise photon number of a JTWPA as

$$G = |u|^2 = \cosh gt^2 + \frac{\Psi^2}{4g^2} \sinh gt^2 + \frac{i\Psi}{2g} \sinh gt \cosh gt \quad (3.97)$$

$$\langle \mathcal{N} \rangle = |v|^2 \left[\langle (\hat{a}_{\omega',0})^\dagger \hat{a}_{\omega',0} \rangle + 1 \right] + iu^*v \langle (\hat{a}_{\omega,0})^\dagger (\hat{a}_{\omega',0})^\dagger \rangle - iuv^* \langle \hat{a}_{\omega',0} \hat{a}_{\omega,0} \rangle \quad (3.98)$$

In the case where the phase mismatch can be neglected $\Upsilon^2 \gg \frac{\Psi^2}{4}$ (this happens for low values of C_J and L_g , which reduce the chromatic dispersion in the line) the gain becomes

$$G \approx \cosh^2 gt \quad (3.99)$$

in accordance with the classical approach given by [64]. It is now worth making

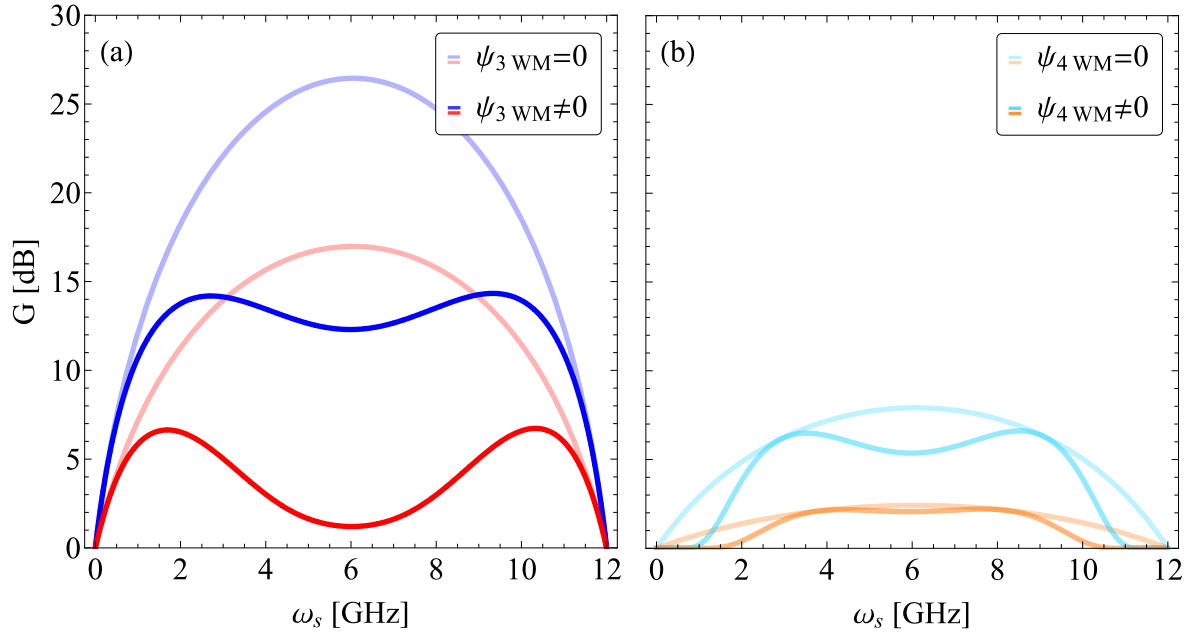


Figure 3.4: Gain profiles in the 3WM (a) and 4WM (b) regimes as function of the signal frequency. The darker coloured curves are calculated considering the contribution of the phase mismatch while the light coloured curved in the approximation of negligible phase mismatch.

(a) The pump currents are (blue) $I_p/I_c = 0.06$ and (red) $I_p/I_c = 0.04$. (b) The pump currents are (light blue) $I_p/I_c = 0.13$ and (orange) $I_p/I_c = 0.10$.

few observations on equations (3.97) and (3.98). The gain G depends only on the

layout of the amplifier, hence the set of parameters that defines the circuit, and on the amplitude and frequency of the pump tone. In other words, the gain does not depend on the input state, just as expected from a linear amplifier.

Some plots of G in the 3WM and 4WM cases are shown in Fig. 3.4 as function of the signal frequency. Fig. 3.4 (a) shows the gain calculated in the 3WM regime, for a pump frequency of 12 GHz, in the case of non-negligible (dark colour) and negligible (light colour) phase-mismatch. The first thing to notice is that the bandwidth has a maximum at half the pump frequency, as expected since considering a PDC process we know that the probability for a scattering event to take place is enhanced getting closer to the degenerate condition $\omega_s = \omega_p/2$, due to the reduced phase mismatch. Moreover, the figure shows that the set of circuit parameters taken into account (which gives low chromatic dispersion to the line) does not allow to consider valid the negligible phase mismatch approximation due to a large difference in the maximum value of G in the middle of the bandwidth (> 10 dB). We clearly see that the effect of the phase mismatch greatly reduces the gain at half bandwidth.

On the other hand, Fig. 3.4 (b) shows the gain profile in the 4WM case with a pump frequency of 6 GHz, the choice to halve the pump frequency follows so as to make the profiles in the 3WM and 4WM cases comparable in the same frequency range. One should note first that the pump power used to calculate these curves is ten times higher than the pump current used for the 3WM plots. This fact tells us that in general, the amplification given by the 4WM process is less power efficient with respect to the 3WM one under the same bandwidth. We can understand this by considering the absolute values of the 3WM and 4WM coupling constants that take part in the definition of the interaction parameters (3.75) and (3.84), indeed, looking at Fig. 3.3 one sees that $\chi_3^{\{p,s,i\}}$ is on average two orders of magnitude higher than $\chi_4^{\{p,p,s,j\}}$. This means that to achieve the same amplification one has to deliver much more pump power when working in a 4WM regime respect to the 3WM one. Another aspect to point out is that in the 4WM regime there is a more pronounced difference between the curves calculated considering and neglecting the contribution of the phase mismatch. One sees that in the low pump current curve (light orange) the peak difference between the curves calculated with and without phase mismatch is about 2.5 dB, and this difference grows to 8 dB in the high pump current curve (light blue). This fact leads us to the conclusion that in 4WM regime the amplifier is more affected by the phase mismatch effect.

The average value of the noise photon number operator $\langle \hat{N} \rangle$ has a non-trivial dependence on the annihilation and creation operators, and it is interesting to evaluate this quantity for two simple cases hence a Fock input state $|\psi_F\rangle = |N_{in}^S\rangle_s |N_{in}^I\rangle_i$ and

a coherent input state $|\psi_c\rangle = |\alpha\rangle_s |\beta\rangle_i$. Some simple algebra brings us to

$$\langle \hat{\mathcal{N}} \rangle_F = |v|^2 (1 + N_{\text{in}}^I) \quad (3.100)$$

$$\langle \hat{\mathcal{N}} \rangle_C = |v|^2 (1 + |\beta|^2) - iuv^* \alpha \beta + iu^* v \alpha^* \beta^* \quad (3.101)$$

Regardless of its non-trivial dependence, it turns out that if the input idler mode is in its vacuum state ($N_{\text{in}}^I = \beta = 0$) the noise photon number simplifies, giving the same result in both cases $\langle \hat{\mathcal{N}} \rangle_F = \langle \hat{\mathcal{N}} \rangle_C = |v|^2$.

We evaluate now the added noise number \mathcal{A} previously defined in (2.87). This quantity can be defined as the ratio between the symmetric variance of $\hat{L} = iv^* \hat{a}_{\omega',0}$ and the gain given by equation (3.97)

$$\begin{aligned} \mathcal{A} &= \frac{\langle |\Delta \hat{L}|^2 \rangle}{G} \\ &= \frac{\langle |\hat{L}|^2 \rangle - |\langle \hat{L} \rangle|^2}{G} \\ &= \frac{\frac{1}{2}|v|^2 \langle \hat{a}_{\omega',0} \hat{a}_{\omega',0}^\dagger + \hat{a}_{\omega',0}^\dagger \hat{a}_{\omega',0} \rangle - |v|^2 |\langle a_{\omega',0} \rangle|^2}{|u|^2} \\ &= \frac{|v|^2}{|u|^2} \left(\frac{1}{2} + \langle \hat{a}_{\omega',0}^\dagger a_{\omega',0} \rangle - |\langle \hat{a}_{\omega',0} \rangle|^2 \right) \end{aligned} \quad (3.102)$$

It's interesting noting that in general Eq. (3.102) has a non-trivial dependence on the ladder operators of the idler modes, so it can vary for different input quantum states. Again, we calculate \mathcal{A} in the particular case of an input Fock or coherent state obtaining

$$\mathcal{A}_F = \frac{|v|^2}{|u|^2} \left(\frac{1}{2} + N_{\text{in}}^I \right) \quad (3.103)$$

$$\mathcal{A}_C = \frac{1}{2} \frac{|v|^2}{|u|^2} \quad (3.104)$$

As in the case of the operator $\langle \hat{\mathcal{N}} \rangle$, if the idler mode is in the vacuum state the two expressions give the same result

$$\mathcal{A}_F = \mathcal{A}_C = \frac{1}{2} \frac{|v|^2}{|u|^2} \quad (3.105)$$

A final remark must be done about the added noise. The laws of quantum mechanics impose a lower bound for the added noise number for a linear amplifier in the high gain limit, that is $\mathcal{A} > 1/2$. This concept can be visualised in Fig. 3.5 where the added noise number is plotted as function of the pump current, the curves show \mathcal{A} for an input coherent state and for a Fock input state with no and one idler photon.

From Eq. (3.104) one can see that \mathcal{A}_C has no dependence on the number of input idler photons, meaning that, regardless of its occupation numbers, a coherent state is the state that in the high gain limit (equivalent in this case to the high pump power limit) saturates the lower bound on the added noise. Similarly, a Fock state that has no idler photons in input saturates as well this limit, but we see that \mathcal{A}_F grows rapidly as N_{in}^I increases.

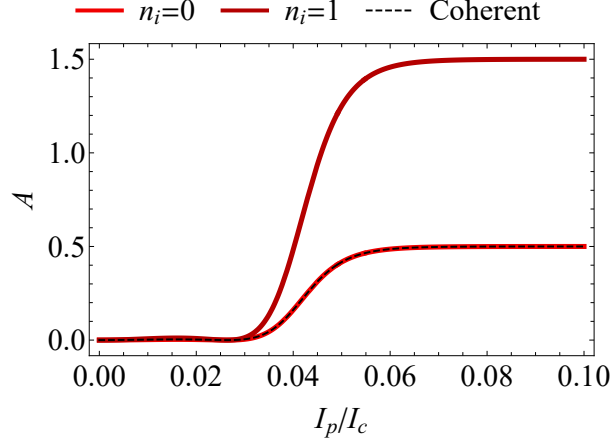


Figure 3.5: Added noise number as a function of the normalised pump current, calculated for a coherent input state (dashed) and a Fock input state with no (light red) and one (dark red) idler input photons. The plots are done considering a pump frequency of 12 GHz and a signal frequency of 5 GHz.

3.1.6 Squeezing

The correlation of the signal and idler modes results in a so-called squeezed output field of a JTWPA, that can be typically measured in experiments using heterodyne techniques [21]. These correlations generally occur when the fluctuations of one of the two entangled modes gets "squeezed" below the standard quantum limit, while the other gets enlarged above it. This kind of correlation has a frequency dependence and is usually treated in terms of quadratures of the signal.

One can define [24, 58] the thermal photon number as

$$N(\omega) = \int_0^\infty d\omega' (\langle \hat{a}_\omega^\dagger \hat{a}_{\omega'} \rangle - \langle \hat{a}_\omega^\dagger \rangle \langle \hat{a}_{\omega'} \rangle) \quad (3.106)$$

and the squeezing parameter as

$$M(\omega) = \int_0^\infty d\omega' (\langle \hat{a}_\omega \hat{a}_{\omega'} \rangle - \langle \hat{a}_\omega \rangle \langle \hat{a}_{\omega'} \rangle) \quad (3.107)$$

which defines the squeezing angle (θ) through the relation $M(\omega) = |M(\omega)|e^{i\theta}$. One can introduce the quadratures as

$$\hat{Y}^\theta(\omega) = i(e^{i\theta/2}\hat{a}_\omega^\dagger - e^{-i\theta/2}\hat{a}_\omega) \quad (3.108)$$

with their associated fluctuations $\Delta\hat{Y}^\theta(\omega) = \hat{Y}^\theta(\omega) - \langle\hat{Y}^\theta(\omega)\rangle$. From the previous definitions one can easily compute (see Appendix F) the relation between the squeezing spectrum $S(\omega)$, the thermal photon number and the squeezing parameter

$$S(\omega) = \int_0^\infty d\omega' \langle\Delta\hat{Y}^\theta(\omega)\Delta\hat{Y}^\theta(\omega')\rangle = 1 + 2N(\omega) - 2|M(\omega)| \quad (3.109)$$

Considering a vacuum input state, one can see that (see (F.6))

$$N(\omega) = |v(\omega, t)|^2 = \left|\frac{\Upsilon}{g} \sinh gt\right|^2 \quad (3.110)$$

and exploiting (3.88) the squeezing parameter can be written as

$$\begin{aligned} M(\omega) &= \int_0^\infty d\omega' (\langle\hat{a}_\omega\hat{a}_{\omega'}\rangle - \langle\hat{a}_\omega\rangle\langle\hat{a}_{\omega'}\rangle) = \\ &= \int_0^\infty d\omega' \langle\hat{a}_\omega\hat{a}_{\omega'}\rangle = \\ &= \int_0^\infty d\omega' \langle vac| \left(u(\omega, t)\hat{a}_{\omega,0} + iv(\omega, t)\hat{a}_{(2)\omega_p-\omega,0}^\dagger \right) \left(u(\omega', t)\hat{a}_{\omega',0} + iv(\omega', t)\hat{a}_{(2)\omega_p-\omega'}^\dagger \right) |vac\rangle e^{-i\Psi t} = \\ &= e^{-i\Psi t} \int_0^\infty d\omega' \langle vac| \left(u(\omega, t)u(\omega', t)\hat{a}_{\omega,0}\hat{a}_{\omega',0} + iu(\omega, t)v(\omega', t)\hat{a}_{\omega,0}\hat{a}_{(2)\omega_p-\omega',0}^\dagger + \right. \\ &\quad \left. + iv(\omega, t)u(\omega', t)\hat{a}_{(2)\omega_p-\omega,0}^\dagger\hat{a}_{\omega',0} - v(\omega, t)v(\omega', t)\hat{a}_{(2)\omega_p-\omega,0}^\dagger\hat{a}_{(2)\omega_p-\omega',0}^\dagger \right) |vac\rangle = \\ &= iu(\omega, t)e^{-i\Psi t} \int_0^\infty d\omega' v(\omega', t) \langle vac| \hat{a}_{\omega,0}\hat{a}_{(2)\omega_p-\omega',0}^\dagger |vac\rangle = \\ &= iu(\omega, t)e^{-i\Psi t} \int_0^\infty d\omega' v(\omega', t) \langle vac| \left(\hat{a}_{(2)\omega_p-\omega',0}^\dagger\hat{a}_{\omega,0} + \delta(\omega - (2)\omega_p + \omega') \right) |vac\rangle = \\ &= iu(\omega, t)v((2)\omega_p - \omega, t)e^{-i\Psi t} = \\ &= iu(\omega, t)v(\omega, t)e^{-i\Psi t} = \\ &= \left(\frac{\Psi\Upsilon}{2g^2} \sinh^2(gt) - i\frac{\Upsilon}{g} \sinh(gt) \cosh(gt) \right) e^{-i\Psi t} = \\ &= \sqrt{\left| \frac{\Psi\Upsilon}{2g^2} \sinh^2(gt) \right|^2 + \left| \frac{\Upsilon}{g} \sinh(gt) \cosh(gt) \right|^2} e^{-i\frac{2g}{\Psi} \frac{\cosh(gt)}{\sinh(gt)}} e^{-i\Psi t} = \\ &= |u(\omega, t)v(\omega, t)| e^{-i\left(\arctan\left(\frac{2g}{\Psi} \coth(gt) \right) + \Psi t \right)} = \\ &= |M(\omega)| e^{i\theta} \end{aligned} \quad (3.111)$$

In the calculation to explicit Eq. (3.111) the mode index of the ladder operators $(2)\omega_p - \omega$ remarks the fact that the mathematics is just the same if we consider 3WM or 4WM. Moreover, we made use of the property $v(\omega_p - \omega) = v(\omega)$ and identified the squeezing angle as

$$\theta = -\left(\arctan\left(\frac{2g}{\Psi} \coth gt\right) + \Psi t \right) \quad (3.112)$$

Furthermore, one can easily find the relation between $M(\omega)$ and $N(\omega)$ as

$$\begin{aligned} |M(\omega)|^2 &= |u(\omega, t)v(\omega, t)|^2 \\ &= |u(\omega, t)|^2 |v(\omega, t)|^2 \\ &= \left(|v(\omega, t)|^2 + 1 \right) |v(\omega, t)|^2 \\ &= N(\omega)[N(\omega) + 1] \end{aligned} \quad (3.113)$$

that is the maximum allowed by the Heisenberg uncertainty principle and implies that the amplification is quantum limited [24]. In the case where the input state is

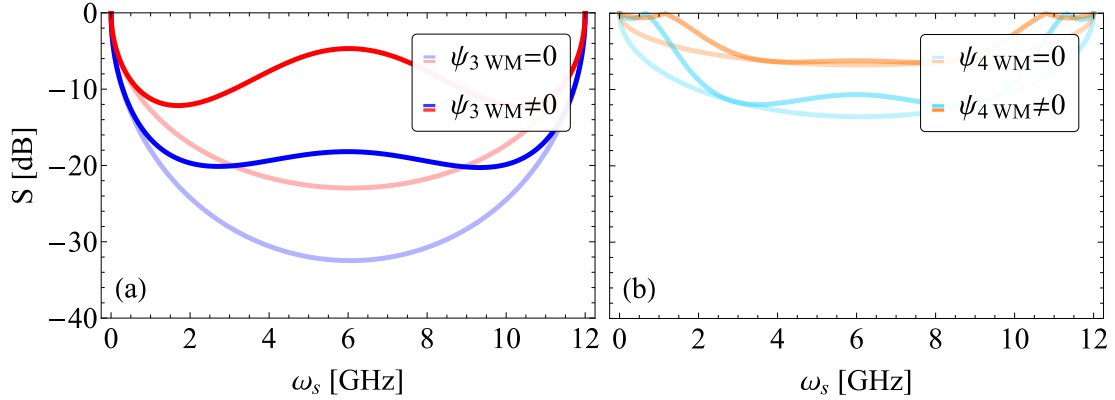


Figure 3.6: Squeezing spectra in the 3WM (a) and 4WM (b) regimes as function of the signal frequency. The dashed curves are calculated considering the contribution of the phase mismatch while the solid curved in the approximation of negligible phase mismatch.

(a) The pump currents are (blue) $I_p/I_c = 0.06$ and (red) $I_p/I_c = 0.04$. (b) The pump currents are (light blue) $I_p/I_c = 0.13$ and (orange) $I_p/I_c = 0.10$.

a vacuum state we can calculate the squeezing spectrum from (3.109)

$$\begin{aligned} S(\omega) &= 1 + 2N(\omega) - 2|M(\omega)| \\ &= 1 + 2|v(\omega, t)|^2 - 2\sqrt{|v(\omega, t)|^2(|v(\omega, t)|^2 + 1)} \\ &= 1 + 2|v(\omega, t)|^2 - 2|v(\omega, t)|\sqrt{|v(\omega, t)|^2 + 1} \end{aligned} \quad (3.114)$$

That under the zero total phase mismatch assumption ($\Psi \approx 0$) is

$$S(\omega) = 1 + 2|\sinh gt|^2 - 2|\sinh gt|\sqrt{|\sinh gt|^2 + 1} \quad (3.115)$$

and the squeezing angle becomes $\theta \approx -\pi/2$. Equations (3.114) and (3.115) are plotted in Fig. 3.6 for different values of pump current as a function of the signal frequency. Similar considerations can be made as done for the gain profiles shown in Fig. 3.4, indeed we see that the maximum squeezing is achieved in 3WM at half bandwidth closer to degeneracy. For the squeezing spectrum it is confirmed that the negligible phase mismatch approximation does not hold in both 3WM and 4WM cases. Again, in this case the pump power used for the 4WM plots is ten times higher than in 3WM, testifying the latter as a more efficient process than the former.

3.2 JTWPA with high chromatic dispersion

3.2.1 Resonant Phase Matching

Recent works [17] have shown that in practical realisations of JTWPAs the generation of high frequency modes emerges as a strong gain limitation. This happens because a great amount of pump and signal power get converted in these stray modes instead of been transferred to the signal, hence allowing amplification. Fig. 3.7 shows a sketch of an ideal vs real frequency mixing scheme of a JTWPA working in PDC regime having in input a weak signal ω_s and a strong pump ω_p . In the ideal case we would assist to a single wave mixing between ω_p and ω_s , that would generate an idler mode $\omega_i = \omega_p - \omega_s$ and would determine an efficient parametric amplification. By the way, wave mixing processes not only apply to signal and idler, but rather to each combination of modes into the JTWPA. Indeed Fig. 3.7 shows also part of the real set of modes that gets generated in the TL, namely $\omega_{p+p} = \omega_p + \omega_p$ (Second Pump Harmonic Generation), $\omega_{p+s} = \omega_p + \omega_s$ (Signal Up-Conversion), $\omega_{p+i} = \omega_p + \omega_i$ (Idler Up-Conversion) and many more. To suppress the generation of these unwanted modes two different paths can be followed. The first one is to lower the cutoff frequency of the line below the frequency of the stray tones, preventing in this way their propagation. By the way, this approach can introduce some serious limitations to the functionality of the device for different reasons. First of all, the wavelength of the traveling tones, $\lambda = 2\pi\omega_0/\omega$ would become shorter, about the size of only few tenth cells. For this reason the discreteness of the line would not be negligible anymore, so the gain could exhibit high ripples. Second, in order to keep the impedance unchanged both inductance and ground capacitance should be increased, what is only possible with enlarging their physical sizes. Third, the maximum pump power would be small, hence causing pump depletion at rather low signal power [65].

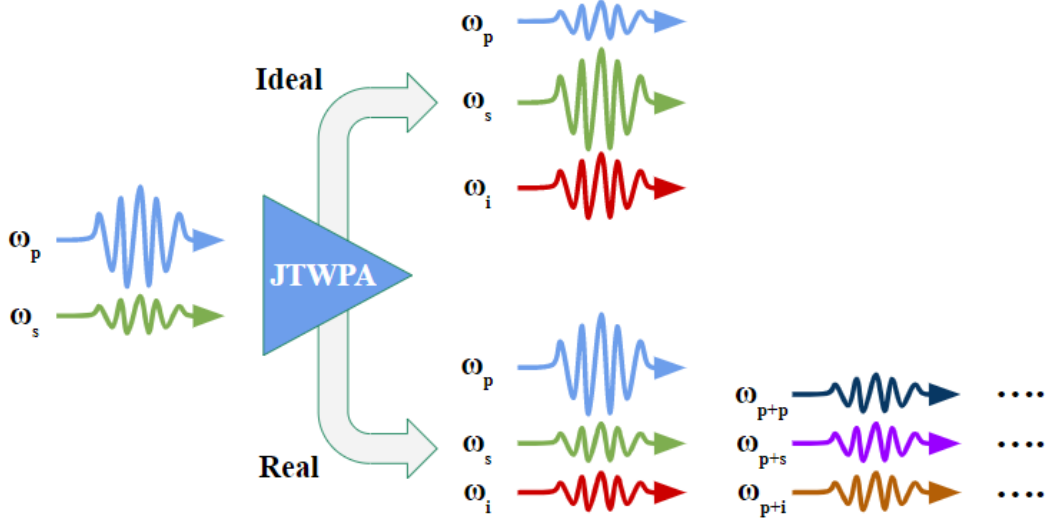


Figure 3.7: Ideal vs real frequency mixing scheme in PDC regime. The JTWPA receives in input a pump mode ω_p and a signal mode ω_s , giving in output a ideal set of modes, namely ω_p , ω_s and $\omega_i = \omega_p - \omega_s$ and a real set of modes, hence ω_p , ω_s , $\omega_i = \omega_p - \omega_s$, $\omega_{p+p} = \omega_p + \omega_p$ (Second Pump Harmonic Generation), $\omega_{p+s} = \omega_p + \omega_s$ (Signal Up-Conversion), $\omega_{p+i} = \omega_p + \omega_i$ (Idler Up-Conversion) and many more.

On the contrary, the second path, that we wish to explore in this section, is to introduce dispersion in the line by, for example, lowering the plasma frequency of the rf-SQUIDS defined as

$$\omega_J = \frac{1}{\sqrt{L_g C_J}} \quad (3.116)$$

This approach allows to introduce phase mismatch between the pump and its higher harmonics, preventing the pump from being depleted by the presence of these stray tones. By the way, lowering the plasma frequency adds inevitably a smaller amount of phase mismatch among the tones that are intended to be amplified, preventing in this way an efficient amplification. To fix this, caused by the high chromatic dispersion, a modified dispersion relation should be introduced, in order to re-phase the pump, signal and idler tones.

The quantum theory developed in sections 3.1.1, 3.1.2, 3.1.3, 3.1.4, 3.1.6 and 3.1.5 is based on the assumption that the transmission line presents low chromatic dispersion, hence $\Delta k a N \ll 1$. Moreover, this quantum theory is a 3-wave treatment of the problem and does not account for higher harmonics that, as said, are a main cause of gain limitation. For these reasons, to extend the discussion of JTWPAs in the case of high chromatic dispersion, we will make use of a set of classical Coupled Mode Equations (CME) introduced in [17], that allows to describe the dynamics of

a multi-wave system, and we will readjust it in the case of high chromatic dispersion and engineered dispersion relation. For this purpose, we will treat the case of the PDC amplification only, hence a 3WM regime, since the 4WM case have already been extensively studied [24, 57, 36]. Moreover, in all the numerical evaluations

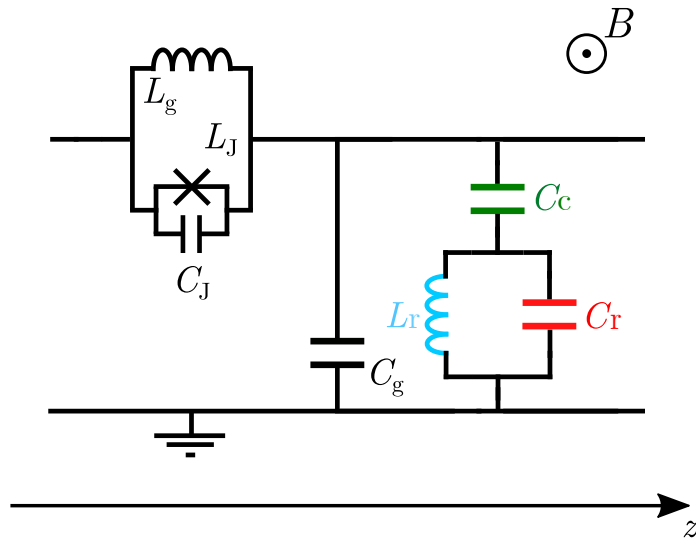


Figure 3.8: Unit cell of a JTWPA equipped with RPM. The LC resonator that shunts the signal line to ground is capacitively couples through a coupling capacitance C_c and is formed by an inductance L_r and a capacitance C_r .

that follow we will use the set of parameters shown in Tab. A.2, if not differently indicated.

The Resonant Phase Matching [43] is a technique that allows to engineer the dispersion relation of a TL by introducing LC resonators capacitively coupled between the signal line and the ground plane. Fig. 3.8 shows how the unit cell gets modified by the introduction of the resonator, composed by an inductance L_r , a capacitance C_r and a coupling capacitance C_c . For simplicity, in the figure a resonator is coupled to each rf-SQUID of the JTWPA, but in practical realisations [57] one resonator can be used to re-phase the contribution of a certain number of cells, hence drastically reducing the complexity of the circuit. Anyway, just to keep things simple, and without lack of generality, here we model our TL, in the hypothesis that every rf-SQUID has its own resonator.

We can easily take into account the effect of the resonator on the circuit by considering the *ensemble* behaviour of the cluster formed by C_g plus resonator, and then defining a fictitious frequency dependant ground capacitance $C_g(\omega)$. The equation that governs $C_g(\omega)$ can be obtained by considering the impedance to ground (see

Appendix G) of the cluster formed by the resonator plus C_g that is

$$Z_{\text{res}+C_g} = \frac{1 - (C_c + C_r)L_r\omega^2}{i\omega\left(C_g(1 - (C_c + C_r)L_r\omega^2) + C_c(1 - C_rL_r\omega^2)\right)} \quad (3.117)$$

If now we suppose to substitute a frequency dependant capacitance with the same impedance of Eq (3.117) we find

$$C_g(\omega) = \frac{1}{i\omega Z_{\text{res}+C_g}} = \frac{C_0(1 - (C_c + C_r)L_r\omega^2) + C_c(1 - C_rL_r\omega^2)}{1 - (C_c + C_r)L_r\omega^2} \quad (3.118)$$

The dispersion relation of a ladder-type TL which does not include RPM has been

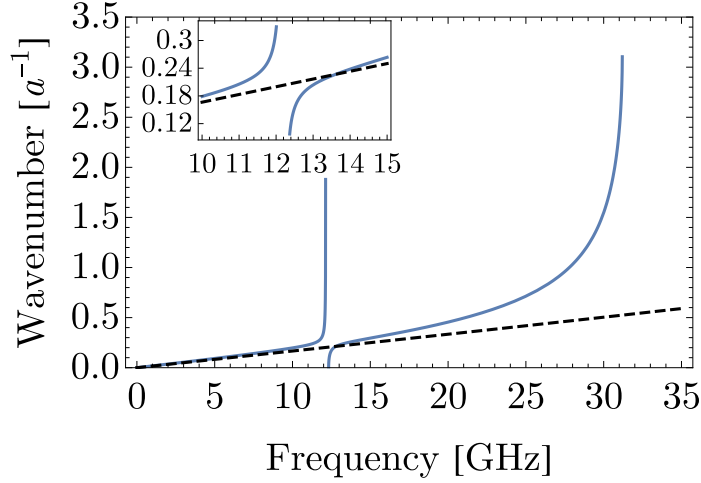


Figure 3.9: Comparison between the engineered dispersion relation (3.119) (blue) and a linear dispersion relation with low chromatic dispersion. Inset: zoom of the stop band opened by the presence of the RPM.

calculated in [65], and corresponds to

$$k(\omega) = 2 \arcsin \left(\frac{\omega/2\omega_0}{\sqrt{1 - \omega^2/\omega_j^2}} \right) \quad (3.119)$$

with $\omega_0 = 1/\sqrt{L_g C_g}$ the *characteristic frequency* of the line. To include the effect of the resonator in Eq. (3.119) it is sufficient to perform the substitution $C_g \mapsto C_g(\omega)$ in the definition of ω_0 .

In Fig. 3.9 one can see the dispersion relation of the JTWPA with an inset showing the stop band created by the presence of the resonator, characterised by a negative and a positive asymptote, respectively at the right and left hand sides of the stop

band.

The RPM technique works by placing the pump frequency in correspondence with one or the other asymptote, depending if working in 3WM or 4WM, giving in this way an extra amount of phase that with a smooth dispersion relation could not be given, thus reducing the phase-mismatch among the traveling tones. To see this concept we define the phase mismatch in PDC regime as

$$\Delta k(\omega_p, \omega_s) = k(\omega_p) - k(\omega_s) - k(\omega_p - \omega_s) \quad (3.120)$$

Plotting (3.120) it is ready visible the effect of the RPM on the overall phase

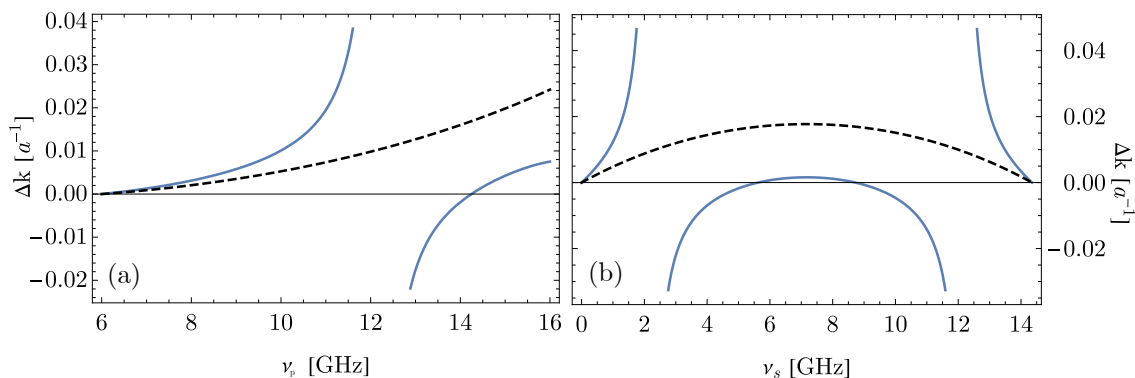


Figure 3.10: (a) Phase mismatch calculated sweeping on the pump frequency for $\omega_s = 6$ GHz. Both the blue solid line and the black dashed line are calculated for the set of parameters in Table A.2 but for the latter the stop band introduced by the resonator has been removed.

(b) Phase mismatch calculated sweeping on the signal frequency for a fixed pump frequency of $\omega_p = 14.4$ GHz. Both the blue solid line and the black dashed line are calculated for the set of parameters in Table A.2 but for the latter the stop band introduced by the resonator has been removed.

mismatch. In Fig. 3.10 (a) one sees two plots of $\Delta k(\omega_p, \omega_s)$ as function of ω_p for $\omega_s = 6$ GHz, with RPM (blue solid curve) and without RPM (black dashed curve). From $\Delta k(\omega_p, \omega_s)$ with RPM we see that, differently from the case without RPM, the phase mismatch crosses the frequency axis in 14.4 GHz, meaning that in this point the phase mismatch is zero. The condition of negligible phase mismatch is of key importance for an efficient amplification, indeed recalling Eq. (3.97) one sees that in the case of $\Psi \approx 0$ the gain becomes

$$G \approx \cosh gt^2 \quad (3.121)$$

hence giving an exponential growth of the signal through all the length of the amplifier.

In Fig. 3.10 (b) $\Delta k(\omega_p, \omega_s)$ is calculated sweeping on the signal frequency, for $\omega_p = 14.4$ GHz. In this case the comparison between the two curves shows us that in the case without RPM we observe that $\Delta k(\omega_p, \omega_s)$ is negligible just at the extreme positions of the considered range, hence where the signal or the idler are very close to the pump, on the other hand in the case with RPM we see that the region where $\Delta k(\omega_p, \omega_s) \approx 0$ is positioned in the center of the range, and extends for several GHz. For these considerations we conclude that an engineered dispersion relation allows to greatly extend the region of negligible phase mismatch $\Delta k(\omega_p, \omega_s) \approx 0$, and hence the bandwidth with exponential gain.

3.2.2 Coupled Mode Equations

Following the approach and notation developed in [17], we describe the dynamics of the traveling waves in the amplifier through the CME method. CME are a system of differential equations normally used to describe the dynamics of signals in parametric amplifiers, and to the lowest orders include just 3 differential equations, describing the pump, signal and idler tones. In [17] an extension of this method has been developed to take into account all the pump-mediated tones up to the K -th pump harmonic, for this reason the system takes the name CME- K . To describe our system we will make use of CME-2, because the set of circuit parameters chosen allows to have a real wavevector up to the second pump harmonic (around 24 GHz), making the tones at higher frequencies evanescent waves not important for the overall evolution of the system (see Fig. 3.9). The choice of this set of parameters is made in order to have $\omega_j = 35.6$ GHz, hence between the second and third pump harmonics. This is to induce enough phase mismatch for the second pump harmonic but not to introduce too much mismatch for the signal tone, that otherwise would require too experimentally stringent conditions for an efficient re-phasing.

The dynamical description of the JTWPA can be made considering the flux wave through a modal decomposition [64, 59] including the signal, pump, idler, pump+idler, pump+signal and pump+pump tones

$$\Phi = \frac{1}{2} \sum_{j=i,s,p,p+i,p+s,2p} A_j(x) e^{i(k_j x - \omega_j t)} + c.c \quad (3.122)$$

where $A_j(x)$ is the wave amplitude of the j -th mode at the coordinate $x = X/a$, with X the physical coordinate that runs over the length of the amplifier and a the unit cell length. The wave equation that the flux wave has to satisfy in a JTWPA in pure 3WM regime is [64, 59]

$$\frac{\partial^2 \Phi}{\partial x^2} - \omega_0^{-2} \frac{\partial^2 \Phi}{\partial t^2} + \omega_j^{-2} \frac{\partial^4 \Phi}{\partial x^2 \partial t^2} + \frac{\beta_L}{2} \frac{\partial}{\partial x} \left[\left(\frac{\partial \Phi}{\partial x} \right) \right] = 0 \quad (3.123)$$

with

$$\beta_L = \frac{2\pi L_g I_c}{\Phi_0}$$

It can be shown that plugging Eq. (3.122) into (3.123) a system of differential equations that regulates the spatial evolution of the wave amplitudes $A_j(x)$ can be derived. We call this system CME-2 and it takes the form

$$\begin{aligned} \frac{dA_i}{dx} &= \frac{\beta_L}{4} \left(k_p k_s A_p A_s^* e^{i(k_p - k_s)x} + k_p k_{p+i} A_p A_{p+i}^* e^{i(k_p - k_{p+i})x} + k_{2p} k_{p+s} A_{2p} A_{p+s}^* e^{i(k_{2p} - k_{p+s})x} \right) e^{-ik_i x} \\ \frac{dA_s}{dx} &= \frac{\beta_L}{4} \left(k_p k_i A_p A_i^* e^{i(k_p - k_i)x} + k_p k_{p+s} A_p A_{p+s}^* e^{i(k_p - k_{p+s})x} + k_{2p} k_{p+i} A_{2p} A_{p+i}^* e^{i(k_{2p} - k_{p+i})x} \right) e^{-ik_s x} \\ \frac{dA_p}{dx} &= \frac{\beta_L}{4} \left(-k_s k_i A_s A_i^* e^{i(k_s + k_i)x} + k_s k_{p+s} A_s A_{p+s}^* e^{i(k_s - k_{p+s})x} + k_i k_{p+i} A_i A_{p+i}^* e^{i(k_i - k_{p+i})x} + \right. \\ &\quad \left. + k_{2p} k_p A_{2p} A_p^* e^{i(k_{2p} - k_p)x} \right) e^{-ik_p x} \\ \frac{dA_{p+i}}{dx} &= \frac{\beta_L}{4} \left(-k_p k_i A_p A_i^* e^{i(k_p + k_i)x} + k_{2p} k_s A_{2p} A_s^* e^{i(k_{2p} - k_s)x} \right) e^{-ik_{p+i} x} \\ \frac{dA_{p+s}}{dx} &= \frac{\beta_L}{4} \left(-k_p k_s A_p A_s^* e^{i(k_p + k_s)x} + k_{2p} k_i A_{2p} A_i^* e^{i(k_{2p} - k_i)x} \right) e^{-ik_{p+s} x} \\ \frac{dA_{2p}}{dx} &= \frac{\beta_L}{4} \left(-\frac{k_p^2 A_p^2}{2} e^{i(k_p + k_p)x} - k_{p+i} k_s A_{p+i} A_s^* e^{i(k_{p+i} + k_s)x} - k_{p+s} k_i A_{p+s} A_i^* e^{i(k_{p+s} + k_i)x} \right) e^{-ik_{2p} x} \end{aligned}$$

where A_j is the amplitude of one of the six modes considered and k_{th} is its wavenumber.

In this framework we can define the gain of the JTWPA as

$$G = \frac{|A_s(\text{end of amplifier})|^2}{|A(0)|^2} \quad (3.124)$$

hence as the ration between the modulus square of the signal amplitude at the end of the amplifier on the one at the beginning of the amplifier. Eq. 3.124 is the definition of power gain since the power of a microwave tone is proportional to the modulus square of its amplitude. Ref. [17] has shown that the CME approach better fits the numerical simulations performed by the WRspice simulator when sitting in the low power regime, for this reason we identify the link between the power of the microwave modes $P(z)$ and their amplitudes $|A(z)|$ as

$$P(z) = \left(\frac{\sqrt{Z_0} |A(z)| \omega I_c}{\omega_0 \beta_L} \right)^2 \quad (3.125)$$

where Z_0 is the characteristic impedance of the line, ω is the frequency of the mode and I_c is the critical current of the junctions.

In all the numerical computations we will always keep the power of the considered signals well above the single photon limit, hence where the classical CME theory can be safely used, but below the high power limit, where the model fails due to the excitation of higher modes not taken into account by a pure PDC theory. In the next sections we will make use of the CME-K approach both to analyse and understand experimental results (Sec. 4.3) and to engineer a novel kind of JTWPA with a modified dispersion relation (Sec. 4.4).

Chapter 4

Fabrication and cryogenic characterisation of JTWPAs

4.1 Fabrication and characterisation of JJs

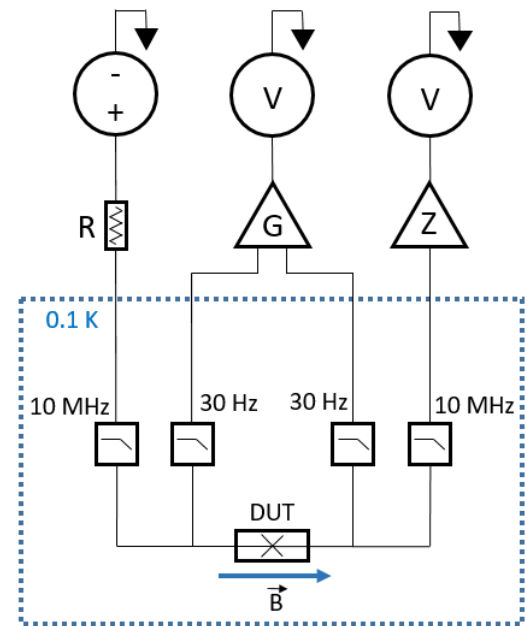


Figure 4.1: Scheme of the measurement setup used to measure the critical currents of JJs. A voltage generator in series of a resistor R supply the excitation current to the DUT, which is then measured by a voltmeter in series of a transimpedance amplifier with gain Z . The voltage drop across the DUT is measured by a second voltmeter in series of a voltage amplifier with gain G . The current and voltage lines are filtered with low pass filters in order to reduce the presence of high frequency noise. An in-plane field \vec{B} is provided to the DUT.

The JTWPA is entirely produced by standard Al deposition utilising a single lithographic step. For the fabrication of the JJs a double angled evaporation is used [18, 22], so as to create an overlap between two superconducting leads, hence the junction area, by the superposition of two distinct metal layers produced by two separated depositions. The creation of the oxide layer between the two leads of the junctions is of fundamental importance, since it is directly related to the critical current density and the associated junction capacitance. Its creation takes place through an oxidation process of the first Al layer operated using a continuous flow of pure oxygen, in a vacuum chamber where the atmospheric pressure is under constant control. There is indeed a direct relation between the oxidation time, the oxidation pressure and the critical current density of a JJ, that allows to predict with a certain precision the critical current of a JJ given the oxidation conditions and the overlap area. The critical current density of a JJ can be considered a function of the $\sqrt{P} \cdot t$ product [29], where P is the oxidation pressure while t is the oxidation time, indeed the easiest and more accurate way to obtain the J_c vs $\sqrt{P} \cdot t$ relation is to directly measure the critical currents of JJ with known area, and then build an experimental curve that interpolates the measured data. Fig. 4.2 shows a micrograph of a typical JJ realised by the shadow mask evaporation technique in Al.

The measurements of the critical currents taken to create the J_c vs $\sqrt{P} \cdot t$ curve were

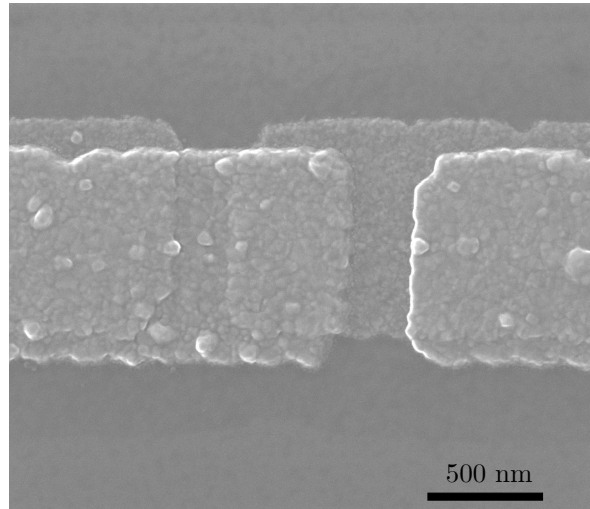


Figure 4.2: Micrograph of a JJ embedded in the rf-SQUIDs.

performed in a wet dilution refrigerator Leiden CF-MCK50-100, using the experimental setup shown in Fig. 4.1. The IV characteristics were measured through a 4 terminal scheme, where the DUT is powered by a voltage source Yokogawa GS200 in series with a resistor with resistance $R = 10 \text{ k}\Omega$. The current supplied is then

measured after the DUT through a transimpedance amplifier FEMTO DDPCA-300 with gain $Z = 10^5$ V/A, of which the output voltage is measured using a multimeter Keithley 2400. The voltage drop across the DUT is measured using a second Keithley 2400, preamplified by a voltage amplifier Aivon dVPA-B with gain $G = 100$. Both the current and voltage lines are filtered with RC low pass filters with respectively 10 MHz and 30 Hz cutoff frequency. The choice of the different cutoff frequencies is lead by power dissipation considerations taking place in the current and voltage lines, indeed a lower cutoff frequency means in general a higher series resistance in the filter, that is a suitable choice for a line in which a low current is flowing, so as not to generate too much heat in the cryostat. Similarly, a higher cutoff frequency is given by a low series resistance, that is a good choice for high current lines. The measurement setup is provided with a superconducting magnet that can generate an in-plane magnetic field (indicated in Fig. 4.1 by \vec{B}) up to 3 T.

In Fig. 4.3 one can see the IV characteristic of a typical JJ fabricated for the de-

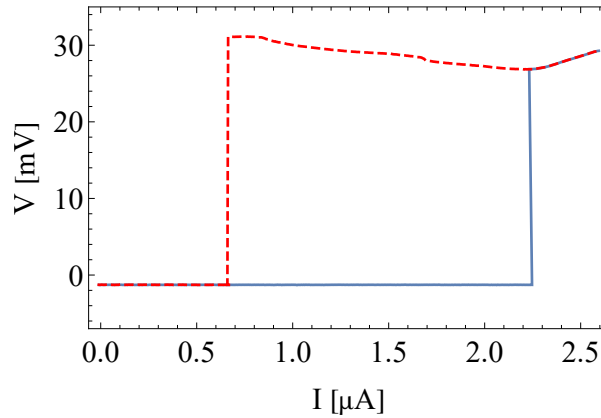


Figure 4.3: IV characteristic of a JJ. The blue solid line represents the positive branch while the red dashed line the retrapping branch.

termination of the J_c vs $\sqrt{P} \cdot t$ curve. The blue solid line represents the positive branch where the critical current is measured, while the red dashed line the retrapping branch of the IV characteristic.

Fig. 4.4 shows the critical current measured (black dots) as a function of the in-plane applied magnetic field. This measurement is commonly used as a criterion for testing the uniformity of the tunneling current in a JJ, since the shape of this experimental curve depends on the critical current density distribution of the JJ, which is linked to the shape of the potential barrier [2]. In general, the potential barrier has not the same high in all the area of the JJ, locally causing spikes or attenuations of the critical current density. This phenomenon has a major role in the case of high-current-density junctions ($> 10^8$ A/m²) since the tunneling current is exponentially dependent on the barrier thickness, by the way, our JJs have

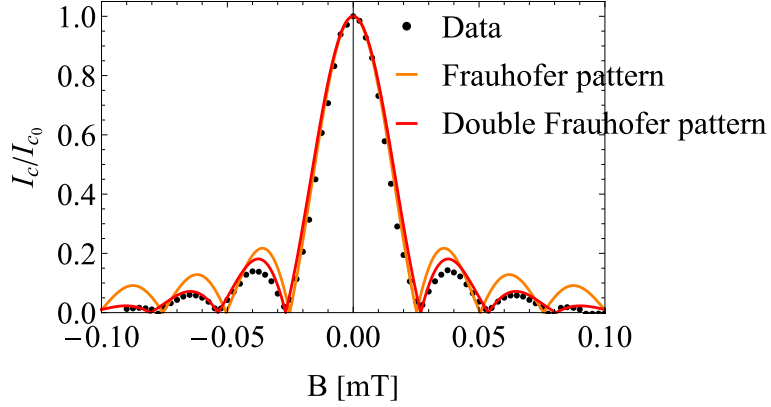


Figure 4.4: Critical current of a JJ measured as a function of the in-plane magnetic field (black dots). The orange and red curves represent two fits calculated using respectively a Fraunhofer pattern (4.1) and a double Fraunhofer pattern (4.2).

critical current densities always lower than 10^7 A/m^2 , limit that puts ourselves in a regime where the tunnel barrier can be considered thick and uniform. The case of a rectangular junction, with a uniform tunnel barrier pierced laterally by a magnetic field, can be analytically treated and the resultant Josephson critical current as a function of the magnetic flux is found to be equal to a so-called Fraunhofer pattern, of equation

$$I_c(B) = I_{c,0} \left| \frac{\sin\left(\frac{\pi BLh}{\Phi_0}\right)}{\frac{\pi BLh}{\Phi_0}} \right| \quad (4.1)$$

where $I_{c,0}$ is the critical current with no magnetic field applied, B is the magnetic field, L is length of the junction and $h = 2\lambda_L + t$, with λ_L the London penetration length and t the thickness of the oxide layer. It can be shown that, if the magnetic field applied has nonzero components along two different in-plane axis of the junction, the dependence of I_c from Φ is given by the product of two Fraunhofer patterns

$$I_c(B) = I_{c,0} \left| \frac{\sin\left(\frac{\pi BLh}{\Phi_0} \cos \alpha\right)}{\frac{\pi BLh}{\Phi_0} \cos \alpha} \right| \left| \frac{\sin\left(\frac{\pi BW h}{\Phi_0} \sin \alpha\right)}{\frac{\pi BW h}{\Phi_0} \sin \alpha} \right| \quad (4.2)$$

with L and W the length and width of the two sides of the junction and α the angle between the applied field direction and the normal versor to the L side of the junction. Fig. 4.4 shows two curves representing fits of the experimental data using Eq. (4.1) (orange) and Eq. 4.2 (red), where we introduced the fitting parameters $a = \frac{\pi Ld}{\Phi_0}$ for Eq. (4.1) and $b = \frac{\pi Ld}{\Phi_0} \cos \alpha$ and $c = \frac{\pi Wd}{\Phi_0} \sin \alpha$ for Eq. (4.2).

Parameter	Value	Standard Error	Unit
a	124.59	1.07	1/T
b	116.96	1.05	1/T
c	26.96	2.25	1/T

Calculating the sum of the residuals between the fitting curves and the experimental data we obtain

$$\Sigma_{residuals}(Fraunhofer) = 5.12 \cdot 10^{-7} \quad (4.3)$$

$$\Sigma_{residuals}(doub.Fraunhofer) = 2.77 \cdot 10^{-7} \quad (4.4)$$

which testify that the double Fraunhofer pattern better fits the experimental data. In conclusion, the experimental data shown in Fig. 4.4 are well fitted by a double Fraunhofer pattern, meaning that the shape of the potential barrier is uniform in all the area of the junction and that the magnetic field direction enters the side of the junction with an angle different from 90° . From the fit of the experimental data is possible to obtain some interesting features of our JJs, like the angle α and the length h . Indeed from Eq. (4.2) we obtain the relation between the fit parameters and the geometric features of the JJ

$$\begin{cases} h \cos \alpha = \frac{a\Phi_0}{\pi L} \\ h \sin \alpha = \frac{b\Phi_0}{\pi W} \end{cases} \quad (4.5)$$

which can be recast in

$$\alpha = \arctan \left(\frac{bL}{aW} \right) \quad (4.6)$$

$$h = \frac{b\Phi_0}{\pi W \sin \alpha} \quad (4.7)$$

It turns out that, considering the results of the double Fraunhofer pattern fit and the geometrical dimensions of the JJ used to perform the measurements in Fig. 4.4 $L = 2 \mu\text{m}$ and $W = 500 \text{ nm}$, the angle $\alpha = (43 \pm 2)^\circ$ and $h = (52 \pm 5) \text{ nm}$. From the value of h one can hence make an estimate of λ_L for our Al thin film. If one assumes that the thickness of the oxide barrier is $\approx 1 \text{ nm}$ we obtain $\lambda_L \approx 25 \text{ nm}$.

The relation between the oxidation pressure, oxidation time and critical current density can be deduced through the $\sqrt{P} \cdot t$ rule studied in [29, 56]. In the microscopic theory of the Josephson effect the relation between the critical current density and the width of the potential barrier of a JJ is found to be [2]

$$J_c = \frac{e\hbar k}{m_e} \frac{\sqrt{n_1 n_2}}{\sinh(2kd)} \quad (4.8)$$

where m_e is the electron mass, $n_{1,2}$ are the supercarrier densities in the two leads of the JJ and k is the decay constant of the barrier. We can obtain the equation for the thickness of the barrier as a function of the $\sqrt{P} \cdot t$ product in terms of the extended Cabrera-Mott theory for the formation of very thin oxide films as

$$d^{3/2} = 6.05 \log(138 \cdot P^{1/2} \cdot t + c) \quad (4.9)$$

where d is the thickness of the oxide barrier in Å, c is a fitting adimensional constant and pressure and time are expressed in torr and min respectively. In this specific analysis we choose to express the pressure and time units in torr and minutes since these are more widely used than the standard SI units Pa and s in fabrication context. Putting (4.9) into (4.8) leads to

$$J_c = \frac{ak}{\sinh(2k[6.05 \log(138 \cdot P^{1/2} \cdot t + c)]^{2/3})} \quad (4.10)$$

with a a multiplication constant that for superconducting Al at $T = 0$ is $a = 1.3 \cdot 10^6 \mu\text{A} \cdot \text{Å}$.

We performed 4 measurement sessions, where in each session we measured between 10 and 15 Josephson critical currents relative to the same oxidation process. In Fig. 4.5 one can see a fit of the experimental points made with Eq. (4.10), where each point correspond to a different measurement session. The parameters of the fit are

Parameter	Value	Standard Error	Unit
k	$1551 \cdot 10^7$	$6 \cdot 10^7$	$1/\text{Å}$
c	4.9	0.1	

The measurements reported in Fig. 4.5 have uncertainty on the $\sqrt{P} \cdot t$ axes given mainly by the pressure fluctuations recorded during the oxidation processes, and on the J_c axes calculated as the standard deviation on the whole number of measurements performed during the different runs.

Considering that the geometrical layout of our JJ involves an area of $\approx 0.4 \mu\text{m}^2$, in order to obtain a critical current of $1.3 \mu\text{A}$ we need $J_c = 1.3 \mu\text{A}/0.4 \mu\text{m}^2 \approx 3.25 \mu\text{A}/\mu\text{m}^2$, which, making use of the curve shown in Fig. 4.5, corresponds to $\sqrt{P} \cdot t \approx 0.175 \sqrt{\text{torr} \cdot \text{min}}$.

Finally, the intrinsic Josephson capacitance can be estimated from the geometric dimensions of the junction and physical properties of the oxide layer, if we consider it comparable to a parallel plate capacitor of capacitance

$$C = \epsilon_0 \epsilon_r \frac{A}{d} \quad (4.11)$$

where ϵ_0 is the dielectric constant of vacuum, $\epsilon_r = 9.34$ is the relative dielectric constant of the dielectric layer, A is the junction area and d is the oxide thickness.

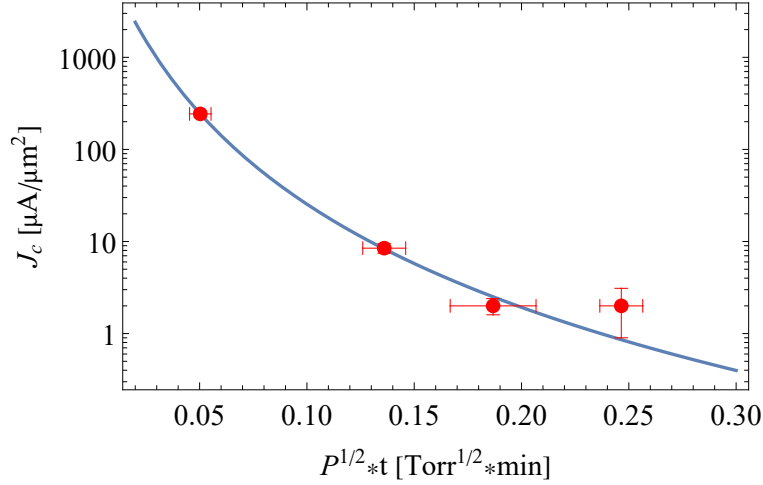


Figure 4.5: The figure shows a fitting curve of the J_c vs $\sqrt{P} \cdot t$ relation interpolating some experimental measurements (red dots) of JJ critical current densities.

Fig. 4.6 (a) and (b) show respectively the thickness of the oxide barrier and the capacitance of a parallel plate capacitor calculated using Eq. (4.11), where the dielectric layer thickness is d and the area is $A = 0.4 \mu\text{m}^2$. Hence, the target value of $I_c = 1.3 \mu\text{A}$ corresponds to a junction capacitance $C_J \approx 28.5 \text{ fF}$.

4.2 Electromagnetic simulations for the layout definition of the JTWPA

Our JTWPA is realised in a coplanar waveguide form, embedding the rf-SQUIDs into the signal line, realising the ground capacitances through interdigitated capacitors and the geometric inductances through meander inductors.

There are, by the way, some observations to make about the simple schematic proposed in [64] and about its physical realisation. This circuit does not take into account some parasitic inductances and capacitances that in practical realisations can never be totally eliminated, and that we need to take into account for a good impedance matching of the transmission line and in general for the proper operation of the device. For example, the rf-SQUIDs are posed at a certain distance between each other, and the connection between them is realised by a piece of coplanar waveguide. This means that there always is a linear inductance connecting two subsequent rf-SQUIDs, that gets longer the further the rf-SQUIDs are. An other stray inductance is represented by the pieces of the rf-SQUID loop that connect the Josephson junction with the rest of the circuit, which very few times can be considered negligible given their reduced width. Moreover, the total ground capacitance of the elementary cell is given by a superposition of the interdigitated

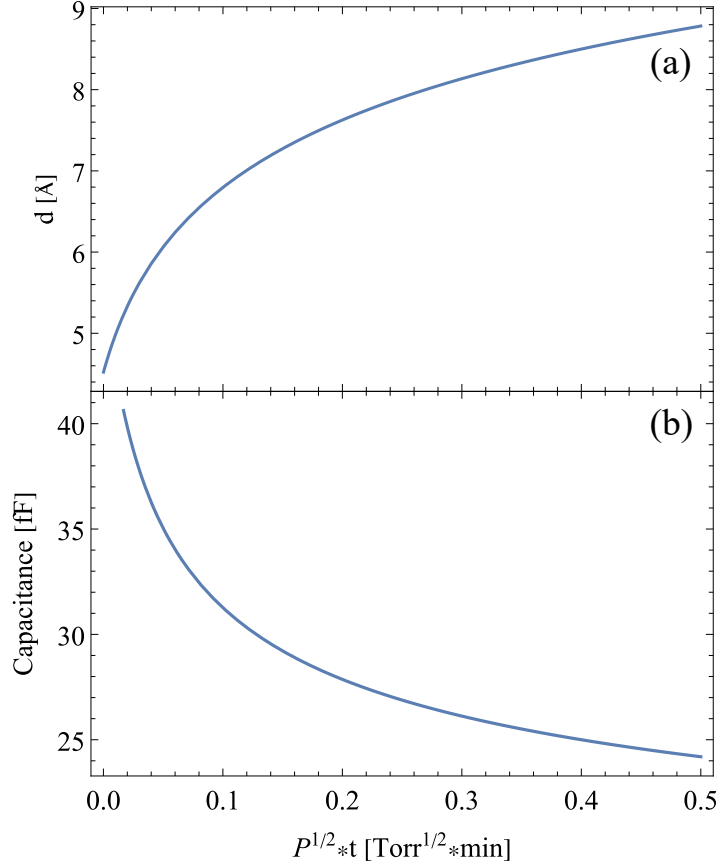


Figure 4.6: (a) Plot of the oxide barrier thickness as a function of the oxidation parameters. (b) Intrinsic capacitance of a JJ with area $0.4 \mu\text{m}^2$ and dielectric thickness d .

capacitors plus the distributed capacitance between the signal line and the ground planes, making the sizing of this feature not straightforward. A schematic of the circuit which includes the parasitic inductances and capacitances is given in Fig. 4.7.

C_{inter} is the capacitance due to the interdigitated capacitors while C_{dist} is the distributed capacitance given by the coupling between the signal line and the ground planes. These two contributions are in parallel and for this reason can be unified in a single ground capacitance, here they are indicated separated just to underline their physical origin. The superconducting loop that forms the rf-SQUID in [64] has a total inductance L_g , that in Fig. 4.7 is divided into three different contributions, namely L_{meander} , the inductance given by the meander inductor in parallel with the Josephson junction, L_{g1} , the inductance due to the input feedline of the Josephson junction and L_{g2} , the inductance due to the output feedline of the Josephson

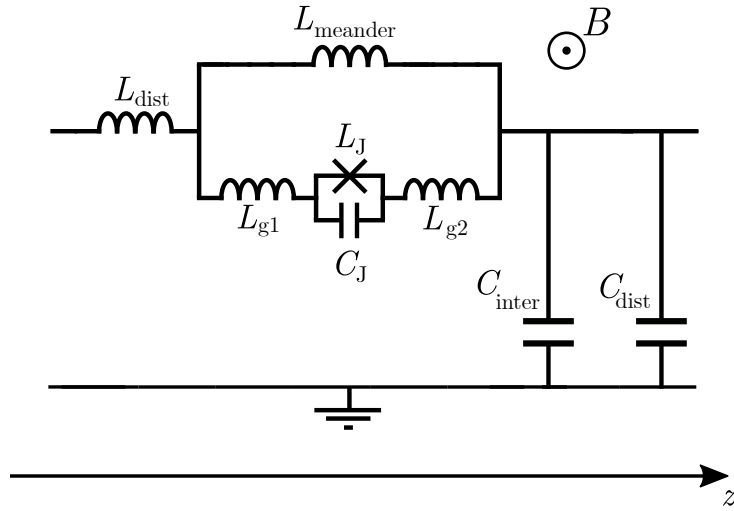


Figure 4.7: The picture shows a schematic of the JTWPA elementary cell complete of its stray inductances and capacitances.

junction. Finally, L_{dist} indicates the distributed series inductance due to the bare coplanar waveguide that joins two rf-SQUIDs.

To realise the physical components of the circuit we made use of the electromagnetic simulation software Sonnet. The stackup used for the simulations is composed of a

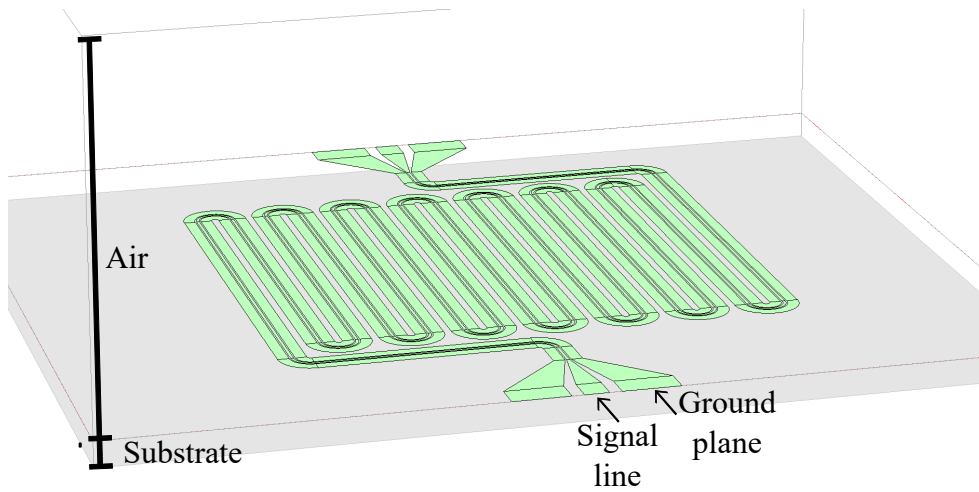


Figure 4.8: Picture of the CPW meander used to house the nonlinear elements, indicating the structure of the stackup used for the simulations.

p-doped Si wafer 500 μm thick with on top of it a 300 nm thick layer of Si dioxide. The tangent loss of the dielectric substrate is involved only in the calculation of

the signal attenuation due to dielectric losses, while the conductivity is used to compute ohmic losses. Their values at cryogenic temperature and microwave frequency is strongly dependant on the particular material experimentally realised for the fabrication of the device, for this reason we can give just an estimate based on measurements found in literature. Typical magnitudes [44] for these parameters at ≈ 100 mK suggest that in the case of crystalline Si we have $\tan \delta \approx 5 \cdot 10^{-6}$ while in the case of Si dioxide $\tan \delta \approx 3 \cdot 10^{-4}$. We choose to use these numbers to characterise the dielectric layers composing the stackup, considering in addition a negligible value for the conductivity of the substrate being at cryogenic temperature.

The relative dielectric constants of the stackup layers are used to calculate the reflected microwave power at the ports and calculating some important quantities like the effective dielectric constant of the transmission lines. Typical values found in literature for the cryogenic relative dielectric constant of Si substrates highlight a weak temperature dependence at microwave frequencies, giving a value of $\epsilon_r = 11.4$ at 77 K [63], that we will use for our simulations. The relative dielectric constant of Si dioxide has a weak temperature dependence as well and is set to $\epsilon_r = 3.7$ [39]. On top of the substrate we then find 4 cm of air, with $\epsilon_r = 1$. The metal used to simulate superconducting Al is a perfectly conductive metal with a sheet inductance $L_{\square} = 0.0201$ pH/sq. The sheet inductance custom-defined is added in order to simulate the presence of the weak kinetic inductance typical of the superconducting Al. We add this feature to the simulation for completeness, by the way it can be shown that this contribution is most of times negligible when considering micro-sized elements fabricated using state-of-the-art Al thin films.

Fig. 4.8 shows a picture of the CPW meander used as the housing for the nonlinear elements. The signal line, $32 \mu\text{m}$ wide, is accompanied by two ground planes $118 \mu\text{m}$ wide, separated by a gap of $16 \mu\text{m}$. These dimensions ensure a 50Ω characteristic impedance [49].

The parameter constraints considered to realise the device are mainly two. First, the screening parameter β_L of the rf-SQUIDs has to be smaller than 1, so as not to incur in a hysteretic behaviour of the rf-SQUIDs. β_L should also not be too close to 1 because we need to take into account that due to fabrication imperfections some of the hundreds of junctions could have a smaller or larger I_c , causing important fluctuations in β_L . For this reason, we choose a fault-tolerant value of $\beta_L \approx 0.2$. Second, the characteristic impedance of the line should be $Z_0 = \sqrt{L/C} = 50 \Omega$, imposing a constraint on the mutual value of the cell series inductance L and cell ground capacitance C .

4.2.1 L_g

First of all, we determine the geometry of L_{meander} , L_{g1} and L_{g2} , of which the sum gives L_g . Fig. 4.9 and 4.10 show the physical layout and the simulated in-

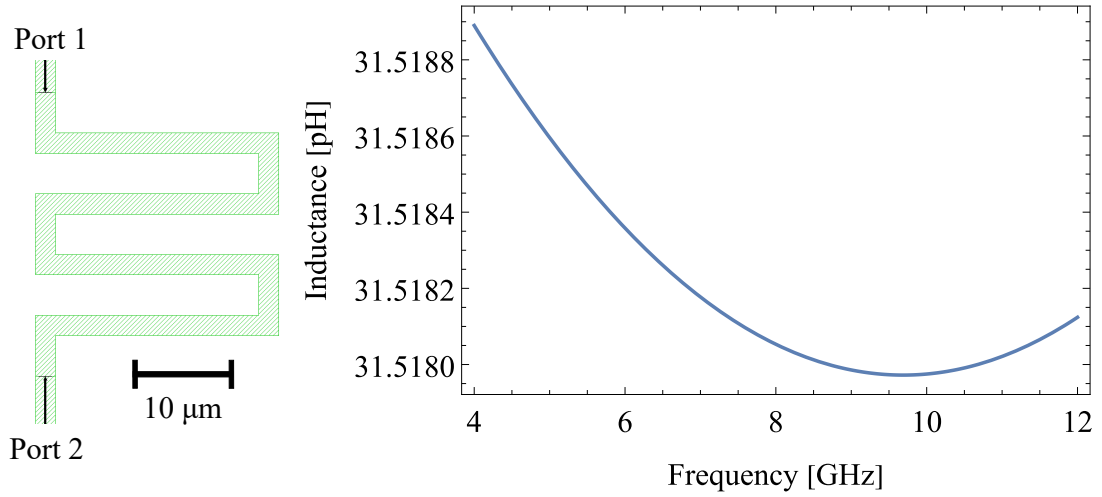


Figure 4.9: Physical layout of L_{meander} and simulated inductance.

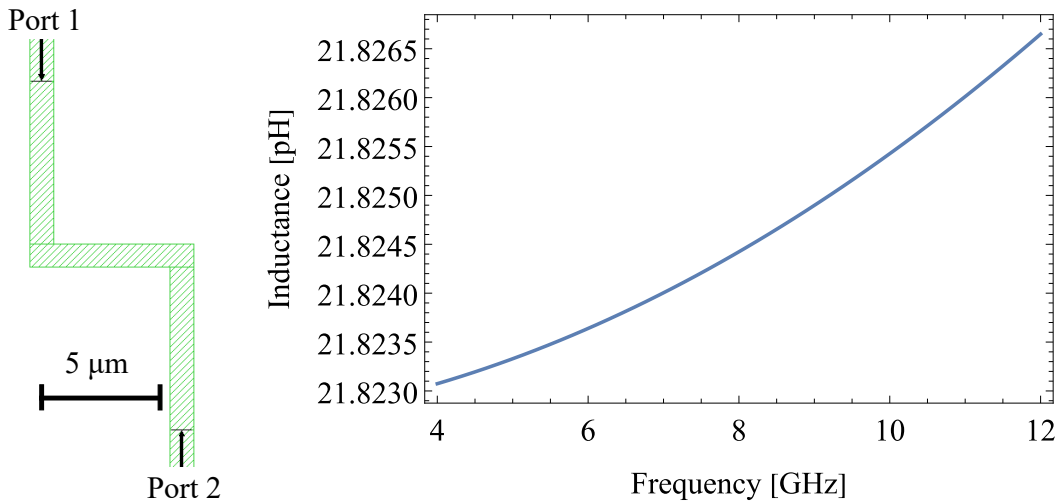


Figure 4.10: Physical layout of $L_{g1} + L_{g2}$ and simulated inductance.

ductance of the meander inductor and Josephson feedline respectively, in the range of frequency 4 – 12 GHz. The geometric inductance of the whole loop can then be straightforwardly calculated as $L_g \approx 31.5 \text{ pH} + 21.8 \text{ pH} = 53.3 \text{ pH}$.

As a benchmark for the electromagnetic simulations we estimate the value of L_{meander} , L_{g1} and L_{g2} through analytic expressions taken from Ref. [50, 15]. The analytic formula for a meander inductor (for which the reader can refer to Ref. [50]) takes into account the self-inductance of the striplines constituting the meander and their mutual inductance contributions. The value obtained is $L_{\text{meander}} = 29.8 \text{ pH}$, resulting in a difference of about 5% between the two results. The inductance of L_{g1} and L_{g2} is calculated considering the inductance of a piece of stripline with the same length of $L_{g1} + L_{g2}$ [50] through the formula

$$L = 0.00508l \left(\ln \left(\frac{2l}{w+h} \right) + 0.5 + 0.2235 \frac{w+h}{l} \right) \quad (4.12)$$

with l the length of the microstrip segment, w its width and h the dielectric layer thickness (all the length are expressed in inches). The resulting inductance is $L_{g1} + L_{g2} = 15.4 \text{ pH}$, that differs from the simulated value of about 30%. In this case the discrepancy between the two results is significantly larger since the mutual inductances between the segments is not taken into account. Nonetheless, we see good agreement between the numerical and analytical approach.

4.2.2 L_{dist}

Now, we determine the distributed series inductance of the elementary cell by simulating a piece of 50Ω matched coplanar waveguide and calculating its associated inductance per unit length. Fig. 4.11 shows the geometrical dimensions of the CPW used for the simulation and its associated inductance for a length of $700 \mu\text{m}$. To extrapolate inductance per unit length of our CPW we simply divide the total inductance by the length of the TL, finding $\approx 280 \text{ pH}/700 \mu\text{m} = 0.4 \text{ pH}/\mu\text{m}$. Considering that the portion of coplanar waveguide composing a single elementary cell is $46 \mu\text{m}$, the distributed series inductance is $L_{\text{dist}} = 46 \mu\text{m} \cdot 0.4 \text{ pH}/\mu\text{m} = 19.3 \text{ pH}$. Calculating the value of the distributed inductance through [49]

$$L_{\text{dist}} = \frac{\mu_0}{4} \frac{K\left(\sqrt{1 - \left(\frac{s}{s+2w}\right)^2}\right)}{K\left(\frac{s}{s+2w}\right)} \quad (4.13)$$

with s the signal line width, w the gap width, μ_0 the magnetic permeability of vacuum and $K(x)$ the complete elliptic integral of the first kind of argument x , we find $L_{\text{dist}} = 0.4 \text{ pH}$, in perfect agreement with the numerical simulations.

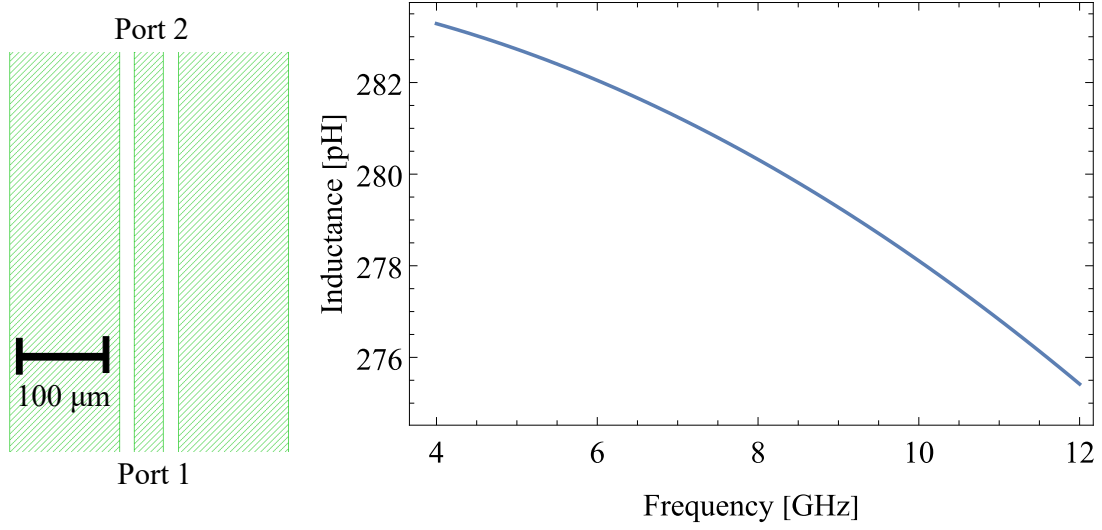


Figure 4.11: Physical layout of the coplanar waveguide used to extrapolate L_{dist} and simulated inductance.

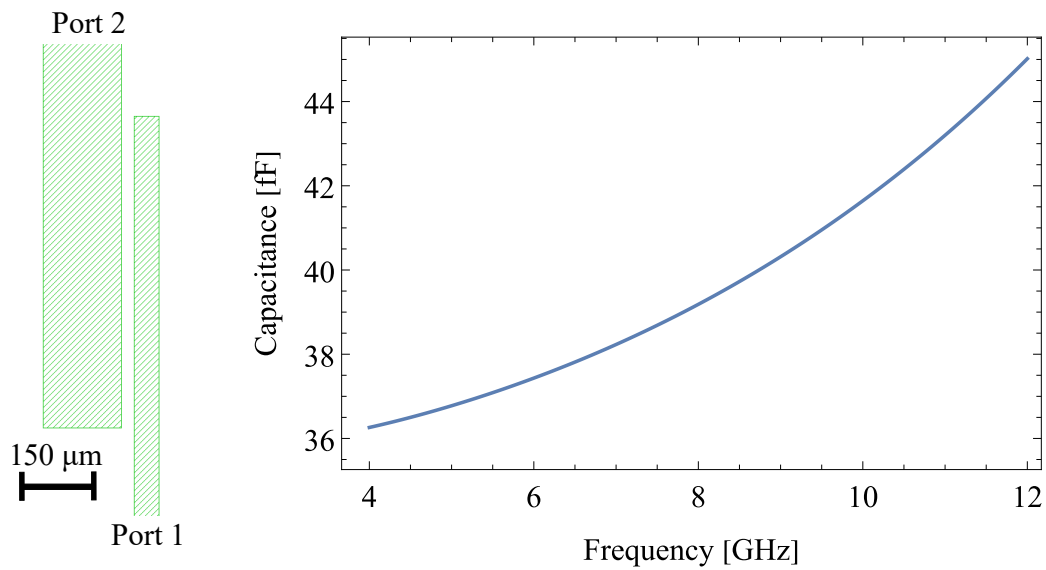


Figure 4.12: Simulated metalization used to extrapolate the distributed capacitance of the coplanar waveguide.

4.2.3 C_{dist}

We now evaluate the distributed ground capacitance C_{dist} given by the coupling between the signal line and the ground planes. To this end, we draw the circuit shown in Fig. 4.12, that is simply composed by two pieces of metallization representing the signal line (connected to Port 1) and one of the two ground planes (connected to Port 2), coupled for a total length of $400\ \mu\text{m}$. We then simulate the capacitance between the two metal strips and obtain the distributed capacitance per unit length as $\approx 40\ \text{fF}/400\ \mu\text{m} \approx 0.1\ \text{fF}/\mu\text{m}$. The distributed capacitance to ground of a single cell is then readily calculated considering again that the portion of coplanar waveguide composing the elementary cell is $46\ \mu\text{m}$, hence $C_{\text{dist}} = (46\ \mu\text{m} \cdot 0.1\ \text{fF}/\mu\text{m}) \cdot 2 \approx 9.2\ \text{fF}$. We underline that the overall capacitance has been multiplied by a factor of 2 since the TL has two ground planes. We can evaluate C_{dist} analytically considering the formula for the distributed capacitance of a coplanar waveguide [49]

$$C_{\text{dist}} = 2\epsilon_0(\epsilon_r + 1) \frac{K\left(\frac{s}{s+2w}\right)}{K\left(\sqrt{1 - \left(\frac{s}{s+2w}\right)^2}\right)} \quad (4.14)$$

where ϵ_r is the relative dielectric constant of the substrate and ϵ_0 is the dielectric constant of vacuum. We obtain $C_{\text{dist}} = 0.17\ \text{fF}/\mu\text{m}$, that underestimate the capacitance of about 15% with respect to the electromagnetic simulations. This is probably caused by the fact that Sonnet is able to take into account the cross-capacitance effects of the whole metallization, considering corrections that are missing in the analytical formula.

4.2.4 C_{inter}

Finally, we estimate the interdigitated ground capacitance through the circuit depicted in Fig. 4.13. As one can see the capacitance supplied by a single capacitor is around $5.5\ \text{fF}$ in all the range, meaning that the total capacitance due to these components in a single cell is around $11\ \text{fF}$.

We estimate the value of the interdigitated capacitors using also the analytical approach given in Ref. [28], where an analytic form for the capacitance of interdigitated capacitors on multilayer substrate is developed. This approach gives a capacitance value for the capacitor shown in Fig. 4.13 of $C_{\text{inter}} = 8.3\ \text{fF}$, that is about 50% higher with respect to the value obtained through electromagnetic simulations. Ref. [28] gives many comparisons between their values obtained by the analytical approach and experimental values or electromagnetic simulations, always giving optimal agreement. Nonetheless, the scale length at which the model is used in Ref. [28] is cm, resulting in capacitances in the order of hundreds of pF. Given this consideration and the discrepancy obtained between analytical model and our electromagnetic simulations we think that at smaller scales, say tenth of μm , the

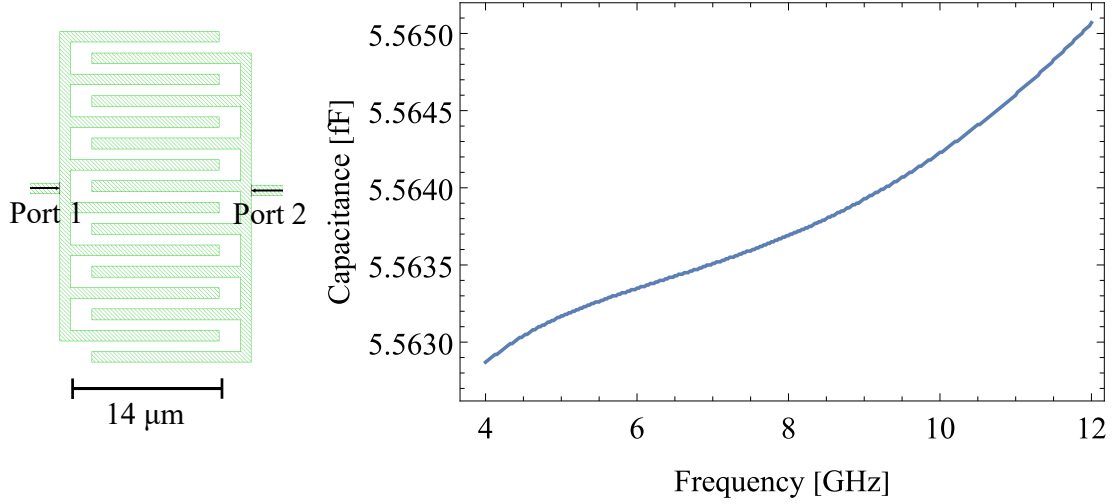


Figure 4.13: Physical layout of C_{inter} and simulated capacitance.

hypothesis made to obtain a closed form for the capacitance do not hold anymore, overestimating the overall capacitance.

4.2.5 L_J and C_J

The geometry of the Josephson feedlines shown in Fig. 4.10 has been chosen in order to give a solid mechanical stability to the suspended mask used in the doubled-angle evaporation process, since the need of fabricating nearly one thousand junctions in a single device imposes severe constraints in terms of lithographic reliability. On the other hand, this same geometry limits the maximum area that a single junction can have, because the limited angle and thickness of the mask does not allow to achieve large overlaps, hence large areas. As a consequence, C_J and I_c cannot have any value, but will have some kind of upper limit.

Referring to Eq. (2.96), we see that a Josephson junction with a certain critical current has an associated inductance that has to be taken into account when we make characteristic impedance balances. Given $L_g = 53.3$ pH we need the critical current to be $I_c \approx 1.3$ pA to have $\beta_L \approx 0.2$ fulfilled. It follows that in a 3WM working point the JJ corresponds to an inductance of which the value is much higher than L_{meander} , say $L_J \approx 400$ pH. This contribution can be taken into account in the simulation by defining a custom metal with a sheet inductance such that its enclosure in the TL circuit mimics the electromagnetic behaviour of the JJ in the rf-SQUID at the working point. To this end, a piece of custom metal with sheet

inductance $L_{\square} = 400 \text{ pH/sq}$ is defined and placed in the physical layout in substitution of the JJ.

As explained in Sec. 4.1, an intrinsic capacitance is always attributed to JJs when made by thin superconducting films, given by the overlap of the two leads. To take into account this contribution a lumped element capacitor C_J is placed between the two leads of the JJ. The Sonnet Suite allows to insert ideal electrical components with a custom value between any two metal polygons, so we use this feature to simulate C_J . In this case the lumped element capacitor will have a capacitance 28.5 fF , just as estimated at the end of 4.1.

4.2.6 Characteristic impedance

Given the results above, we can now evaluate the characteristic impedance of the line calculating the total series inductance and ground capacitance of the elementary cell. It turns out that the characteristic impedance is very close to 50Ω

$$Z_0 = \sqrt{\frac{L}{C}} = \sqrt{\frac{L_{\text{dist}} + L_{\text{meander}}}{C_{\text{inter}} + C_{\text{dist}}}} = \sqrt{\frac{(19.3 + 31.5) \text{ pH}}{(11 + 9.2) \text{ fF}}} = 50.1 \Omega \quad (4.15)$$

It has to be noted that the Josephson branch of the rf-SQUID does not give any contribution to the characteristic impedance since the series inductance of $L_{g1} + L_{g2} + L_J$ is much larger than L_{meander} . The method just described to realise a 50Ω matched TL estimates separately all the contributions of the circuit components and then calculates at the end the characteristic impedance of the line. By the way, for more complicated and irregular devices this method can be somehow limiting because it does not take into account the non-trivial electromagnetic interactions between the components, and hence can lead to errors due to the underestimation of some features. To avoid this problem, an electromagnetic simulation of the whole device is preferable and in the following we show how to design the same 50Ω matched TL in a more straightforward way.

We start by choosing again a value of $\beta_L \approx 0.2$, so that we can use the simulations shown in Fig. 4.9 and 4.10 to find L_g . The definition of the other circuit components is done through a parametric electromagnetic simulation, where the parameter is represented by the length of the interdigitated capacitor fingers of C_g . Fig. 4.14 shows a screenshot of the unit cell with the length of the interdigitated capacitor fingers parameterized by the "Grd" parameter. We choose this dimensional parameter because the capacitance to ground of the unit cell is directly related to the length of the interdigitated capacitors fingers $C_{\text{inter}} \propto \text{Length}(\text{Grd})$, and by modifying this length we can easily tune C_{inter} and consequently the characteristic impedance of the line. Indeed by looking at Eq. (4.15) we see that removing the capacitance contribution given by C_{inter} we would obtain a characteristic impedance

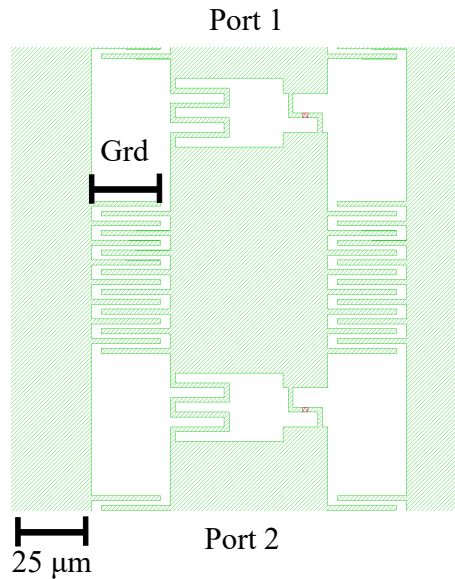


Figure 4.14: Physical layout of the elementary cell showing the dimensional parameter "Grd" indicating the length of the fingers of the interdigitated ground capacitors.

of about $\approx 62\Omega$, hence this circuit element is essential to balance the inductive contribution of the unit cell, hence lowering the characteristic impedance of the line. The simulation is then performed by sweeping the length of "Grd" at a fixed frequency (6 GHz), monitoring the transmission of the TL by looking at the value of S21. When the magnitude of S21 is maximum we have the best power transmission possible, hence the characteristic impedance matching. Fig. 4.14 reports the results of some parametric simulation, calculated for different numbers of elementary cells, as a function of the length of the parameter "Grd". As can be seen, all the curves present a maximum for $\text{Grd} = 14\mu\text{m}$, meaning the this point presents the best achievable power transmission with the length steps used (probably a higher value of S21 could be reached with thinner steps but we chose to keep $1\mu\text{m}$ in order to limit the computational time). This length corresponds exactly to the one found in Fig. 4.13, giving perfect agreement between the two methods.

One last remark needs to be made on the frequency dependence of the simulations presented in this sections. One can indeed notice that the simulations shown from Figures 4.9 to 4.13 present a weak frequency dependence of the capacitances and inductances of the single circuit components. This fact is known to be a direct consequence of the change in inductance and capacitance of the elementary metallic and dielectric sections of the complex geometries here simulated given by the different frequency response to the electromagnetic field. In other words, we see directly the effect of the complex reactances of inductors and capacitors. We do

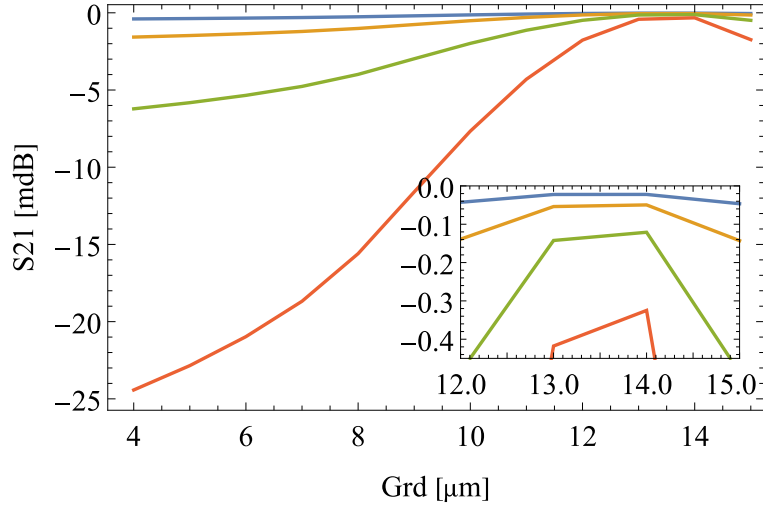


Figure 4.15: Parametric simulations of the S21 amplitude parameter as a function of the length of "Grd". The simulations are performed for different numbers of unit cells (blue = 1 cell, orange = 2 cells, green = 4 cells, red = 8 cells).

not see this effect in the analytical formulas since this is an approximation that works in a generic high frequency regime and do not give an explicit frequency dependence. This said, we notice that the frequency dependence of the simulated objects is weak and can be considered negligible in relation to the magnitude of the simulated quantity. As a consequence, the analytical approach can be considered again a valid approximation.

For a deeper understanding of the electromagnetic behaviour of the TL it is useful analysing the simulations as a function of the number of unit cells in the circuit, in order to extrapolate some important pieces of information for the whole JTWPA, which includes 990. To this end, in Fig. 4.16 we plot the value of S21 at $\text{Grd} = 14 \mu\text{m}$ as a function of the number of cells and analyse its behaviour. The plot shows the simulated points extrapolated from Fig. 4.15 and a parabolic fit of equation $y = a + bx + cx^2$, of which the parameters are

Parameter	Value	Standard Error	Unit
a	$5 \cdot 10^{-4}$	$5 \cdot 10^{-4}$	dB
b	$200 \cdot 10^{-4}$	$3 \cdot 10^{-4}$	dB
c	$259 \cdot 10^{-5}$	$3 \cdot 10^{-5}$	dB

It turns out that the magnitude of S21 has a parabolic behaviour in the number of cells that compose line, and an extrapolation of its value using the parabolic fit

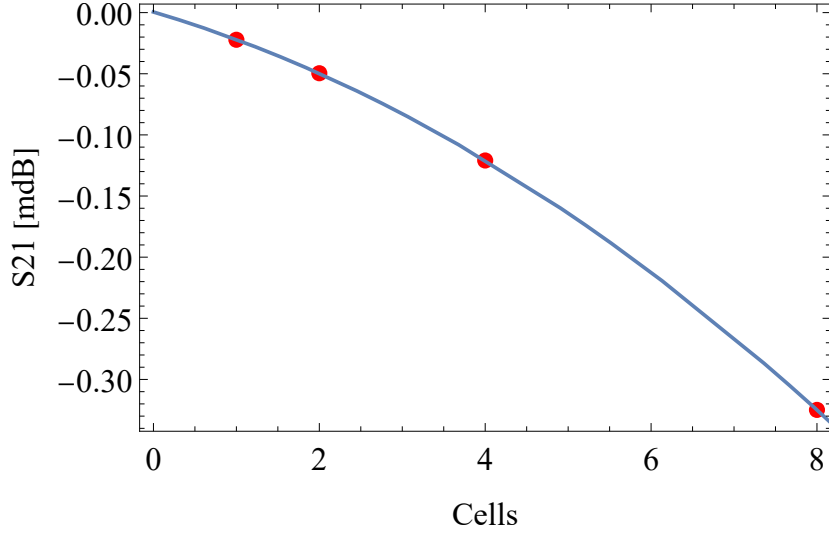


Figure 4.16: S21 magnitude as a function of the number of unit cells. The red dots indicate the simulated points while a blue curve the parabolic fit.

for 990 cells gives $S21(990) = -2.55$ dB, that is the expected insertion loss of the whole device. In the next section we experimentally show some S21 measurements of a JTWPA realised using the circuit parameters found thanks to the method just described, finding a very good agreement between the simulations and the experimental data.

When designing a microwave circuit it is useful understanding the sources of attenuation that play a role in the signal transmission, for example identifying the different contribution of impedance mismatch, ohmic losses and dielectric losses. To this end we study a quantity named Loss Factor (or Efficiency factor or Power Balance), defined as

$$\text{Loss Factor(dB)} = 10 \log_{10} (|S11|^2 + |S21|^2 + \dots + |SN1|^2) \quad (4.16)$$

where N is the number of ports in the network. As an example, the loss factor for a lossless circuit will be 1.0 in magnitude or 0.0 dB, a circuit that loses 20 percent of its power has an efficiency factor of -1 dB, etc. etc. The Loss Factor gives a measurement of how "lossless" a circuit would be if you were able to perfectly impedance match it, giving important hints on the sources of loss located in the circuit. Fig. 4.17 shows the Loss Factor simulated for different numbers of unit cells (blue = 1 cell, orange = 2 cells, green = 4 cells, red = 8 cells) as a function of the length of the parameter Grd. Analysing these plots one sees that for a low value of Grd, hence for short intersections of the capacitors fingers, the modulus of the Loss Factor is always below 0.03 dB, and then it grows monotonously with Grd. This behaviour can be understood considering that the electric field density stored in C_g grows with Grd, hence the dielectric losses grow as well (there are no ohmic

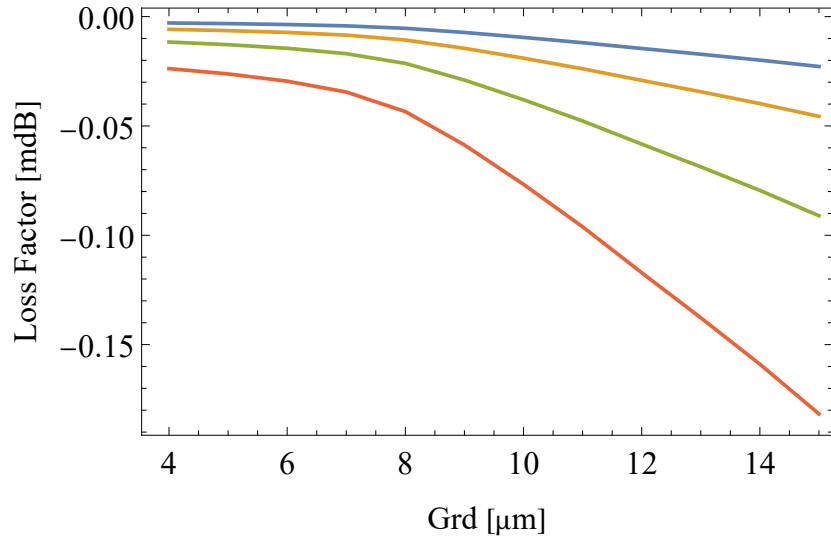


Figure 4.17: Parametric simulations of the Loss Factor as a function of the length of "Grd". The simulations are performed for different numbers of unit cells (blue = 1 cell, orange = 2 cells, green = 4 cells, red = 8 cells).

losses considered since the metal is a perfect conductor). Fig. 4.18 shows the Loss

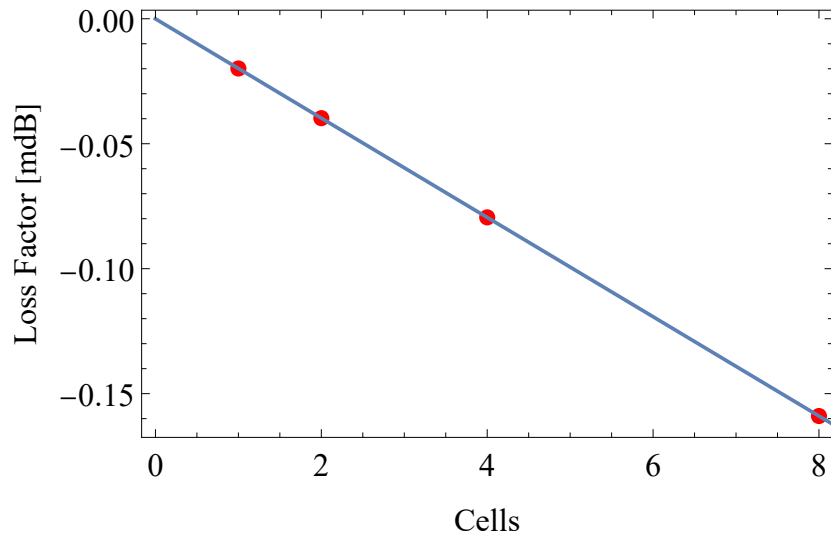


Figure 4.18: Loss Factor as a function of the number of unit cells. The red dots indicate the simulated points while a blue curve the linear fit.

Factor as a function of the number of cells. The red dots represent the simulations performed for 1, 2, 4 and 8 cells for $Grd = 14 \mu\text{m}$, while the blue curve is a linear fit of the simulated points of equation $y = a + bx$, of which the parameters are

Parameter	Value	Standard Error	Unit
a	-0.00003	0.00002	dB
b	-0.019864	0.000004	dB

The linear fit testify a simple but important fact, hence that every cell gives the same amount of losses. Using the linear fit we extrapolate a Loss Factor at 990 cells of Loss Factor (990) = -0.02 dB, that is much less than the attenuation previously found of $S_{21}(990) = -2.55$ dB. This fact makes us understand that the main cause of attenuation in the circuit is mainly a result of impedance mismatch instead of dielectric losses.

A final remark about this second method of defining the layout of a $50\ \Omega$ matched TL. This method intrinsically takes into account all the electromagnetic interactions between the components of the circuit since the device is simulated as a whole geometry. We can find in this case accordance between the two methods because the structure of the TL is simple and the single parts tend not to electromagnetically interact between each other in complicated ways.

Fig. 4.19 shows a micrograph of the whole elementary cell, of which the set of circuit parameters can be summarised as

Component	Value	Unit
L_{meander}	31.5	pH
$L_{g1} + L_{g2}$	21.4	pH
L_{dist}	19.3	pH
C_{dist}	9.2	fF
C_{inter}	11	fF
I_c	1.3	μA
C_J	28.5	fF

4.3 Cryogenic measurements of JTWPA

The cryogenic characterisations of JTWPAs were performed on two different samples to which we will refer as sample A and sample B.

We start the RF characterisation of the JTWPA-A measuring the power transmission of the TL, so as to evaluate the overall attenuation due to the impedance mismatch and losses. The cryogenic setup used for the characterisation is a DRY ICE 300 mK He-3 system with base temperature 300 mK (Fig. 4.20 left). The schematic of the circuit is shown in the right side of Fig. 4.20. The system is a closed loop He refrigerator studied to allow very long measurement sessions (> 1 month) always keeping base temperature. It presents 4 cold stages, at 50 K, 3 K,

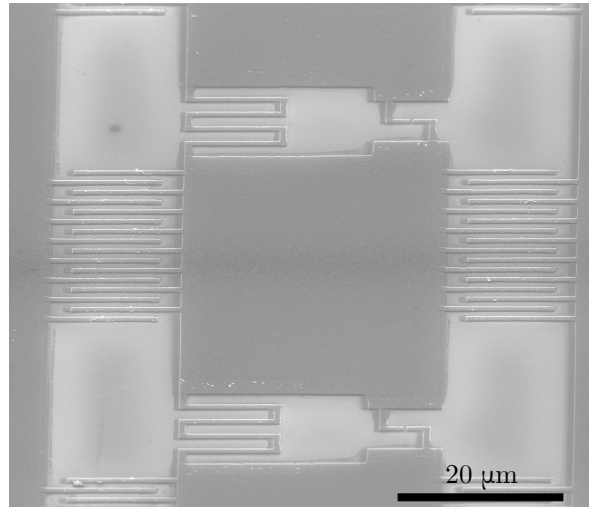


Figure 4.19: Micrograph of a JTWPA.

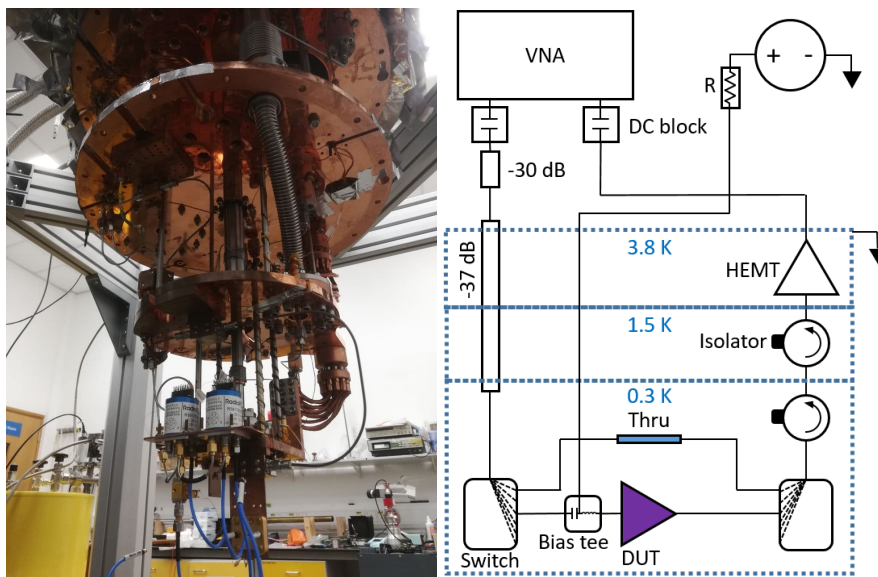


Figure 4.20: Left: picture of the refrigerator DRY ICE 300 mK used to characterise sample A. Right: schematic of the microwave circuit used for the VNA characterisation of sample A.

1.5 K and 300 mK, and is provided with four microwave lines that link the outside of the refrigerator with the coldest stage passing through all the temperature stages. The 300 mK stage is then connected to room temperature again through a superconducting output line that minimises signal losses. The DUT is mounted at the 300 mK stage while the circuitry necessary to perform the experiment, like amplifiers and circulators, are placed at the 1.5 K and 3 K, so as not to thermally

overload the coldest stage. The input line has 30 dB of attenuation at room temperature given by attenuators put in front of the Vector Network Analyzer 2-port PNA-X-P9372A (VNA), then about 37 dB of attenuation given by the input line inside the refrigerator (composed by the coaxial wires plus the input switch plus the bias tee). The input and output lines have about 3 dB each (6 dB in total) of extra attenuation given by the presence of the room temperature cables connecting the VNA and the fridge. A bias tee put in front of the DUT allows to bias the amplifier using a DC current (the circuit of the DC bias is closed to ground through the isolators, hence there is no need of two bias tees) generated at room temperature by a standard voltage generator in series of a resistor R of resistance 13 k Ω (much higher than the resistance of all the DC circuit, hence the voltage generator + R makes a good approximation of current generator). The JTWPA is placed between the two RF switches. The characterisation required the use of a channel connected to a thru (e. g. a bare piece of coaxial cable), so as to estimate in situ the overall losses of the setup, and a channel connected to the device to be characterised. The superconducting (NbTi) output line has two stages of isolation in series of 20 dB each and a final amplification stage obtained through a High Electron Mobility Transistor (HEMT), placed at the 3 K stage, that provides about 36 dB in a range between 4 and 12 GHz.

Fig. 4.21 (a) shows some transmission spectra taken on sample A for different input signal powers. One can see a comparison between the power transmission of the thru channel and the transmission of the JTWPA for a probe tone power of -107 dBm, -97 dBm and -87 dBm (calculated at the JTWPA input). Fig. 4.21 (b) shows the spectra after the line attenuation subtraction. Looking at the attenuation subtracted spectra one can notice that the overall insertion loss given by the introduction of the JTWPA in the line ranges between 2 dB and 4 dB for low probe power (RF power = -107 dBm) and goes eventually to 6 dB for high powers and high frequencies.

This measurement confirms two important facts. First, the device has a characteristic impedance of approximately 50 Ω and low losses. Due to the structure of the measurement setup it was impossible to measure the reflected power at the DUT input, it is hence impossible to determine the distinct contributions of losses and reflections of the overall insertion loss. Moreover, the growing loss at higher frequencies is compatible with the RF behaviour of a CPW. Second, the signal transmission gets worse for high power probe tones. This fact can be explained by considering that due to the nonlinear nature of the JTWPA a higher portion of RF power gets converted into higher harmonics if the probe tone is more intense, resulting ultimately in a reduced transmission when measuring the scattering parameters. Transmission measurements performed sweeping the DC current bias did not highlight a real dependence of the insertion losses from this parameter.

We finally underline that the measurements just presented are in very good agreement with the simulations of the S_{21} parameter presented in the previous section.

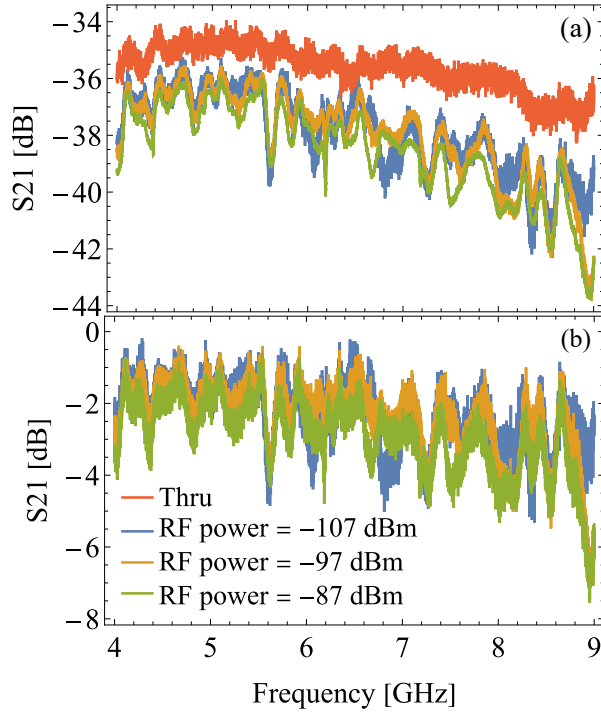


Figure 4.21: (a) Transmission spectra of the JTWPA measured for different pump powers. (b) Subtraction between the transmission spectra shown in (a) and the Thru trace.

The modulation of the quadratic and cubic nonlinearities can be tested by measuring the power of the 3WM and 4WM idlers as function of the DC bias current. This measurement has been carried out on sample B, in a Leiden Cryogenics cryostat CF-CS110, of which the circuit schematic is reported in Fig. 4.22. A 2 tones measurement is performed by supplying in input a weak signal tone supplied by an Agilent E5071C 300 kHz-20 GHz VNA, and a pump tone given by a Rohde&Schwarz SMA100B 8 kHz-20 GHz signal generator. The microwave signals enter the dilution refrigerator and passing through several attenuation stages, get to the metamaterial after have been gone through a directional coupler and a first isolation stage provided by a circulator. The microwave tones are then detected at room temperature after passing through a HEMT amplifier placed on the 4 K stage, which provides 30 dB of amplification. Before getting at room temperature the output microwave passes through an isolation stage realised by means of two circulators. A voltage source in series to a 10 k Ω resistor is connected to the device via a couple of bias tees, providing the DC current bias to the device. We supply a pump tone at 6.8 GHz and -52 dBm and a signal tone at 3.3 GHz and -64 dBm

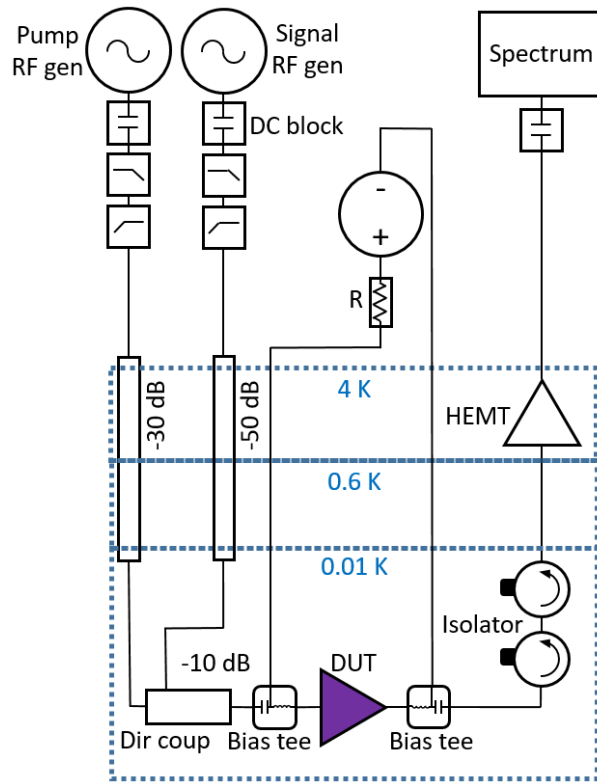


Figure 4.22: Schematic of the microwave circuit used for the idlers power measurement of sample B.

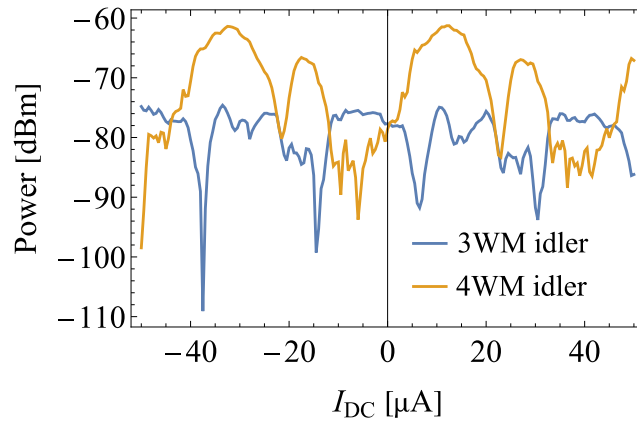


Figure 4.23: Plot of the 3WM and 4WM idlers power as a function of the DC bias current provided to the JTWPA.

(the power is considered at the device input), thus, we will find the 3WM idler at 3.5 GHz and the 4WM idler at 10.3 GHz. Fig. 4.23 shows the modulation of the idlers as a function of the DC bias. Analysing the 3WM idler curve it is possible to appreciate four main minima at an average distance of 23.2 μA between each other. These bias points are the ones where the quadratic nonlinearity of the most of the rf-SQUIDs is negligible, hence where the device works as a 4 wave mixer. We notice that the 4 minima have different magnitudes depending on the bias point. This behaviour can be attributed to inhomogeneities among the rf-SQUIDs in terms of critical currents of the junctions or loop inductance, which shifts the periodicity of the single cells creating a non-harmonic characteristic of the total device, hence the non-trivial pattern of the idlers shown here. By the way, the equidistance between the minima and their pronounced dips testifies a overall homogeneity of the rf-SQUIDs along the whole line.

Due to the natural Kerr-nonlinearity of a rf-SQUID with no current bias one would expect at zero bias current that the 3WM idler would not appear, nonetheless we see a non-zero 3WM idler with no DC bias. This fact can be explained considering a magnetic field offset during the cooling down phase of the dilution refrigerator, that has trapped some flux in the rf-SQUIDs, generating a shift in the periodicity of the curves.

Once checked the nonlinear behaviour of the JTWPA through the observation of frequency mixing, we now measure the parametric gain given by the TL. We perform this measurement on sample A, using the circuit depicted in Fig. 4.24. The scheme used for this measurement is similar to the one shown in Fig. 4.20 exception made for the signals generation at room temperature. The signal and pump tones are respectively supplied by a SynthHD PRO 10MHz – 24GHz Dual Channel Microwave Generator and a Keysight signal generator. Both channels have a series of low pass and high pass filters to reduce the presence of higher harmonics given by the generators, and are finally coupled through a directional coupler at room temperature, that injects the microwaves in the cryostat. The signal channel is attenuated 40 dB more than the pump one so as to ensure that the signal power is much lower than the pump power in all the explored power range. With this scheme we measured the output signal power through a Spectrum Analyser USB-SA124B - 12.4 GHz, as a function of the pump power, supplying a pump tone at 11.7 GHz and a signal at variable frequency. Fig. 4.25 shows the signal dependence on the pump power at 6.4 GHz. As can be seen, the output signal power stays unaltered for low pump powers (≈ -75 dBm) and then monotonically decreases supplying a higher pump power, leading to a overall deamplification of the signal tone. This behaviour does not change modifying the signal frequency in a range that goes from 4 GHz to nearly the pump frequency. This fact can be explained as the result of two separated phenomena, hence the generation of higher order tones that takes place in the device and the overall low level of nonlinearity of the TL.

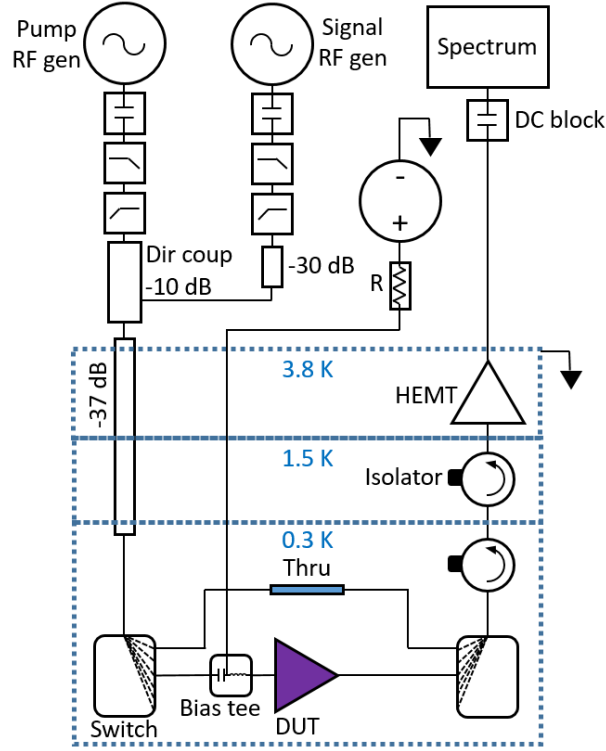


Figure 4.24: Schematic of the microwave circuit used for the measurement of second and third harmonics generation of sample A.

The quantum model of the JTWPA presented in Sec. 3.1 is a 3-waves model, hence the description given by this theory is accurate just as long as all the other modes different from pump, signal and idler can be considered negligibly small. However, we need to ask ourselves if this is the case, hence if with the device parameters used to realise the measured JTWPAs we actually sit in the case where we can consider negligible all the other modes. For this reason, we make use of the CME to simulate the behaviour of our devices. Making use of the circuit parameters listed at the end of Sec. 4.1, we estimate a characteristic frequency of $\omega_0 = \sqrt{1/(L_{\text{meander}} + L_{g1} + L_{g1}) \cdot (C_{\text{dist}} + C_{\text{inter}})} = 156$ GHz and a plasma frequency of $\omega_J = \sqrt{1/(L_{\text{meander}} + L_{g1} + L_{g1}) \cdot (C_J)} = 112$ GHz. Plugging these numbers into the definition of dispersion relation given in (3.119) we find that the system allows real-valued wavenumbers up to ≈ 110 GHz. This gives us the possibility to use CME-5 to simulate the the device, since the highest frequency mode in this case is the 5th pump harmonic, with a frequency of 58.5 GHz. Fig. 4.26 (a) shows the evolution of the signal mode with input power -115 dBm, simulated for different input pump powers, as a function of the JTWPA length. As can be seen, the signal mode is deamplified through all the length of the TL, and this behaviour is emphasized

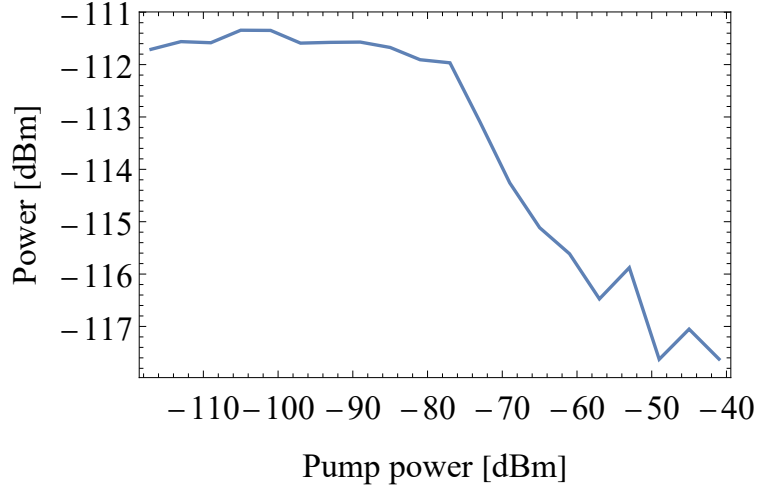


Figure 4.25: Measured signal power as a function of the pump power. The pump frequency is 11.7 GHz, while the signal tone is supplied at 6.4 GHz at about -110 dBm considered at the device input (the pump power in the x axis is considered at the device input while the signal power in the y axis at the device output).

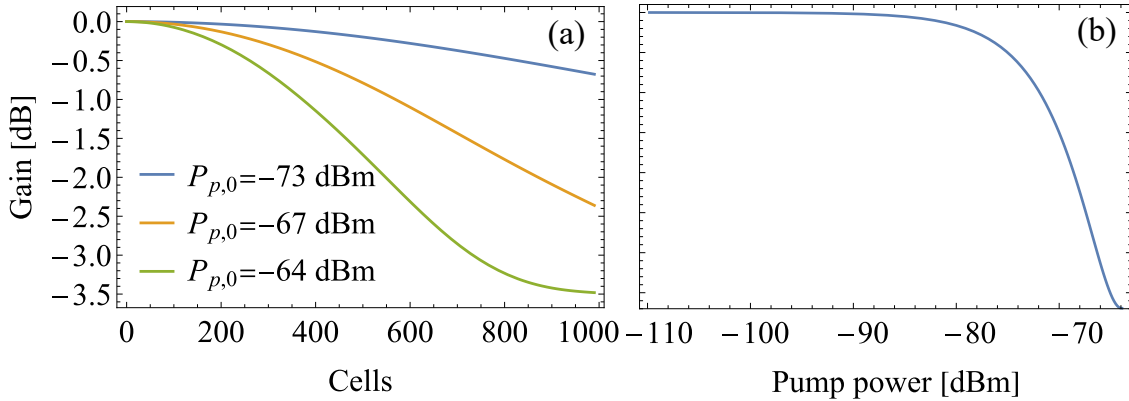


Figure 4.26: Simulations of the JTWPA with $\omega_0 = 156$ GHz and $\omega_J = 112$ GHz using CME-5 (pump frequency 11.7 GHz, signal frequency 6.4 GHz). (a) Gain simulations as a function of the length of the TL for different pump powers. (b) Gain simulation as a function of the pump power.

for higher input pump powers. This feature can be understood if one considers that many of the traveling modes present in the JTWPA require a certain amount of energy directly coming from the signal to be created (pump+signal, pump+idler, pump+pump+signal, etc.). This fact involves necessarily a deamplification of the signal in the first section of the JTWPA, that, if not properly compensated, leads

to a overall signal loss. Moreover, the generation of higher pump harmonics limits in this case the amount of energy transferred to the signal because much more energy is converted in higher frequency modes. The sum of these two effects gives the plot reported in Fig. 4.26 (b), where the signal gain for our JTWPA is plotted as a function of the input pump power. The simulated features result to be in agreement with the experimental data showing deamplification of the signal up to -3.5 dB for a pump power of -65 dBm, after this point the theoretical curve and the experimental data disagree. This last fact is probably due to higher nonlinear modes getting excited in the sample when very high RF power is supplied to the JTWPA, feature that cannot be captured by the CME approach that is limited to pure 3WM modes.

In general, the low nonlinearity given by the small value of β_L contributes as well in preventing the JTWPA from amplifying correctly. Indeed, the unavoidable signal deamplification that takes place in the first part of the JTWPA can be made shorter and even negligible with higher values of β_L , that speeds up the energy transfer between the traveling modes.

To verify the origin of the energy loss mechanism cause of the lack of amplification we measure the intensity of the pump harmonics so as to clarify if these modes can be considered negligible or not. We measure just up to the third harmonic due to limitations of the experimental setup bandwidth, mainly given by the cryogenic amplifiers and circulators. To perform this measurement we adopt a circuit very similar to the one depicted in Fig. 4.24, where this time the signal RF generator is removed together with the directional coupler, and a 30 dB attenuator is added at room temperature in series to the pump RF generator. Thus, we supply a single pump tone at 4.12 GHz, and measure the second and third harmonics, respectively at 8.24 GHz and 12.36 GHz, sweeping on the pump power. We make this measurement at two different DC bias points, where the 3WM idler is minimised (4WM bias) and where the 3WM idler is maximised (3WM bias). Fig. 4.27 shows the power of the second and third pump harmonics considered at the DUT output function of the pump power considered at the DUT input. In this picture the red curves represent the data taken in the 4WM bias while the purple curves in the 3WM bias. One can see that for low pump powers (< -100 dBm) the harmonic generation is negligible since the output stays under the noise level, then after this point, the harmonics start to grow and their power raise up to -100 dBm for an input power of -70 dBm. We notice that the behaviour of these modes is similar in both the bias conditions, besides the fact that in the 3WM bias the harmonic generation seems to be favoured with respect to the 4WM bias, since the power growth of both harmonics starts at lower pump powers. It is not surprising that the second and third harmonics have a similar behaviour both with the bias current and pump power. If we consider which process is responsible for the generation of a particular harmonic we notice that the 3WM process is responsible for both

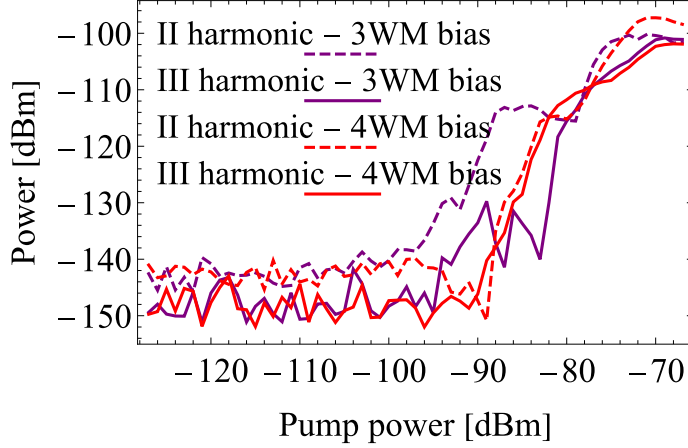


Figure 4.27: Power of the second and third harmonics generated by the JTWPA considered at the device output, as a function of the pump power (considered at the device input) in 3WM and 4WM bias points. The second harmonic is at 8.24 GHz while the third harmonic is at 12.36 GHz.

the second harmonic $\omega_{2p} = \omega_p + \omega_p$, with the sum of two pump photons, and the third harmonic generation, with the sum of a pump photon plus a second harmonic photon $\omega_{2p} = \omega_{2p} + \omega_p$. What we learn from this last measurement is that the harmonic generation is a mechanism that takes a non-negligible amount of energy from the pump tone, hence can be a serious limitation for the energy transferred to the signal that should be amplified. This result is in agreement with the power transmission measurement shown in Fig. 4.21, where we recorded a worse transmission increasing the probe power. Now we can say that this feature can be attributed to the generation of higher harmonics triggered by a high pump power.

We can draw some important conclusions from the measurements just presented. The JTWPA can be used as a reliable TL that is well matched with its electromagnetic environment and is able to transmit RF power without high attenuation under a certain level of RF power. The device presents both 4WM and 3WM phenomena, that can be easily tuned by a DC current bias passing into its signal line. The non homogeneity of the elementary cells leads to non-trivial behaviour in terms of nonlinearity tuning, for this reason, the parameter spread is a crucial aspect for a correct operation of the device. Due to the lack of high nonlinearity, and the generation of pump harmonics that drain the energy away from the signal, the JTWPA does not show signal amplification.

In order to engineer a JTWPA that presents high amplification the up-conversion

processes need to be suppressed and the rf-SQUIDs needs to be made highly nonlinear. To this end we now make use of the CME to obtain a set of circuit parameters to realise a JTWPA equipped with RPM.

4.4 Modeling JTWPA with RPM through CME

In order to model a JTWPA which introduces enough phase mismatch for the up-converted tones to be suppressed and re-phased with RPM the CME method introduced in subsection 3.2.2 is used. Just as for the device described in Sec. 3.1, we fix the working frequency band to be centered around 6 GHz, with the widest bandwidth possible. For this reason, working in a 3WM mode, the device requires to place the pump frequency, and as a consequence the resonator frequency, around 12 GHz. This choice brings the second and third pump harmonics to be at about 24 GHz and 36 GHz, hence the plasma frequency of the the rf-SQUIDs will be placed between these two harmonics. As a consequence, the highest frequency mode with real wavenumber will be the second pump harmonic, thus the system can be described using CME-2.

The plasma frequency of the JTWPA with RPM is chosen to be $\omega_J = 35.5$ GHz, hence between the second and third pump harmonics.

The screening parameter of the rf-SQUIDs is fixed at $\beta_L \approx 0.7$, which is far enough from the unity to be a fault tolerant value during the fabrication process, but still high to ensure enough nonlinearity to the device, hence an efficient wave mixing mechanism.

The characteristic frequency is set to $\omega_0 = 80$ GHz, that is high enough so as to safely sit in the continuous TL approximation, thus neglecting its discrete nature given by the cell structure.

Finally, the 50Ω characteristic impedance of the line fixes definitively the four circuit parameters of the elementary cell, which have to satisfy the above mentioned four constraints.

Given these considerations, we choose for our device the set of parameters given in Tab. A.2, hence with the dispersion relation plotted in Fig. 3.9. It can be easily seen that this set of parameters satisfy all the above mentioned constraints.

In order to find the right pump frequency that minimises the phase mismatch maximising the gain, we plot the gain of the JTWPA as a function of the pump frequency for a sample signal frequency put in the middle of the operation bandwidth, that is 6 GHz. The plot of the gain, function of the pump frequency, is given in Fig. 4.28. As can be seen, the curves, plotted for different values of the initial pump power, present a first peak at about 14.4 GHz, that corresponds to the pump re-phasing due to the RPM, and then a second rise of the gain between 16 GHz

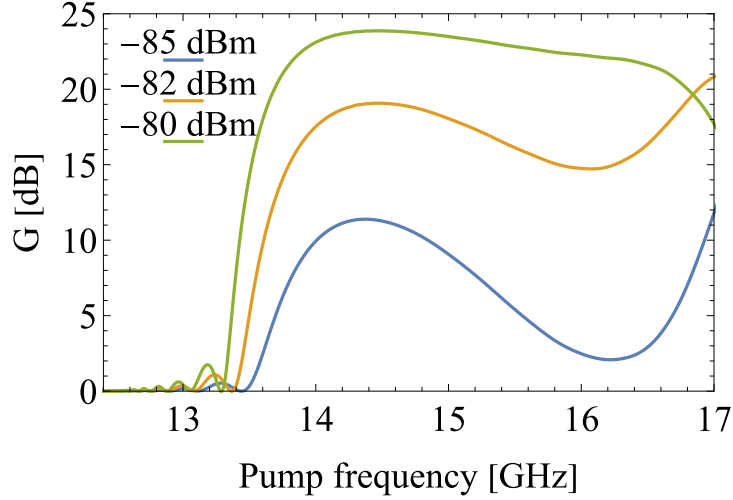


Figure 4.28: Gain of the JTWPA as a function of the pump frequency for a pump power of $P_p(0) = -85$ dBm, $P_p(0) = -82$ dBm and $P_p(0) = -80$ dBm.

and 17 GHz, which correspond to the re-phasing of the idler tone. Nonetheless this second feature seems to be more pronounced we will not take it into account in our discussions since, due to the rapid increase of the phase mismatch in this region, it doesn't allow a wide amplification bandwidth. So, if we focus on the first gain peak, we notice that, considering Fig. 3.10, it is centered at 14.4 GHz, hence where the phase mismatch curve crosses the x axes (have a zero). If we try now to plot the gain as a function of the amplifier's length for two different pump frequencies, namely 14.4 GHz and 13 GHz, we immediately understand the physical reason of the shapes of the curves in Fig. 4.28. In Fig. 4.29 one sees the gain profile, for a signal of 6 GHz, as a function of the number of nodes (hence cells) of the JTWPA for a pump frequency equal to 14.4 GHz, hence centered on the first gain peak, and for a pump frequency of 13 GHz, that is well out of the gain peak. The main difference between these two curves is that if we put the pump frequency where the phase mismatch is close to zero, hence 14.4 GHz, the growth of the signal will be exponential, eventually, like in this case, reaching a point where the pump is depleted, and cannot provide more energy for amplification. The fingerprint of this situation is the maximum of gain reached at the end of the amplifier. On the contrary, putting the pump frequency where the phase mismatch is non-negligible (13 GHz) the signal intensity oscillates with a period of about 200 nodes. This remarkable feature can be explained if one considers the coherence length of the traveling waves defined as

$$l_c = \frac{\pi}{\Delta k(\omega_p, \omega_s)} \quad (4.17)$$

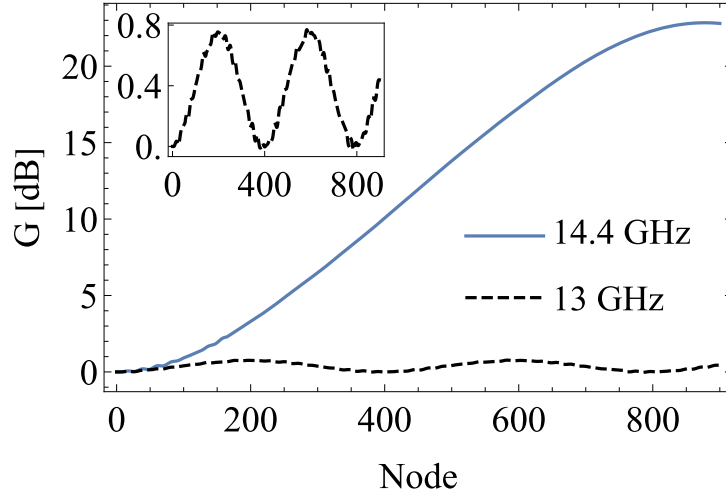


Figure 4.29: Gain profile as a function of the amplifier’s length calculated for a pump frequency of 13 GHz and 4.4 GHz. The inset shows a zoom of the curve calculated for a pump frequency of 13 GHz. The input pump power is $P_p(0) = -81$ dBm while the input signal power is $P_p(0) = -107$ dBm

where $\Delta k(\omega_p, \omega_s)$ is the phase mismatch in 3WM defined in Eq. (3.120). This characteristic length defines the spatial length in the JTWPA for which the traveling waves are in phase between each other. The inset in Fig. 4.29 shows a zoom of the gain profile with the pump frequency set in a high phase mismatch point, and in this plot one can observe that there actually is an initial exponential growth of the signal power, that, on the contrary of the negligible phase mismatched case, ends around the 180 node. This is due to the fact that the coherence length of the device we are simulating, calculated for a signal frequency of 6 GHz and a pump frequency of 13 GHz, is $l_c \approx 178$ node, meaning that the exponential growth must end after this length. If now we consider the coherence length of the traveling tones for frequencies of $\omega_p = 14.4$ GHz and $\omega_s = 6$ GHz we find $l_c \approx 3000$, much longer than the amplifier’s length, meaning that the phase coherence will hold for all the length of the device.

To estimate the bandwidth of our device we now calculate the gain sweeping on the signal frequency, plotting in Fig 4.30 the curves for different input pump powers and an input signal power of $P_p(0) = -107$ dBm. The plots show a clear dependence of the maximum gain on the input pump power, starting from a minimum value of 10 dB for the lowest pump power reaching about 23 dB for the highest pump value. The bandwidth shown by these curves goes from about 5 GHz for low pump powers to a maximum of 6 GHz for high pump values. In the same figure one can see the bandwidth of the same JTWPA without any re-phasing technique, in this case without the presence of a resonator in the cell, of which the corresponding

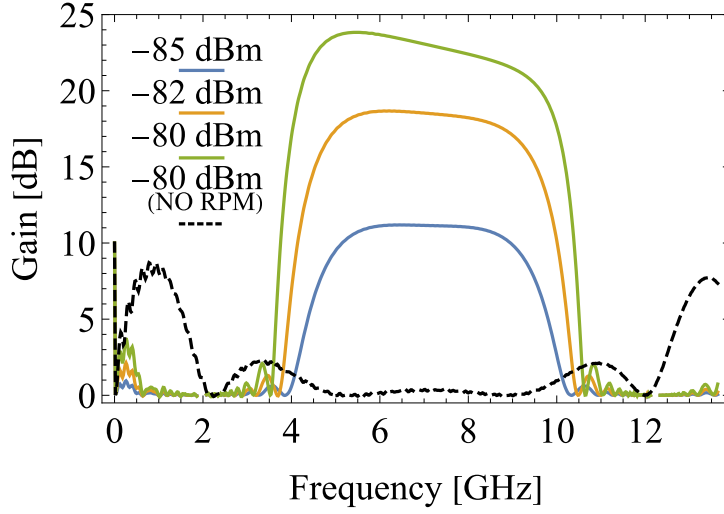


Figure 4.30: Numerical simulation of the gain of a JTWPA with RPM for different pump powers as a function of the signal frequency. The pump frequency is 14.4 GHz for all the curves and the black dashed curve is calculated for a JTWPA without RPM.

phase mismatch can be seen in Fig. (3.10), represented by the black dashed curve. The shape of this bandwidth curve is pretty clear if one looks at it together with its corresponding phase mismatch, indeed where the gain is high, hence for very low and very high frequencies, the phase mismatch is low, because respectively the idler and signal tones are very close in frequency with the pump, hence making in these narrow windows the overall phase mismatch negligible.

The simulations performed in this section tell us that the set of parameters (Tab. A.2) chosen for the realisation of our JTWPA with RPM could in principle lead to an amplifier with an average gain of 20 dB over 6 GHz of bandwidth, capable of amplify very tiny signals using low pump powers.

4.5 Layout definition of JTWPA with RPM through electromagnetic simulations

The CME approach helped us finding a set of circuit parameters that could give high gain and wide bandwidth to the JTWPA. In this section we perform some electromagnetic simulations to define the physical layout of the circuit components that compose the device, paying particular attention to the impedance matching of the TL. The stackup used for all the simulations is the same described in the introductory part of section 4.2, so refer to this paragraph for more information.

4.5.1 Resonator

We start by defining the geometry of the shunt resonator capacitively coupled to the signal line used to open the band gap in the dispersion relation of our TL (the reader can refer to Fig. 3.8 for a schematic of the circuit). Fig. 4.31 shows the lumped element geometry chosen for the resonator, composed by a meander inductor (L_r) that has a distributed capacitance to ground given by a couple of interdigitated capacitors (C_r) that enter into the meander bends. The coupling capacitance (C_c) is an interdigitated capacitor that has one of the two faces directly leant on the signal line of a CPW. To find the resonance frequency of the resonator we place the excitation ports at the two ends of the signal line and simulate its transmission. Fig. 4.31 shows the result of the S21 simulation. The plot highlights

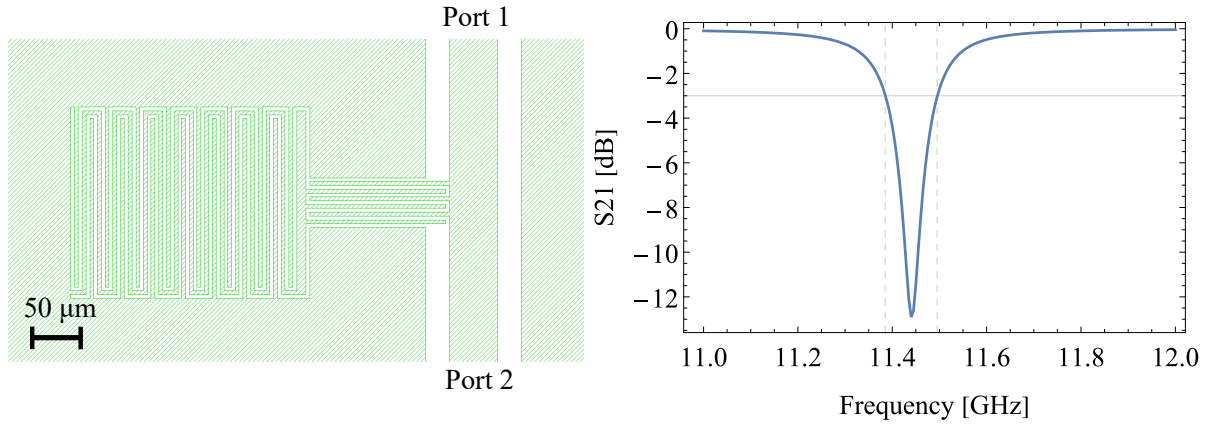


Figure 4.31: Left: layout of the resonator capacitively coupled to a CPW used for the simulations. Right: S21 scattering parameter simulated between Port 1 and Port 2 of the layout on the left. The dashed vertical lines indicate the frequencies at the -3 dB point, indicated by the horizontal solid line.

a dip in the transmission with central frequency at 11.44 GHz and the -3 dB points at 11.385 GHz and 11.495 GHz.

Engineering a resonator with the right quality factor is of fundamental importance when projecting a JTWPA with RPM. Indeed it has been shown in some recent works [32] through a SPICE simulation approach that when dealing with statistical spread of the Josephson critical currents a wider resonance dip can help recovering phase matching by avoiding a too strict constraint on the pump frequency choice. It has been shown that a random spread of the Josephson critical currents of about the 5%, that is a reasonable experimental requirement, can be recovered by shunt resonators with $Q \approx 100$. Choosing this value as the goal for our resonators we

now estimate the quality factor and find

$$Q = \frac{f_0}{\Delta f_0} \approx 104 \quad (4.18)$$

4.5.2 L_g

The approach for the layout definition of L_g is similar to the one adopted in section 4.2. Given a goal value of $L_g = 120$ pH, we have to estimate separately the inductive contributions of L_{meander} , L_{g1} and L_{g2} which together give L_g . From Fig. 4.32 and 4.33 we find that $L_{\text{meander}} = 86.2$ pH and $L_{g1} + L_{g2} = 34.3$ pH, which together give $L_g = 86.2$ pH + 34.3 pH = 120.7 pH.

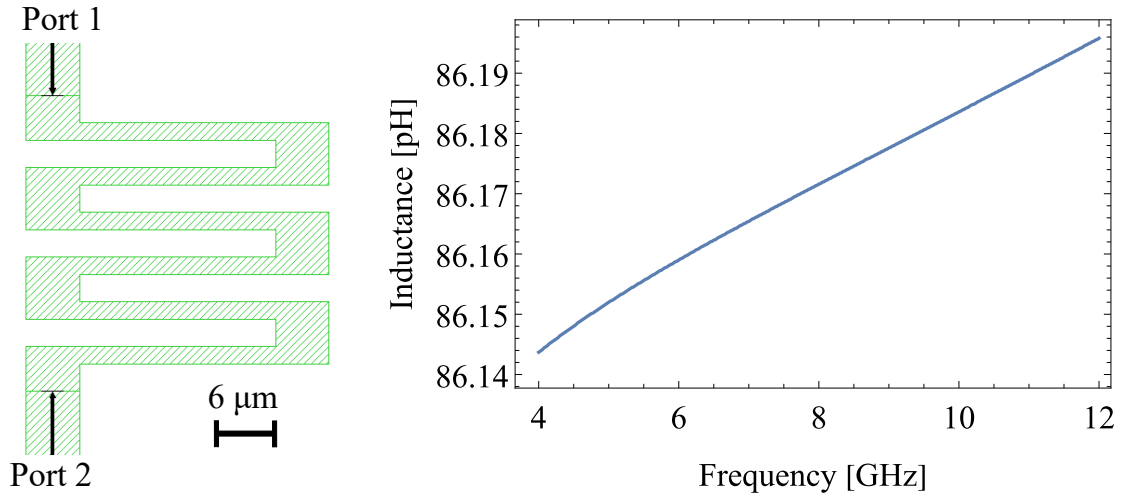


Figure 4.32: Left: layout of L_{meander} . Right: inductance simulated between Port 1 and Port 2.

4.5.3 L_J and C_J

We take into account the electromagnetic contribution of the JJ the same way we did in Subsec. 4.2.5. Referring to Eq. (2.96), we see that a Josephson junction with critical current $I_c = 2$ μA biased in a 3WM working point corresponds to an inductance again much higher than L_{meander} , say again $L_J \approx 400$ pH. This contribution can be taken into account by defining a custom metal with a sheet inductance such that its enclosure in the TL circuit mimics the electromagnetic behaviour of the JJ in the rf-SQUID at the working point. The piece of custom metal has sheet inductance $L_{\square} = 400$ pH/sq, and this piece of metal will be inserted in the Josephson feedline in the complete layout.

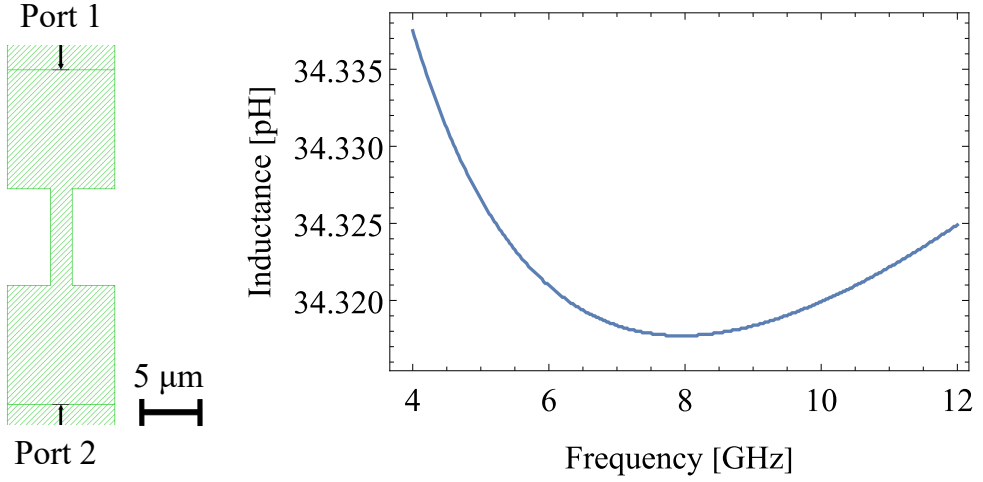


Figure 4.33: Left: layout of $L_{g1} + L_{g2}$. Right: inductance simulated between Port 1 and Port 2.

The Josephson intrinsic capacitance C_J is taken into account by placing a lumped element ideal capacitor between the two leads of the JJ. Given the simulations performed in Sec. 4.4, of which the set of parameters is listed in A.2, the value for this component is taken as $C_J = 200$ fF.

4.5.4 Characteristic impedance

We implement the impedance matching of the JTWPA to 50Ω through the parametric sweep method illustrated at the end of subsection 4.2.6. For this purpose we draw the layout shown in Fig. 4.34. The simulation is performed considering a series of four rf-SQUIDs with their respectively ground capacitors together with a single resonator instead of one each rf-SQUID. This choice has been made to reduce the complexity of the circuit since it has been calculated [32] that one resonator each four rf-SQUIDs is enough to rephase the traveling waves in the signal line. The simulation in Fig. 4.34 shows a maximum of S21 for $\text{Grd} = 68\mu\text{m}$.

4.5.5 Cutoff

Given the results in the previous sections we can define the final cells layout of the JTWPA equipped with RPM with a 50Ω characteristic impedance. In section 4.4 we explained how the choice of the characteristic frequencies of the TL ω_0 and ω_J are of great importance for proper operation of the RPM technique. For this reason it is an important benchmark for the definition of the layout a wide

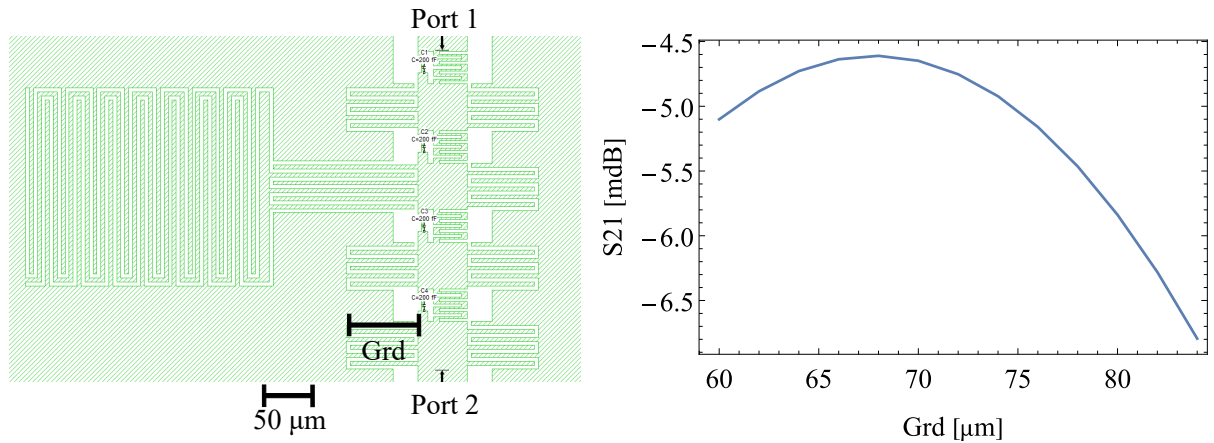


Figure 4.34: Left: layout of a cluster formed by 4 elementary cells plus 1 resonator. Right: parametric simulation of the S21 scattering parameter as a function of the length of the interdigitated capacitance fingers "Grd".

range frequency simulation that catches the behaviour of the device at higher frequencies, where unwanted harmonics are generated. Fig. 4.35 shows the S11 and

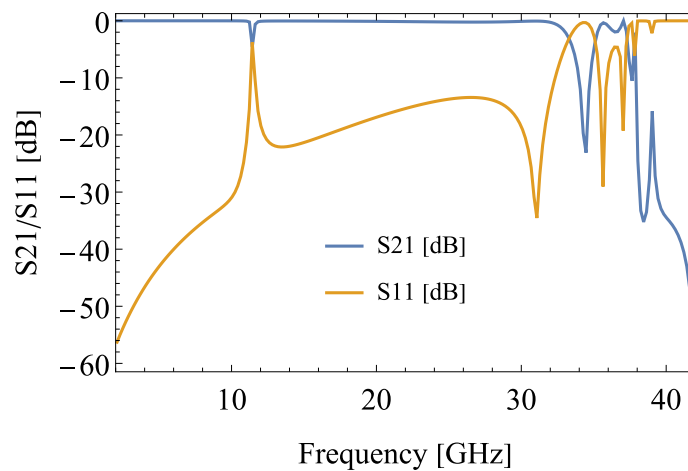


Figure 4.35: Simulation of the S11 and S21 scattering parameters for the JTWPA equipped with RPM with a $50\ \Omega$ characteristic impedance between 2 GHz and 42 GHz.

S21 scattering parameters simulation of the JTWPA $50\ \Omega$ matched layout between 2 GHz and 42 GHz. Analyzing these spectra we can draw some important conclusions about the TL just modeled. At low frequencies (< 12 GHz) the TL presents a good transmission with an S21 parameter close to 0 dB. At about 12 GHz the

spectra show a peak of reflection given by the activation of the resonator that locally greatly modify the characteristic impedance of the line. The transmission has a sudden drop around 32 GHz and after some oscillations goes to -60 dB, meaning that the TL does not carry any signal from this point on. The sudden drop in the transmission is the footprint of the cutoff frequency, hence the frequency from which the TL is not able to carry signals anymore. Following the CME approach this frequency should be between the second and the third pump harmonics, hence around 35 GHz, that is pretty close to the value just found in Fig. 4.35.

Chapter 5

Conclusions and perspectives

In this thesis we showed the theoretical description, engineering, realisation and characterisation of a JTWPA.

In this process, we developed a quantum mechanical approach through c-QED techniques in order to obtain a description of the JTWPA at the single photon level. This approach allowed us to describe the JTWPA in both 3WM and 4WM regimes, calculating important figures of merit like coupling constants, gain and noise, studied as a function of the device's constructive parameters.

The quantum theoretical description together with a wide use of electromagnetic simulations allowed to define first a set of circuit parameter and then a physical layout of a JTWPA, that was consequently realised and characterised in a cryogenic microwave setup. The realisation of a JTWPA required a precise calibration of the JJs fabrication process, which moreover requires a high yield.

The cryogenic characterisation of the produced JTWPA showed the clear presence of wave mixing both in a 3WM and 4WM fashion, together with a precise control of the nonlinearities through an external control parameter like a DC current bias. Nonetheless, the characterised JTWPA did not show high gain and wide bandwidth as expected.

The reason for such deviation from the expected behaviour of the JTWPA lies in the restrictive hypothesis used to write the analytic quantum model. Indeed, the quantum description does not take into account some non-negligible effects like higher harmonics generation and phase mismatch between the traveling modes that change the overall dynamics of the device.

For this reason we developed a modified version of the JTWPA, including a so called Resonant-Phase Matching technique. This modification, that practically consists in periodically loading the TL with shunt LC resonator, allows to greatly reduce the phase mismatch issue by modifying the dispersion relation of the device. This solution needed the development of a new theoretical approach able to describe the new dynamics of the system. To this end we developed a modified version of a classical numerical approach, known as Coupled Mode Equations. This method takes

into account the modified dispersion relation and generation of higher harmonics, allowing to study the JTWPA as a function of its circuit parameters.

The latter gave us a new set of circuit parameters, able in theory to provide a JTWPA with modified dispersion relation through RPM technique. We finally engineer through electromagnetic simulations a physical layout of the new device, that respects all the constraints given by the physics of the problem.

There are several directions towards future works can go to, but we would restrict the paths mainly to two main topics, that are the ones covered in this thesis. The first direction regards the extension of the quantum model to physical systems with high chromatic dispersion. It is indeed true that it would be almost straightforward to modify the dispersion relation of the analytic model described in Chapter 3 taking into account the effect of the resonators used in the RPM technique (Eq. (3.118)). Nonetheless, the use of RPM and the addition of high chromatic dispersion would place the whole system out of the approximation made with Eq. (3.33), making necessary to evaluate differently many terms in the Hamiltonian. This extension could by the way be of a certain interest, since in this regime the 3-wave description would be valid given the suppression of higher frequency modes, and the JTWPA equipped with RPM could become a reliable platform to study the generation and manipulation of quantum states starting from an exact Hamiltonian description.

The second path is clearly the fabrication and testing of the JTWPA equipped with RPM of which a physical layout has been developed in Sec. 4.5. This work would be of great interest since it could prove experimentally the validity of the numerical model and electromagnetic simulation approach developed, providing a platform for cryogenic single photon microwave in the quantum regime.

Appendix A

Tables of circuital parameter sets

In the following one can find the sets of parameters used for the computations in the Quantum Mechanical case [A.1](#) and in the Couple Mode Equation case [A.2](#).

Parameter	Value	Description
I_c	2 μ A	Josephson critical current
C_g	58 fF	Ground capacitance
L_g	100 pH	Geometrical inductance
C_J	40 fF	Josephson capacitance
a	60 μ m	Unit cell length
N	900	Number of unit cells
ω_p	$2\pi \cdot 12$ GHz	Pump frequency
ω_s	$2\pi \cdot 7$ GHz	Signal frequency
ω_i	$2\pi \cdot 5$ GHz	3WM idler frequency
ω_j	$2\pi \cdot 17$ GHz	4WM idler frequency
$\Delta\Phi_{DC,3WM}/\Phi_0$	0.335	3WM working point
$\Delta\Phi_{DC,4WM}/\Phi_0$	0.50	4WM working point

Table A.1: Circuit parameters and magnetic field flux bias (working points) used for numerical evaluations in the Quantum Mechanical approach.

Parameter	Value	Description
I_c	2 μ A	Josephson critical current
C_g	40 fF	Ground capacitance
L_g	120 pH	Geometrical inductance
C_J	200 fF	Josephson capacitance
a	60 μ m	Unit cell length
N	900	Number of unit cells
C_c	30 fF	Resonator coupling capacitance
C_r	1 pF	Resonator capacitance
L_r	172.5 pH	Resonator inductance

Table A.2: Circuit parameters used for numerical evaluations in the CME approach.

Appendix B

Curly brackets operators algebra and time derivatives

In order to simplify the notation during the derivation of the Hamiltonian in the second quantization framework we can define the curly brackets operator

$$\{\hat{a} + \hat{a}^\dagger\}_{n,l} \equiv (\hat{a}_n + \hat{a}_n^\dagger)(\hat{a}_l + \hat{a}_l^\dagger) \quad (\text{B.1})$$

This definition can be easily extended to an arbitrary number of indexes as

$$\{\hat{a} + \hat{a}^\dagger\}_{n,l,m,\dots} \equiv (\hat{a}_n + \hat{a}_n^\dagger)(\hat{a}_l + \hat{a}_l^\dagger)(\hat{a}_m + \hat{a}_m^\dagger)\dots$$

Using the usual bosonic commutation relations

$$[\hat{a}_n, \hat{a}_l] = \hat{a}_n \hat{a}_l - \hat{a}_l \hat{a}_n = 0 \quad (\text{B.2})$$

$$[\hat{a}_n^\dagger, \hat{a}_l^\dagger] = \hat{a}_n^\dagger \hat{a}_l^\dagger - \hat{a}_l^\dagger \hat{a}_n^\dagger = 0 \quad (\text{B.3})$$

$$[\hat{a}_n, \hat{a}_l^\dagger] = \hat{a}_n \hat{a}_l^\dagger - \hat{a}_l^\dagger \hat{a}_n = \delta_{n,l} \quad (\text{B.4})$$

we can demonstrate the commutative property of the curly bracket operators. For a double index operator

$$\begin{aligned} \{\hat{a} + \hat{a}^\dagger\}_{n,l} &= (\hat{a}_n + \hat{a}_n^\dagger)(\hat{a}_l + \hat{a}_l^\dagger) = \hat{a}_n \hat{a}_l + \hat{a}_n \hat{a}_l^\dagger + \hat{a}_n^\dagger \hat{a}_l + \hat{a}_n^\dagger \hat{a}_l^\dagger = \\ &= \hat{a}_l \hat{a}_n + (\delta_{n,l} + \hat{a}_l^\dagger \hat{a}_n) + (-\delta_{n,l} + \hat{a}_l \hat{a}_n^\dagger) + \hat{a}_l^\dagger \hat{a}_n^\dagger = \\ &= \hat{a}_l \hat{a}_n + \hat{a}_l^\dagger \hat{a}_n + \hat{a}_l \hat{a}_n^\dagger + \hat{a}_l^\dagger \hat{a}_n^\dagger = (\hat{a}_l + \hat{a}_l^\dagger)(\hat{a}_n + \hat{a}_n^\dagger) = \{\hat{a} + \hat{a}^\dagger\}_{l,n} \end{aligned} \quad (\text{B.5})$$

This property can be easily generalized to the case of a curly brackets operator with more than two indexes. For instance, for a three-index operator

$$\{\hat{a} + \hat{a}^\dagger\}_{l,m,n} = (\hat{a}_l + \hat{a}_l^\dagger) \{\hat{a} + \hat{a}^\dagger\}_{m,n} = (\hat{a}_l + \hat{a}_l^\dagger) \{\hat{a} + \hat{a}^\dagger\}_{n,m} = \{\hat{a} + \hat{a}^\dagger\}_{l,n,m} \quad (\text{B.6})$$

and, with the same approach, we can demonstrate the equivalence for any index commutation. Furthermore, again with the intent of simplify the notation, we can define the quantities $\Delta\omega_{n,l,m,s,\dots}$ and $\Delta k_{n,l,m,s,\dots}$ as

$$\Delta\omega_{n,l,m,s,\dots} = \pm\omega_n \pm \omega_l \pm \omega_m \pm \omega_s \pm \dots \quad \text{and} \quad (\text{B.7})$$

$$\Delta k_{n,l,m,s,\dots} = \pm k_n \pm k_l \pm k_m \pm k_s \pm \dots \quad (\text{B.8})$$

where the sign is determined by the combination of creation and annihilation operators that precede this quantity. For instance, we can compact the following product of three terms as

$$\begin{aligned} & \left(\hat{a}_n^\dagger e^{-i(k_n z - \omega_n t)} \right) \cdot \left(\hat{a}_l e^{i(k_l z - \omega_l t)} \right) \cdot \left(\hat{a}_m^\dagger e^{-i(k_m z - \omega_m t)} \right) = \\ & \hat{a}_n^\dagger \hat{a}_l \hat{a}_m^\dagger e^{i[(-k_n + k_l - k_m)z - (-\omega_n + \omega_l - \omega_m)t]} = \hat{a}_n^\dagger \hat{a}_l \hat{a}_m^\dagger e^{i(\Delta k_{n,l,m} z - \Delta\omega_{n,l,m} t)} \end{aligned} \quad (\text{B.9})$$

where, in this specific case $\Delta k_{n,l,m} = -k_n + k_l - k_m$ and $\Delta\omega_{n,l,m} = -\omega_n + \omega_l - \omega_m$. Hence, in Eqs. (B.7) and (B.8) we take a plus sign if the index is related to an annihilation operator (i.e., $a_i \rightarrow +\omega_i, +k_i$), while we take a minus sign if the index is related to a creation operator (i.e., $a_i^\dagger \rightarrow -\omega_i, -k_i$)

Exploiting these compact notations in the case of a single index, we can write $\delta\hat{\Phi}_n^{(0)}$ (whose expression is given in Eq. (3.24)) as

$$\begin{aligned} \delta\Phi_n^{(0)} & \equiv c_n \left(\hat{a}_n e^{i(k_n z - \omega_n t)} + \hat{a}_n^\dagger e^{-i(k_n z - \omega_n t)} \right) \\ & = c_n \left\{ \hat{a} + \hat{a}^\dagger \right\}_n e^{i(\Delta k_n z - \Delta\omega_n t)} \end{aligned}$$

In terms of this formalism, under the *slowly variant operator* assumption (i.e., $\partial\hat{a}_n^{(\dagger)}/\partial t \approx 0$ and $\partial\hat{a}_n^{(\dagger)}/\partial z \approx 0$) we can express:

$$\begin{aligned} \frac{\partial}{\partial z} [\delta\Phi^{(0)}] & = \frac{\partial}{\partial z} \left[\sum_n \delta\Phi_n^{(0)} \right] = \sum_n \frac{\partial}{\partial z} [\delta\phi_n^{(0)}] = \\ & = \sum_n \frac{\partial}{\partial z} \left[c_n \left(\hat{a}_n e^{i(k_n z - \omega_n t)} + \hat{a}_n^\dagger e^{-i(k_n z - \omega_n t)} \right) \right] = \\ & = \sum_n c_n \left[\hat{a}_n (ik_n) e^{i(k_n z - \omega_n t)} + \hat{a}_n^\dagger (-ik_n) e^{-i(k_n z - \omega_n t)} \right] = \\ & = \sum_n ic_n \Delta k_n \left\{ a + a^\dagger \right\}_n e^{i(\Delta k_n z - \Delta\omega_n t)} = \sum_n i\Delta k_n \delta\Phi_n^{(0)} \end{aligned} \quad (\text{B.11})$$

and, similarly,

$$\frac{\partial^2}{\partial z^2} [\delta\Phi^{(0)}] = - \sum_n c_n (\Delta k_n)^2 \left\{ a + a^\dagger \right\}_n e^{i(\Delta k_n z - \Delta\omega_n t)} = - \sum_n (\Delta k_n)^2 \delta\Phi_n^{(0)} \quad (\text{B.12})$$

$$\frac{\partial}{\partial t} [\delta\Phi^{(0)}] = - \sum_n ic_n \Delta\omega_n \left\{ a + a^\dagger \right\}_n e^{i(\Delta k_n z - \Delta\omega_n t)} = - \sum_n i\Delta\omega_n \delta\Phi_n^{(0)} \quad (\text{B.13})$$

$$\frac{\partial^2}{\partial t^2} [\delta\Phi^{(0)}] = - \sum_n c_n (\Delta\omega_n)^2 \left\{ a + a^\dagger \right\}_n e^{i(\Delta k_n z - \Delta\omega_n t)} = - \sum_n (\Delta\omega_n)^2 \delta\Phi_n^{(0)} \quad (\text{B.14})$$

Appendix C

\hat{H}_N vs. $\delta\Phi$ in the second quantization regime

This appendix is devoted to the explicit calculation of the terms composing the second quantization Hamiltonian. We start calculating the second and the third power of $\delta\hat{\Phi}$, truncating them to the fourth power in $\delta\hat{\Phi}_i^{(0)}$. This choice limit our treatment to the investigations of scattering phenomena that involve at most four photons.

$$\begin{aligned} (\delta\hat{\Phi})^2 &= \left(\sum_n \left[q_{0,n} + q_{1,n} \left(\delta\hat{\Phi}^{(0)} \right) + q_{2,n} \left(\delta\hat{\Phi}^{(0)} \right)^2 + q_{3,n} \left(\delta\hat{\Phi}^{(0)} \right)^3 \right] \delta\hat{\Phi}_n^{(0)} \right) \cdot \\ &\cdot \left(\sum_l \left[q_{0,l} + q_{1,l} \left(\delta\hat{\Phi}^{(0)} \right) + q_{2,l} \left(\delta\hat{\Phi}^{(0)} \right)^2 + q_{3,l} \left(\delta\hat{\Phi}^{(0)} \right)^3 \right] \delta\hat{\Phi}_l^{(0)} \right) = \\ &= \sum_{n,l} \left[q_{0,n}q_{0,l} + (q_{0,n}q_{1,l} + q_{1,n}q_{0,l}) \left(\delta\hat{\Phi}^{(0)} \right) + \right. \\ &\quad \left. + (q_{0,n}q_{2,l} + q_{1,l}q_{1,n} + q_{2,n}q_{0,l}) \left(\delta\hat{\Phi}^{(0)} \right)^2 + \right. \\ &\quad \left. + (q_{0,n}q_{3,l} + q_{1,n}q_{2,l} + q_{2,n}q_{1,l} + q_{3,n}q_{0,l}) \left(\delta\hat{\Phi}^{(0)} \right)^3 \right] \delta\hat{\Phi}_n^{(0)} \delta\hat{\Phi}_l^{(0)} \quad (\text{C.1}) \end{aligned}$$

and, exploiting the definition $\delta\Phi^{(0)} = \sum_m \delta\Phi_m^{(0)}$ and Eq. (3.24), Eq. (C.1) can be written as

$$\begin{aligned}
 (\delta\hat{\Phi})^2 &= \sum_{n,l} \left[q_{0,n}q_{0,l} + (q_{0,n}q_{1,l} + q_{1,n}q_{0,l}) \left(\sum_m \delta\Phi_m^{(0)} \right) + \right. \\
 &\quad \left. + (q_{0,n}q_{2,l} + q_{1,l}q_{1,n} + q_{2,n}q_{0,l}) \left(\sum_{m,s} \delta\Phi_m^{(0)} \delta\Phi_s^{(0)} \right) \right] \delta\Phi_n^{(0)} \delta\Phi_l^{(0)} = \\
 &= \sum_{n,l} \left[q_{0,n}q_{0,l} c_n c_l \left\{ \hat{a} + \hat{a}^\dagger \right\}_{n,l} e^{i(\Delta k_{n,l} z - \Delta\omega_{n,l} z)} \right] + \\
 &+ \sum_{n,l,m} \left[(q_{0,n}q_{1,l} + q_{1,n}q_{0,l}) c_n c_l c_m \left\{ \hat{a} + \hat{a}^\dagger \right\}_{n,l,m} e^{i(\Delta k_{n,l,m} z - \Delta\omega_{n,l,m} z)} \right] + \\
 &+ \sum_{n,l,m,s} \left[(q_{0,n}q_{2,l} + q_{1,l}q_{1,n} + q_{2,n}q_{0,l}) c_n c_l c_m c_s \left\{ \hat{a} + \hat{a}^\dagger \right\}_{n,l,m,s} e^{i(\Delta k_{n,l,m,s} z - \Delta\omega_{n,l,m,s} z)} \right]
 \end{aligned} \tag{C.2}$$

Exploiting the commutativity of both the coefficients q and of the curly brackets operator we can reduce Eq. (C.2) to

$$\begin{aligned}
 (\delta\hat{\Phi})^2 &= \sum_{n,l} \left[q_{0,n}q_{0,l} + (q_{0,n}q_{1,l} + q_{1,n}q_{0,l}) \left(\sum_m \delta\Phi_m^{(0)} \right) + \right. \\
 &\quad \left. + (q_{0,n}q_{2,l} + q_{1,l}q_{1,n} + q_{2,n}q_{0,l}) \left(\sum_{m,s} \delta\Phi_m^{(0)} \delta\Phi_s^{(0)} \right) \right] \delta\Phi_n^{(0)} \delta\Phi_l^{(0)} = \\
 &= \sum_{n,l} \left[q_{0,n}q_{0,l} c_n c_l \left\{ \hat{a} + \hat{a}^\dagger \right\}_{n,l} e^{i(\Delta k_{n,l} z - \Delta\omega_{n,l} z)} \right] + \\
 &+ \sum_{n,l,m} \left[2 q_{0,n}q_{1,l} c_n c_l c_m \left\{ \hat{a} + \hat{a}^\dagger \right\}_{n,l,m} e^{i(\Delta k_{n,l,m} z - \Delta\omega_{n,l,m} z)} \right] + \\
 &+ \sum_{n,l,m,s} \left[(2 q_{0,n}q_{2,l} + q_{1,l}q_{1,n}) c_n c_l c_m c_s \left\{ \hat{a} + \hat{a}^\dagger \right\}_{n,l,m,s} e^{i(\Delta k_{n,l,m,s} z - \Delta\omega_{n,l,m,s} z)} \right]
 \end{aligned} \tag{C.3}$$

For what the third power of $\delta\Phi$ is concerning, exploiting Eq. (C.1):

$$\begin{aligned}
 (\delta\hat{\Phi})^3 &= (\delta\hat{\Phi}) \cdot (\delta\hat{\Phi})^2 = \\
 &= \left(\sum_n \left[q_{0,n} + q_{1,n} \left(\delta\hat{\Phi}^{(0)} \right) + q_{2,n} \left(\delta\hat{\Phi}^{(0)} \right)^2 + q_{3,n} \left(\delta\hat{\Phi}^{(0)} \right)^3 \right] \delta\hat{\Phi}_n^{(0)} \right) \cdot \\
 &\quad \cdot \left(\sum_{l,m} \left[q_{0,l}q_{0,m} + (q_{0,l}q_{1,m} + q_{1,l}q_{0,m}) \left(\delta\hat{\Phi}^{(0)} \right) + \right. \right. \\
 &\quad \left. \left. + (q_{0,l}q_{2,m} + q_{1,l}q_{1,m} + q_{2,l}q_{0,m}) \left(\delta\hat{\Phi}^{(0)} \right)^2 \right] \delta\hat{\Phi}_l^{(0)} \delta\hat{\Phi}_m^{(0)} \right) = \\
 &= \sum_{n,l,m} \left[q_{0,n}q_{0,l}q_{0,m} + (q_{1,n}q_{0,l}q_{0,m} + q_{0,n}(q_{0,l}q_{1,m} + q_{1,l}q_{0,m})) \left(\delta\hat{\Phi}^{(0)} \right) \right] \delta\hat{\Phi}_n^{(0)} \delta\hat{\Phi}_l^{(0)} \delta\hat{\Phi}_m^{(0)} = \\
 &= \sum_{n,l,m} \left[q_{0,n}q_{0,l}q_{0,m} + (q_{1,n}q_{0,l}q_{0,m} + q_{0,n}(q_{0,l}q_{1,m} + q_{1,l}q_{0,m})) \left(\sum_s \delta\hat{\Phi}_s^{(0)} \right) \right] \delta\hat{\Phi}_n^{(0)} \delta\hat{\Phi}_l^{(0)} \delta\hat{\Phi}_m^{(0)} \\
 &\hspace{15em} \text{(C.4)}
 \end{aligned}$$

exploiting Eq.(3.24), Eq. (C.4) can be written as

$$\begin{aligned}
 (\delta\hat{\Phi})^3 &= \sum_{n,l,m} \left[q_{0,n}q_{0,l}q_{0,m} c_n c_l c_m \left\{ \hat{a} + \hat{a}^\dagger \right\}_{n,l,m} e^{i(\Delta k_{n,l,m} z - \Delta\omega_{n,l,m} t)} \right] + \\
 &\quad + \sum_{n,l,m,s} \left[(q_{1,n}q_{0,l}q_{0,m} + q_{0,n}q_{0,l}q_{1,m} + q_{0,n}q_{1,l}q_{0,m}) c_n c_l c_m c_s \left\{ \hat{a} + \hat{a}^\dagger \right\}_{n,l,m,s} \right. \\
 &\quad \left. \cdot e^{i(\Delta k_{n,l,m,s} z - \Delta\omega_{n,l,m,s} t)} \right] \hspace{10em} \text{(C.5)}
 \end{aligned}$$

This time again, exploiting the commutativity of both the coefficients q and the curly brackets operators, we can write Eq. (C.4) as

$$\begin{aligned}
 (\delta\hat{\Phi})^3 &= \sum_{n,l,m} \left[q_{0,n}q_{0,l}q_{0,m} c_n c_l c_m \left\{ \hat{a} + \hat{a}^\dagger \right\}_{n,l,m} e^{i(\Delta k_{n,l,m} z - \Delta\omega_{n,l,m} t)} \right] + \\
 &\quad + \sum_{n,l,m,s} \left[3 q_{1,n}q_{0,l}q_{0,m} c_n c_l c_m c_s \left\{ \hat{a} + \hat{a}^\dagger \right\}_{n,l,m,s} e^{i(\Delta k_{n,l,m,s} z - \Delta\omega_{n,l,m,s} t)} \right] \hspace{2em} \text{(C.6)}
 \end{aligned}$$

For what the fourth power of $\delta\Phi$ is concerning, exploiting Eq. (C.4):

$$\begin{aligned}
 (\delta\hat{\Phi})^4 &= (\delta\hat{\Phi}) \cdot (\delta\hat{\Phi})^3 = \\
 &= \left(\sum_s \left[q_{0,s} + q_{1,s} \left(\delta\hat{\Phi}^{(0)} \right) + q_{2,s} \left(\delta\hat{\Phi}^{(0)} \right)^2 + q_{3,s} \left(\delta\hat{\Phi}^{(0)} \right)^3 \right] \delta\hat{\Phi}_s^{(0)} \right) \cdot \\
 &\quad \cdot \left(\sum_{n,l,m} \left[q_{0,n}q_{0,l}q_{0,m} + (q_{1,n}q_{0,l}q_{0,m} + q_{0,n}(q_{0,l}q_{1,m} + q_{1,l}q_{0,m})) \right] \left(\sum_o \delta\Phi_o^{(0)} \right) \right) \delta\Phi_n^{(0)} \delta\Phi_l^{(0)} \delta\Phi_m^{(0)} = \\
 &= \sum_{n,l,m,s} q_{0,n}q_{0,l}q_{0,m}q_{0,s} \delta\Phi_n^{(0)} \delta\Phi_l^{(0)} \delta\Phi_m^{(0)} \delta\Phi_s^{(0)} \tag{C.7}
 \end{aligned}$$

This time again, exploiting the curly brackets operators, we can write Eq. (C.7) as

$$(\delta\hat{\Phi})^4 = \sum_{n,l,m,s} \left[q_{0,n}q_{0,l}q_{0,m}q_{0,s} c_n c_l c_m c_s \left\{ \hat{a} + \hat{a}^\dagger \right\}_{n,l,m,s} e^{i(\Delta k_{n,l,m,s} z - \Delta \omega_{n,l,m,s} t)} \right] \tag{C.8}$$

We can now calculate the time derivative of $\delta\hat{\Phi}$, starting from its approximate form given in Eq. (3.26):

$$\begin{aligned}
 \frac{\partial}{\partial t} [\delta\hat{\Phi}] &= \frac{\partial}{\partial t} \left[\sum_n \left[q_{0,n} + q_{1,n} \left(\delta\hat{\Phi}^{(0)} \right) + q_{2,n} \left(\delta\hat{\Phi}^{(0)} \right)^2 + q_{3,n} \left(\delta\hat{\Phi}^{(0)} \right)^3 \right] \delta\hat{\Phi}_n^{(0)} \right] = \\
 &= \sum_n \left[q_{1,n} \frac{\partial}{\partial t} \left[\delta\hat{\Phi}^{(0)} \right] + 2q_{2,n} \left(\delta\hat{\Phi}^{(0)} \right) \frac{\partial}{\partial t} \left[\delta\hat{\Phi}^{(0)} \right] + 3q_{3,n} \left(\delta\hat{\Phi}^{(0)} \right)^2 \frac{\partial}{\partial t} \left[\delta\hat{\Phi}^{(0)} \right] \right] \delta\hat{\Phi}_n^{(0)} + \\
 &+ \sum_n \left[q_{0,n} + q_{1,n} \left(\delta\hat{\Phi}^{(0)} \right) + q_{2,n} \left(\delta\hat{\Phi}^{(0)} \right)^2 + q_{3,n} \left(\delta\hat{\Phi}^{(0)} \right)^3 \right] \frac{\partial}{\partial t} \left[\delta\hat{\Phi}_n^{(0)} \right] = \\
 &= \sum_n \left[\left(q_{1,n} + 2q_{2,n} \left(\delta\hat{\Phi}^{(0)} \right) + 3q_{3,n} \left(\delta\hat{\Phi}^{(0)} \right)^2 \right) \frac{\partial}{\partial t} \left[\delta\hat{\Phi}^{(0)} \right] \delta\hat{\Phi}_n^{(0)} + \right. \\
 &\quad \left. + \left(q_{0,n} + q_{1,n} \left(\delta\hat{\Phi}^{(0)} \right) + q_{2,n} \left(\delta\hat{\Phi}^{(0)} \right)^2 + q_{3,n} \left(\delta\hat{\Phi}^{(0)} \right)^3 \right) \frac{\partial}{\partial t} \left[\delta\hat{\Phi}_n^{(0)} \right] \right] \tag{C.9}
 \end{aligned}$$

and

$$\begin{aligned}
 \left(\frac{\partial}{\partial t} [\delta\hat{\Phi}]\right)^2 &= \sum_n \left[\left(q_{1,n} + 2q_{2,n} (\delta\hat{\Phi}^{(0)}) + 3q_{3,n} (\delta\hat{\Phi}^{(0)})^2 \right) \frac{\partial}{\partial t} [\delta\hat{\Phi}^{(0)}] \delta\hat{\Phi}_n^{(0)} + \right. \\
 &\quad \left. + \left(q_{0,n} + q_{1,n} (\delta\hat{\Phi}^{(0)}) + q_{2,n} (\delta\hat{\Phi}^{(0)})^2 + q_{3,n} (\delta\hat{\Phi}^{(0)})^3 \right) \frac{\partial}{\partial t} [\delta\hat{\Phi}_n^{(0)}] \right] \cdot \\
 &\quad \cdot \sum_l \left[\left(q_{1,l} + 2q_{2,l} (\delta\hat{\Phi}^{(0)}) + 3q_{3,l} (\delta\hat{\Phi}^{(0)})^2 \right) \frac{\partial}{\partial t} [\delta\hat{\Phi}^{(0)}] \delta\hat{\Phi}_l^{(0)} + \right. \\
 &\quad \left. + \left(q_{0,l} + q_{1,l} (\delta\hat{\Phi}^{(0)}) + q_{2,l} (\delta\hat{\Phi}^{(0)})^2 + q_{3,l} (\delta\hat{\Phi}^{(0)})^3 \right) \frac{\partial}{\partial t} [\delta\hat{\Phi}_l^{(0)}] \right]
 \end{aligned}
 \tag{C.10}$$

Truncating this product to the fourth power in $\delta\hat{\Phi}_i^{(0)}$ we obtain

$$\begin{aligned}
 \left(\frac{\partial}{\partial t} [\delta\hat{\Phi}]\right)^2 = & \sum_{n,l} \left[q_{0,n}q_{0,l} \frac{\partial}{\partial t} [\delta\hat{\Phi}_n^{(0)}] \frac{\partial}{\partial t} [\delta\hat{\Phi}_l^{(0)}] + \right. \\
 & + q_{1,n}q_{0,l} \frac{\partial}{\partial t} [\delta\hat{\Phi}_n^{(0)}] \frac{\partial}{\partial t} [\delta\hat{\Phi}_l^{(0)}] \delta\hat{\Phi}_n^{(0)} + \\
 & + q_{0,n}q_{1,l} \frac{\partial}{\partial t} [\delta\hat{\Phi}_n^{(0)}] \frac{\partial}{\partial t} [\delta\hat{\Phi}_l^{(0)}] \delta\hat{\Phi}_l^{(0)} + \\
 & + q_{0,n}q_{1,l} \frac{\partial}{\partial t} [\delta\hat{\Phi}_n^{(0)}] \frac{\partial}{\partial t} [\delta\hat{\Phi}_l^{(0)}] \delta\hat{\Phi}_l^{(0)} + \\
 & + q_{1,n}q_{0,l} \frac{\partial}{\partial t} [\delta\hat{\Phi}_n^{(0)}] \frac{\partial}{\partial t} [\delta\hat{\Phi}_l^{(0)}] \delta\hat{\Phi}_l^{(0)} + \\
 & + q_{1,n}q_{1,l} \frac{\partial}{\partial t} [\delta\hat{\Phi}_n^{(0)}] \frac{\partial}{\partial t} [\delta\hat{\Phi}_l^{(0)}] \delta\hat{\Phi}_n^{(0)} \delta\hat{\Phi}_l^{(0)} + \\
 & + q_{1,n}q_{1,l} \frac{\partial}{\partial t} [\delta\hat{\Phi}_n^{(0)}] \frac{\partial}{\partial t} [\delta\hat{\Phi}_l^{(0)}] \delta\hat{\Phi}_l^{(0)} \delta\hat{\Phi}_l^{(0)} + \\
 & + 2q_{2,n}q_{0,l} \frac{\partial}{\partial t} [\delta\hat{\Phi}_n^{(0)}] \frac{\partial}{\partial t} [\delta\hat{\Phi}_l^{(0)}] \delta\hat{\Phi}_l^{(0)} \delta\hat{\Phi}_n^{(0)} + \\
 & + 2q_{0,n}q_{2,l} \frac{\partial}{\partial t} [\delta\hat{\Phi}_n^{(0)}] \frac{\partial}{\partial t} [\delta\hat{\Phi}_l^{(0)}] \delta\hat{\Phi}_l^{(0)} \delta\hat{\Phi}_l^{(0)} + \\
 & + q_{0,n}q_{2,l} \frac{\partial}{\partial t} [\delta\hat{\Phi}_n^{(0)}] \frac{\partial}{\partial t} [\delta\hat{\Phi}_l^{(0)}] \left(\delta\hat{\Phi}_l^{(0)}\right)^2 + \\
 & + q_{1,n}q_{1,l} \frac{\partial}{\partial t} [\delta\hat{\Phi}_n^{(0)}] \frac{\partial}{\partial t} [\delta\hat{\Phi}_l^{(0)}] \left(\delta\hat{\Phi}_l^{(0)}\right)^2 + \\
 & + q_{2,n}q_{0,l} \frac{\partial}{\partial t} [\delta\hat{\Phi}_n^{(0)}] \frac{\partial}{\partial t} [\delta\hat{\Phi}_l^{(0)}] \left(\delta\hat{\Phi}_l^{(0)}\right)^2 + \\
 & \left. + q_{1,n}q_{1,l} \left(\frac{\partial}{\partial t} [\delta\hat{\Phi}_n^{(0)}]\right)^2 \delta\hat{\Phi}_n^{(0)} \delta\hat{\Phi}_l^{(0)} \right]
 \end{aligned} \tag{C.11}$$

Defining each terms as a function of $\delta\hat{\Phi}_i^{(0)}$ (exploiting the time-derivative properties expressed in Eq. (B.13))

$$\begin{aligned}
\left(\frac{\partial}{\partial t} [\delta\hat{\Phi}]\right)^2 &= - \sum_{n,l} q_{0,n}q_{0,l} \Delta\omega_n\Delta\omega_l \delta\hat{\Phi}_n^{(0)}\delta\hat{\Phi}_l^{(0)} + \\
&\quad - \sum_{n,l,m} \left[q_{0,n}q_{1,l} \Delta\omega_n\Delta\omega_{m,l} + q_{1,n}q_{0,l} \Delta\omega_l\Delta\omega_{n,l} \right] \delta\hat{\Phi}_n^{(0)}\delta\hat{\Phi}_l^{(0)}\delta\hat{\Phi}_m^{(0)} + \\
&\quad - \sum_{n,l,m,s} \left[q_{1,n}q_{1,l} (\Delta\omega_m\Delta\omega_s + \Delta\omega_m\Delta\omega_l + \Delta\omega_n\Delta\omega_m + \Delta\omega_n\Delta\omega_l) + \right. \\
&\quad\quad \left. + q_{2,n}q_{0,l} \Delta\omega_l\Delta\omega_{2m,n} + q_{0,n}q_{2,l} \Delta\omega_n\Delta\omega_{2m,l} \right] \delta\hat{\Phi}_n^{(0)}\delta\hat{\Phi}_l^{(0)}\delta\hat{\Phi}_m^{(0)}\delta\hat{\Phi}_s^{(0)} = \\
&= - \sum_{n,l} q_{0,n}q_{0,l} \Delta\omega_n\Delta\omega_l \delta\hat{\Phi}_n^{(0)}\delta\hat{\Phi}_l^{(0)} + \\
&\quad - \sum_{n,l,m} \left[q_{0,n}q_{1,l} \Delta\omega_n\Delta\omega_{m,l} + q_{1,n}q_{0,l} \Delta\omega_l\Delta\omega_{n,l} \right] \delta\hat{\Phi}_n^{(0)}\delta\hat{\Phi}_l^{(0)}\delta\hat{\Phi}_m^{(0)} + \\
&\quad - \sum_{n,l,m,s} \left[q_{1,n}q_{1,l} (\Delta\omega_m\Delta\omega_s + \Delta\omega_m\Delta\omega_l + \Delta\omega_n\Delta\omega_m + \Delta\omega_n\Delta\omega_l) + \right. \\
&\quad\quad \left. + q_{2,n}q_{0,l} \Delta\omega_l\Delta\omega_{2m,n} + q_{0,n}q_{2,l} \Delta\omega_n\Delta\omega_{2m,l} \right] \delta\hat{\Phi}_n^{(0)}\delta\hat{\Phi}_l^{(0)}\delta\hat{\Phi}_m^{(0)}\delta\hat{\Phi}_s^{(0)} \tag{C.12}
\end{aligned}$$

Lastly, exploiting the definition of $\delta\hat{\Phi}_i^{(0)}$ given in Eq. (3.30):

$$\begin{aligned}
\left(\frac{\partial}{\partial t} [\delta\hat{\Phi}]\right)^2 &= - \sum_{n,l} q_{0,n}q_{0,l} \Delta\omega_n\Delta\omega_l c_n c_l \left\{ \hat{a} + \hat{a}^\dagger \right\}_{n,l} e^{i(\Delta k_{n,l}z - \Delta\omega_{n,l}t)} + \\
&\quad - \sum_{n,l,m} \left[q_{0,n}q_{1,l} \Delta\omega_n\Delta\omega_{m,l} + q_{1,n}q_{0,l} \Delta\omega_l\Delta\omega_{n,m} \right] \cdot \\
&\quad\quad \cdot c_n c_l c_m \left\{ \hat{a} + \hat{a}^\dagger \right\}_{n,l,m} e^{i(\Delta k_{n,l,m}z - \Delta\omega_{n,l,m}t)} \\
&\quad - \sum_{n,l,m,s} \left[q_{1,n}q_{1,l} (\Delta\omega_m\Delta\omega_s + \Delta\omega_m\Delta\omega_l + \Delta\omega_n\Delta\omega_m + \Delta\omega_n\Delta\omega_l) + \right. \\
&\quad\quad \left. + q_{2,n}q_{0,l} \Delta\omega_l\Delta\omega_{2m,n} + q_{0,n}q_{2,l} \Delta\omega_n\Delta\omega_{2m,l} \right] \cdot \\
&\quad\quad c_n c_l c_m c_s \left\{ \hat{a} + \hat{a}^\dagger \right\}_{n,l,m,s} e^{i(\Delta k_{n,l,m,s}z - \Delta\omega_{n,l,m,s}t)} \tag{C.13}
\end{aligned}$$

We can now space-integrate the different components of (3.31):

$$h_0 = \frac{1}{2a} \int_0^{aN} dz \left[2I_c \varphi_0 (1 - p_1) + \frac{\Delta\Phi_{DC}^2}{Lg} \right] = N \left[I_c \varphi_0 (1 - p_1) + \frac{\Delta\Phi_{DC}^2}{2Lg} \right] \tag{C.14}$$

$$\hat{H}_I = \frac{1}{2a} \int_0^{aN} dz \left[\left(2I_c p_2 + \frac{2\Delta\Phi_{DC}}{Lg} \right) \delta\hat{\Phi} \right] = \left(\frac{I_c p_2}{a} + \frac{\Delta\Phi_{DC}}{aLg} \right) \int_0^{aN} \delta\hat{\Phi} dz$$

and, exploiting the third-order approximated expression of $\delta\hat{\Phi}$ given in Eq. (3.26)

$$\begin{aligned}
 \hat{H}_I &= \left(\frac{I_c p_2}{a} + \frac{\Delta\Phi_{DC}}{aL_g} \right) \cdot \int_0^{aN} dz \sum_n \left[q_{0,n} + q_{1,n} \left(\delta\hat{\Phi}^{(0)} \right) + q_{2,n} \left(\delta\hat{\Phi}^{(0)} \right)^2 + q_{3,n} \left(\delta\hat{\Phi}^{(0)} \right)^3 \right] \delta\hat{\Phi}_n^{(0)} = \\
 &= \left(\frac{I_c p_2}{a} + \frac{\Delta\Phi_{DC}}{aL_g} \right) \cdot \int_0^{aN} dz \left[\sum_n q_{0,n} c_n \left\{ \hat{a} + \hat{a}^\dagger \right\}_n e^{i(\Delta k_n z - \Delta\omega_n t)} + \right. \\
 &\quad + \sum_{n,l} q_{1,n} c_n c_l \left\{ \hat{a} + \hat{a}^\dagger \right\}_{n,l} e^{i(\Delta k_{n,l} z - \Delta\omega_{n,l} t)} + \\
 &\quad + \sum_{n,l,m} q_{2,n} c_n c_l c_m \left\{ \hat{a} + \hat{a}^\dagger \right\}_{n,l,m} e^{i(\Delta k_{n,l,m} z - \Delta\omega_{n,l,m} t)} + \\
 &\quad \left. + \sum_{n,l,m,s} q_{3,n} c_n c_l c_m c_s \left\{ \hat{a} + \hat{a}^\dagger \right\}_{n,l,m,s} e^{i(\Delta k_{n,l,m,s} z - \Delta\omega_{n,l,m,s} t)} \right] \tag{C.15}
 \end{aligned}$$

and performing the spatial integration we obtain

$$\begin{aligned}
 \hat{H}_I &= \left(\frac{I_c p_2}{a} + \frac{\Delta\Phi_{DC}}{aL_g} \right) \cdot \left[- \sum_n q_{0,n} c_n \left\{ \hat{a} + \hat{a}^\dagger \right\}_n \frac{i}{\Delta k_n} \left(e^{i\Delta k_n aN} - 1 \right) e^{-i\Delta\omega_n t} + \right. \\
 &\quad - \sum_{n,l} q_{1,n} c_n c_l \left\{ \hat{a} + \hat{a}^\dagger \right\}_{n,l} \frac{i}{\Delta k_{n,l}} \left(e^{i\Delta k_{n,l} aN} - 1 \right) e^{-i\Delta\omega_{n,l} t} + \\
 &\quad - \sum_{n,l,m} q_{2,n} c_n c_l c_m \left\{ \hat{a} + \hat{a}^\dagger \right\}_{n,l,m} \frac{i}{\Delta k_{n,l,m}} \left(e^{i\Delta k_{n,l,m} aN} - 1 \right) e^{-i\Delta\omega_{n,l,m} t} + \\
 &\quad \left. - \sum_{n,l,m,s} q_{3,n} c_n c_l c_m c_s \left\{ \hat{a} + \hat{a}^\dagger \right\}_{n,l,m,s} \frac{i}{\Delta k_{n,l,m,s}} \left(e^{i\Delta k_{n,l,m,s} aN} - 1 \right) e^{-i\Delta\omega_{n,l,m,s} t} \right] \tag{C.16}
 \end{aligned}$$

We can now calculate separately the two components of \hat{H}_{II} :

$$\hat{H}_{II} = \hat{H}_{II,a} + \hat{H}_{II,b} = \frac{1}{2a} \int_0^{aN} \left[\left(\frac{I_c p_1}{\varphi_0} + \frac{1}{L_g} \right) \delta\hat{\Phi}^2 \right] dz + \frac{1}{2a} \int_0^{aN} C_g \hat{V}_{C_g}^2 dz \tag{C.17}$$

For what $\hat{H}_{II,a}$ is concerning, exploiting the definition of $\delta\hat{\Phi}^2$ given in Eq. (C.2)

$$\begin{aligned}
 \hat{H}_{II,a} &= \frac{1}{2a} \left(\frac{I_c p_1}{\varphi_o} + \frac{1}{L_g} \right) \int_0^{aN} \delta\hat{\Phi}^2 dz = \\
 &= \frac{1}{2a} \left(\frac{I_c p_1}{\varphi_o} + \frac{1}{L_g} \right) \cdot \\
 &\quad \cdot \int_0^{aN} dz \left[\sum_{n,l} q_{0,n} q_{0,l} c_n c_l \{ \hat{a} + \hat{a}^\dagger \}_{n,l} e^{i(\Delta k_{n,l} z - \Delta \omega_{n,l} t)} + \right. \\
 &\quad + \sum_{n,l,m} 2q_{0,n} q_{1,l} c_n c_l c_m \{ \hat{a} + \hat{a}^\dagger \}_{n,l,m} e^{i(\Delta k_{n,l,m} z - \Delta \omega_{n,l,m} t)} + \\
 &\quad \left. + \sum_{n,l,m,s} (2q_{0,n} q_{2,l} + q_{1,n} q_{1,l}) c_n c_l c_m c_s \{ \hat{a} + \hat{a}^\dagger \}_{n,l,m,s} e^{i(\Delta k_{n,l,m,s} z - \Delta \omega_{n,l,m,s} t)} \right]
 \end{aligned} \tag{C.18}$$

and performing the spatial integration:

$$\begin{aligned}
 \hat{H}_{II,a} &= \frac{1}{2a} \left(\frac{I_c p_1}{\varphi_o} + \frac{1}{L_g} \right) \cdot \\
 &\quad \cdot \left[- \sum_{n,l} q_{0,n} q_{0,l} c_n c_l \{ \hat{a} + \hat{a}^\dagger \}_{n,l} \frac{i}{\Delta k_{n,l}} \left(e^{i\Delta k_{n,l} aN} - 1 \right) e^{-i\Delta \omega_{n,l} t} + \right. \\
 &\quad - \sum_{n,l,m} 2q_{0,n} q_{1,l} c_n c_l c_m \{ \hat{a} + \hat{a}^\dagger \}_{n,l,m} \frac{i}{\Delta k_{n,l,m}} \left(e^{i\Delta k_{n,l,m} aN} - 1 \right) e^{-i\Delta \omega_{n,l,m} t} + \\
 &\quad \left. - \sum_{n,l,m,s} (2q_{0,n} q_{2,l} + q_{1,n} q_{1,l}) c_n c_l c_m c_s \{ \hat{a} + \hat{a}^\dagger \}_{n,l,m,s} \frac{i}{\Delta k_{n,l,m,s}} \left(e^{i\Delta k_{n,l,m,s} aN} - 1 \right) e^{-i\Delta \omega_{n,l,m,s} t} \right]
 \end{aligned} \tag{C.19}$$

Instead, for what $\hat{H}_{II,b}$ is concerning, exploiting the definition of \hat{V}_{C_g} given in Eq. (3.15)

$$\begin{aligned}
 \hat{H}_{II,b} &= \frac{C_g}{2a} \int_0^{aN} dz \hat{V}_{C_g}^2 = \frac{C_g}{2a} \int_0^{aN} dz \frac{\hbar}{2C_g N} \sum_{n,l} \sqrt{\omega_n \omega_l} \{ \hat{a} + \hat{a}^\dagger \}_{n,l} e^{i(\Delta k_{n,l} z - \Delta \omega_{n,l} t)} = \\
 &= - \frac{\hbar}{4aN} \sum_{n,l} \sqrt{\omega_n \omega_l} \{ \hat{a} + \hat{a}^\dagger \}_{n,l} \frac{i}{\Delta k_{n,l}} \left(e^{i\Delta k_{n,l} aN} - 1 \right) e^{-i\Delta \omega_{n,l} t}
 \end{aligned} \tag{C.20}$$

We can now calculate the space integral of \hat{H}_{III} exploiting the expression for $\delta\hat{\Phi}^3$ given in Eq. (C.6)

$$\begin{aligned}
 \hat{H}_{III} &= -\frac{1}{2a} \frac{I_c p_2}{3\varphi_0^2} \int_0^{aN} \delta\hat{\Phi}^3 dz = \\
 &= -\frac{I_c p_2}{6a\varphi_0^2} \int_0^{aN} dz \left[\sum_{n,l,m} q_{0,n} q_{0,l} q_{0,m} c_n c_l c_m \left\{ \hat{a} + \hat{a}^\dagger \right\}_{n,l,m} e^{i(\Delta k_{n,l,m} z - \Delta\omega_{n,l,m} t)} + \right. \\
 &\quad \left. + \sum_{n,l,m,s} 3 q_{1,n} q_{0,l} q_{0,m} c_n c_l c_m c_s \left\{ \hat{a} + \hat{a}^\dagger \right\}_{n,l,m,s} e^{i(\Delta k_{n,l,m,s} z - \Delta\omega_{n,l,m,s} t)} \right] = \\
 &= \frac{I_c p_2}{6a\varphi_0^2} \left[\sum_{n,l,m} q_{0,n} q_{0,l} q_{0,m} c_n c_l c_m \left\{ \hat{a} + \hat{a}^\dagger \right\}_{n,l,m} \frac{i}{\Delta k_{n,l,m}} \left(e^{i\Delta k_{n,l,m} aN} - 1 \right) e^{-i(\Delta\omega_{n,l,m} t)} + \right. \\
 &\quad \left. + \sum_{n,l,m,s} 3 q_{1,n} q_{0,l} q_{0,m} c_n c_l c_m c_s \left\{ \hat{a} + \hat{a}^\dagger \right\}_{n,l,m,s} \frac{i}{\Delta k_{n,l,m,s}} \left(e^{i\Delta k_{n,l,m,s} aN} - 1 \right) e^{-i(\Delta\omega_{n,l,m,s} t)} \right] \tag{C.21}
 \end{aligned}$$

We can now calculate the space integral of \hat{H}_{IV} exploiting the expression for $\delta\hat{\Phi}^4$ given in Eq. (C.6)

$$\begin{aligned}
 \hat{H}_{IV} &= \frac{1}{2a} \frac{I_c p_1}{12\varphi_0^3} \int_0^{aN} \delta\hat{\Phi}^4 dz = \\
 &= \frac{1}{2a} \frac{I_c p_1}{12\varphi_0^3} \int_0^{aN} dz \left[\sum_{n,l,m,s} q_{0,n} q_{0,l} q_{0,m} q_{0,s} c_n c_l c_m c_s \left\{ \hat{a} + \hat{a}^\dagger \right\}_{n,l,m,s} e^{i(\Delta k_{n,l,m,s} z - \Delta\omega_{n,l,m,s} t)} \right] = \\
 &= \frac{I_c p_1}{24a\varphi_0^3} \left[\sum_{n,l,m,s} q_{0,n} q_{0,l} q_{0,m} q_{0,s} c_n c_l c_m c_s \left\{ \hat{a} + \hat{a}^\dagger \right\}_{n,l,m,s} \frac{i}{\Delta k_{n,l,m,s}} \left(e^{i\Delta k_{n,l,m,s} aN} - 1 \right) e^{-i(\Delta\omega_{n,l,m,s} t)} \right] \tag{C.22}
 \end{aligned}$$

Lastly, we can space integrate \hat{H}_V

$$\begin{aligned}
 \hat{H}_V &= \frac{C_J}{2a} \int_0^{aN} \left(\frac{\partial}{\partial t} [\delta\hat{\Phi}] \right)^2 dz = \\
 &= -\frac{C_J}{2a} \int_0^{aN} dz \left[\sum_{n,l} q_{0,n} q_{0,l} \Delta\omega_n \Delta\omega_l c_n c_l \{ \hat{a} + \hat{a}^\dagger \}_{n,l} e^{i(\Delta k_{n,l} z - \Delta\omega_{n,l} t)} + \right. \\
 &\quad + \sum_{n,l,m} [q_{0,n} q_{1,l} \Delta\omega_n \Delta\omega_{m,l} + q_{1,n} q_{0,l} \Delta\omega_l \Delta\omega_{n,m}] c_n c_l c_m \{ \hat{a} + \hat{a}^\dagger \}_{n,l,m} e^{i(\Delta k_{n,l,m} z - \Delta\omega_{n,l,m} t)} + \\
 &\quad + \sum_{n,l,m,s} [q_{1,n} q_{1,l} (\Delta\omega_m \Delta\omega_s + \Delta\omega_m \Delta\omega_l + \Delta\omega_n \Delta\omega_m + \Delta\omega_n \Delta\omega_l) + q_{2,n} q_{0,l} \Delta\omega_l \Delta\omega_{2m,n} + q_{0,n} q_{2,l} \Delta\omega_l \Delta\omega_{2n,m} \\
 &\quad \left. \cdot c_n c_l c_m c_s \{ \hat{a} + \hat{a}^\dagger \}_{n,l,m,s} e^{i(\Delta k_{n,l,m,s} z - \Delta\omega_{n,l,m,s} t)} \right] = \\
 &= -\frac{C_J}{2a} \left[\sum_{n,l} q_{0,n} q_{0,l} \Delta\omega_n \Delta\omega_l c_n c_l \{ \hat{a} + \hat{a}^\dagger \} \frac{i}{\Delta k_{n,l}} (e^{i\Delta k_{n,l} aN} - 1) e^{-i\Delta\omega_{n,l} t} + \right. \\
 &\quad + \sum_{n,l,m} [q_{0,n} q_{1,l} \Delta\omega_n \Delta\omega_{m,l} + q_{1,n} q_{0,l} \Delta\omega_l \Delta\omega_{n,m}] c_n c_l c_m \{ \hat{a} + \hat{a}^\dagger \}_{n,l,m} \frac{i}{\Delta k_{n,l,m}} (e^{i\Delta k_{n,l,m} aN} - 1) e^{-i\Delta\omega_{n,l,m} t} + \\
 &\quad + \sum_{n,l,m,s} [q_{1,n} q_{1,l} (\Delta\omega_m \Delta\omega_s + \Delta\omega_m \Delta\omega_l + \Delta\omega_n \Delta\omega_m + \Delta\omega_n \Delta\omega_l) + q_{2,n} q_{0,l} \Delta\omega_l \Delta\omega_{2m,n} + q_{0,n} q_{2,l} \Delta\omega_l \Delta\omega_{2n,m} \\
 &\quad \left. \cdot c_n c_l c_m c_s \{ \hat{a} + \hat{a}^\dagger \}_{n,l,m,s} \frac{i}{\Delta k_{n,l,m,s}} (e^{i\Delta k_{n,l,m,s} aN} - 1) e^{-i\Delta\omega_{n,l,m,s} t} \right] \tag{C.23}
 \end{aligned}$$

Appendix D

Curly brackets development and energy-conservative permutations selection

If we consider the combination of creation and annihilation operators given by

$$\begin{aligned}
 \{a + a^\dagger\}_{n,l,m,s} &= (a_n + a_n^\dagger)(a_l + a_l^\dagger)(a_m + a_m^\dagger)(a_s + a_s^\dagger) = \\
 &= (a_n a_l + a_n a_l^\dagger + a_n^\dagger a_l + a_n^\dagger a_l^\dagger)(a_m a_s + a_m a_s^\dagger + a_m^\dagger a_s + a_m^\dagger a_s^\dagger) = \\
 &= a_n a_l a_m a_s + a_n a_l a_m a_s^\dagger + a_n a_l a_m^\dagger a_s + a_n a_l a_m^\dagger a_s^\dagger + \\
 &\quad + a_n a_l^\dagger a_m a_s + a_n a_l^\dagger a_m a_s^\dagger + a_n a_l^\dagger a_m^\dagger a_s + a_n a_l^\dagger a_m^\dagger a_s^\dagger + \\
 &\quad + a_n^\dagger a_l a_m a_s + a_n^\dagger a_l a_m a_s^\dagger + a_n^\dagger a_l a_m^\dagger a_s + a_n^\dagger a_l a_m^\dagger a_s^\dagger + \\
 &\quad + a_n^\dagger a_l^\dagger a_m a_s + a_n^\dagger a_l^\dagger a_m a_s^\dagger + a_n^\dagger a_l^\dagger a_m^\dagger a_s + a_n^\dagger a_l^\dagger a_m^\dagger a_s^\dagger
 \end{aligned} \tag{D.1}$$

the only terms that can fulfill the energy conservation requirement are those made of 2 creation and 2 annihilation operators. These terms can describe one of the following events:

- Annihilation of 2 pump photons and creation of a couple of signal-idler photons (these are mixing terms);
- Annihilation of a couple of signal-idler photons and creation of 2 pump photons;
- Creation and annihilation of a couple of tones (non-mixing terms).

Hence, under the energy conservation hypothesis we get:

$$\sum_{n,l,m,s=\{p,s,i\}} \hbar \left[\chi_4^{(n,l,m^\dagger,s^\dagger)} a_n a_l a_m^\dagger a_s^\dagger + \chi_4^{(n,l^\dagger,m,s^\dagger)} a_n a_l^\dagger a_m a_s^\dagger + \chi_4^{(n,l^\dagger,m^\dagger,s)} a_n a_l^\dagger a_m^\dagger a_s + \right. \\ \left. + \chi_4^{(n^\dagger,l,m,s^\dagger)} a_n^\dagger a_l a_m a_s^\dagger + \chi_4^{(n^\dagger,l,m^\dagger,s)} a_n^\dagger a_l a_m^\dagger a_s + \chi_4^{(n^\dagger,l^\dagger,m,s)} a_n^\dagger a_l^\dagger a_m a_s \right] \quad (\text{D.2})$$

D.1 Development of the energy-conservative terms in 4WM

$$\sum_{n,l,m,s=\{p,s,i\}} \chi_4^{(n,l,m^\dagger,s^\dagger)} a_n a_l a_m^\dagger a_s^\dagger = \\ = \chi_4^{(p,p,p^\dagger,p^\dagger)} a_p a_p a_p^\dagger a_p^\dagger + \chi_4^{(s,s,s^\dagger,s^\dagger)} a_s a_s a_s^\dagger a_s^\dagger + \chi_4^{(i,i,i^\dagger,i^\dagger)} a_i a_i a_i^\dagger a_i^\dagger + \\ + \chi_4^{(p,s,p^\dagger,s^\dagger)} a_p a_s a_p^\dagger a_s^\dagger + \chi_4^{(p,s,s^\dagger,p^\dagger)} a_p a_s a_s^\dagger a_p^\dagger + \chi_4^{(s,p,p^\dagger,s^\dagger)} a_s a_p a_p^\dagger a_s^\dagger + \chi_4^{(s,p,s^\dagger,p^\dagger)} a_s a_p a_s^\dagger a_p^\dagger \\ + \chi_4^{(p,i,p^\dagger,i^\dagger)} a_p a_i a_p^\dagger a_i^\dagger + \chi_4^{(p,i,i^\dagger,p^\dagger)} a_p a_i a_i^\dagger a_p^\dagger + \chi_4^{(i,p,p^\dagger,i^\dagger)} a_i a_p a_p^\dagger a_i^\dagger + \chi_4^{(i,p,i^\dagger,p^\dagger)} a_i a_p a_i^\dagger a_p^\dagger + \\ + \chi_4^{(s,i,s^\dagger,i^\dagger)} a_s a_i a_s^\dagger a_i^\dagger + \chi_4^{(s,i,i^\dagger,s^\dagger)} a_s a_i a_i^\dagger a_s^\dagger + \chi_4^{(i,s,s^\dagger,i^\dagger)} a_i a_s a_s^\dagger a_i^\dagger + \chi_4^{(i,s,i^\dagger,s^\dagger)} a_i a_s a_i^\dagger a_s^\dagger + \\ + \chi_4^{(p,p,s^\dagger,i^\dagger)} a_p a_p a_s^\dagger a_i^\dagger + \chi_4^{(p,p,i^\dagger,s^\dagger)} a_p a_p a_i^\dagger a_s^\dagger + \\ + \chi_4^{(s,i,p^\dagger,p^\dagger)} a_s a_i a_p^\dagger a_p^\dagger + \chi_4^{(i,s,p^\dagger,p^\dagger)} a_i a_s a_p^\dagger a_p^\dagger = \\ = \chi_4^{(p,p,p^\dagger,p^\dagger)} a_p^\dagger a_p a_p^\dagger a_p + 3\chi_4^{(p,p,p^\dagger,p^\dagger)} a_p^\dagger a_p + 2\chi_4^{(p,p,p^\dagger,p^\dagger)} + \\ + \chi_4^{(s,s,s^\dagger,s^\dagger)} a_s^\dagger a_s a_s^\dagger a_s + 3\chi_4^{(s,s,s^\dagger,s^\dagger)} a_s^\dagger a_s + 2\chi_4^{(s,s,s^\dagger,s^\dagger)} + \\ + \chi_4^{(i,i,i^\dagger,i^\dagger)} a_i^\dagger a_i a_i^\dagger a_i + 3\chi_4^{(i,i,i^\dagger,i^\dagger)} a_i^\dagger a_i + 2\chi_4^{(i,i,i^\dagger,i^\dagger)} + \\ + \left[\chi_4^{(p,s,p^\dagger,s^\dagger)} + \chi_4^{(p,s,s^\dagger,p^\dagger)} + \chi_4^{(s,p,p^\dagger,s^\dagger)} + \chi_4^{(s,p,s^\dagger,p^\dagger)} \right] \cdot (a_p^\dagger a_p a_s^\dagger a_s + a_p^\dagger a_p + a_s^\dagger a_s + 1) + \\ + \left[\chi_4^{(p,i,p^\dagger,i^\dagger)} + \chi_4^{(p,i,i^\dagger,p^\dagger)} + \chi_4^{(i,p,p^\dagger,i^\dagger)} + \chi_4^{(i,p,i^\dagger,p^\dagger)} \right] \cdot (a_p^\dagger a_p a_i^\dagger a_i + a_p^\dagger a_p + a_i^\dagger a_i + 1) + \\ + \left[\chi_4^{(s,i,s^\dagger,i^\dagger)} + \chi_4^{(s,i,i^\dagger,s^\dagger)} + \chi_4^{(i,s,s^\dagger,i^\dagger)} + \chi_4^{(i,s,i^\dagger,s^\dagger)} \right] \cdot (a_s^\dagger a_s a_i^\dagger a_i + a_s^\dagger a_s + a_i^\dagger a_i + 1) + \\ + \left[\chi_4^{(p,p,s^\dagger,i^\dagger)} + \chi_4^{(p,p,i^\dagger,s^\dagger)} \right] a_p a_p a_s^\dagger a_i^\dagger + \\ + \left[\chi_4^{(s,i,p^\dagger,p^\dagger)} + \chi_4^{(i,s,p^\dagger,p^\dagger)} \right] a_p^\dagger a_p^\dagger a_s a_i \quad (\text{D.3})$$

$$\begin{aligned}
 \sum_{n,l,m,s=\{p,s,i\}} \chi_4^{(n,l^\dagger,m,s^\dagger)} a_n a_l^\dagger a_m a_s^\dagger &= \\
 &= \chi_4^{(p,p^\dagger,p,p^\dagger)} a_p a_p^\dagger a_p a_p^\dagger + \chi_4^{(s,s^\dagger,s,s^\dagger)} a_s a_s^\dagger a_s a_s^\dagger + \chi_4^{(i,i^\dagger,i,i^\dagger)} a_i a_i^\dagger a_i a_i^\dagger + \\
 &+ \chi_4^{(p,p^\dagger,s,s^\dagger)} a_p a_p^\dagger a_s a_s^\dagger + \chi_4^{(s,s^\dagger,p,p^\dagger)} a_s a_s^\dagger a_p a_p^\dagger + \chi_4^{(p,s^\dagger,s,p^\dagger)} a_p a_s^\dagger a_s a_p^\dagger + \chi_4^{(s,p^\dagger,p,s^\dagger)} a_s a_p^\dagger a_p a_s^\dagger + \\
 &+ \chi_4^{(p,p^\dagger,i,i^\dagger)} a_p a_p^\dagger a_i a_i^\dagger + \chi_4^{(i,i^\dagger,p,p^\dagger)} a_i a_i^\dagger a_p a_p^\dagger + \chi_4^{(p,i^\dagger,i,p^\dagger)} a_p a_i^\dagger a_i a_p^\dagger + \chi_4^{(i,p^\dagger,p,i^\dagger)} a_i a_p^\dagger a_p a_i^\dagger + \\
 &+ \chi_4^{(s,s^\dagger,i,i^\dagger)} a_s a_s^\dagger a_i a_i^\dagger + \chi_4^{(i,i^\dagger,s,s^\dagger)} a_i a_i^\dagger a_s a_s^\dagger + \chi_4^{(s,i^\dagger,i,s^\dagger)} a_s a_i^\dagger a_i a_s^\dagger + \chi_4^{(i,s^\dagger,s,i^\dagger)} a_i a_s^\dagger a_s a_i^\dagger + \\
 &+ \chi_4^{(p,s^\dagger,p,i^\dagger)} a_p a_s^\dagger a_p a_i^\dagger + \chi_4^{(p,i^\dagger,p,s^\dagger)} a_p a_i^\dagger a_p a_s^\dagger + \\
 &+ \chi_4^{(s,p^\dagger,i,p^\dagger)} a_s a_p^\dagger a_i a_p^\dagger + \chi_4^{(i,p^\dagger,s,p^\dagger)} a_i a_p^\dagger a_s a_p^\dagger = \\
 &= \left[\chi_4^{(p,p^\dagger,p,p^\dagger)} \right] (a_p^\dagger a_p a_p^\dagger a_p + 2a_p^\dagger a_p + 1) + \\
 &+ \left[\chi_4^{(s,s^\dagger,s,s^\dagger)} \right] (a_s^\dagger a_s a_s^\dagger a_s + 2a_s^\dagger a_s + 1) + \\
 &+ \left[\chi_4^{(i,i^\dagger,i,i^\dagger)} \right] (a_i^\dagger a_i a_i^\dagger a_i + 2a_i^\dagger a_i + 1) + \\
 &+ \left[\chi_4^{(p,p^\dagger,s,s^\dagger)} + \chi_4^{(s,s^\dagger,p,p^\dagger)} + \chi_4^{(p,s^\dagger,s,p^\dagger)} + \chi_4^{(s,p^\dagger,p,s^\dagger)} \right] a_p^\dagger a_p a_s^\dagger a_s + \left[\chi_4^{(p,p^\dagger,s,s^\dagger)} + \chi_4^{(s,s^\dagger,p,p^\dagger)} + \chi_4^{(p,s^\dagger,s,p^\dagger)} + \chi_4^{(s,p^\dagger,p,s^\dagger)} \right] a_s^\dagger a_s + \left[\chi_4^{(p,p^\dagger,s,s^\dagger)} + \chi_4^{(s,s^\dagger,p,p^\dagger)} \right] + \\
 &+ \left[\chi_4^{(p,p^\dagger,i,i^\dagger)} + \chi_4^{(i,i^\dagger,p,p^\dagger)} + \chi_4^{(p,i^\dagger,i,p^\dagger)} + \chi_4^{(i,p^\dagger,p,i^\dagger)} \right] a_p^\dagger a_p a_i^\dagger a_i + \left[\chi_4^{(p,p^\dagger,i,i^\dagger)} + \chi_4^{(i,i^\dagger,p,p^\dagger)} + \chi_4^{(p,i^\dagger,i,p^\dagger)} + \chi_4^{(i,p^\dagger,p,i^\dagger)} \right] a_i^\dagger a_i + \left[\chi_4^{(p,p^\dagger,i,i^\dagger)} + \chi_4^{(i,i^\dagger,p,p^\dagger)} \right] + \\
 &+ \left[\chi_4^{(s,s^\dagger,i,i^\dagger)} + \chi_4^{(i,i^\dagger,s,s^\dagger)} + \chi_4^{(s,i^\dagger,i,s^\dagger)} + \chi_4^{(i,s^\dagger,s,i^\dagger)} \right] a_s^\dagger a_s a_i^\dagger a_i + \left[\chi_4^{(s,s^\dagger,i,i^\dagger)} + \chi_4^{(i,i^\dagger,s,s^\dagger)} + \chi_4^{(s,i^\dagger,i,s^\dagger)} + \chi_4^{(i,s^\dagger,s,i^\dagger)} \right] a_i^\dagger a_i + \left[\chi_4^{(s,s^\dagger,i,i^\dagger)} + \chi_4^{(i,i^\dagger,s,s^\dagger)} \right] + \\
 &+ \left[\chi_4^{(p,s^\dagger,p,i^\dagger)} + \chi_4^{(p,i^\dagger,p,s^\dagger)} \right] a_p a_p a_s^\dagger a_i^\dagger + \\
 &+ \left[\chi_4^{(s,p^\dagger,i,p^\dagger)} + \chi_4^{(i,p^\dagger,s,p^\dagger)} \right] a_p^\dagger a_p^\dagger a_s a_i
 \end{aligned} \tag{D.4}$$

$$\begin{aligned}
 \sum_{n,l,m,s=\{p,s,i\}} \chi_4^{(n,l^\dagger,m^\dagger,s)} a_n a_l^\dagger a_m^\dagger a_s = & \\
 = \chi_4^{(p,p^\dagger,p^\dagger,p)} a_p a_p^\dagger a_p^\dagger a_p + \chi_4^{(s,s^\dagger,s^\dagger,s)} a_s a_s^\dagger a_s^\dagger a_s + \chi_4^{(i,i^\dagger,i^\dagger,i)} a_i a_i^\dagger a_i^\dagger a_i + & \\
 + \chi_4^{(p,p^\dagger,s^\dagger,s)} a_p a_p^\dagger a_s^\dagger a_s + \chi_4^{(s,s^\dagger,p^\dagger,p)} a_s a_s^\dagger a_p^\dagger a_p + \chi_4^{(p,s^\dagger,p^\dagger,s)} a_p a_s^\dagger a_p^\dagger a_s + \chi_4^{(s,p^\dagger,s^\dagger,p)} a_s a_p^\dagger a_s^\dagger a_p + & \\
 + \chi_4^{(p,p^\dagger,i^\dagger,i)} a_p a_p^\dagger a_i^\dagger a_i + \chi_4^{(i,i^\dagger,p^\dagger,p)} a_i a_i^\dagger a_p^\dagger a_p + \chi_4^{(p,i^\dagger,p^\dagger,i)} a_p a_i^\dagger a_p^\dagger a_i + \chi_4^{(i,p^\dagger,i^\dagger,p)} a_i a_p^\dagger a_i^\dagger a_p + & \\
 + \chi_4^{(s,s^\dagger,i^\dagger,i)} a_s a_s^\dagger a_i^\dagger a_i + \chi_4^{(i,i^\dagger,s^\dagger,s)} a_i a_i^\dagger a_s^\dagger a_s + \chi_4^{(s,i^\dagger,s^\dagger,i)} a_s a_i^\dagger a_s^\dagger a_i + \chi_4^{(i,s^\dagger,i^\dagger,s)} a_i a_s^\dagger a_i^\dagger a_s + & \\
 + \chi_4^{(p,s^\dagger,i^\dagger,p)} a_p a_s^\dagger a_i^\dagger a_p + \chi_4^{(p,i^\dagger,s^\dagger,p)} a_p a_i^\dagger a_s^\dagger a_p + & \\
 + \chi_4^{(s,p^\dagger,p^\dagger,i)} a_s a_p^\dagger a_p^\dagger a_i + \chi_4^{(i,p^\dagger,p^\dagger,s)} a_i a_p^\dagger a_p^\dagger a_s = & \\
 = \left[\chi_4^{(p,p^\dagger,p^\dagger,p)} \right] (a_p^\dagger a_p a_p^\dagger a_p + a_p^\dagger a_p) + & \\
 + \left[\chi_4^{(s,s^\dagger,s^\dagger,s)} \right] (a_s^\dagger a_s a_s^\dagger a_s + a_s^\dagger a_s) + & \\
 + \left[\chi_4^{(i,i^\dagger,i^\dagger,i)} \right] (a_i^\dagger a_i a_i^\dagger a_i + a_i^\dagger a_i) + & \\
 + \left[\chi_4^{(p,p^\dagger,s^\dagger,s)} + \chi_4^{(s,s^\dagger,p^\dagger,p)} + \chi_4^{(p,s^\dagger,p^\dagger,s)} + \chi_4^{(s,p^\dagger,s^\dagger,p)} \right] a_p^\dagger a_p a_s^\dagger a_s + & \\
 + \left[\chi_4^{(s,s^\dagger,p^\dagger,p)} + \chi_4^{(s,p^\dagger,s^\dagger,p)} \right] a_p^\dagger a_p + \left[\chi_4^{(p,p^\dagger,s^\dagger,s)} + \chi_4^{(p,s^\dagger,p^\dagger,s)} \right] a_s^\dagger a_s + & \\
 + \left[\chi_4^{(p,p^\dagger,i^\dagger,i)} + \chi_4^{(i,i^\dagger,p^\dagger,p)} + \chi_4^{(p,i^\dagger,p^\dagger,i)} + \chi_4^{(i,p^\dagger,i^\dagger,p)} \right] a_p^\dagger a_p a_i^\dagger a_i + & \\
 + \left[\chi_4^{(i,i^\dagger,p^\dagger,p)} + \chi_4^{(i,p^\dagger,i^\dagger,p)} \right] a_p^\dagger a_p + \left[\chi_4^{(p,p^\dagger,i^\dagger,i)} + \chi_4^{(p,i^\dagger,p^\dagger,i)} \right] a_i^\dagger a_i + & \\
 + \left[\chi_4^{(s,s^\dagger,i^\dagger,i)} + \chi_4^{(i,i^\dagger,s^\dagger,s)} + \chi_4^{(s,i^\dagger,s^\dagger,i)} + \chi_4^{(i,s^\dagger,i^\dagger,s)} \right] a_s^\dagger a_s a_i^\dagger a_i + & \\
 + \left[\chi_4^{(i,i^\dagger,s^\dagger,s)} + \chi_4^{(i,s^\dagger,i^\dagger,s)} \right] a_s^\dagger a_s + \left[\chi_4^{(s,s^\dagger,i^\dagger,i)} + \chi_4^{(s,i^\dagger,s^\dagger,i)} \right] a_i^\dagger a_i + & \\
 + \left[\chi_4^{(p,s^\dagger,i^\dagger,p)} + \chi_4^{(p,i^\dagger,s^\dagger,p)} \right] a_p a_p a_s^\dagger a_i^\dagger + & \\
 + \left[\chi_4^{(s,p^\dagger,p^\dagger,i)} + \chi_4^{(i,p^\dagger,p^\dagger,s)} \right] a_p^\dagger a_p^\dagger a_s a_i & \tag{D.5}
 \end{aligned}$$

$$\begin{aligned}
 \sum_{n,l,m,s=\{p,s,i\}} \chi_4^{(n^\dagger,l,m,s^\dagger)} a_n^\dagger a_l a_m a_s^\dagger &= \\
 &= \chi_4^{(p^\dagger,p,p,p^\dagger)} a_p^\dagger a_p a_p a_p^\dagger + \chi_4^{(s^\dagger,s,s,s^\dagger)} a_s^\dagger a_s a_s a_s^\dagger + \chi_4^{(i^\dagger,i,i,i^\dagger)} a_i^\dagger a_i a_i a_i^\dagger + \\
 &+ \chi_4^{(p^\dagger,p,s,s^\dagger)} a_p^\dagger a_p a_s a_s^\dagger + \chi_4^{(s^\dagger,s,p,p^\dagger)} a_s^\dagger a_s a_p a_p^\dagger + \chi_4^{(p^\dagger,s,p,s^\dagger)} a_p^\dagger a_s a_p a_s^\dagger + \chi_4^{(s^\dagger,p,s,p^\dagger)} a_s^\dagger a_p a_s a_p^\dagger + \\
 &+ \chi_4^{(p^\dagger,p,i,i^\dagger)} a_p^\dagger a_p a_i a_i^\dagger + \chi_4^{(i^\dagger,i,p,p^\dagger)} a_i^\dagger a_i a_p a_p^\dagger + \chi_4^{(p^\dagger,i,p,i^\dagger)} a_p^\dagger a_i a_p a_i^\dagger + \chi_4^{(i^\dagger,p,i,p^\dagger)} a_i^\dagger a_p a_i a_p^\dagger + \\
 &+ \chi_4^{(s^\dagger,s,i,i^\dagger)} a_s^\dagger a_s a_i a_i^\dagger + \chi_4^{(i^\dagger,i,s,s^\dagger)} a_i^\dagger a_i a_s a_s^\dagger + \chi_4^{(s^\dagger,i,s,i^\dagger)} a_s^\dagger a_i a_s a_i^\dagger + \chi_4^{(i^\dagger,s,i,s^\dagger)} a_i^\dagger a_s a_i a_s^\dagger + \\
 &+ \chi_4^{(s^\dagger,p,p,i^\dagger)} a_s^\dagger a_p a_p a_i^\dagger + \chi_4^{(i^\dagger,p,p,s^\dagger)} a_i^\dagger a_p a_p a_s^\dagger + \\
 &+ \chi_4^{(p^\dagger,s,i,p^\dagger)} a_p^\dagger a_s a_i a_p^\dagger + \chi_4^{(p^\dagger,i,s,p^\dagger)} a_p^\dagger a_i a_s a_p^\dagger = \\
 &= \left[\chi_4^{(p^\dagger,p,p,p^\dagger)} \right] (a_p^\dagger a_p a_p^\dagger a_p + a_p^\dagger a_p) + \\
 &+ \left[\chi_4^{(s^\dagger,s,s,s^\dagger)} \right] (a_s^\dagger a_s a_s^\dagger a_s + a_s^\dagger a_s) + \\
 &+ \left[\chi_4^{(i^\dagger,i,i,i^\dagger)} \right] (a_i^\dagger a_i a_i^\dagger a_i + a_i^\dagger a_i) + \\
 &+ \left[\chi_4^{(p^\dagger,p,s,s^\dagger)} + \chi_4^{(s^\dagger,s,p,p^\dagger)} + \chi_4^{(p^\dagger,s,p,s^\dagger)} + \chi_4^{(s^\dagger,p,s,p^\dagger)} \right] a_p^\dagger a_p a_s^\dagger a_s + \\
 &\quad + \left[\chi_4^{(p^\dagger,p,s,s^\dagger)} + \chi_4^{(p^\dagger,s,p,s^\dagger)} \right] a_p^\dagger a_p + \left[\chi_4^{(s^\dagger,s,p,p^\dagger)} + \chi_4^{(s^\dagger,p,s,p^\dagger)} \right] a_s^\dagger a_s + \\
 &+ \left[\chi_4^{(p^\dagger,p,i,i^\dagger)} + \chi_4^{(i^\dagger,i,p,p^\dagger)} + \chi_4^{(p^\dagger,i,p,i^\dagger)} + \chi_4^{(i^\dagger,p,i,p^\dagger)} \right] a_p^\dagger a_p a_i^\dagger a_i + \\
 &\quad + \left[\chi_4^{(p^\dagger,p,i,i^\dagger)} + \chi_4^{(p^\dagger,i,p,i^\dagger)} \right] a_p^\dagger a_p + \left[\chi_4^{(i^\dagger,i,p,p^\dagger)} + \chi_4^{(i^\dagger,p,i,p^\dagger)} \right] a_i^\dagger a_i + \\
 &+ \left[\chi_4^{(s^\dagger,s,i,i^\dagger)} + \chi_4^{(i^\dagger,i,s,s^\dagger)} + \chi_4^{(s^\dagger,i,s,i^\dagger)} + \chi_4^{(i^\dagger,s,i,s^\dagger)} \right] a_s^\dagger a_s a_i^\dagger a_i + \\
 &\quad + \left[\chi_4^{(s^\dagger,s,i,i^\dagger)} + \chi_4^{(s^\dagger,i,s,i^\dagger)} \right] a_s^\dagger a_s + \left[\chi_4^{(i^\dagger,i,s,s^\dagger)} + \chi_4^{(i^\dagger,s,i,s^\dagger)} \right] a_i^\dagger a_i + \\
 &+ \left[\chi_4^{(s^\dagger,p,p,i^\dagger)} + \chi_4^{(i^\dagger,p,p,s^\dagger)} \right] a_p a_p a_s^\dagger a_i^\dagger + \\
 &+ \left[\chi_4^{(p^\dagger,s,i,p^\dagger)} + \chi_4^{(p^\dagger,i,p,p^\dagger)} \right] a_p^\dagger a_p^\dagger a_s a_i
 \end{aligned} \tag{D.6}$$

$$\begin{aligned}
 & \sum_{n,l,m,s=\{p,s,i\}} \chi_4^{(n^\dagger,l,m^\dagger,s)} a_n^\dagger a_l a_m^\dagger a_s = \\
 & = \chi_4^{(p^\dagger,p,p^\dagger,p)} a_p^\dagger a_p a_p^\dagger a_p + \chi_4^{(s^\dagger,s,s^\dagger,s)} a_s^\dagger a_s a_s^\dagger a_s + \chi_4^{(i^\dagger,i,i^\dagger,i)} a_i^\dagger a_i a_i^\dagger a_i + \\
 & + \chi_4^{(p^\dagger,p,s^\dagger,s)} a_p^\dagger a_p a_s^\dagger a_s + \chi_4^{(s^\dagger,s,p^\dagger,p)} a_s^\dagger a_s a_p^\dagger a_p + \chi_4^{(p^\dagger,s,s^\dagger,p)} a_p^\dagger a_s a_s^\dagger a_p + \chi_4^{(s^\dagger,p,p^\dagger,s)} a_s^\dagger a_p a_p^\dagger a_s + \\
 & + \chi_4^{(p^\dagger,p,i^\dagger,i)} a_p^\dagger a_p a_i^\dagger a_i + \chi_4^{(i^\dagger,i,p^\dagger,p)} a_i^\dagger a_i a_p^\dagger a_p + \chi_4^{(p^\dagger,i,i^\dagger,p)} a_p^\dagger a_i a_i^\dagger a_p + \chi_4^{(i^\dagger,p,p^\dagger,i)} a_i^\dagger a_p a_p^\dagger a_i + \\
 & + \chi_4^{(s^\dagger,s,i^\dagger,i)} a_s^\dagger a_s a_i^\dagger a_i + \chi_4^{(i^\dagger,i,s^\dagger,s)} a_i^\dagger a_i a_s^\dagger a_s + \chi_4^{(s^\dagger,i,i^\dagger,s)} a_s^\dagger a_i a_i^\dagger a_s + \chi_4^{(i^\dagger,s,s^\dagger,i)} a_i^\dagger a_s a_s^\dagger a_i + \\
 & + \chi_4^{(s^\dagger,p,i^\dagger,p)} a_s^\dagger a_p a_i^\dagger a_p + \chi_4^{(i^\dagger,p,s^\dagger,p)} a_i^\dagger a_p a_s^\dagger a_p + \\
 & + \chi_4^{(p^\dagger,s,p^\dagger,i)} a_p^\dagger a_s a_p^\dagger a_i + \chi_4^{(p^\dagger,i,p^\dagger,s)} a_p^\dagger a_i a_p^\dagger a_s = \\
 & = \chi_4^{(p^\dagger,p,p^\dagger,p)} a_p^\dagger a_p a_p^\dagger a_p + \chi_4^{(s^\dagger,s,s^\dagger,s)} a_s^\dagger a_s a_s^\dagger a_s + \chi_4^{(i^\dagger,i,i^\dagger,i)} a_i^\dagger a_i a_i^\dagger a_i + \\
 & + \left[\chi_4^{(p^\dagger,p,s^\dagger,s)} + \chi_4^{(s^\dagger,s,p^\dagger,p)} + \chi_4^{(p^\dagger,s,s^\dagger,p)} + \chi_4^{(s^\dagger,p,p^\dagger,s)} \right] a_p^\dagger a_p a_s^\dagger a_s + \left[\chi_4^{(p^\dagger,s,s^\dagger,p)} \right] a_p^\dagger a_p + \left[\chi_4^{(s^\dagger,p,p^\dagger,s)} \right] a_s^\dagger a_s \\
 & + \left[\chi_4^{(p^\dagger,p,i^\dagger,i)} + \chi_4^{(i^\dagger,i,p^\dagger,p)} + \chi_4^{(p^\dagger,i,i^\dagger,p)} + \chi_4^{(i^\dagger,p,p^\dagger,i)} \right] a_p^\dagger a_p a_i^\dagger a_i + \left[\chi_4^{(p^\dagger,i,i^\dagger,p)} \right] a_p^\dagger a_p + \left[\chi_4^{(i^\dagger,p,p^\dagger,i)} \right] a_i^\dagger a_i \\
 & + \left[\chi_4^{(s^\dagger,s,i^\dagger,i)} + \chi_4^{(i^\dagger,i,s^\dagger,s)} + \chi_4^{(s^\dagger,i,i^\dagger,s)} + \chi_4^{(i^\dagger,s,s^\dagger,i)} \right] a_s^\dagger a_s a_i^\dagger a_i + \left[\chi_4^{(s^\dagger,i,i^\dagger,s)} \right] a_s^\dagger a_s + \left[\chi_4^{(i^\dagger,s,s^\dagger,i)} \right] a_i^\dagger a_i \\
 & + \left[\chi_4^{(s^\dagger,p,i^\dagger,p)} + \chi_4^{(i^\dagger,p,s^\dagger,p)} \right] a_p a_p a_s^\dagger a_i^\dagger + \\
 & + \left[\chi_4^{(p^\dagger,s,p^\dagger,i)} + \chi_4^{(p^\dagger,i,p^\dagger,s)} \right] a_p^\dagger a_p^\dagger a_s a_i
 \end{aligned} \tag{D.7}$$

$$\begin{aligned}
 \sum_{n,l,m,s=\{p,s,i\}} \chi_4^{(n^\dagger,l^\dagger,m,s)} a_n^\dagger a_l^\dagger a_m a_s &= \\
 &= \chi_4^{(p^\dagger,p^\dagger,p,p)} a_p^\dagger a_p^\dagger a_p a_p + \chi_4^{(s^\dagger,s^\dagger,s,s)} a_s^\dagger a_s^\dagger a_s a_s + \chi_4^{(i^\dagger,i^\dagger,i,i)} a_i^\dagger a_i^\dagger a_i a_i + \\
 &+ \chi_4^{(p^\dagger,s^\dagger,p,s)} a_p^\dagger a_s^\dagger a_p a_s + \chi_4^{(p^\dagger,s^\dagger,s,p)} a_p^\dagger a_s^\dagger a_s a_p + \chi_4^{(s^\dagger,p^\dagger,p,s)} a_s^\dagger a_p^\dagger a_p a_s + \chi_4^{(s^\dagger,p^\dagger,s,p)} a_s^\dagger a_p^\dagger a_s a_p + \\
 &+ \chi_4^{(p^\dagger,i^\dagger,p,i)} a_p^\dagger a_i^\dagger a_p a_i + \chi_4^{(p^\dagger,i^\dagger,i,p)} a_p^\dagger a_i^\dagger a_i a_p + \chi_4^{(i^\dagger,p^\dagger,p,i)} a_i^\dagger a_p^\dagger a_p a_i + \chi_4^{(i^\dagger,p^\dagger,i,p)} a_i^\dagger a_p^\dagger a_i a_p + \\
 &+ \chi_4^{(s^\dagger,i^\dagger,s,i)} a_s^\dagger a_i^\dagger a_s a_i + \chi_4^{(s^\dagger,i^\dagger,i,s)} a_s^\dagger a_i^\dagger a_i a_s + \chi_4^{(i^\dagger,s^\dagger,s,i)} a_i^\dagger a_s^\dagger a_s a_i + \chi_4^{(i^\dagger,s^\dagger,i,s)} a_i^\dagger a_s^\dagger a_i a_s + \\
 &+ \chi_4^{(s^\dagger,i^\dagger,p,p)} a_s^\dagger a_i^\dagger a_p a_p + \chi_4^{(i^\dagger,s^\dagger,p,p)} a_i^\dagger a_s^\dagger a_p a_p + \\
 &+ \chi_4^{(p^\dagger,p^\dagger,s,i)} a_p^\dagger a_p^\dagger a_s a_i + \chi_4^{(p^\dagger,p^\dagger,i,s)} a_p^\dagger a_p^\dagger a_i a_s = \\
 &= \left[\chi_4^{(p^\dagger,p^\dagger,p,p)} \right] (a_p^\dagger a_p a_p^\dagger a_p - a_p^\dagger a_p) + \\
 &+ \left[\chi_4^{(s^\dagger,s^\dagger,s,s)} \right] (a_s^\dagger a_s a_s^\dagger a_s - a_s^\dagger a_s) + \\
 &+ \left[\chi_4^{(i^\dagger,i^\dagger,i,i)} \right] (a_i^\dagger a_i a_i^\dagger a_i - a_i^\dagger a_i) + \\
 &+ \left[\chi_4^{(p^\dagger,s^\dagger,p,s)} + \chi_4^{(p^\dagger,s^\dagger,s,p)} + \chi_4^{(s^\dagger,p^\dagger,p,s)} + \chi_4^{(s^\dagger,p^\dagger,s,p)} \right] a_p^\dagger a_p a_s^\dagger a_s + \\
 &+ \left[\chi_4^{(p^\dagger,i^\dagger,p,i)} + \chi_4^{(p^\dagger,i^\dagger,i,p)} + \chi_4^{(i^\dagger,p^\dagger,p,i)} + \chi_4^{(i^\dagger,p^\dagger,i,p)} \right] a_p^\dagger a_p a_i^\dagger a_i + \\
 &+ \left[\chi_4^{(s^\dagger,i^\dagger,s,i)} + \chi_4^{(s^\dagger,i^\dagger,i,s)} + \chi_4^{(i^\dagger,s^\dagger,s,i)} + \chi_4^{(i^\dagger,s^\dagger,i,s)} \right] a_s^\dagger a_s a_i^\dagger a_i + \\
 &+ \left[\chi_4^{(s^\dagger,i^\dagger,p,p)} + \chi_4^{(i^\dagger,s^\dagger,p,p)} \right] a_p a_p a_s^\dagger a_i^\dagger + \\
 &+ \left[\chi_4^{(p^\dagger,p^\dagger,s,i)} + \chi_4^{(p^\dagger,p^\dagger,i,s)} \right] a_p^\dagger a_p^\dagger a_s a_i
 \end{aligned} \tag{D.8}$$

D.2 Self-phase, cross-phase and 4WM coupling constant

Summing e reordering all the terms of Eq. (D.2):

$$\begin{aligned}
 H_{4\text{WM}} = & \hbar \left[2\chi_4^{(p,p,p^\dagger,p^\dagger)} + \chi_4^{(p,p^\dagger,p,p^\dagger)} + 2\chi_4^{(s,s,s^\dagger,s^\dagger)} + \chi_4^{(s,s^\dagger,s,s^\dagger)} + 2\chi_4^{(i,i,i^\dagger,i^\dagger)} + \chi_4^{(i,i^\dagger,i,i^\dagger)} + \right. \\
 & + \chi_4^{(p,s,p^\dagger,s^\dagger)} + \chi_4^{(p,s,s^\dagger,p^\dagger)} + \chi_4^{(s,p,p^\dagger,s^\dagger)} + \chi_4^{(s,p,s^\dagger,p^\dagger)} + \chi_4^{(p,p^\dagger,s,s^\dagger)} + \chi_4^{(s,s^\dagger,p,p^\dagger)} \\
 & + \chi_4^{(p,i,p^\dagger,i^\dagger)} + \chi_4^{(p,i,i^\dagger,p^\dagger)} + \chi_4^{(i,p,p^\dagger,i^\dagger)} + \chi_4^{(i,p,i^\dagger,p^\dagger)} + \chi_4^{(p,p^\dagger,i,i^\dagger)} + \chi_4^{(i,i^\dagger,p,p^\dagger)} + \\
 & \left. + \chi_4^{(s,i,s^\dagger,i^\dagger)} + \chi_4^{(s,i,i^\dagger,s^\dagger)} + \chi_4^{(i,s,s^\dagger,i^\dagger)} + \chi_4^{(i,s,i^\dagger,p^\dagger)} + \chi_4^{(s,s^\dagger,i,i^\dagger)} + \chi_4^{(i,i^\dagger,s,s^\dagger)} \right] \mathbf{1} + \\
 & + \hbar \left[3\chi_4^{(p,p,p^\dagger,p^\dagger)} + 2\chi_4^{(p,p^\dagger,p,p^\dagger)} + \chi_4^{(p,p^\dagger,p^\dagger,p)} + \chi_4^{(p^\dagger,p,p,p^\dagger)} - \chi_4^{(p^\dagger,p^\dagger,p,p)} + \right. \\
 & + \chi_4^{(p,s,p^\dagger,s^\dagger)} + \chi_4^{(p,s,s^\dagger,p^\dagger)} + \chi_4^{(s,p,p^\dagger,s^\dagger)} + \chi_4^{(s,p,s^\dagger,p^\dagger)} + \chi_4^{(p,p^\dagger,s,s^\dagger)} + \chi_4^{(s,s^\dagger,p,p^\dagger)} + \\
 & + \chi_4^{(s,p^\dagger,p,s^\dagger)} + \chi_4^{(s,s^\dagger,p^\dagger,p)} + \chi_4^{(s,p^\dagger,s^\dagger,p)} + \chi_4^{(p^\dagger,p,s,s^\dagger)} + \chi_4^{(p^\dagger,s,p,s^\dagger)} + \chi_4^{(p^\dagger,s,s^\dagger,p)} + \\
 & + \chi_4^{(p,i,p^\dagger,i^\dagger)} + \chi_4^{(p,i,i^\dagger,p^\dagger)} + \chi_4^{(i,p,p^\dagger,i^\dagger)} + \chi_4^{(i,p,i^\dagger,p^\dagger)} + \chi_4^{(p,p^\dagger,i,i^\dagger)} + \chi_4^{(i,i^\dagger,p,p^\dagger)} + \\
 & \left. + \chi_4^{(i,p^\dagger,p,i^\dagger)} + \chi_4^{(i,i^\dagger,p^\dagger,p)} + \chi_4^{(i,p^\dagger,i^\dagger,p)} + \chi_4^{(p^\dagger,p,i,i^\dagger)} + \chi_4^{(p^\dagger,i,p,i^\dagger)} + \chi_4^{(p^\dagger,i,i^\dagger,p)} \right] a_p^\dagger a_p + \\
 & + \hbar \left[3\chi_4^{(s,s,s^\dagger,s^\dagger)} + 2\chi_4^{(s,s^\dagger,s,s^\dagger)} + \chi_4^{(s,s^\dagger,s^\dagger,s)} + \chi_4^{(s^\dagger,s,s,s^\dagger)} - \chi_4^{(s^\dagger,s^\dagger,s,s)} + \right. \\
 & + \chi_4^{(p,s,p^\dagger,s^\dagger)} + \chi_4^{(p,s,s^\dagger,p^\dagger)} + \chi_4^{(s,p,p^\dagger,s^\dagger)} + \chi_4^{(s,p,s^\dagger,p^\dagger)} + \chi_4^{(p,p^\dagger,s,s^\dagger)} + \chi_4^{(s,s^\dagger,p,p^\dagger)} + \\
 & + \chi_4^{(p,s^\dagger,s,p^\dagger)} + \chi_4^{(p,p^\dagger,s^\dagger,s)} + \chi_4^{(p,s^\dagger,p^\dagger,s)} + \chi_4^{(s^\dagger,s,p,p^\dagger)} + \chi_4^{(s^\dagger,p,s,p^\dagger)} + \chi_4^{(s^\dagger,p,p^\dagger,s)} + \\
 & + \chi_4^{(s,i,s^\dagger,i^\dagger)} + \chi_4^{(s,i,i^\dagger,s^\dagger)} + \chi_4^{(i,s,s^\dagger,i^\dagger)} + \chi_4^{(i,s,i^\dagger,s^\dagger)} + \chi_4^{(s,s^\dagger,i,i^\dagger)} + \chi_4^{(i,i^\dagger,s,s^\dagger)} + \\
 & \left. + \chi_4^{(i,s^\dagger,s,i^\dagger)} + \chi_4^{(i,i^\dagger,s^\dagger,s)} + \chi_4^{(i,s^\dagger,i^\dagger,s)} + \chi_4^{(s^\dagger,s,i,i^\dagger)} + \chi_4^{(s^\dagger,i,s,i^\dagger)} + \chi_4^{(s^\dagger,i,i^\dagger,s)} \right] a_s^\dagger a_s + \\
 & + \hbar \left[3\chi_4^{(i,i,i^\dagger,i^\dagger)} + 2\chi_4^{(i,i^\dagger,i,i^\dagger)} + \chi_4^{(i,i^\dagger,i^\dagger,i)} + \chi_4^{(i^\dagger,i,i,i^\dagger)} - \chi_4^{(i^\dagger,i^\dagger,i,i)} + \right. \\
 & + \chi_4^{(p,i,p^\dagger,i^\dagger)} + \chi_4^{(p,i,i^\dagger,p^\dagger)} + \chi_4^{(i,p,p^\dagger,i^\dagger)} + \chi_4^{(i,p,i^\dagger,p^\dagger)} + \chi_4^{(p,p^\dagger,i,i^\dagger)} + \chi_4^{(i,i^\dagger,p,p^\dagger)} + \\
 & + \chi_4^{(p,i^\dagger,i,p^\dagger)} + \chi_4^{(p,p^\dagger,i^\dagger,i)} + \chi_4^{(p,i^\dagger,p^\dagger,i)} + \chi_4^{(i^\dagger,i,p,p^\dagger)} + \chi_4^{(i^\dagger,i,p,p^\dagger)} + \chi_4^{(i^\dagger,p,p^\dagger,i)} + \\
 & + \chi_4^{(s,i,s^\dagger,i^\dagger)} + \chi_4^{(s,i,i^\dagger,s^\dagger)} + \chi_4^{(i,s,s^\dagger,i^\dagger)} + \chi_4^{(i,s,i^\dagger,s^\dagger)} + \chi_4^{(s,s^\dagger,i,i^\dagger)} + \chi_4^{(i,i^\dagger,s,s^\dagger)} + \\
 & \left. + \chi_4^{(s,i^\dagger,i,s^\dagger)} + \chi_4^{(s,s^\dagger,i^\dagger,i)} + \chi_4^{(s,i^\dagger,s^\dagger,i)} + \chi_4^{(i^\dagger,i,s,s^\dagger)} + \chi_4^{(i^\dagger,i,s,s^\dagger)} + \chi_4^{(i^\dagger,s,s^\dagger,i)} \right] a_i^\dagger a_i +
 \end{aligned}
 \tag{D.9}$$

$$\begin{aligned}
 & + \hbar \left[\chi_4^{(p,p,p^\dagger,p^\dagger)} + \chi_4^{(p,p^\dagger,p,p^\dagger)} + \chi_4^{(p,p^\dagger,p^\dagger,p)} + \chi_4^{(p^\dagger,p,p,p^\dagger)} + \chi_4^{(p^\dagger,p,p^\dagger,p)} + \chi_4^{(p^\dagger,p^\dagger,p,p)} \right] a_p^\dagger a_p a_p^\dagger a_p + \\
 & + \hbar \left[\chi_4^{(s,s,s^\dagger,s^\dagger)} + \chi_4^{(s,s^\dagger,s,s^\dagger)} + \chi_4^{(s,s^\dagger,s^\dagger,s)} + \chi_4^{(s^\dagger,s,s,s^\dagger)} + \chi_4^{(s^\dagger,s,s^\dagger,s)} + \chi_4^{(s^\dagger,s^\dagger,s,s)} \right] a_s^\dagger a_s a_s^\dagger a_s + \\
 & + \hbar \left[\chi_4^{(i,i,i^\dagger,i^\dagger)} + \chi_4^{(i,i^\dagger,i,i^\dagger)} + \chi_4^{(i,i^\dagger,i^\dagger,i)} + \chi_4^{(i^\dagger,i,i,i^\dagger)} + \chi_4^{(i^\dagger,i,i^\dagger,i)} + \chi_4^{(i^\dagger,i^\dagger,i,i)} \right] a_i^\dagger a_i a_i^\dagger a_i + \\
 & + \hbar \left[\chi_4^{(p,s,p^\dagger,s^\dagger)} + \chi_4^{(p,s,s^\dagger,p^\dagger)} + \chi_4^{(s,p,p^\dagger,s^\dagger)} + \chi_4^{(s,p,s^\dagger,p^\dagger)} + \chi_4^{(p,p^\dagger,s,s^\dagger)} + \chi_4^{(s,s^\dagger,p,p^\dagger)} + \chi_4^{(p,s^\dagger,s,p^\dagger)} + \chi_4^{(s,p^\dagger,p,s^\dagger)} \right. \\
 & \quad + \chi_4^{(p,p^\dagger,s^\dagger,s)} + \chi_4^{(s,s^\dagger,p^\dagger,p)} + \chi_4^{(p,s^\dagger,p^\dagger,s)} + \chi_4^{(s,p^\dagger,s^\dagger,p)} + \chi_4^{(p^\dagger,p,s,s^\dagger)} + \chi_4^{(s^\dagger,s,p,p^\dagger)} + \\
 & \quad + \chi_4^{(p^\dagger,s,p,s^\dagger)} + \chi_4^{(s^\dagger,p,s,p^\dagger)} + \chi_4^{(p^\dagger,p,s^\dagger,s)} + \chi_4^{(s^\dagger,s,p^\dagger,p)} + \chi_4^{(p^\dagger,s,s^\dagger,p)} + \chi_4^{(s^\dagger,p,p^\dagger,s)} + \\
 & \quad \left. + \chi_4^{(p^\dagger,s^\dagger,p,s)} + \chi_4^{(p^\dagger,s^\dagger,s,p)} + \chi_4^{(s^\dagger,p^\dagger,p,s)} + \chi_4^{(s^\dagger,p^\dagger,s,p)} \right] a_p^\dagger a_p a_s^\dagger a_s + \\
 & + \hbar \left[\chi_4^{(p,i,p^\dagger,i^\dagger)} + \chi_4^{(p,i,i^\dagger,p^\dagger)} + \chi_4^{(i,p,p^\dagger,i^\dagger)} + \chi_4^{(i,p,i^\dagger,p^\dagger)} + \chi_4^{(p,p^\dagger,i,i^\dagger)} + \chi_4^{(i,i^\dagger,p,p^\dagger)} + \chi_4^{(p,i^\dagger,i,p^\dagger)} + \chi_4^{(i,p^\dagger,p,i^\dagger)} \right. \\
 & \quad + \chi_4^{(p,p^\dagger,i^\dagger,i)} + \chi_4^{(i,i^\dagger,p^\dagger,p)} + \chi_4^{(p,i^\dagger,p^\dagger,i)} + \chi_4^{(i,p^\dagger,i^\dagger,p)} + \chi_4^{(p^\dagger,p,i,i^\dagger)} + \chi_4^{(i^\dagger,i,p,p^\dagger)} + \\
 & \quad + \chi_4^{(p^\dagger,i,p,i^\dagger)} + \chi_4^{(i^\dagger,p,i,p^\dagger)} + \chi_4^{(p^\dagger,p,i^\dagger,i)} + \chi_4^{(i^\dagger,i,p^\dagger,p)} + \chi_4^{(p^\dagger,i,i^\dagger,p)} + \chi_4^{(i^\dagger,p,p^\dagger,i)} + \\
 & \quad \left. + \chi_4^{(p^\dagger,i^\dagger,p,i)} + \chi_4^{(p^\dagger,i^\dagger,i,p)} + \chi_4^{(i^\dagger,p^\dagger,p,i)} + \chi_4^{(i^\dagger,p^\dagger,i,p)} \right] a_p^\dagger a_p a_i^\dagger a_i + \\
 & + \hbar \left[\chi_4^{(s,i,s^\dagger,i^\dagger)} + \chi_4^{(s,i,i^\dagger,s^\dagger)} + \chi_4^{(i,s,s^\dagger,i^\dagger)} + \chi_4^{(i,s,i^\dagger,s^\dagger)} + \chi_4^{(s,s^\dagger,i,i^\dagger)} + \chi_4^{(i,i^\dagger,s,s^\dagger)} + \chi_4^{(s,i^\dagger,i,s^\dagger)} + \chi_4^{(i,s^\dagger,s,i^\dagger)} \right. \\
 & \quad + \chi_4^{(s,s^\dagger,i^\dagger,i)} + \chi_4^{(i,i^\dagger,s^\dagger,s)} + \chi_4^{(s,i^\dagger,s^\dagger,i)} + \chi_4^{(i,s^\dagger,i^\dagger,s)} + \chi_4^{(s^\dagger,s,i,i^\dagger)} + \chi_4^{(i^\dagger,i,s,s^\dagger)} + \\
 & \quad + \chi_4^{(s^\dagger,i,s,i^\dagger)} + \chi_4^{(i^\dagger,s,i,s^\dagger)} + \chi_4^{(s^\dagger,s,i^\dagger,i)} + \chi_4^{(i^\dagger,i,s^\dagger,s)} + \chi_4^{(s^\dagger,i,i^\dagger,s)} + \chi_4^{(i^\dagger,s,s^\dagger,i)} + \\
 & \quad \left. + \chi_4^{(s^\dagger,i^\dagger,s,i)} + \chi_4^{(s^\dagger,i^\dagger,i,s)} + \chi_4^{(i^\dagger,s^\dagger,s,i)} + \chi_4^{(i^\dagger,s^\dagger,i,s)} \right] a_s^\dagger a_s a_i^\dagger a_i + \\
 & + \hbar \left[\chi_4^{(p,p,s^\dagger,i^\dagger)} + \chi_4^{(p,p,i^\dagger,s^\dagger)} + \chi_4^{(p,s^\dagger,p,i^\dagger)} + \chi_4^{(p,i^\dagger,p,s^\dagger)} + \chi_4^{(p,s^\dagger,i^\dagger,p)} + \chi_4^{(p,i^\dagger,s^\dagger,p)} \right. \\
 & \quad \left. + \chi_4^{(s^\dagger,p,p,i^\dagger)} + \chi_4^{(i^\dagger,p,p,s^\dagger)} + \chi_4^{(s^\dagger,p,i^\dagger,p)} + \chi_4^{(i^\dagger,p,s^\dagger,p)} + \chi_4^{(s^\dagger,i^\dagger,p,p)} + \chi_4^{(i^\dagger,s^\dagger,p,p)} \right] a_p a_p a_s^\dagger a_i^\dagger + \\
 & + \hbar \left[\chi_4^{(p^\dagger,p^\dagger,s,i)} + \chi_4^{(p^\dagger,p^\dagger,i,s)} + \chi_4^{(p^\dagger,s,p^\dagger,i)} + \chi_4^{(p^\dagger,i,p^\dagger,s)} + \chi_4^{(p^\dagger,s,i,p^\dagger)} + \chi_4^{(p^\dagger,i,s,p^\dagger)} \right. \\
 & \quad \left. + \chi_4^{(s,p^\dagger,p^\dagger,i)} + \chi_4^{(i,p^\dagger,p^\dagger,s)} + \chi_4^{(s,p^\dagger,i,p^\dagger)} + \chi_4^{(i,p^\dagger,s,p^\dagger)} + \chi_4^{(s,i,p^\dagger,p^\dagger)} + \chi_4^{(i,s,p^\dagger,p^\dagger)} \right] a_p^\dagger a_p^\dagger a_s a_i
 \end{aligned} \tag{D.10}$$

Moreover, we can define the *self-phase modulation parameter* of the pump ξ_{pp} as the sum of all the coefficients $\chi_4^{(n,l,m,s)}$ associated to the energy conservative permutation of four ladder operators with $n, l, m, s = \{p\}$

$$\xi_{pp} \equiv \sum_{n,l,m,s=\{p\}} \chi_4^{(n,l,m,s)} = \chi_4^{(p,p,p^\dagger,p^\dagger)} + \chi_4^{(p,p^\dagger,p,p^\dagger)} + \chi_4^{(p,p^\dagger,p^\dagger,p)} + \chi_4^{(p^\dagger,p,p,p^\dagger)} + \chi_4^{(p^\dagger,p,p^\dagger,p)} + \chi_4^{(p^\dagger,p^\dagger,p,p)} \tag{D.11}$$

the *self-phase modulation parameter* of the signal ξ_{ss} as the sum of all the coefficients $\chi_4^{(n,l,m,s)}$ associated to the energy-conservative permutation of four ladder operators with $n, l, m, s = \{s\}$

$$\xi_{ss} \equiv \sum_{n,l,m,s=\{s\}} \chi_4^{(n,l,m,s)} = \chi_4^{(s,s,s^\dagger,s^\dagger)} + \chi_4^{(s,s^\dagger,s,s^\dagger)} + \chi_4^{(s,s^\dagger,s^\dagger,s)} + \chi_4^{(s^\dagger,s,s,s^\dagger)} + \chi_4^{(s^\dagger,s,s^\dagger,s)} + \chi_4^{(s^\dagger,s^\dagger,s,s)} \quad (\text{D.12})$$

and the *self-phase modulation parameter* of the idler ξ_{ii} as the sum of all the coefficients $\chi_4^{(n,l,m,s)}$ associated to the energy-conservative permutation of four ladder operators with $n, l, m, s = \{i\}$

$$\xi_{ii} \equiv \sum_{n,l,m,s=\{i\}} \chi_4^{(n,l,m,s)} = \chi_4^{(i,i,i^\dagger,i^\dagger)} + \chi_4^{(i,i^\dagger,i,i^\dagger)} + \chi_4^{(i,i^\dagger,i^\dagger,i)} + \chi_4^{(i^\dagger,i,i,i^\dagger)} + \chi_4^{(i^\dagger,i,i^\dagger,i)} + \chi_4^{(i^\dagger,i^\dagger,i,i)} \quad (\text{D.13})$$

Furthermore, we can define the *cross-phase modulation parameter* between pump and signal ξ_{ps} as the sum of all the coefficients $\chi_4^{(n,l,m,s)}$ associated to the energy-conservative permutation of four ladder operators with $n, l, m, s = \{p, s\}$

$$\begin{aligned} \xi_{ps} \equiv \sum_{n,l,m,s=\{p,s\}} \chi_4^{(n,l,m,s)} = & \chi_4^{(p,s,p^\dagger,s^\dagger)} + \chi_4^{(p,s,s^\dagger,p^\dagger)} + \chi_4^{(s,p,p^\dagger,s^\dagger)} + \chi_4^{(s,p,s^\dagger,p^\dagger)} + \\ & + \chi_4^{(p,p^\dagger,s,s^\dagger)} + \chi_4^{(s,s^\dagger,p,p^\dagger)} + \chi_4^{(p,s^\dagger,s,p^\dagger)} + \chi_4^{(s,p^\dagger,p,s^\dagger)} + \\ & + \chi_4^{(p,p^\dagger,s^\dagger,s)} + \chi_4^{(s,s^\dagger,p^\dagger,p)} + \chi_4^{(p,s^\dagger,p^\dagger,s)} + \chi_4^{(s,p^\dagger,s^\dagger,p)} + \\ & + \chi_4^{(p^\dagger,p,s,s^\dagger)} + \chi_4^{(s^\dagger,s,p,p^\dagger)} + \chi_4^{(p^\dagger,s,p,s^\dagger)} + \chi_4^{(s^\dagger,p,s,p^\dagger)} + \\ & + \chi_4^{(p^\dagger,p,s^\dagger,s)} + \chi_4^{(s^\dagger,s,p^\dagger,p)} + \chi_4^{(p^\dagger,s,s^\dagger,p)} + \chi_4^{(s^\dagger,p,p^\dagger,s)} + \\ & + \chi_4^{(p^\dagger,s^\dagger,p,s)} + \chi_4^{(p^\dagger,s^\dagger,s,p)} + \chi_4^{(s^\dagger,p^\dagger,p,s)} + \chi_4^{(s^\dagger,p^\dagger,s,p)} \quad (\text{D.14}) \end{aligned}$$

the *cross-phase modulation parameter* between pump and idler ξ_{pi} as the sum of all the coefficients $\chi_4^{(n,l,m,s)}$ associated to the energy-conservative permutation of four ladder operators with $n, l, m, s = \{p, i\}$

$$\begin{aligned} \xi_{pi} \equiv \sum_{n,l,m,s=\{p,i\}} \chi_4^{(n,l,m,s)} = & \chi_4^{(p,i,p^\dagger,i^\dagger)} + \chi_4^{(p,i,i^\dagger,p^\dagger)} + \chi_4^{(i,p,p^\dagger,i^\dagger)} + \chi_4^{(i,p,i^\dagger,p^\dagger)} + \\ & + \chi_4^{(p,p^\dagger,i,i^\dagger)} + \chi_4^{(i,i^\dagger,p,p^\dagger)} + \chi_4^{(p,i^\dagger,i,p^\dagger)} + \chi_4^{(i,p^\dagger,p,i^\dagger)} + \\ & + \chi_4^{(p,p^\dagger,i^\dagger,i)} + \chi_4^{(i,i^\dagger,p^\dagger,p)} + \chi_4^{(p,i^\dagger,p^\dagger,i)} + \chi_4^{(i,p^\dagger,i^\dagger,p)} + \\ & + \chi_4^{(p^\dagger,p,i,i^\dagger)} + \chi_4^{(i^\dagger,i,p,p^\dagger)} + \chi_4^{(p^\dagger,i,p,i^\dagger)} + \chi_4^{(i^\dagger,p,i,p^\dagger)} + \\ & + \chi_4^{(p^\dagger,p,i^\dagger,i)} + \chi_4^{(i^\dagger,i,p^\dagger,p)} + \chi_4^{(p^\dagger,i,i^\dagger,p)} + \chi_4^{(i^\dagger,p,p^\dagger,i)} + \\ & + \chi_4^{(p^\dagger,i^\dagger,p,i)} + \chi_4^{(p^\dagger,i^\dagger,i,p)} + \chi_4^{(i^\dagger,p^\dagger,p,i)} + \chi_4^{(i^\dagger,p^\dagger,i,p)} \quad (\text{D.15}) \end{aligned}$$

and the *cross-phase modulation parameter* between signal and idler ξ_{si} as the sum of all the coefficients $\chi_4^{(n,l,m,s)}$ associated to the energy-conservative permutation of

four ladder operators with $n, l, m, s = \{s, i\}$

$$\begin{aligned}
 \xi_{si} \equiv \sum_{n,l,m,s=\{p,i\}} \chi_4^{(n,l,m,s)} = & \chi_4^{(s,i,s^\dagger,i^\dagger)} + \chi_4^{(s,i,i^\dagger,s^\dagger)} + \chi_4^{(i,s,s^\dagger,i^\dagger)} + \chi_4^{(i,s,i^\dagger,s^\dagger)} + \\
 & + \chi_4^{(s,s^\dagger,i,i^\dagger)} + \chi_4^{(i,i^\dagger,s,s^\dagger)} + \chi_4^{(s,i^\dagger,i,s^\dagger)} + \chi_4^{(i,s^\dagger,s,i^\dagger)} + \\
 & + \chi_4^{(s,s^\dagger,i^\dagger,i)} + \chi_4^{(i,i^\dagger,s^\dagger,s)} + \chi_4^{(s,i^\dagger,s^\dagger,i)} + \chi_4^{(i,s^\dagger,i^\dagger,s)} + \\
 & + \chi_4^{(s^\dagger,s,i,i^\dagger)} + \chi_4^{(i^\dagger,i,s,s^\dagger)} + \chi_4^{(s^\dagger,i,s,i^\dagger)} + \chi_4^{(i^\dagger,s,i,s^\dagger)} + \\
 & + \chi_4^{(s^\dagger,s,i^\dagger,i)} + \chi_4^{(i^\dagger,i,s^\dagger,s)} + \chi_4^{(s^\dagger,i,i^\dagger,s)} + \chi_4^{(i^\dagger,s,s^\dagger,i)} + \\
 & + \chi_4^{(s^\dagger,i^\dagger,s,i)} + \chi_4^{(s^\dagger,i^\dagger,i,s)} + \chi_4^{(i^\dagger,s^\dagger,s,i)} + \chi_4^{(i^\dagger,s^\dagger,i,s)} \quad (D.16)
 \end{aligned}$$

Eventually, exploiting the fact that it can be easily demonstrated that the coefficient $\chi_4^{(n,l,m,s)}$ associated to a particular ladder operator combination and the one associated to the hermitian conjugate of this combination are identical (i.e., $\chi_4^{(p,p,s^\dagger,i^\dagger)} = \chi_4^{(p^\dagger,p^\dagger,s,i)}$, $\chi_4^{(s^\dagger,p,i^\dagger,p)} = \chi_4^{(s,p^\dagger,i,s^\dagger)}$, etc ...) we can define the *four-wave mixing term* $\hbar\chi_4^{\{p,p,s,i\}}$ as one half of the sum of all the coefficients $\chi_4^{(n,l,m,s)}$ associated to the energy-conservative permutation of four ladder operators with two indexes equal to p , one index equal to s and the last one equal to i

$$\begin{aligned}
 \chi_4^{\{p,p,s,i\}} \equiv & \chi_4^{(p,p,s^\dagger,i^\dagger)} + \chi_4^{(p,p,i^\dagger,s^\dagger)} + \chi_4^{(p,s^\dagger,p,i^\dagger)} + \chi_4^{(p,i^\dagger,p,s^\dagger)} + \chi_4^{(p,s^\dagger,i^\dagger,p)} + \chi_4^{(p,i^\dagger,s^\dagger,p)} + \\
 & + \chi_4^{(s^\dagger,p,p,i^\dagger)} + \chi_4^{(i^\dagger,p,p,s^\dagger)} + \chi_4^{(s^\dagger,p,i^\dagger,p)} + \chi_4^{(i^\dagger,p,s^\dagger,p)} + \chi_4^{(s^\dagger,i^\dagger,p,p)} + \chi_4^{(i^\dagger,s^\dagger,p,p)} = \\
 = & \chi_4^{(p^\dagger,p^\dagger,s,i)} + \chi_4^{(p^\dagger,p^\dagger,i,s)} + \chi_4^{(p^\dagger,s,p^\dagger,i)} + \chi_4^{(p^\dagger,i,p^\dagger,s)} + \chi_4^{(p^\dagger,s,i,p^\dagger)} + \chi_4^{(p^\dagger,i,s,p^\dagger)} \\
 & + \chi_4^{(s,p^\dagger,p^\dagger,i)} + \chi_4^{(i,p^\dagger,p^\dagger,s)} + \chi_4^{(s,p^\dagger,i,p^\dagger)} + \chi_4^{(i,p^\dagger,s,p^\dagger)} + \chi_4^{(s,i,p^\dagger,p^\dagger)} + \chi_4^{(i,s,p^\dagger,p^\dagger)} \quad (D.17)
 \end{aligned}$$

The term proportional to no ladder operators is defined ξ_0 , while the terms proportional to a couple of creation-annihilation operators respectively of the pump, signal and idler tones are ξ_p , ξ_s , and ξ_i

$$\begin{aligned}
 \xi_0 \equiv & 2\chi_4^{(p,p,p^\dagger,p^\dagger)} + \chi_4^{(p,p^\dagger,p,p^\dagger)} + 2\chi_4^{(s,s,s^\dagger,s^\dagger)} + \chi_4^{(s,s^\dagger,s,s^\dagger)} + 2\chi_4^{(i,i,i^\dagger,i^\dagger)} + \chi_4^{(i,i^\dagger,i,i^\dagger)} + \\
 & + \chi_4^{(p,s,p^\dagger,s^\dagger)} + \chi_4^{(p,s,s^\dagger,p^\dagger)} + \chi_4^{(s,p,p^\dagger,s^\dagger)} + \chi_4^{(s,p,s^\dagger,p^\dagger)} + \chi_4^{(p,p^\dagger,s,s^\dagger)} + \chi_4^{(s,s^\dagger,p,p^\dagger)} + \\
 & + \chi_4^{(p,i,p^\dagger,i^\dagger)} + \chi_4^{(p,i,i^\dagger,p^\dagger)} + \chi_4^{(i,p,p^\dagger,i^\dagger)} + \chi_4^{(i,p,i^\dagger,p^\dagger)} + \chi_4^{(p,p^\dagger,i,i^\dagger)} + \chi_4^{(i,i^\dagger,p,p^\dagger)} + \\
 & + \chi_4^{(s,i,s^\dagger,i^\dagger)} + \chi_4^{(s,i,i^\dagger,s^\dagger)} + \chi_4^{(i,s,s^\dagger,i^\dagger)} + \chi_4^{(i,s,i^\dagger,p^\dagger)} + \chi_4^{(s,s^\dagger,i,i^\dagger)} + \chi_4^{(i,i^\dagger,s,s^\dagger)} \quad (D.18)
 \end{aligned}$$

$$\begin{aligned}
 \xi_p \equiv & 3\chi_4^{(p,p,p^\dagger,p^\dagger)} + 2\chi_4^{(p,p^\dagger,p,p^\dagger)} + \chi_4^{(p,p^\dagger,p^\dagger,p)} + \chi_4^{(p^\dagger,p,p,p^\dagger)} - \chi_4^{(p^\dagger,p^\dagger,p,p)} + \\
 & + \chi_4^{(p,s,p^\dagger,s^\dagger)} + \chi_4^{(p,s,s^\dagger,p^\dagger)} + \chi_4^{(s,p,p^\dagger,s^\dagger)} + \chi_4^{(s,p,s^\dagger,p^\dagger)} + \chi_4^{(p,p^\dagger,s,s^\dagger)} + \chi_4^{(s,s^\dagger,p,p^\dagger)} + \\
 & + \chi_4^{(s,p^\dagger,p,s^\dagger)} + \chi_4^{(s,s^\dagger,p^\dagger,p)} + \chi_4^{(s,p^\dagger,s^\dagger,p)} + \chi_4^{(p^\dagger,p,p,s^\dagger)} + \chi_4^{(p^\dagger,s,p,s^\dagger)} + \chi_4^{(p^\dagger,s,s^\dagger,p)} + \\
 & + \chi_4^{(p,i,p^\dagger,i^\dagger)} + \chi_4^{(p,i,i^\dagger,p^\dagger)} + \chi_4^{(i,p,p^\dagger,i^\dagger)} + \chi_4^{(i,p,i^\dagger,p^\dagger)} + \chi_4^{(p,p^\dagger,i,i^\dagger)} + \chi_4^{(i,i^\dagger,p,p^\dagger)} + \\
 & + \chi_4^{(i,p^\dagger,p,i^\dagger)} + \chi_4^{(i,i^\dagger,p^\dagger,p)} + \chi_4^{(i,p^\dagger,i^\dagger,p)} + \chi_4^{(p^\dagger,p,i,i^\dagger)} + \chi_4^{(p^\dagger,i,p,i^\dagger)} + \chi_4^{(p^\dagger,i,i^\dagger,p)} \quad (D.19)
 \end{aligned}$$

$$\begin{aligned}
 \xi_s \equiv & 3\chi_4^{(s,s,s^\dagger,s^\dagger)} + 2\chi_4^{(s,s^\dagger,s,s^\dagger)} + \chi_4^{(s,s^\dagger,s^\dagger,s)} + \chi_4^{(s^\dagger,s,s,s^\dagger)} - \chi_4^{(s^\dagger,s^\dagger,s,s)} + \\
 & + \chi_4^{(p,s,p^\dagger,s^\dagger)} + \chi_4^{(p,s,s^\dagger,p^\dagger)} + \chi_4^{(s,p,p^\dagger,s^\dagger)} + \chi_4^{(s,p,s^\dagger,p^\dagger)} + \chi_4^{(p,p^\dagger,s,s^\dagger)} + \chi_4^{(s,s^\dagger,p,p^\dagger)} + \\
 & + \chi_4^{(p,s^\dagger,s,p^\dagger)} + \chi_4^{(p,p^\dagger,s^\dagger,s)} + \chi_4^{(p,s^\dagger,p^\dagger,s)} + \chi_4^{(s^\dagger,s,p,p^\dagger)} + \chi_4^{(s^\dagger,p,s,p^\dagger)} + \chi_4^{(s^\dagger,p,p^\dagger,s)} + \\
 & + \chi_4^{(s,i,s^\dagger,i^\dagger)} + \chi_4^{(s,i,i^\dagger,s^\dagger)} + \chi_4^{(i,s,s^\dagger,i^\dagger)} + \chi_4^{(i,s,i^\dagger,s^\dagger)} + \chi_4^{(s,s^\dagger,i,i^\dagger)} + \chi_4^{(i,i^\dagger,s,s^\dagger)} + \\
 & + \chi_4^{(i,s^\dagger,s,i^\dagger)} + \chi_4^{(i,i^\dagger,s^\dagger,s)} + \chi_4^{(i,s^\dagger,i^\dagger,s)} + \chi_4^{(s^\dagger,s,i,i^\dagger)} + \chi_4^{(s^\dagger,i,s,i^\dagger)} + \chi_4^{(s^\dagger,i,i^\dagger,s)} \quad (D.20)
 \end{aligned}$$

and

$$\begin{aligned}
 \xi_i \equiv & 3\chi_4^{(i,i,i^\dagger,i^\dagger)} + 2\chi_4^{(i,i^\dagger,i,i^\dagger)} + \chi_4^{(i,i^\dagger,i^\dagger,i)} + \chi_4^{(i^\dagger,i,i,i^\dagger)} - \chi_4^{(i^\dagger,i^\dagger,i,i)} + \\
 & + \chi_4^{(p,i,p^\dagger,i^\dagger)} + \chi_4^{(p,i,i^\dagger,p^\dagger)} + \chi_4^{(i,p,p^\dagger,i^\dagger)} + \chi_4^{(i,p,i^\dagger,p^\dagger)} + \chi_4^{(p,p^\dagger,i,i^\dagger)} + \chi_4^{(i,i^\dagger,p,p^\dagger)} + \\
 & + \chi_4^{(p,i^\dagger,i,p^\dagger)} + \chi_4^{(p,p^\dagger,i^\dagger,i)} + \chi_4^{(p,i^\dagger,p^\dagger,i)} + \chi_4^{(i^\dagger,i,p,p^\dagger)} + \chi_4^{(i^\dagger,i,p,p^\dagger)} + \chi_4^{(i^\dagger,p,p^\dagger,i)} + \\
 & + \chi_4^{(s,i,s^\dagger,i^\dagger)} + \chi_4^{(s,i,i^\dagger,s^\dagger)} + \chi_4^{(i,s,s^\dagger,i^\dagger)} + \chi_4^{(i,s,i^\dagger,s^\dagger)} + \chi_4^{(s,s^\dagger,i,i^\dagger)} + \chi_4^{(i,i^\dagger,s,s^\dagger)} + \\
 & + \chi_4^{(s,i^\dagger,i,s^\dagger)} + \chi_4^{(s,s^\dagger,i^\dagger,i)} + \chi_4^{(s,i^\dagger,s^\dagger,i)} + \chi_4^{(i^\dagger,i,s,s^\dagger)} + \chi_4^{(i^\dagger,i,s,s^\dagger)} + \chi_4^{(i^\dagger,s,s^\dagger,i)} \quad (D.21)
 \end{aligned}$$

The total Hamiltonian can finally be rewritten as

$$\begin{aligned}
 \hat{H}_4 = & \hbar\xi_0 + \hbar\xi_p\hat{a}_p^\dagger\hat{a}_p + \hbar\xi_s\hat{a}_s^\dagger\hat{a}_s + \hbar\xi_i\hat{a}_i^\dagger\hat{a}_i + \\
 & + \hbar\xi_{pp}\hat{a}_p^\dagger\hat{a}_p\hat{a}_p^\dagger\hat{a}_p + \hbar\xi_{ss}\hat{a}_s^\dagger\hat{a}_s\hat{a}_s^\dagger\hat{a}_s + \hbar\xi_{ii}\hat{a}_i^\dagger\hat{a}_i\hat{a}_i^\dagger\hat{a}_i + \\
 & + \hbar\xi_{ps}\hat{a}_p^\dagger\hat{a}_p\hat{a}_s^\dagger\hat{a}_s + \hbar\xi_{pi}\hat{a}_p^\dagger\hat{a}_p\hat{a}_i^\dagger\hat{a}_i + \hbar\xi_{si}\hat{a}_s^\dagger\hat{a}_s\hat{a}_i^\dagger\hat{a}_i + \\
 & + \hbar\chi_4^{\{p,p,s,i\}}(\hat{a}_p^\dagger\hat{a}_p^\dagger\hat{a}_s\hat{a}_i + \hat{a}_p\hat{a}_p\hat{a}_s^\dagger\hat{a}_i^\dagger) \quad (D.22)
 \end{aligned}$$

Appendix E

Solution of the coupled mode equations for $\hat{a}_s^{CR}(t)$ and $\hat{a}_i^{CR}(t)$

To solve the system composed by

$$\frac{d\hat{a}_s^{CR}}{dt} = -i\chi_3|A_{p,0}| \left(\hat{a}_i^{CR}\right)^\dagger e^{-i\Psi t} \quad (\text{E.1})$$

and

$$\frac{d\hat{a}_i^{CR}}{dt} = -i\chi_3|A_{p,0}| \left(\hat{a}_s^{CR}\right)^\dagger e^{-i\Psi t} \quad (\text{E.2})$$

we can first time-derivate Eq. (E.1)

$$\begin{aligned} \frac{d^2}{dt^2} [\hat{a}_s^{CR}] &= \frac{d}{dt} \left[\frac{d\hat{a}_s^{CR}}{dt} \right] = \frac{d}{dt} \left[-i\chi_3|A_{p,0}| \left(\hat{a}_i^{CR}\right)^\dagger e^{-i\Psi t} \right] = \\ &= -i\chi_3|A_{p,0}| \left(\frac{d\left(\hat{a}_i^{CR}\right)^\dagger}{dt} e^{-i\Psi t} + \left(\hat{a}_i^{CR}\right)^\dagger (-i\Psi) e^{-i\Psi t} \right) \end{aligned} \quad (\text{E.3})$$

and substituting the expression for $d\left(\hat{a}_i^{CR}\right)^\dagger/dt$ obtained from Eq. (E.2):

$$\begin{aligned} \frac{d^2}{dt^2} [\hat{a}_s^{CR}] &= -i\chi_3|A_{p,0}| \left(\left(i\chi_3|A_{p,0}| \hat{a}_s^{CR} e^{i\Psi t} \right) - i\Psi \left(\hat{a}_i^{CR}\right)^\dagger \right) e^{-i\Psi t} = \\ &= \chi_3^2|A_{p,0}|^2 \hat{a}_s^{CR} - \chi_3|A_{p,0}| \Psi \left(\hat{a}_i^{CR}\right)^\dagger e^{-i\Psi t} \end{aligned} \quad (\text{E.4})$$

From Eq. (E.1) we also obtain

$$\left(\hat{a}_i^{CR}\right)^\dagger = \frac{i}{\chi_3|A_{p,0}|} \frac{d\hat{a}_s^{CR}}{dt} e^{i\Psi t} \quad (\text{E.5})$$

Substituting Eq. (E.5) in Eq. (E.4) we obtain

$$\frac{d^2}{dt^2} [\hat{a}_s^{CR}] = \chi_3^2 |A_{p,0}|^2 \hat{a}_s^{CR} - \chi_3 |A_{p,0}| \Psi \left(\frac{i}{\chi_3 |A_{p,0}|} \frac{d\hat{a}_s^{CR}}{dt} e^{i\Psi t} \right) e^{-i\Psi t} = \chi_3^2 |A_{p,0}|^2 \hat{a}_s^{CR} - i\Psi \frac{d\hat{a}_s^{CR}}{dt} \quad (\text{E.6})$$

that can be recasted as

$$\frac{d^2 \hat{a}_s^{CR}}{dt^2} + i\Psi \frac{d\hat{a}_s^{CR}}{dt} - \chi_3^2 |A_{p,0}|^2 \hat{a}_s^{CR} = 0 \quad (\text{E.7})$$

also known as *Sturm-Liouville equation*. Similarly, one can demonstrate that

$$\frac{d^2 \hat{a}_i^{CR}}{dt^2} + i\Psi \frac{d\hat{a}_i^{CR}}{dt} - \chi_3^2 |A_{p,0}|^2 \hat{a}_i^{CR} = 0 \quad (\text{E.8})$$

The general solution of these two uncoupled equations are

$$\hat{a}_s^{CR}(t) = (\alpha_s \cosh(gt) + \beta_s \sinh(gt)) e^{-i(\Psi/2)t} \quad (\text{E.9})$$

$$\hat{a}_i^{CR}(t) = (\alpha_i \cosh(gt) + \beta_i \sinh(gt)) e^{-i(\Psi/2)t} \quad (\text{E.10})$$

where α_s , β_s , α_i and β_i are coefficients whose values are fixed by the boundary condition. The complex factor g can be determined substituting these solutions, and their time-derivatives, in the Sturm-Liouville equations. For instance, we have

$$\begin{aligned} \frac{d}{dt} [\hat{a}_s^{CR}] &= \frac{d}{dt} [(\alpha_s \cosh(gt) + \beta_s \sinh(gt)) e^{-i(\Psi/2)t}] = \\ &= (\alpha_s g \sinh(gt) + \beta_s g \cosh(gt)) e^{-i(\Psi/2)t} + (\alpha_s \cosh(gt) + \beta_s \sinh(gt)) \left(-i \frac{\Psi}{2} \right) e^{-i(\Psi/2)t} \end{aligned} \quad (\text{E.11})$$

and

$$\begin{aligned}
 \frac{d^2}{dt^2} [\hat{a}_s^{CR}] &= \frac{d}{dt} \left[g (\alpha_s \sinh (gt) + \beta_s \cosh (gt)) e^{-i(\Psi/2)t} + \right. \\
 &\quad \left. + (\alpha_s \cosh (gt) + \beta_s \sinh (gt)) \left(-i \frac{\Psi}{2} \right) e^{-i(\Psi/2)t} \right] = \\
 &= g^2 (\alpha_s \cosh (gt) + \beta_s \sinh (gt)) e^{-i(\Psi/2)t} + \\
 &\quad + g (\alpha_s \sinh (gt) + \beta_s \cosh (gt)) \left(-i \frac{\Psi}{2} \right) e^{-i(\Psi/2)t} + \\
 &\quad + g (\alpha_s \sinh (gt) + \beta_s \cosh (gt)) \left(-i \frac{\Psi}{2} \right) e^{-i(\Psi/2)t} + \\
 &\quad + (\alpha_s \cosh (gt) + \beta_s \sinh (gt)) \left(-\frac{\Psi^2}{4} \right) e^{-i(\Psi/2)t} = \\
 &= \left(g^2 - \frac{\Psi}{4} \right) [\alpha_s \cosh (gt) + \beta_s \sinh (gt)] e^{-i(\Psi/2)t} - \\
 &\quad - (ig\Psi) [\alpha_s \sinh (gt) + \beta_s \cosh (gt)] e^{-i(\Psi/2)t} \tag{E.12}
 \end{aligned}$$

Substituting Eq. (E.11) and Eq. (E.12) in Eq. (E.7) we obtain:

$$\begin{aligned}
 &\left(g^2 - \frac{\Psi^2}{4} \right) [\alpha_s \cosh (gt) + \beta_s \sinh (gt)] e^{-i(\Psi/2)t} - (ig\Psi) [\alpha_s \sinh (gt) + \beta_s \cosh (gt)] e^{-i(\Psi/2)t} + \\
 &\quad + (ig\Psi) [\alpha_s \sinh (gt) + \beta_s \cosh (gt)] e^{-i(\Psi/2)t} - i\Psi \left(i \frac{\Psi}{2} \right) [\alpha_s \cosh (gt) + \beta_s \sinh (gt)] e^{-i(\Psi/2)t} + \\
 &\quad - \chi_3^2 |A_{p,0}|^2 [\alpha_s \cosh (gt) + \beta_s \sinh (gt)] e^{-i(\Psi/2)t} = 0 \tag{E.13}
 \end{aligned}$$

that can be rewritten as

$$\left(g^2 + \frac{\Psi^2}{4} - \chi_3^2 |A_{p,0}|^2 \right) [\alpha_s \cosh (gt) + \beta_s \sinh (gt)] e^{-i(\Psi/2)t} = 0 \tag{E.14}$$

This means that it must be

$$g^2 = -\frac{\Psi}{4} + \chi_3^2 |A_{p,0}|^2 \quad \text{hence} \quad g = \sqrt{\chi_3^2 |A_{p,0}|^2 - \left(\frac{\Psi}{2} \right)^2} \tag{E.15}$$

The same solution can be found considering the second Sturm-Liouville equation (i.e, the one for \hat{a}_i^{CR}).

To determine the expressions for the coefficients α_s , β_s , α_i and β_i we can exploit, as boundary conditions, that at $t = 0$ it must be

$$\hat{a}_s^{CR}(0) = \hat{a}_{s,0}^{CR} \quad \text{and} \quad \hat{a}_i^{CR}(0) = \hat{a}_{i,0}^{CR} \tag{E.16}$$

Imposing this condition in Eq. (E.9) and Eq. (E.10) we obtain

$$\alpha_s = \hat{a}_{s,0}^{CR} \quad \text{and} \quad \alpha_i = \hat{a}_{i,0}^{CR} \quad (\text{E.17})$$

Thus, we obtain

$$\hat{a}_s^{CR}(t) = \left(\hat{a}_{s,0}^{CR} \cosh(gt) + \beta_s \sinh(gt) \right) e^{-i(\Psi/2)t} \quad (\text{E.18})$$

and

$$\hat{a}_i^{CR}(t) = \left(\hat{a}_{i,0}^{CR} \cosh(gt) + \beta_i \sinh(gt) \right) e^{-i(\Psi/2)t} \quad (\text{E.19})$$

Substituting Eq. (E.18) and Eq. (E.19) in Eq. (E.1) we obtain:

$$\begin{aligned} & \frac{d}{dt} \left[\left(\hat{a}_{s,0}^{CR} \cosh(gt) + \beta_s \sinh(gt) \right) e^{i(\Psi/2)t} \right] = \\ & = g \left(\hat{a}_{s,0}^{CR} \sinh(gt) + \beta_s \cosh(gt) \right) e^{-i(\Psi/2)t} + \left(\hat{a}_{s,0}^{CR} \cosh(gt) + \beta_s \sinh(gt) \right) \left(-i \frac{\Psi}{2} \right) e^{-i(\Psi/2)t} = \\ & = -i\chi_3 |A_{p,0}| \left[\left(\hat{a}_{i,0}^{CR} \cosh(gt) + \beta_i \sinh(gt) \right)^\dagger \right] e^{i(\Psi/2)t} e^{-i\Psi t} \end{aligned} \quad (\text{E.20})$$

from which

$$g \left(\hat{a}_{s,0}^{CR} \sinh(gt) + \beta_s \cosh(gt) \right) - i \frac{\Psi}{2} \left(\hat{a}_{s,0}^{CR} \cosh(gt) + \beta_s \sinh(gt) \right) \quad (\text{E.21})$$

$$= -i\chi_3 |A_{p,0}| \left(\hat{a}_{i,0}^{CR} \cosh(gt) + \beta_i \sinh(gt) \right)^\dagger \quad (\text{E.22})$$

This relation must be fulfilled in each instant t , at $t = 0$ we have

$$g\beta_s - i \frac{\Psi}{2} \hat{a}_{s,0}^{CR} = -i\chi_3 |A_{p,0}| \left(\hat{a}_{i,0}^{CR} \right)^\dagger \quad \text{hence} \quad \beta_s = \frac{i}{g} \left(\frac{\Psi}{2} \hat{a}_{s,0}^{CR} - \chi_3 |A_{p,0}| \left(\hat{a}_{i,0}^{CR} \right)^\dagger \right) \quad (\text{E.23})$$

Similarly, we obtain

$$\beta_i = \frac{i}{g} \left(\frac{\Psi}{2} \hat{a}_{i,0}^{CR} - \chi_3 |A_{p,0}| \left(\hat{a}_{s,0}^{CR} \right)^\dagger \right) \quad (\text{E.24})$$

Thus, the solutions of Eq. (E.1) and Eq. (E.2) are:

$$\begin{aligned} \hat{a}_{s(i)}^{CR}(t) &= \left[\hat{a}_{s(i),0}^{CR} \cosh(gt) + \frac{i}{g} \left(\frac{\Psi}{2} \hat{a}_{s(i),0}^{CR} - \chi_3 |A_{p,0}| \left(\hat{a}_{i(s),0}^{CR} \right)^\dagger \right) \sinh(gt) \right] e^{-i(\Psi/2)t} = \\ &= \left[\hat{a}_{s(i),0}^{CR} \left(\cosh(gt) + \frac{i\Psi}{2g} \sinh(gt) \right) - \frac{i\chi_3 |A_{p,0}|}{g} \hat{a}_{i(s),0}^\dagger \sinh(gt) \right] \end{aligned} \quad (\text{E.25})$$

Appendix F

Identities for the squeezing spectrum calculation

Proof of the identity (3.109).

We first express the integrand of Eq. (3.109) in terms of the definition (3.108)

$$\begin{aligned}
\langle \Delta \hat{Y}^\theta(\omega) \Delta \hat{Y}^\theta(\omega') \rangle &= \langle (\hat{Y}^\theta(\omega) - \langle \hat{Y}^\theta(\omega) \rangle) (\hat{Y}^\theta(\omega') - \langle \hat{Y}^\theta(\omega') \rangle) \rangle \\
&= \langle \hat{Y}^\theta(\omega) \hat{Y}^\theta(\omega') - \hat{Y}^\theta(\omega) \langle \hat{Y}^\theta(\omega') \rangle - \langle \hat{Y}^\theta(\omega) \rangle \hat{Y}^\theta(\omega') + \langle \hat{Y}^\theta(\omega) \rangle \langle \hat{Y}^\theta(\omega') \rangle \rangle \\
&= \langle \hat{Y}^\theta(\omega) \hat{Y}^\theta(\omega') \rangle - \langle \hat{Y}^\theta(\omega) \rangle \langle \hat{Y}^\theta(\omega') \rangle - \langle \hat{Y}^\theta(\omega) \rangle \langle \hat{Y}^\theta(\omega') \rangle + \langle \hat{Y}^\theta(\omega) \rangle \langle \hat{Y}^\theta(\omega') \rangle \\
&= \langle \hat{Y}^\theta(\omega) \hat{Y}^\theta(\omega') \rangle - \langle \hat{Y}^\theta(\omega) \rangle \langle \hat{Y}^\theta(\omega') \rangle \tag{F.1}
\end{aligned}$$

Now using the definition of $\hat{Y}^\theta(\omega)$ given in (3.108) we can write that

$$\begin{aligned}
\hat{Y}^\theta(\omega) \hat{Y}^\theta(\omega') &= i(e^{i\frac{\theta}{2}} \hat{a}_\omega^\dagger - e^{-i\frac{\theta}{2}} \hat{a}_\omega) \cdot i(e^{i\frac{\theta}{2}} \hat{a}_{\omega'}^\dagger - e^{-i\frac{\theta}{2}} \hat{a}_{\omega'}) \\
&= -(e^{i\theta} \hat{a}_\omega^\dagger \hat{a}_{\omega'}^\dagger - \hat{a}_\omega^\dagger \hat{a}_{\omega'} - \hat{a}_\omega \hat{a}_{\omega'}^\dagger + e^{-i\theta} \hat{a}_\omega \hat{a}_{\omega'}) \tag{F.2}
\end{aligned}$$

and then calculating the expectation value

$$\langle \hat{Y}^\theta(\omega) \hat{Y}^\theta(\omega') \rangle = -(e^{i\theta} \langle \hat{a}_\omega^\dagger \hat{a}_{\omega'}^\dagger \rangle - \langle \hat{a}_\omega^\dagger \hat{a}_{\omega'} \rangle - \langle \hat{a}_\omega \hat{a}_{\omega'}^\dagger \rangle + e^{-i\theta} \langle \hat{a}_\omega \hat{a}_{\omega'} \rangle) \tag{F.3}$$

$$\langle \hat{Y}^\theta(\omega) \rangle \langle \hat{Y}^\theta(\omega') \rangle = -(e^{i\theta} \langle \hat{a}_\omega^\dagger \rangle \langle \hat{a}_{\omega'}^\dagger \rangle - \langle \hat{a}_\omega^\dagger \rangle \langle \hat{a}_{\omega'} \rangle - \langle \hat{a}_\omega \rangle \langle \hat{a}_{\omega'}^\dagger \rangle + e^{-i\theta} \langle \hat{a}_\omega \rangle \langle \hat{a}_{\omega'} \rangle) \tag{F.4}$$

We can non substitute (F.1) into (3.109), exploiting also (F.3) and (F.4)

$$\begin{aligned}
 S(\omega) &= \int_0^\infty d\omega' (-e^{i\theta} \langle \hat{a}_\omega^\dagger \hat{a}_{\omega'}^\dagger \rangle + \langle \hat{a}_\omega^\dagger \hat{a}_{\omega'} \rangle + \langle \hat{a}_\omega \hat{a}_{\omega'}^\dagger \rangle - e^{-i\theta} \langle \hat{a}_\omega \hat{a}_{\omega'} \rangle + \\
 &\quad + e^{i\theta} \langle \hat{a}_\omega \rangle \langle \hat{a}_{\omega'}^\dagger \rangle - \langle \hat{a}_\omega^\dagger \rangle \langle \hat{a}_{\omega'} \rangle - \langle \hat{a}_\omega \rangle \langle \hat{a}_{\omega'}^\dagger \rangle + e^{-i\theta} \langle \hat{a}_\omega \rangle \langle \hat{a}_{\omega'} \rangle) = \\
 &= 2N(\omega) + \int_0^\infty d\omega' (-e^{i\theta} \langle \hat{a}_\omega^\dagger \hat{a}_{\omega'}^\dagger \rangle - e^{-i\theta} \langle \hat{a}_\omega \hat{a}_{\omega'} \rangle + e^{i\theta} \langle \hat{a}_\omega^\dagger \rangle \langle \hat{a}_{\omega'}^\dagger \rangle + e^{-i\theta} \langle \hat{a}_\omega \rangle \langle \hat{a}_{\omega'} \rangle + \delta(\omega - \omega')) = \\
 &= 2N(\omega) + 1 + \int_0^\infty d\omega' (-e^{i\theta} \langle \hat{a}_\omega^\dagger \hat{a}_{\omega'}^\dagger \rangle - e^{-i\theta} \langle \hat{a}_\omega \hat{a}_{\omega'} \rangle + e^{i\theta} \langle \hat{a}_\omega^\dagger \rangle \langle \hat{a}_{\omega'}^\dagger \rangle + e^{-i\theta} \langle \hat{a}_\omega \rangle \langle \hat{a}_{\omega'} \rangle) = \\
 &= 2N(\omega) + 1 - \int_0^\infty d\omega' e^{i\theta} (\langle \hat{a}_\omega^\dagger \hat{a}_{\omega'}^\dagger \rangle - \langle \hat{a}_\omega^\dagger \rangle \langle \hat{a}_{\omega'}^\dagger \rangle) - \int_0^\infty d\omega' e^{-i\theta} (\langle \hat{a}_\omega \hat{a}_{\omega'} \rangle - \langle \hat{a}_\omega \rangle \langle \hat{a}_{\omega'} \rangle) = \\
 &= 2N(\omega) + 1 - M^*(\omega) e^{-i\theta} - M(\omega) e^{i\theta} = \\
 &= 2N(\omega) + 1 - |M(\omega)| e^{-i\theta} e^{i\theta} - |M(\omega)| e^{i\theta} e^{-i\theta} = \\
 &= 2N(\omega) + 1 - 2|M(\omega)| \tag{F.5}
 \end{aligned}$$

Where we have used the definition of the squeezing angle $M(\omega) = |M(\omega)| e^{i\theta}$ and its complex conjugate.

Proof of the identity (3.110).

It is first good to compute $N(\omega)$ for an input vacuum state.

$$\begin{aligned}
 N(\omega) &= \int_0^\infty d\omega' (\langle vac | \hat{a}_\omega^\dagger \hat{a}_{\omega'} | vac \rangle - \langle vac | \hat{a}_\omega^\dagger | vac \rangle \langle vac | \hat{a}_{\omega'} | vac \rangle) \\
 &= \int_0^\infty d\omega' \langle vac | \hat{a}_\omega^\dagger \hat{a}_{\omega'} | vac \rangle
 \end{aligned}$$

We can now notice that the integrand is just the photon number operator, already used to calculate the gain G in (3.95). Hence, for example, in the 3WM case (similarly for 4WM)

$$\begin{aligned}
 N(\omega) &= \int_0^\infty d\omega' \langle vac | \hat{a}_\omega^\dagger \hat{a}_{\omega'} | vac \rangle \\
 &= \int_0^\infty d\omega' \langle vac | \left(u^*(\omega, t) \hat{a}_{\omega,0}^\dagger - iv^*(\omega, t) \hat{a}_{\omega_p - \omega,0} \right) \left(u(\omega', t) \hat{a}_{\omega',0} + iv(\omega', t) \hat{a}_{\omega_p - \omega',0}^\dagger \right) | vac \rangle \\
 &= \int_0^\infty d\omega' \langle vac | \left(u^*(\omega, t) u(\omega', t) \hat{a}_{\omega,0}^\dagger \hat{a}_{\omega',0} + v^*(\omega, t) v(\omega', t) \hat{a}_{\omega_p - \omega,0} \left(\hat{a}_{\omega_p - \omega',0} \right)^\dagger + \right. \\
 &\quad \left. + iu^*(\omega, t) v(\omega', t) \hat{a}_{\omega,0}^\dagger \left(\hat{a}_{\omega_p - \omega',0} \right)^\dagger - iv^*(\omega, t) u(\omega', t) \hat{a}_{\omega_p - \omega,0} \hat{a}_{\omega',0} \right) | vac \rangle \\
 &= v^*(\omega, t) \int_0^\infty d\omega' v(\omega', t) \langle vac | \left(\hat{a}_{\omega_p - \omega,0}^\dagger \hat{a}_{\omega_p - \omega',0} + \delta(\omega' - \omega) \right) | vac \rangle \\
 &= |v(\omega, t)|^2 \\
 &= \left| \frac{\Upsilon}{g} \sinh g(\omega) t \right|^2 \tag{F.6}
 \end{aligned}$$

Appendix G

Calculation of resonator plus C_g equivalent impedance

Calculating the equivalent impedance of the cluster formed by the resonator plus C_g requires the knowledge of the impedances of all the circuit elements that compose it. We recall that the impedance of a simple capacitance and inductance are

$$\begin{aligned}Z_C &= \frac{1}{i\omega C} \\Z_L &= i\omega L\end{aligned}$$

The impedance of the cluster resonator + C_g is found as

$$\begin{aligned}\frac{1}{Z_{\text{res}+C_g}} &= \frac{1}{Z_{\text{res}}} + \frac{1}{Z_{C_g}} \\ &= \frac{1}{Z_{C_c} + Z_{L_r} // Z_{C_r}} + \frac{1}{Z_{C_g}}\end{aligned}\tag{G.1}$$

where C_c is the coupling capacitance, C_r is the resonator capacitance, L_r is the resonator inductance and the symbol $Z_x // Z_y$ stands for the parallel impedance of the elements x and y . Thus, we find

$$\begin{aligned}\frac{1}{Z_{L_r} // Z_{C_r}} &= \frac{1}{i\omega L_r} + i\omega C_r \\ &= \frac{1 - \omega^2 L_r C_r}{i\omega L_r} \\ \rightarrow Z_{L_r} // Z_{C_r} &= \frac{i\omega L_r}{1 - \omega^2 L_r C_r}\end{aligned}\tag{G.2}$$

and

$$\begin{aligned} Z_{\text{res}} &= \frac{1}{i\omega C_c} + \frac{i\omega L_r}{1 - \omega^2 L_r C_r} \\ &= \frac{1 - \omega^2 L_r C_c - \omega^2 L_r C_c}{i\omega C_c(1 - \omega^2 L_r C_r)} \end{aligned} \quad (\text{G.3})$$

The impedance of the cluster is then found as

$$\begin{aligned} \frac{1}{Z_{\text{res}+C_g}} &= \frac{i\omega C_c(1 - \omega^2 L_r C_r)}{1 - \omega^2 L_r C_c - \omega^2 L_r C_c} + i\omega C_g \\ \rightarrow Z_{\text{res}+C_g} &= \frac{1 - (C_c + C_r)L_r\omega^2}{i\omega\left(C_g(1 - (C_c + C_r)L_r\omega^2) + C_c(1 - C_r L_r\omega^2)\right)} \end{aligned} \quad (\text{G.4})$$

Bibliography

- [1] F. Arute et al. “Quantum supremacy using a programmable superconducting processor”. In: *Nature* 574 (2019), pp. 505–510.
- [2] A. Barone and G. Paternò. *Physics and Applications of the Josephson Effect*. John Wiley & Sons Inc, pag. 330, 1982.
- [3] S. Barzanjeh et al. “Microwave quantum illumination using a digital receiver”. In: *Sci. Adv.* 6 (19 2020).
- [4] N. Bergeal et al. “Analog information processing at the quantum limit with a Josephson ring modulator”. In: *Nat. Phys.* 6.296–302 (2010).
- [5] N. Bergeal et al. “Phase-preserving amplification near the quantum limit with a Josephson ring modulator”. In: *Nature* 465.64–68 (2010).
- [6] A. Blais et al. “Circuit quantum electrodynamics”. In: *Rev. Mod. Phys.* 93 (2 2021), p. 025005.
- [7] Alexandre Blais et al. “Cavity quantum electrodynamics for superconducting electrical circuits: An architecture for quantum computation”. In: *Phys. Rev. A* 69 (6 2004), p. 062320.
- [8] M. A. Castellanos-Beltran and K. W. Lehnert. “Widely tunable parametric amplifier based on a superconducting quantum interference device array resonator”. In: *Appl. Phys. Lett.* 91 (083509 2007).
- [9] C. M. Caves. “Quantum limits on noise in linear amplifiers”. In: *Phys. Rev. D* 1817.26 (1982).
- [10] C. M. Caves et al. “Quantum limits on phase-preserving linear amplifiers”. In: *Phys. Rev. A* 063802.86 (2012).
- [11] G. Cerullo and S. De Silvestri. “Ultrafast optical parametric amplifiers”. In: *Rev. Sci. Instrum.* 1.74 (2003).
- [12] S. Chaudhuri et al. “Broadband parametric amplifiers based on nonlinear kinetic inductance artificial transmission lines”. In: *Appl. Phys. Lett.* 110 (152610 2017).
- [13] M. J. Collett and D. F. Walls. “Quantum Limits to Light Amplifiers”. In: *Phys. Rev. Lett.* 2442.61 (1988).

- [14] A. L. Cullen. “Theory of the travelling-wave parametric amplifier”. In: *Proceedings of the IEEE - Part B: Electronic and Communication Engineering*. 1959 107 (32 1991).
- [15] G. W. Dahimann and E. M. Yeatman. “Microwave characteristics of meander inductors fabricated by 3D self-assembly”. In: *8th IEEE International Symposium on High Performance Electron Devices for Microwave and Optoelectronic Applications (Cat. No.00TH8534)* 21 (06 2000).
- [16] C. L. Degen, F. Reinhard, and P. Cappellaro. “Quantum sensing”. In: *Rev. Mod. Phys.* 89 (3 2017).
- [17] T. Dixon et al. “Capturing Complex Behavior in Josephson Traveling-Wave Parametric Amplifiers”. In: *Phys. Rev. App.* 034058.14 (2020).
- [18] G. J. Dolan. “Offset masks for lift-off photoprocessing”. In: *Appl. Phys. Lett.* 337.31 (1977).
- [19] J. Dowling and G. J. Milburn. “Quantum technology: the second quantum revolution”. In: *Phil. Trans. R. Soc. A.* 1655-1674.361 (2003).
- [20] L Fasolo, A. Greco, and E. Enrico. *Superconducting Josephson-Based Metamaterials for Quantum-Limited Parametric Amplification: A Review*. Intech Open, 2017.
- [21] E. Flurin et al. “Generating Entangled Microwave Radiation Over Two Transmission Lines”. In: *Phys. Rev. Lett.* 183901.109 (2012).
- [22] T. A. Fulton and G. J. Dolan. “Observation of single-electron charging effects in small tunnel junctions”. In: *Phys. Rev. Lett.* 109.59 (1987).
- [23] Angelo Greco et al. “Quantum model for rf-SQUID-based metamaterials enabling three-wave mixing and four-wave mixing traveling-wave parametric amplification”. In: *Phys. Rev. B* 104 (18 2021).
- [24] A. L. Grimsmo and A. Blais. “Squeezing and quantum state engineering with Josephson travelling wave amplifiers”. In: *Npj Quantum Inf.* 20.3 (2017).
- [25] H. A. Haus and J. A. Mullen. “Quantum Noise in Linear Amplifiers”. In: *Phys. Rev.* 2407.128 (1962).
- [26] M. O. Hecht, A. J. Cobarrubia, and K. M. Sundquist. “An Engineer’s Brief Introduction to Microwave Quantum Optics and a Single-Port State-Space Representation”. In: *IEEE Trans. on Quantum Eng.* 2.4100508 (2021).
- [27] “<https://www.lownoisefactory.com/>”. In: ().
- [28] R. Igreja and C. J. Dias. “Analytical evaluation of the interdigital electrodes capacitance for a multi-layered structure”. In: *Physical is Sens. Actuator A Phys.* 112 (2-3 2004).

- [29] Boggio. J. “The pressure dependence of the oxidation of aluminum at 298 °K”. In: *Surf. Sci.* 14.1 (1969).
- [30] M. B. Ketchen et al. “Sub- μm , planarized, Nb-AlO_x-Nb Josephson process for 125 mm wafers developed in partnership with Si technology”. In: *Appl. Phys. Lett.* 59 (2609 1991).
- [31] D. Kinion and J. Clarke. “Superconducting quantum interference device as a near-quantum-limited amplifier for the axion dark-matter experiment”. In: *Appl. Phys. Lett.* 98.202503 (2011).
- [32] C. Kissling et al. “Parameter spread tolerance in a dispersion-engineered Josephson Traveling-Wave Parametric Amplifier with three-wave-mixing”. In: *Poster at EUCAS2021* (2021).
- [33] P. Krantz et al. “A quantum engineer’s guide to superconducting qubits”. In: *Appl. Phys. Rev.* 6 (021318 2019), p. 025005.
- [34] R. Loudon. *The Quantum Theory of Light, Third Edition*. Oxford Science Publication, 2000.
- [35] L. Maccone and C. Ren. “Quantum Radar”. In: *Phys. Rev. Lett.* 124 (20 2020).
- [36] C. Macklin et al. “A near-quantum-limited Josephson traveling-wave parametric amplifier”. In: *Science* 350.6258 (2015).
- [37] M. Malnou et al. “Three-Wave Mixing Kinetic Inductance Traveling-Wave Amplifier with Near-Quantum-Limited Noise Performance”. In: *PRX Quantum* 2 (1 2021).
- [38] Alessandro Miano and Oleg A. Mukhanov. “Symmetric Traveling Wave Parametric Amplifier”. In: *IEEE Transactions on Applied Superconductivity* 29.5 (2019), pp. 1–6.
- [39] F.A. Miranda et al. “Measurements of complex permittivity of microwave substrates in the 20 to 300 K temperature range from 26.5 to 40.0 GHz”. In: *Proceeding Jul 1989; 10 p; International cryogenic materials conference; Los Angeles, CA (USA)* 21 (06 1989).
- [40] B. R. Mollow and R. J. Glauber. “Quantum Theory of Parametric Amplification. I”. In: *Phys. Rev.* 1076.160 (1967).
- [41] P. Navez et al. “Towards the Heisenberg limit in microwave photon detection by a qubit array”. In: *Phys. Rev. B* 103 (6 2021).
- [42] C. Nguyen. *Radio-Frequency Integrated-Circuit Engineering*. Wiley, 2015.
- [43] K. O’Brien et al. “Resonant Phase Matching of Josephson Junction Traveling Wave Parametric Amplifiers”. In: *Phys. Rev. Lett.* 157001.113 (2014).

- [44] A. D. O’Connell et al. “Microwave dielectric loss at single photon energies and millikelvin temperatures”. In: *Appl. Phys. Lett.* 92.112903 (2008).
- [45] E. Petrakou and for CAPP/IBS. “Haloscope searches for dark matter axions at the Center for Axion and Precision Physics Research”. In: *EPJ Web Conf.* 164 (01012 2017).
- [46] A. Ranadive et al. “Kerr reversal in Josephson meta-material and traveling wave parametric amplification”. In: *Nat. Commun.* 13.1737 (2022).
- [47] L. Ranzani et al. “Kinetic inductance traveling-wave amplifiers for multiplexed qubit readout”. In: *Appl. Phys. Lett.* 113 (242602 2018).
- [48] T Roy et al. “Broadband parametric amplification with impedance engineering: Beyond the gain-bandwidth product”. In: *Appl. Phys. Lett.* 107 (262601 2015).
- [49] R. N. Simons. *Coplanar Waveguide Circuits, Components, and Systems*. Wiley, 2001.
- [50] G. Stojanovic, L. Zivanov, and M. Damjanovic. “Compact Form of Expressions for Inductance Calculation of Meander Inductors”. In: *Serb. J. Electr. Eng.* 1 (3 2004).
- [51] M. Sweeny and R. Mahler. “A travelling-wave parametric amplifier utilizing Josephson junctions”. In: *IEEE Trans. Magn.* 21.2 (1985).
- [52] T. H. A. Van der Reep. “Mesoscopic Hamiltonian for Josephson traveling-wave parametric amplifiers”. In: *Phys. Rev. A* 063838.99 (2019).
- [53] R. Vijay, D. H. Slichter, and I. Siddiqi. “Observation of Quantum Jumps in a Superconducting Artificial Atom”. In: *Phys. Rev. Lett.* 106 (11 2011), p. 110502.
- [54] M. R. Vissers et al. “Low-noise kinetic inductance traveling-wave amplifier using three-wave mixing”. In: *Appl. Phys. Lett.* 108 (012601 2016).
- [55] U. Vool and M. Devoret. “Introduction to Quantum Electromagnetic Circuit”. In: *Int. J. of Circuit Theory and Appl.* 897.45 (2017).
- [56] L. Wang. “Fabrication stability of Josephson junctions for superconducting qubits”. In: *Technische Universitat Munchen* (2015).
- [57] T. C. White et al. “Traveling wave parametric amplifier with Josephson junctions using minimal resonator phase matching”. In: *Phys. Rev. Lett.* 242601.106 (2015).
- [58] W. Wustmann and V. Shumeiko. “Parametric resonance in tunable superconducting cavities”. In: *Phys. Rev. B* 184501.87 (2013).
- [59] O. Yaakobi et al. “Parametric amplification in Josephson junction embedded transmission lines”. In: *Phys. Rev. B* 87.144301 (2013).

- [60] T. Yamamoto et al. “Flux-driven Josephson parametric amplifier”. In: *Appl. Phys. Lett.* 93 (042510 2008).
- [61] J. Q. You and F. Nori. “Atomic physics and quantum optics using superconducting circuits”. In: *Nature* 589–597.474 (2011).
- [62] B. Yurke et al. “A low-noise series-array Josephson junction parametric amplifier”. In: *Appl. Phys. Lett.* 69 (3078 1996).
- [63] K. Zhou et al. “Dielectric Constant and Loss Tangent of Silicon at 700–900 GHz at Cryogenic Temperatures”. In: *IEEE Microw. Wirel. Compon. Lett.* 29.7 (2019).
- [64] A. B. Zorin. “Josephson Traveling-Wave Parametric Amplifier with Three-Wave Mixing”. In: *Phys. Rev. Applied* 034006.6 (2016).
- [65] A. B. Zorin. “Quasi-phasematching in a poled Josephson traveling-wave parametric amplifier with three-wave mixing”. In: *App. Phys. Lett.* 222601.118 (2021).
- [66] A. B. Zorin et al. “Traveling-Wave Parametric Amplifier Based on Three-Wave Mixing in a Josephson Metamaterial”. In: *2017 16th International Superconductive Electronics Conference (ISEC)* (2017), pp. 1–3.

This Ph.D. thesis has been typeset by means of the T_EX-system facilities. The typesetting engine was pdfL^AT_EX. The document class was `toptesi`, by Claudio Beccari, with option `tipotesi=scudo`. This class is available in every up-to-date and complete T_EX-system installation.